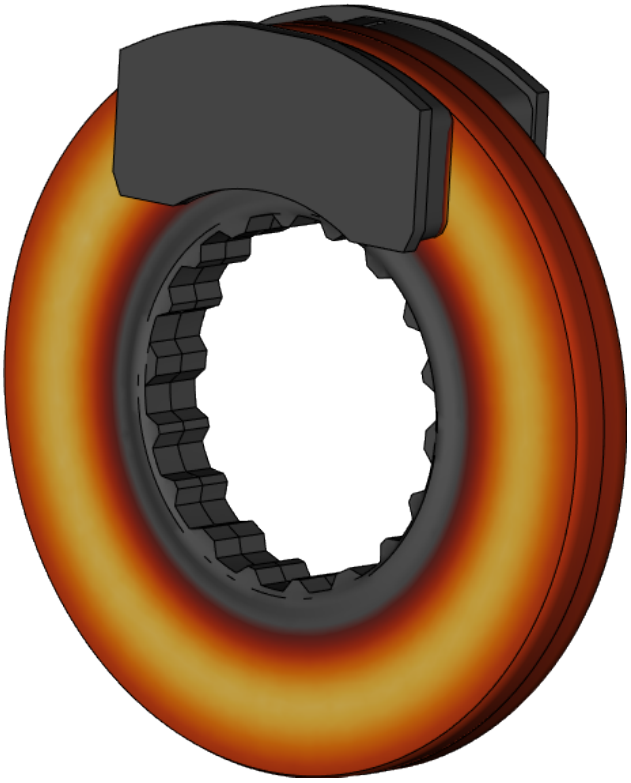

Finite Element Analysis of Wear and Temperature Development in Heavy-Duty Disc Brakes

Axisymmetric and 3D FE-Modelling with Rig-Test Validation and Parameter Calibration

Master's thesis in Applied Mechanics

MELVIN GLANS
EMIL SJÖSTRÖM

DEPARTMENT OF INDUSTRIAL AND MATERIALS SCIENCE
CHALMERS UNIVERSITY OF TECHNOLOGY
Gothenburg, Sweden 2026
www.chalmers.se

Master's thesis 2026

Finite Element Analysis of Wear and Temperature Development in Heavy-Duty Disc Brakes

Axisymmetric and 3D FE-Modelling with Rig-Test Validation and Parameter Calibration

MELVIN GLANS
EMIL SJÖSTRÖM

CHALMERS
UNIVERSITY OF TECHNOLOGY

Department of Industrial and Materials Science
Division of Computational Mechanics and Materials Engineering
Chalmers University of Technology
Gothenburg, Sweden 2026

Finite Element Analysis of Wear and Temperature Development in Heavy-Duty Disc Brakes
Axisymmetric and 3D FE-Modelling with Rig-Test Validation and Parameter calibration
MELVIN GLANS
EMIL SJÖSTRÖM

Supervisor: Tore Vernersson, Department of Mechanics and Maritime Sciences, Division of Dynamics
Martin Petersson, Volvo Group, Trucks Technology and Industrial Division
Examiner: Magnus Ekh, Department of Industrial and Materials Science, Division of Computational Mechanics and Materials Engineering

Master's Thesis 2026
Department of Industrial and Materials Science
Division of Computational Mechanics and Materials Engineering
Chalmers University of Technology
SE-412 96 Gothenburg
Telephone +46 31 772 1000

Cover: Isometric heat map visualization of a red-hot disc brake made in META.

Typeset in LaTeX
Printed by Chalmers Reproservice
Gothenburg, Sweden 2026

Finite Element Analysis of Wear and Temperature Development in Heavy-Duty Disc Brakes
Axisymmetric and 3D FE-Modelling with Rig-Test Validation and Parameter Calibration
MELVIN GLANS
EMIL SJÖSTRÖM
Department of Industrial and Materials Science
Chalmers University of Technology

Abstract

As exhaust emissions from vehicles continue to decline, non-exhaust emissions, particularly those arising from brake and tire wear, have become a critical area of interest and regulatory focus. The EU Euro 7 regulation will, for the first time, set requirements on the particle emission behaviour of brake systems and tires. Hence, the aim of this MSc thesis is to investigate wear and temperature development in truck disc brakes through the development of finite element (FE) models, which is validated against rig-test data. In addition, material parameters are calibrated towards measured data.

The FE-modelling consisted of axisymmetric and three-dimensional representations of both the entire brake assembly and a simplified half-model. Thermal and thermomechanical simulations of disc crack tests were performed on the models using the commercial software Abaqus to study the wear and temperature development. The thermal models were used with the optimisation software modeFRONTIER to fit and calibrate thermal material parameters. The results of the different models were compared with each other and with rig-test data.

The results showed that thermal axisymmetric models are efficient for fast temperature prediction and parameter fitting, but are limited in their ability to capture local contact effects, hot-spotting and non-uniform wear. The thermomechanical models provided a more detailed description of the interaction between contact pressure, temperature and wear, and showed that local temperature peaks and wear patterns can strongly influence the brake response. The 3D-model further demonstrated the importance of circumferential variations in the pad and disc, although its computational cost limited the possible mesh refinement and the duration that could be simulated. For multiple stop simulations, the use of a temperature dependent wear scaling factor gave a temperature development closer to the rig-test data, while the constant wear scaling factor gave wear results closer to the measured values. The parameter calibration showed that modeFRONTIER can be used to fit thermal and wear-related parameters, but also highlighted the risk of compensating for model simplifications with parameter tuning.

Keywords: brake, disc, pad, FE, wear, temperature, Euro 7, modeFRONTIER, Abaqus.

Preface

This report presents the results of a master's thesis project carried out at the Department of Industrial and Materials Science at Chalmers University of Technology in collaboration with Volvo Group during the spring of 2026.

Acknowledgements

We want to give our thanks to all those who have helped us during the course of this master's thesis project.

We would like to especially thank our supervisor at Chalmers, associate professor Tore Vernersson, whom has given us invaluable help, and whom's experience and guidance has been crucial. We would also like to thank our examiner, Magnus Ekh, for his guidance and for taking the time to read through our very long report.

At Volvo our supervisor Martin Petersson has helped a lot by giving us the information and advice needed to complete this master's thesis, and for that we are grateful. Others at Volvo have also been very helpful. For example we have had a lot of support from Zafer Yüce, Reza Khansari, Sara Salig and Jonas Löfgren with the CAE-aspect of our work, and they have been a tremendous help with their experience in that field. We would also like to thank Mathias Johansson in the CAE support team, whom has made sure that everything has worked smoothly for us.

We also want to thank our peer-reviewers and fellow master's thesis workers at Volvo, Linus Börjesson and Fredrik Hansson, for their feedback.

Many others at Volvo and at Chalmers have aided us during this projects course, and even though they are to many to list here, we are grateful for their help.

Lastly, we want to thank our group manager at Volvo, Ingela Stjärnvy. We want to thank her for her help and support, and for giving us the opportunity to do this master's thesis project.

Use Disclaimer Regarding AI

We take full responsibility for the content of this thesis work. AI was not used for writing any text. The only use of AI was to help find and review errors in Abaqus input files and in code, and in some instances suggested solutions in coding was used. This input from AI was however not trusted implicitly, and manual debugging was done. When AI was used it was the internal Volvo GPT service.

Melvin Glans, Emil Sjöström, Gothenburg, June 2026

Nomenclature

Abbreviations

3D	Three-dimensional
ALE	Arbitrary Lagrangian-Eulerian
ALM	Augmented Lagrange Method
CFD	Computational fluid dynamics
COF	Coefficient of friction
EU	European Union
FE	Finite element
FEA	Finite element analysis
MAE	Mean absolute error
MSE	Mean square error
OC	Organic composite
PDE	Partial differential equation
PID	Part-id
PINN	Physics-informed neural network
TEI	Thermoelastic instability

Subscripts

a	Air
d	Brake disc
p	Brake pad

Variables

α	Accommodation coefficient [-]
α	Linear thermal expansion coefficient [K^{-1}]
α^*	Normalisation factor for linear thermal expansion coefficient [-]
β_v	Volumetric thermal expansion coefficient [K^{-1}]
ΔW	Rate of change in wear volume [$\mathrm{m}^3 \cdot \mathrm{s}^{-1}$]
$\dot{E}$	Rate of change in thermal energy [W]
$\dot{K}$	Rate of change in kinetic energy [W]
$\dot{M}$	Rate of change in mechanical energy [W]
$\dot{U}$	Rate of change in potential energy [W]
ϵ	Emissivity [-]
$\frac{D}{Dt}$	Material time derivative operator [s^{-1}]
Γ	Boundary of domain
λ	Mean free path [m]
λ_L/λ_R	Hyperparameter of Lasso/Ridge regularisation [-]
λ_{th}	Thermal diffusivity
$\mathcal{D}$	Dissipation rate [W]

$\mathcal{E}$	Internal heat source [W/kg]
$\mathcal{L}$	Loss term of cost function [-]
μ	Coefficient of friction [-]
μ_a	Dynamic viscosity of air [Pas]
ν	Poisson's ratio [-]
ω	Angular velocity [rad $\cdot$ s^{-1}]
ϕ_0	Angle of brake pad [rad]
ρ	Density [kg/m^3]
ρ^*	Normalisation factor for density [-]
σ	Heat partition coefficient [-]
σ_B	Stefan-Boltzmann constant [W/(m^{2}K^4)]
τ	Torque [N $\cdot$ m]
θ	Angle coordinate [rad]
$\boldsymbol{\sigma}$	Cauchy stress tensor [Pa]
$\boldsymbol{\theta}$	Tensor of parameters of neural network
$\boldsymbol{\varepsilon}$	Total strain [-]
$\boldsymbol{\varepsilon}_e$	Elastic strain [-]
$\boldsymbol{\varepsilon}_{th}$	Thermal strain [-]
$\boldsymbol{v}$	Velocity tensor [m/s]
$\zeta(t)$	Time-dependent parameter of mixed constant wear-pressure pressure distribution [-]
c_p	Isobaric specific heat capacity [J/(kgK)]
c_p^*	Normalisation factor for specific heat [-]
D	Disc diameter [m]
d	Mean plane distance [m]
E	Thermal energy [J]
E	Young's modulus [Pa]
e	Specific internal energy [J/kg]
F_N	Normal force [N]
F_{clamp}	Clamp force [N]
F_{dp}	Mutual radiation factor between pad and disc surfaces [-]
F_{fric}	Frictional force [N]
g_1, g_2	Correction lengths [m]
H	Material (Vickers) hardness [Pa]
h	Heat transfer coefficient of convection [W/(m^{2}K)]
h_c	Thermal contact conductance [W/(m^{2}K)]
h_w	Wear depth [m]
h_{av}	Average wear depth [m]
h_{s0}	Thermal resistance coefficient [W/(m^{2}K)]
J	Moment of inertia [kgm^2]
K	Kinetic energy [J]
k	Wear scaling factor [-]
k^*	Normalisation factor for wear scaling factors [-]
k_g/k_a	Thermal conductivity of gas/air [W/(mK)]
k_t	Thermal conductivity [W/(mK)]
k_t^*	Normalisation factor for conductivity and gap conductance [-]
k_w	Contact pair dependent wear coefficient [-]
M	Mechanical energy [J]

m	Mass [kg]
P	Power [W]
p	Contact pressure [Pa]
p_1	Pressure of constant pressure distribution [Pa]
p_2	Maximum pressure of constant wear pressure distribution [Pa]
P_{fric}	Frictional power [W]
Q	Heat [J]
q, $\boldsymbol{q}$	Heat flux [W/m^2]
R	Thermal resistance [m^{2}K/W]
r	Radius [m]
r_1	Inner radius of brake disc [m]
r_2	Inner radius of brake pads [m]
r_3	Outer radius of brake pads [m]
r_4	Outer radius of brake disc [m]
r_{eq}	Equivalent radius [m]
S	Frictional contact area [m^2]
s	Sliding distance [m]
T	Temperature [K]
t	Time [s]
T_0	Initial temperature [K]
T_e	Ambient temperature [K]
U	Potential energy [J]
v	Velocity [m $\cdot$ s^{-1}]
W	Wear volume [m^3]
w	Parameter in calculation of conductance through contact spots [-]
z	Through thickness coordinate [m]
Pr	Prandtl number [-]
Re	Reynolds number [-]

Contents

1
Introduction

In this chapter, the thesis project is introduced. Based on the project background, the aim, the delimitations and goal are presented.

1.1 Background

The development of new vehicles for heavy-duty transport is guided by the emergence of new regulations. These exist to make vehicles safer and limit their environmental impact. To reduce the strain on the environment, regulatory bodies such as the European Union (EU) have put restrictions on the exhaust emissions from new vehicles [1], [2].

However, as emissions of exhaust particles decrease for each new generation of vehicles [1], another emission source has been largely untouched, namely non-exhaust emissions from wear of components such as tires and brakes. Those emissions will for the first time be regulated in the upcoming Euro 7 regulation by the EU [2].

These new regulations necessitate a better understanding of how the emissions from disc brakes develop and spread in the environment. It is known that both wear and the emission rate of the particles are dependent on the braking temperature [3].

To accurately predict particle emissions, a first step is to study the wear of the disc brakes. It is thus pertinent to develop finite element (FE) models for the study of temperature and wear distribution in the brake disc and brake pads during different driving conditions.

1.2 Aim

This master's thesis project was carried out in collaboration between Volvo Group and Chalmers University of Technology as a support for their ongoing FFI ("Fordonsstrategisk forskning och innovation") project "Reduction of brake particle emissions from urban heavy-duty transports" (sv. "Reduktion av bromspartikelemissioner från urbana lastbilstransporter"). The thesis will in part entail development of existing FE-models at Volvo, and also explore capabilities of finite element analysis (FEA) when it comes to the thermo-mechanical contact problem of the disc brake, with special attention to local temperatures and wear. In addition, it will explore the use of machine learning with data from tests in brake rigs to further improve the model.

1.3 Delimitations

This project is part of a 20-week master's thesis running from 19 January 2026 to 7 June 2026. Given the limited time-frame, delimitations are necessary to narrow the project scope and ensure that the most relevant results are obtained.

Given the limited time-frame, this project does not include a parametric study of brake geometry or performance optimisation. All models will therefore share the same geometry and be evaluated under identical load cases. Geometry and loading conditions are defined to match the test data provided by Volvo Group to support validation.

Certain assumptions will have to be made to save computational cost and ensure a tractable solution. The following assumptions and delimitations are introduced.

- The response is assumed to be thermoelastic.
- All materials behave isotropically.
- The initiation and propagation of cracks in the brake disc is not considered.
- The brake is assumed to operate under dry conditions, and the effect of moisture and lubrication is disregarded.
- All frictional work is assumed to be converted into thermal energy. Losses due to vibration, squeal and other dynamic effects are neglected.
- For most models, only part of the brake assembly is modelled.
- The temperature of the surrounding air is assumed to be constant.
- Thermal conduction from the brake assembly is simplified
- The clamp force is assumed to be constant during a brake cycle.
- Only models of a solid disc are considered, how to model ventilated discs is only discussed.

1.4 Goals

The overarching aim of the thesis is to develop FE-models that can accurately simulate the temperature development in the brake disc under different braking events. Goals of the thesis are:

- To develop and compare axisymmetric and three-dimensional models.
- To develop and compare thermal (only temperature with prescribed contact pressure and friction) and thermomechanical (temperature and stress/strain with simulated contact pressure) models.
- To compare models with data from brake rig-tests.
- To explore methods of fitting parameters of FE-models (thermal conductivity, specific heat, clamp force, etc.) such that errors of models are minimised.
- To explore the capabilities of FEA when it comes to thermomechanical contact problems, as found in disc brakes, with special attention to local temperatures and wear.

1.5 Confidentiality

For this project, information was used that is proprietary to Volvo Group and/or their suppliers. Sensitive information in the report will therefore be removed in order to protect Volvo and affiliates. In some instances, this may mean that no values are given for input parameters used in simulations or in tests. In other instances, values may be given, but will be normalised using scaling factors.

2
Theory

This chapter details the relevant theory for this thesis project. This includes information on brakes used in heavy-duty vehicles, the mechanics and thermodynamics of braking, as well as sections on phenomena such as friction, wear and hot-spotting.

2.1 Brakes in Heavy-Duty Vehicles

The definition of a brake is the deceleration of a moving machine part with the exertion of a force by a stationary machine part. In friction brakes, mechanical energy is converted into thermal energy by frictional heat generation [4]. Brakes are a crucial vehicle component when it comes to safety. They must be able to operate under any reasonably foreseeable condition. This includes differing road conditions, vehicle loads, driving scenarios and driver experience. [5, p. 1].

2.1.1 Service Brakes

The function of service brakes is to decelerate the vehicle by friction braking and they are the primary braking system. Three types of service brakes are drum, band and disc brakes [4] [6] [5]. For heavy-duty vehicles, the two friction braking systems in use are the drum and disc brakes [7].

Both drum and disc brakes consist of a rotating machine part and a stationary machine part consisting of some sort of friction material. When the stationary machine part is pressed against the rotating machine part, the frictional force between the two exerts a counteracting torque on the rotating machine part, causing deceleration. The stationary machine part consisting of the friction material is called pads for disc brakes and linings for drum brakes. For drum brakes the linings press outwards in the radial direction on a rotating cylinder called the brake drum. Compared to disc brakes, brake pads axially clamp the rotating part called the brake disc or brake rotor [7] [4]. The pads only cover approximately 70° of the friction surface for disc brakes [7]. The brake type that will be in focus in this study is disc brakes.

Although the design principle of a disc brake is relatively simple, many variants have been developed since it was first created. Okamura and Yumoto [8] classified brake disc designs into five main types, which are as follows:

- Outer-hat without neck
- Outer-hat with neck
- Inner-hat without holes in hat
- Inner-hat with holes in hat
- Floating

Hat discs are cast in one piece and mounted directly to the wheel hub via the hat which is beneficial for manufacturing but hinders the disc from expanding due to thermal loads. Floating discs are made in two pieces that allow the disc to expand in the radial and axial directions, thus lowering internal stresses in the disc [7].

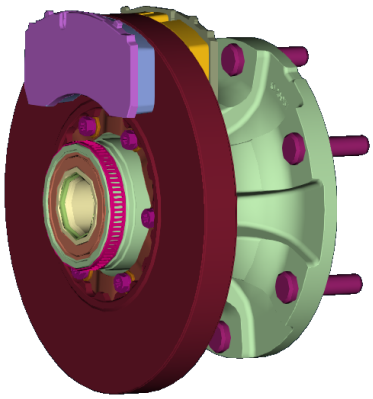

Figure 2.1: *Volvo CAD-rendering of a solid floating disc (burgundy) which is connected to the wheel hub (light green). The blue and yellow parts are the inner and outer brake pads respectively.*

The Volvo-design which will be used in this thesis is shown in Figure 2.1. It can be classed as a floating type, with the connection to the wheel hub consisting of splines and a ring-spring.

The studied disc is ”solid”, which means that it is not a ventilated disc. A ventilated disc has vanes in the middle of disc, which allows cooling airflow to pass through it, whilst a solid disc is solid through the thickness. Several different design variants exist for ventilated discs. They can have vanes, which may be straight, curved, or pillars, and the number and placement of them may vary [7].

When talking about disc and pads we often differentiate by calling one side the inboard side, and the other for the outboard. The outboard side is the one that is the side closer to the wheels (i.e. on the ”outside” of the vehicle), see [7, p.21]. Consequently, in Figure 2.1, the yellow pad is the outboard pad and the blue pad is the inboard pad.

2.2 The Energy of Braking

The principle of braking is to convert the mechanical energy of the vehicle into thermal energy through the application of a frictional force that exerts a torque on the axle [9].

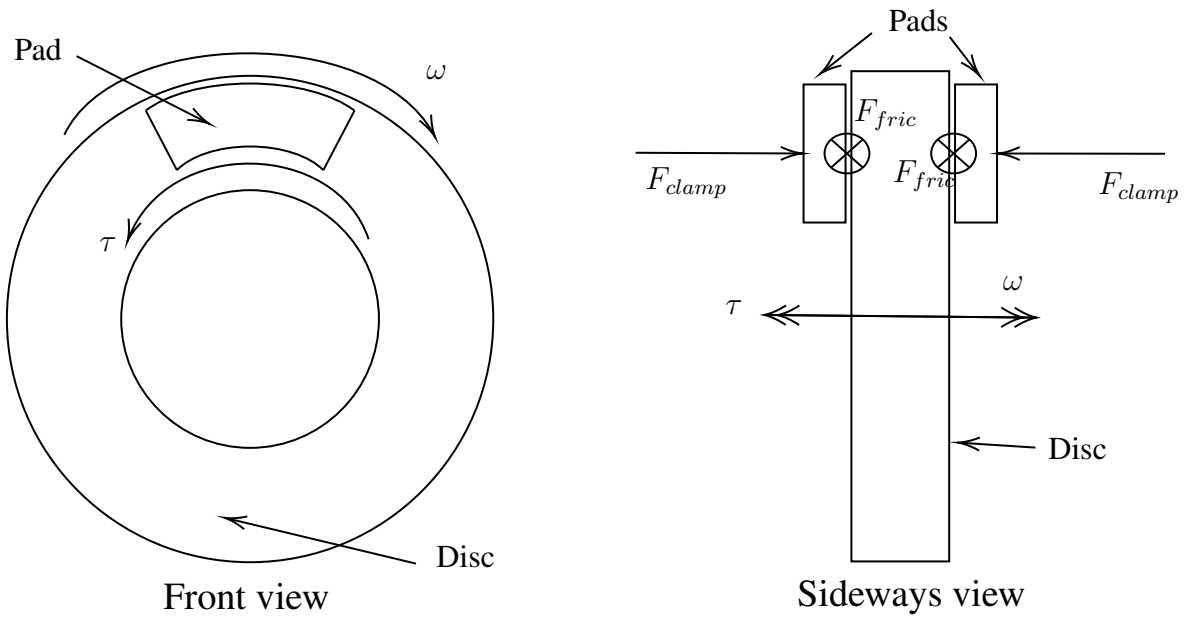

Figure 2.2: *Sketch of a disc brake with the disc rotating with an angular speed ω, and the pads clamping with a clamp force F_{clamp} resulting in a frictional force F_{fric} and a torque τ acting on the disc. Note that F_{fric} acts in the opposite direction on the pads.*

Figure 2.2 shows a schematics of a disc brake, with the brake disc being in rotational motion and the brake pads being pressed against the disc causing a torque that counters the motion.

Brake discs and pads come in several different materials. Commonly the brake discs are made of cast iron, whilst the friction material of the brake pads are some organic composite. The friction material of the pads is attached to a backing plate, that can be made of for example steel [7], [10], but also cast iron.

It is known, that if the mass of the vehicle is m and the speed is v then the kinetic energy of the vehicle is

$$K = \frac{1}{2}mv^2. \tag{2.1}$$

The total mechanical energy is

$$M = K + U, \tag{2.2}$$

where U is the potential energy of the vehicle.

Assuming that there is no energy from the truck that is dissipated from the vehicle other than from the brakes (for example no energy loss from the friction between wheels and the ground), and that no energy is added to the system (no acceleration, only deceleration), the change in mechanical energy equals [11]

$$\dot{M} = \dot{K} + \dot{U} = -\left(\dot{E} + \mathcal{D}\right), \tag{2.3}$$

where $\dot{}$ denotes the material time derivative $\frac{D}{Dt}$, E is the internal (thermal) energy of the brakes, and $\mathcal{D}$ is the dissipation rate of the energy in the brakes. $\mathcal{D}$ contains cooling terms associated with the convectional and radiation heat transfer from the brakes.

The energy division between the brake disc and brake pads can be modelled by a heat partition coefficient σ, such that

$$\begin{aligned} -\dot{M} &= \sum_i P_{fric,i} = \sum_i P_{d,i} + P_{p,i} \\ P_d &= \sigma P_{fric} \\ P_p &= (1-\sigma) P_{fric} \end{aligned} \tag{2.4}$$

where P_{fric} denotes the work per unit time done by the frictional force on one disc-pad interface, i.e. P_d and P_p denotes the heat rate going into the disc and pads respectively. Equation (2.4) is a rewritten form of equations in [9].

The heat partition coefficient depends on a number of factors, such as the contact surface, thermal properties, velocity and the temperature on the surface. It is however often assumed to be constant. The manner in which the heat partition coefficient is determined is also up for debate, and is based on assumptions about how the temperature on the two surfaces relates. For example, in one approach the maximum temperature is equated, and on another the mean temperature [12], [13].

If the contact pressure between pad and disc is p then the work done per time unit by the frictional force on a surface element $\mathrm{d}A = \phi_0 r \mathrm{d}r$ (ϕ_0 being the pad angle) is [9]

$$\mathrm{d}P_{fric} = \omega r \mu p \phi_0 r \mathrm{d}r = \omega \mu p \phi_0 r^2 \mathrm{d}r. \tag{2.5}$$

Note that the area $\mathrm{d}A$ is an arc element with arc length $\phi_0 r$ and thickness $\mathrm{d}r$, see Fig. 3 in [9]. The frictional contact areas, the area which experience any contact, for discs and pads are S_d and S_p respectively with [9]

$$\begin{aligned} \mathrm{d}S_p &= \phi_0 r \mathrm{d}r \\ \mathrm{d}S_d &= 2\pi r \mathrm{d}r. \end{aligned} \tag{2.6}$$

The heat flux to pad and disc respectively are thus [9]

$$\begin{aligned} q_d &= \frac{\mathrm{d}P_d}{\mathrm{d}S_d} = \sigma \frac{\mathrm{d}P_{fric}}{\mathrm{d}S_d} = \frac{\phi_0}{2\pi} \sigma \mu p \omega r \\ q_p &= \frac{\mathrm{d}P_p}{\mathrm{d}S_p} = (1-\sigma) \frac{\mathrm{d}P_{fric}}{\mathrm{d}S_p} = (1-\sigma) \mu p \omega r. \end{aligned} \tag{2.7}$$

Note that these are the heat fluxes if they are applied to the whole surfaces of the disc and pads. In reality both brake disc and brake pad has the surface S_p in contact, the difference is that for the brake disc only $\phi_0/(2\pi)$ of the surface will be in contact at any given time due to the rotation. Hence, the heat flux to the disc must be lowered if applied to the whole surface.

Note that the angular velocity ω will be time dependent for non-constant velocities, i.e. during braking cycles where the velocity goes to zero. Therefore, the heat fluxes can be time dependent both because of changing ω and because of changing p.

The contact pressure p will depend on the surface profiles of the brake discs and pads. Two common assumptions are those of "constant pressure" or "constant wear", see Section

2.7,

$$\begin{aligned} &\text{Constant pressure: } p(r) = p_1 \\ &\text{Constant wear: } p(r) = p_2 \frac{r_2}{r}, \end{aligned} \tag{2.8}$$

where r_2 is the inner radius of the brake pad, and that p_1 and p_2 are values of pressure. Constant pressure corresponds to new pads, whilst constant wear corresponds to pads that have been worn in [4]. The values of p_1 and p_2 can, for a given clamp force F_{clamp}, be determined from that the surface integral of the pressure distribution equals the normal force.

The clamp force F_{clamp} and torque τ must fulfill

$$\begin{aligned} F_{clamp} &= \int_{r_2}^{r_3} \int_{-\phi_0/2}^{\phi_0/2} pr \, \mathrm{d}\theta \, \mathrm{d}r \\ \tau &= 2 \int_{r_2}^{r_3} \int_{-\phi_0/2}^{\phi_0/2} \mu p r^2 \, \mathrm{d}\theta \, \mathrm{d}r, \end{aligned} \tag{2.9}$$

where r_2/r_3 is the inner/outer radius of the brake pads [4]. In other formulas r_1 and r_4 may be used to denote the inner/outer radius of the brake disc. The factor 2 in the brake torque equation comes from that there are two brake pads per brake disc.

The equation of movement for the brake disc is

$$J \frac{\partial \omega}{\partial t} = -\tau(t), \tag{2.10}$$

with J being the constant moment of inertia [4].

When studying the heat flow and pressure distribution between a brake disc and pad, it is important to determine the true contact area. Almost all of the energy dissipated during sliding is converted into heat near or at the contact surface. Due to the inevitable roughness of the contacting surfaces, contact at any moment occurs only at a few small, discrete spots across the nominal contact area. Eriksson, Bergman, and Jacobson [14] found that only about 20% of the brake pad surface was in contact with the disc. Therefore, it has been proposed that very high temperatures can develop at these true contact spots [15].

In thermal simulations of disc brakes, assumptions must therefore be made regarding the thermal contact at the pad-disc interface. A simplification is to assume perfect thermal contact, meaning that pad and disc has the same temperature on the contact surfaces. Alternatively, imperfect thermal contact is modelled by introducing an interfacial thermal resistance (or, equivalently, a thermal contact conductance) to account for a finite temperature jump across the interface. That heat resistance is caused by the formation of a so called third-body layer in the interface between disc and pad. The third-body layer consists of detached particles, trapped in the contact interface, from the disc and pads [9], [16]. The thermal resistance at the contact will depend on factors such as contact spots, hardness, surface roughness, etc. [17]. An example of simulations employing perfect thermal contact is given by Grzes and Kuciej [10].

When imperfect thermal contact is considered, the key modelling choice is how the contact conductance or resistance depends on the contact conditions. For example, Vernersson and Lundén [18] assumed an interfacial thermal resistance inversely proportional to the contact pressure, corresponding to heat transfer dominated by conduction through the real contact spots.

2.3 Thermodynamics

We can consider the problem to consist of three systems, the disc, the pads and the environment (surrounding air). We can also extend the modelling to the components to which the disc and pads are attached. A reasonable initial condition of the problem is that the pad and disc are not in contact and are in thermal equilibrium with the environment, and thus are in thermal equilibrium with each other per the zeroth law of thermodynamics. That thermal equilibrium state would mean that the temperature of both pads and disc equal the environments temperature.

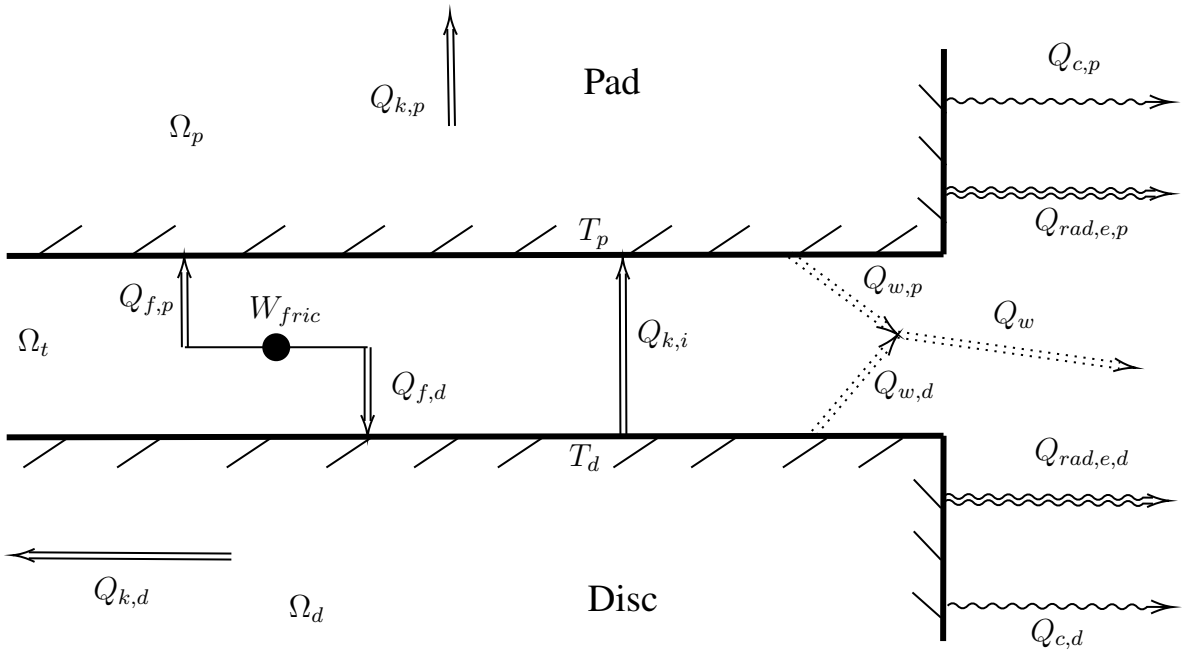

Figure 2.3: *The interface between the disc* Ω_d *and the pad* Ω_p, and the heat exchanges between them and the environment.

Figure 2.3 illustrates the heat transfer between the disc (domain Ω_d), and the pad (domain Ω_p), as well as through the third-body layer (domain Ω_t), where the contact occurs. The third-body layers consists of particles from both disc and pads in "flow" during the braking, which adheres to either one when contact is ended [19]. The heat source of the system is the work done by the frictional force W_{fric}, which is partitioned into heat flows $Q_{f,p}$ and $Q_{f,d}$ entering the pad and disc respectively. This is consistent with equations (2.5) and (2.7), where this is expressed in terms of the infinitesimal frictional power and the corresponding heat fluxes.

Heat is conducted within the disc and pads, represented by $Q_{k,p}$ and $Q_{k,d}$, and is further conducted into adjoining components such as the caliper. Heat is also transferred from the disc and pad surfaces to the environment by radiation and convection, Q_{rad} and Q_c.

In addition, an interfacial heat flow $Q_{k,i}$ is driven by the temperature difference between the contact surfaces. Finally, energy is also lost through the wear of the disc and pads, Q_w, but this energy is very small and is normally neglected.

If the disc surface temperature is T_d and the pad surface temperature is T_p at the interface, the heat flux is driven by the temperature difference,

$$q_{k,i} = h_c \left(T_d, T_p, p\right) \cdot \left(T_d - T_p\right), \tag{2.11}$$

from disc to pad. h_c is the thermal contact conductance and depends both on the temperatures on the surfaces and the contact pressure [20].

The thermal contact conductance h_c can be viewed as the sum of three contributions: heat conductance through spots, through gas in micro-cavities and by radiation. Consequently we have,

$$h_c = \hat{h}_s + \hat{h}_g + \hat{h}_r, \tag{2.12}$$

where the terms are the contributions from each respective part [20].

The contribution from the real contact spots $\hat{h}_s$, is the part that primarily depends on the contact pressure. Several models exist for this dependence, an example of one is

$$\hat{h}_s(p) = h_{s0} \left(\frac{p}{H}\right)^w, \tag{2.13}$$

where H is the hardness of the softer material, h_{s0} is the thermal resistance coefficient and w is an empirical parameter [20].

The contribution from the micro-cavities, $\hat{h}_g$, represents heat transfer by conduction through the gas trapped in the interfacial gaps. It can be expressed as,

$$\hat{h}_g = \frac{k_g}{d + g_1 + g_2}, \tag{2.14}$$

where k_g is the thermal conductivity of the gas, d is the mean plane distance, and g_1 and g_2 are correction lengths introduced to account for non-linear surface effects and temperature discontinuities at the two solid-gas interfaces [20].

The final contribution, $\hat{h}_r$, corresponds to heat transfer by thermal radiation across the interface. The radiative heat flux follows from the Stefan-Boltzmann law (with temperatures in kelvin) as,

$$q_r = F_{dp}\sigma_B \left(T_d^4 - T_p^4\right), \tag{2.15}$$

where F_{dp} is the mutual radiation factor between the two surfaces and $\sigma_B \approx 5.67 \cdot 10^{-8}$ W/(m^{2}K^4) is the Stefan-Boltzmann constant [20], [21]. Writing the radiative exchange in the linearised form $q_r = \hat{h}_r \left(T_d - T_p\right)$ gives the equivalent radiative conductance

$$\hat{h}_r \left(T_d, T_p\right) = F_{dp}\sigma_B \left(T_d^2 + T_p^2\right)\left(T_d + T_p\right), \tag{2.16}$$

which is temperature dependant and increases with increasing surface temperatures [20].

A model for heat fluxes going into disc and pad can in a simplified form be written as

$$\begin{aligned} q_d &= \frac{T_p - T_d}{R_d + R_p} + \frac{R_p}{R_d + R_p} q_{brake} \\ q_p &= \frac{T_d - T_p}{R_d + R_p} + \frac{R_d}{R_d + R_p} q_{brake} \end{aligned} \tag{2.17}$$

where R_d and R_p are the thermal resistances (per unit area) of the disc and pad at the interface. The total heat flux generated from the frictional work is

$$q_{brake} = \mu p \omega r, \tag{2.18}$$

where p is the contact pressure and ωr is the local sliding speed [18].

By Fourier's law, we have that the heat flux from conduction for an isotropic material is

$$\boldsymbol{q} = -k_t \frac{\partial T}{\partial \boldsymbol{x}} = -k_t \nabla T, \tag{2.19}$$

where k_t is the thermal conductivity of the material [11]. The operator $\frac{D}{Dt}$ is the material time derivative [11], see Appendix A.1.

For this problem there is no internal heat source . The heat equation for a solid domain becomes [11]

$$\rho \frac{D}{Dt} \left(c_p T \right) = \nabla \cdot \left(k_t \nabla T \right) + \boldsymbol{\sigma} : \nabla \boldsymbol{v}, \tag{2.20}$$

where c_p is the isobaric specific heat capacity, ρ is the density, $\boldsymbol{\sigma}$ is the Cauchy stress tensor and $\boldsymbol{v}$ is the velocity.

The surfaces of the disc and pad not in contact will either be in contact with other parts, be insulated, or they will cooling due to convection and radiation. The heat flux on the surface due to convection will be modelled as

$$q_c = h \left(T - T_e \right), \tag{2.21}$$

where h is the heat transfer coefficient of convection, T is the surface temperature and T_e is the ambient temperature. The heat flux due to radiation will be (with temperatures in kelvin)

$$q_{rad} = \sigma_B \epsilon \left(T^4 - T_e^4 \right), \tag{2.22}$$

with $0 \leq \epsilon \leq 1$ being the emissivity [11], [21].

2.4 Stress-Strain

The momentum balance equation can be expressed as

$$\nabla \cdot \boldsymbol{\sigma} + \rho \boldsymbol{f} = \rho \dot{\boldsymbol{v}} \tag{2.23}$$

where $\boldsymbol{\sigma}$ is the Cauchy stress tensor, $\boldsymbol{f}$ is the body load and $\dot{\boldsymbol{v}}$ is the acceleration [11].

The Cauchy stress tensor for a thermoelastic solid is

$$\boldsymbol{\sigma} = \boldsymbol{E} : \boldsymbol{\varepsilon}_e = \boldsymbol{E} : (\boldsymbol{\varepsilon} - \boldsymbol{\varepsilon}_{th}), \tag{2.24}$$

where $\boldsymbol{E}$ is the stiffness tensor, $\boldsymbol{\varepsilon}_e$ is the elastic strain, $\boldsymbol{\varepsilon} = \nabla \boldsymbol{u}^T$ is the observable strain, and $\boldsymbol{\varepsilon}_{th}$ is the thermal strain [22].

The thermal strain at temperature T is equal to

$$\boldsymbol{\varepsilon}_{th} = \boldsymbol{\alpha} (T - T_0), \tag{2.25}$$

where T_0 is the initial temperature, and $\boldsymbol{\alpha}$ is a tensor of the linear thermal expansion coefficients α in the different directions [22]. For an isotropic material $\boldsymbol{\alpha} = \alpha \boldsymbol{I}$. The volumetric thermal expansion coefficient is defined as

$$\beta_v = -\frac{1}{\rho} \left(\frac{\partial \rho}{\partial T} \right)_P, \tag{2.26}$$

where subscript P denotes that it is the derivative at constant pressure [11]. The volumetric thermal expansion coefficient is approximately equal to 3α [23], see Appendix A.2.

2.5 Contact Mechanics

Let Γ_c denote the potential contact boundary. The normal gap is denoted by g_N (with the contact condition $g_N \geq 0$), and the normal contact traction by t_N. In a variational setting, the contact contribution enters the weak form through interface virtual work terms and through a specific treatment of the unilateral constraint where two standard choices are the Lagrange multiplier method and the penalty method [20].

In the Lagrange multiplier formulation, the contact constraint is enforced by introducing an additional unknown field λ_N on Γ_c. For frictionless contact, λ_N represents the normal contact pressure (up to sign conventions) and acts as a reaction quantity enforcing non-penetration. A typical mixed contact functional contribution is

$$\Pi_c^{\mathrm{LM}} = \int_{\Gamma_c} \lambda_N \, g_N \, dA \tag{2.27}$$

Taking variations with respect to the displacement field and the multiplier field yields

$$\delta \Pi_c^{\mathrm{LM}} = \int_{\Gamma_c} \lambda_N \, \delta g_N \, dA + \int_{\Gamma_c} \delta \lambda_N \, g_N \, dA \tag{2.28}$$

The second term imposes the constraint in weak form via the stationarity condition with respect to λ_N, while the first term contributes the virtual work of the contact traction in the equilibrium equations. The resulting discrete problem is of mixed type, with the multiplier degrees of freedom augmenting the system of equations [20].

In the penalty method, the constraint is not enforced exactly. Instead, constraint violations are penalised by relating the contact traction to the gap through a penalty parameter

$\epsilon_N > 0$, which can be interpreted as an interface stiffness. A common penalty potential for frictionless contact is

$$\Pi_c^{\mathrm{P}} = \frac{1}{2} \int_{\Gamma_c} \epsilon_N \langle -g_N \rangle^2 \, dA \tag{2.29}$$

where $\langle x \rangle = \max(x, 0)$ activates the penalty only in compression. The first variation provides the contact contribution to the weak form,

$$\delta\Pi_c^{\mathrm{P}} = \int_{\Gamma_c} \epsilon_N \langle -g_N \rangle \, \delta g_N \, dA \tag{2.30}$$

Larger values of ϵ_N reduce penetration but increase ill-conditioning of the discrete system; smaller values improve conditioning but allow larger constraint violations. In the limit $\epsilon_N \to \infty$, the penalty solution approaches exact constraint enforcement, but this limit is not practical numerically [20].

Combined methods containing both the Lagrange multiplier and the Penalty components are often employed in contact formulations in order to accurately enforce constraints while improving the numerical behaviour. In Abaqus, this can be done numerically using the Augmented Lagrange Method (ALM). The linear penalty method is then used in an augmentation iteration scheme to limit the gap penetration [24]. This can also be done using a state-dependent combination. In the article by Dufrenoy [25], a transient dynamic contact methodology was employed in the contact analysis of brake disc and pad in order to consider both surfaces as non-rigid bodies. Here, a combined method based on the penalty function was applied, with Lagrangian multiplier force components computed locally and iteratively [26]. This method performs well with complex distortions due to thermal loads and wear as unrealistic contact penetration and local overestimated reactions are avoided.

2.6 Friction

Friction is a force that opposes motion between two surfaces in contact. Between two solid surfaces in contact, friction is either kinetic (when the surfaces slide against each other) or static (when they do not slide but tend to). Friction between sliding surfaces results from local adhesive interactions at the microscopic contact spots where surface asperities come into real or molecular contact [27]. The most fundamental formula for the friction force F_{fric} is given by Coulomb's law of dry friction [4]

$$F_{fric} = \mu F_N \tag{2.31}$$

where μ is the dimensionless coefficient of friction (COF) and F_N is the normal force perpendicular to the surface.

Since the introduction of the law in 1779, it has become clear that the COF is not a material constant as was first believed. The COF is a dynamic system-dependent quantity that varies with material properties, surface roughness, state of the interface, normal load and pressure, sliding velocity and temperature [19].

Friction experiments often show systematic deviations from the ideal Coulomb assumption of a constant COF. It has been shown that over a broad intermediate range of nominal pressures, both static and kinetic COFs commonly decrease with increasing pressure [19]. However, changes in surface films and interface conditions can lead to other trends, for example, the rupture of brittle oxide films promoting stronger adhesion at higher loads [19].

The kinetic COF may vary with sliding speed, and several typical $\mu(v)$ shapes have been reported, including approximately constant Coulomb-like behaviour and curves that decrease with increasing speed (often associated with frictional heating). At high sliding velocities, severe frictional heating can alter the material properties near the interface and may even lead to increased wear and local melting, further modifying μ [19]. In brake systems specifically, Ostermeyer [28] reports that μ generally decreases with increasing disc heat and friction power, and that a decreasing μ with increasing normal load or pressure is characteristic of brake fading.

In disc brakes, wear plays a direct role in determining μ through the formation and evolution of a tribological friction layer. Ostermeyer [28] describes how the flow of wear particles promotes the formation of hard contact patches on the pad surface, where a large fraction of the dissipation is concentrated. These patches are continuously created and destroyed by wear. As stated by Ostermeyer, "The dynamic behaviour of the friction coefficient is characterised by the equilibrium of flow of birth and death of the contact patches" [28, p. 855]. Consequently, μ depends not only on instantaneous operating conditions but also on the wear history and the current state of the interface. More generally, friction under changing conditions can exhibit non stationary and hysteric behaviour, motivating the use of state variable type descriptions rather than purely instantaneous $\mu(v)$ laws [19], [28].

2.7 Wear

Wear is a complex, system-dependent phenomenon that describes the removal of material of a solid surface as a result of mechanical action. Wear can be interpreted "as flows of third body that are permanently lost from the contact" [19, p. 688]. Most studies on frictional wear of brake discs and pads uses the classical Archard wear equation for adhesive wear [27] given as

$$\Delta W = \frac{k F_N s}{H} \tag{2.32}$$

where ΔW is the change in volume given as a function of the normal force F_N, k is the dimensionless scaling factor, H is the hardness of the material exposed to wear and s is the sliding distance [7]. The local form of Archard's wear equation is commonly implemented when modelling wear in numerical simulations as it makes the wear rate become proportional to the local work performed by friction [29]. The wear rate is then given as

$$\frac{\mathrm{d}h_w}{\mathrm{d}t} = k_w v p \tag{2.33}$$

where h_w is the wear depth, k_w is a contact pair dependent wear coefficient, v is the sliding velocity and p is the local contact pressure.

A common test procedure for measuring wear is a pin-on-disc test. In pin-on-disc tests a small pin slides across the flat surface of a disc. The pin has a known load, and the disc rotates with a constant angular velocity. From these tests one can obtain the friction coefficient and the wear scaling factor with the latter being determined by weighing the pin. An issue is that this small scale testing does not have the same contact temperatures, contact pressure and sliding speed as in full-scale tests, so a trade-off has to be done [7, p. A44].

A key goal of brake pad design is to achieve a uniform contact pressure distribution in the circumferential direction to promote uniform pad wear and a uniform temperature distribution. In practice, however, pad loading is often non-uniform, with higher pressure at the leading end than the trailing end (for rotation from leading end to trailing end). As a result, the contact pressure, and therefore pad wear, can vary not only with radius but also with angular position [5, p. 51]. Limpert [5, pp. 52-53] shows that the maximum pressure at the leading edge is approximately one-third greater than the mean pressure, while the minimum pressure at the trailing edge is approximately two-thirds of the mean pressure. This result assumes a linear pressure variation across the pad width and typical values of friction coefficient, pad thickness, and pad length.

2.8 Thermoelastic Effects

In frictional organs such as brakes, the generated heat can induce thermal distortions that further localise contact areas and lead to hot-spotting. Hot spots are localised regions on a rubbing surface where high temperature gradients develop [30]. Panier, Dufrénoy, and Weichert [30] found that hot spots can occur over multiple spatial scales and classified five types. These are the asperity type, gradients on hot bands, hot bands, macroscopic hot spots and regional hot spots. Longer brake sequences showed that the development of macroscopic hot spots starts off as hot bands. Small gradients then appear on the hot bands that develop into macroscopic hot spots. Furthermore, Panier, Dufrénoy, and Weichert [30] state that the most damaging types of hot-spotting are hot bands, gradients on hot bands, and macroscopic hot spots.

A common interpretation of the development of gradients on hot bands is to treat it as a manifestation of frictionally excited thermoelastic instability (TEI). A local rise in temperature causes local thermal expansion, which in turn increases the local contact pressure. Increased pressure increases frictional heat generation, creating a positive feedback loop [15]. Lee and Barber [31] experimentally identified the onset of TEI in brake discs under drag brake conditions and established a stability boundary in temperature-speed space.

Usual explanations for the development of macroscopic hot spots are also based on the concept of frictionally excited TEI but can also be explained by elastic or plastic buckling [32, 33]. Panier, Dufrénoy, and Weichert [30] found in their experimental investigation of hot spots in railway disc brakes that the anti-symmetrical distribution of macroscopic hot spots between the two sides of the disc showed signs of a circumferentially ”buckled” deformation pattern, caused by plastic flow and metallurgic transformations at high

temperatures.

2.9 Arbitrary Lagrangian-Eulerian

In continuum mechanics, many problems involve domains that evolve over time Yao [34]. For these types of problem, the computational domain must be described as a time dependent set $\Omega(t)$, whose boundary $\partial\Omega(t)$ changes as part of the solution, instead of a fixed spatial region. In a Lagrangian description, the computational mesh is attached to the material and follows its deformation, allowing material boundaries and interfaces to be represented accurately. However, this approach may lead to excessive mesh distortion when large deformations occur. In contrast, an Eulerian description employs a fixed spatial mesh through which the material moves, thereby avoiding mesh distortion but reducing the ability to explicitly track moving boundaries [34].

The Arbitrary Lagrangian-Eulerian (ALE) formulation provides a generalised description of motion that combines the advantages of the classical Lagrangian and Eulerian frameworks [34]. The ALE formulation introduces an independent mesh motion, so that the material velocity $\mathbf{v}$ and the mesh velocity $\mathbf{w}$ do not necessarily coincide. Transport relative to the moving mesh is then governed by the convective velocity $\mathbf{c} = \mathbf{v} - \mathbf{w}$. This decoupling allows the mesh to move in a way that improves numerical quality while the physical conservation laws are still formulated consistently on the evolving computational domain [34].

In FEA, the ALE framework is commonly employed as the theoretical basis for adaptive meshing. In Abaqus, ALE adaptive meshing allows the mesh within prescribed adaptive domains to be smoothed and repositioned during the analysis in order to reduce element distortion and improve the quality of the discretisation [24]. Since the mesh motion is independent of the material motion, the procedure can maintain a suitable element topology without imposing an artificial constraint on the physical deformation. After the mesh has been adjusted, state variables are transferred from the previous mesh configuration to the updated one through an advection, or remapping, procedure [24].

3
Methodology

This chapter describes the methodology used in the project. This includes the workflow, the tools used and the experiments which are used for comparison. It also includes information about the models, such as geometry, simplifications and calculations.

3.1 Overview

This project consisted of four principal parts.

- Literature study.
- Calibration of material parameters.
- Establishing of FE-models.
- Analysis of results.

In the literature study, existing models and theory on temperature development, wear and hot-spotting in disc brakes were reviewed. This included both publicly available research material and confidential work by Volvo and its suppliers.

To ensure accurate modelling it was necessary to review the parameters of the established models, especially the material parameters of the friction material in the pad. The plan was to fit some material parameters to data using a physics-informed neural network (PINN), see Section 3.7 and Appendix E, but due to time and resource considerations this was abandoned. Instead it was attempted to use the optimisation software modeFRONTIER to fit the values, see Section 3.8. However, when experimental values for the material parameters became available from the supplier, they were instead used in the simulations due to higher confidence in those values. The modeFRONTIER scheme was explored on fitting the thermal parameters, especially the thermal conductivity, of the pad, as well as on changing the values of wear scaling factors. This required some Python scripting to both run FE-simulations, and then extract results.

Other parameters such as the heat transfer coefficients of convection and emissivities were taken from literature or from Volvo sources. Temperature dependent values for the wear scaling factors were also determined from tests done by Volvo.

The primary part of the project was establishing FE-models of the brake disc and brake pads for temperature and wear predictions. The modelling was limited to a solid floating D33 brake disc (a brake disc with a diameter of 330 mm), see Figure 2.1. The load case was limited to that of a disc crack test, see Section 3.2. Five variants of models were made, which were

1. Axisymmetric thermal model of brake disc, both brake pads and hub.

2. Axisymmetric thermal model of one brake pad and half of the brake disc.
3. Axisymmetric thermomechanical model of one brake pad and half of the brake disc, for one cycle with wear calculated by the built-in Abaqus functionality CWEAR.
4. Axisymmetric thermomechanical model of one brake pad and half of the brake disc, for several cycles with the wear calculated by a user subroutine.
5. Thermomechanical 3D-model of one brake pad and half the brake disc, for one cycle with wear calculated by the built-in Abaqus functionality CWEAR.

Model 1 was primarily used in modeFRONTIER projects for the thermal material parameters. Models 2 and 3 have the same geometry, the difference being that for Model 2 only temperatures are calculated, disregarding braking deformation, while Model 3 uses a coupled temperature-displacement step. For Model 3 the heat generation happens in the contact as a function of relative motion between the rotating disc and the stationary pad, rather than it being prescribed as a heat flux as for Model 2. Model 3 also has wear included as part of the contact between pad and disc, via a built-in Abaqus functionality. To be able to simulate several steps with extreme wear, user subroutines coded in Fortran was used, which was implemented in Model 4. Lastly, we had Model 5, a thermomechanical 3D-model, which was established to simulate out-of-plane behaviour and to provide results for comparison with the other simplified models. A heat transfer analysis of the 3D-model was not conducted since disc rotation would not be able to be applied in a model that only solves for thermal degrees of freedom.

Pre-processing was done in the software ANSA. This entailed cleaning up the CAD-geometry, meshing, defining sets, adding material parameters, loads, etc. Some pre-processing was also done by editing the input file, either manually or through Python scripts.

The simulations were run remotely on an high-performance computing cluster with Abaqus. For some models it was necessary to use Abaqus version 2026hf2 for full functionality. It was possible to either do one simulation on 12 nodes, two simulations in parallel on four nodes each. This imposed limitations on how many simulations that could be performed within the time frame of the project.

The post-processing of the simulations was done in the post-processor META. This consisted both of taking still images of calculated data throughout the cycles, and of extracting curves of the outputs and of how they varied through time at different places in the disc and pad. As part of the modeFRONTIER projects, some post-processing was also done by using Python scripts to extract temperature values from the Abaqus output database.

The use of Abaqus as described in this thesis, was based on previous experience as well as trial and error. In some instances, information was also taken from Abaqus documentation, see [24].

3.2 Experiments, Brake Cycles and Data

This section contains information about the experimental tests from which data was obtained.

3.2.1 Disc Crack Tests

In order to ensure that new designs of the brake disc and brake pads fulfill performance and safety requirements they are tested in real-driving conditions on the full vehicle, and in a brake dynamometer test rig. The test rig is a controlled environment in which the disc brake is mounted on an axle which can regulate brake torque and rotation of the disc, which makes it possible to test different brake cycles. In the rig, the brake is in an enclosed environment in which cooling air is ventilated in and out. From the tests, it is possible to monitor the brake torque, brake pressure and temperature over time.

To ensure that the final results of the simulations were realistic, and to be able to fit model parameters, the work was based on tests performed in a brake dynamometer test rig at Volvo. The test that was chosen was a so called disc crack test, an accelerated type of extreme testing, which was done on a solid floating D33-disc, see Figure 2.1. The tests are detailed in the Volvo report ER-686465. As the name suggest the purpose of the test is to determine if the brake disc may develop cracks, it is therefore a really severe load case.

For these tests, the temperatures was measured with two thermocouples inside the brake disc, one inboard and one outboard, and with one thermocouple for each of the brake pads. The thermocouples were placed at the effective radius (middle of the rubbing surface) and at a given depth from the surfaces, at the start of the measurements; of 3 mm for the brake disc and of 9 mm for the brake pads. After 400 cycles, the sensors in the pads needed to be moved further in due to the wear.

The test consist of 500 brake cycles, which are repeated after each other for one set of new brake pads and a brake disc. For each braking application, the braking lasted for 40 s with a constant brake torque of 1200 Nm. For these disc crack tests, the angular velocity is constant. The tests were meant to simulate a vehicle with a wheel radius of 0.4 m going at 85 km/h. The angular velocity is thus

$$\omega = \frac{V}{R} = \frac{85/3.6 \text{ m/s}}{0.4 \text{ m}} \approx 59 \text{ rad/s}. \tag{3.1}$$

All cycles, except the first cycle and any cycle after wear had been measured, were started with an initial temperature of 50 °C that was measured at a thermocouple in the disc. The initial temperature for the first cycle, and any cycle after wear had been measured, was room temperature. The temperature of the cooling air was 20 °C and the airflow velocity was 40 km/h. Note that, since the initial temperature of disc and pad generally is not equal to the ambient temperature, they are not in thermal equilibrium with the environment (see Section 2.3), and thus it is unlikely that 50 °C is the temperature throughout the entirety of the disc and pads.

The wear was measured after 300 and 500 cycles. In the pads the wear was measured as the change of the thickness in six points, and of that change the mean was taken. Values of wear of the disc was not measured in the tests.

It is worth considering that before the disc crack tests commence a bedding-in is performed. The bedding-in is a process consisting of several braking applications, which have the purpose of making the pads worn in in such a manner as to make the friction surfaces be entirely in contact [7, p.9]. Thus the pads are already slightly worn down

when the disc crack test is commenced.

The disc crack tests provided data on time, brake torque, brake pressure, speed, and temperatures for cycles 11-20, 51-60, 91-100, 151-160, 191-200, 251-260, 291-300, 351-360, 391-400, 451-460 and 491-500. Data was measured with a frequency of 10 Hz.

It was calculated from equation (2.9), for assumed friction μ of 0.3 and a torque of 1200 Nm, that the clamp force will be approximately equal to 14.8 kN, assuming a constant pressure distribution.

3.2.2 Wear Tests

To obtain temperature dependent values of the wear scaling factor k_w in equation (2.33), measured values from wear tests done in the rig were used, specifically the tests detailed in ER-686005. The wear tests consists of five different sections of cycles, which have initial brake temperatures of 100, 200, 300, 400 and 500 °C respectively. The 100 °C section consisted of 1000 cycles, the 200 and 300 °C sections consisted of 500 cycles each, and the 400 and 500 °C sections consisted of 250 cycles each. In these measurements the pad and disc wear were measured after each section. The pad wear was as in the disc crack tests, see Section 3.2.1, measured as the average change of thickness in six measurements points on each pad. In these tests the disc wear was calculated by the average change of thickness in the disc at four points. As comparison, the change of mass could also be measured to determine the average change of thickness.

The disc used in these tests was a D37-disc with a hat. The cycles are different when compared to the disc crack tests. The initial speed is 60 km/h and the final speed is 0 km/h, with an average deceleration of 2 m/s^2, i.e. the angular velocity decreases linearly to zero. Then we have that

$$\omega = \omega_0 - \frac{\tau}{J}t = \frac{v_0}{r_{wheel}} - \frac{\tau}{J}t, \tag{3.2}$$

where J is the rigs inertia, see equation (2.10). The value of J is given from the report.

Based on this, one can estimate the contact pressure at testing. With a constant pressure assumption and assuming $\phi_0 \approx 80$ °, the contact pressure could be calculated, with the values of the inner and outer radius of the pad for the D37-disc.

Due to confidentiality, the wear depth for the different temperatures will not be listed in this report.

3.3 Model Parameters

To determine several model parameters, such as the contact conductance, the heat transfer coefficient of convection and the wear scaling factors, empirical formulas were used. The details on the derivation of those parameters can be found in Appendix B.1. Some values will also be presented here.

The heat partition coefficient used was $\sigma = 0.96$, and the friction coefficient used was $\mu = 0.3$. The pad angle ϕ_0 was approximated to be 80° based on measurements of the geometry, but that value can differ depending on what points one uses to measure the angle.

On the basis of tests, see Section 3.2.2, the temperature dependent pad and disc wear scaling factors were determined to be as in Table 3.1, where k^* is a confidential normalisation factor.

Table 3.1: Normalised temperature dependent wear scaling factors of the pad and disc.

T [°C]	$k_{w,p}/k^*$ [10^{-8} MPa^{-1}]	$k_{w,d}/k^*$ [10^{-8} MPa^{-1}]
100	1.00	0.675
200	2.00	0.675
300	2.30	0.900
400	4.20	0.450
500	10.2	0.900

The spot and gas conductance values of the disc-pad contact were, based on [17], calculated to be

$$\begin{aligned} \hat{h}_s &\approx 1.34 k_t' p^{0.94} \text{ mW/(mm}^2\text{K)} \\ \hat{h}_g &\approx \frac{26.2 p^{0.097}}{6.33 + 0.257 p^{0.097}} \text{mW/(mm}^2\text{K)}, \end{aligned} \tag{3.3}$$

with p being the contact pressure in MPa and k_t' is the effective thermal conductivity in mW/(mmK).

Lastly, the thermal material parameters, k_t, ρ and c_p were all assumed to be temperature dependent. The values for the cast iron disc were taken from previous simulations done at Volvo. The values for the pad friction material were both determined with an optimisation scheme, see Section 3.8, and by experiments done by the pad supplier. In the results, Sections 4.1 and 4.2, the values used were those determined by the supplier.

3.3.1 Mixed Constant Wear-Pressure Distribution

For a thermal model, the contact pressure distribution is to be assumed, not simulated. Common assumptions are those of constant pressure or constant wear, see equation (2.8). The pressure distribution can then be obtained from torque values by doing the integration in equation (2.9).

A suggested alternative approach is to assume a pressure distribution that is a linear combination of the two as

$$p(r,t) = (1 - \zeta(t))\, p_1 + \zeta(t) p_2 \frac{r_2}{r}, \tag{3.4}$$

where $\zeta(t)$ is a dimensionless parameter such that $0 \leq \zeta(t) \leq 1$ for $0 \leq t \leq t_b$ where t_b is the braking time.

The idea with this mixed form is that one could fit the time-dependence of ζ from experimental values. However, this is easier if a constant clamp force is used and not a constant

brake torque, since the exact brake torque is known from the measurements but not the clamp force. Other effects such as thermal expansion and temperature-dependence of the COF may also affect the possibility to do this fitting.

Unless otherwise indicated the thermal models in this study used $\zeta(t) = 0.5 \forall t$.

3.4 Thermal Models

In this section the set-up of the thermal models are described.

3.4.1 Axisymmetric Models

Two variants of thermal axisymmetric models were used in this project. The first was a half-disc model where the wheel hub was not included and where symmetry was assumed in the middle of the disc. This model is pictured in Figure 3.1. The elements used in the thermal axisymmetric models were linear axisymmetric heat transfer (DCAX) elements.

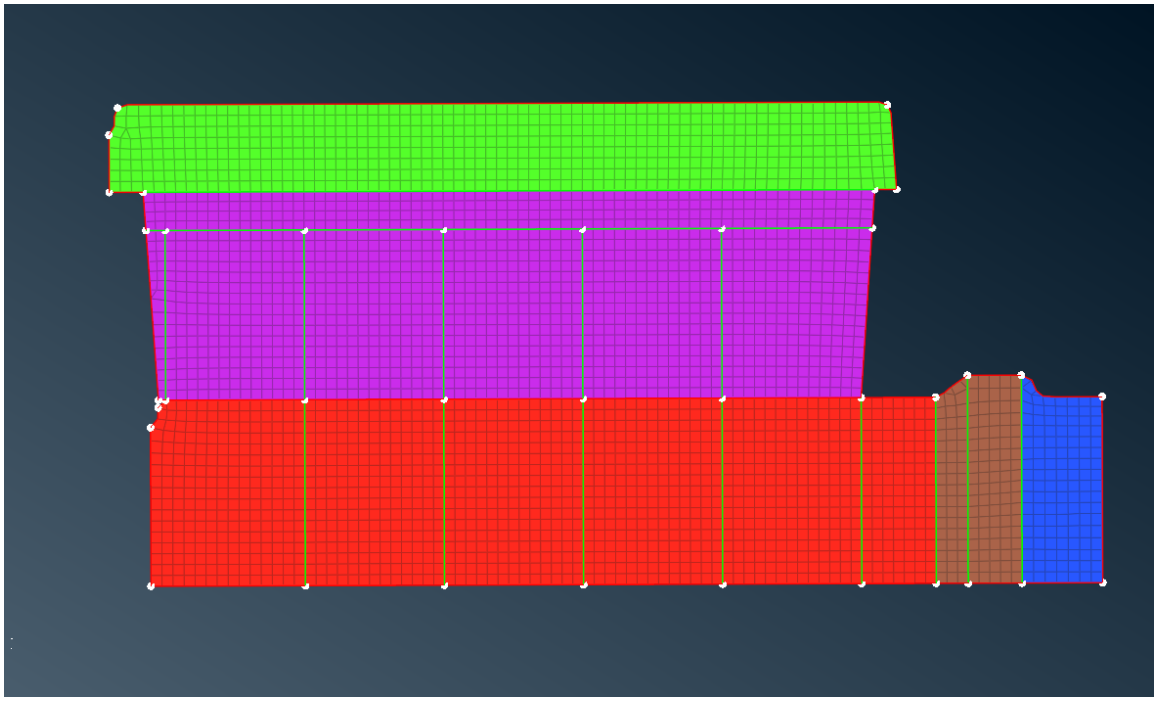

Figure 3.1: *The PIDs of the thermal axisymmetric half-disc model with a* 1 mm *target size mesh. The green part is the backplate, the purple is the pad lining, and the red, brown and blue form the disc and splines which connects to the hub to the right.*

Note that the pad is positioned so that it is at the outer edge of the disc, with the splines being at the discs inner radii. In Figure 3.1 that means that the radial axis is pointed leftwards. In some Figures, primarily in the results, that direction will be switched.

Different parts of the model have different part-ids (PIDs), which were assigned different material properties.

For the axisymmetric half-disc model, see Figure 3.1 the pad lining was assigned a pad friction material, and the disc and splines were assigned a type of cast iron. For most models, the backplate was assigned steel as its material; after discussion with our supervisor we were notified that cast iron was a more common material for the backing plate. Therefore, extra simulations, one thermal and one thermomechanical, were performed with a change of material for the backing plate.

The second variant was a model with the entire disc, both pads and the wheel hub, with imperfect thermal contact (i.e. finite gap conductance) not only between pads and disc but also between disc and hub. This model was mostly used in modeFRONTIER studies, see Section B.5.1. It is pictured in Figure 3.2.

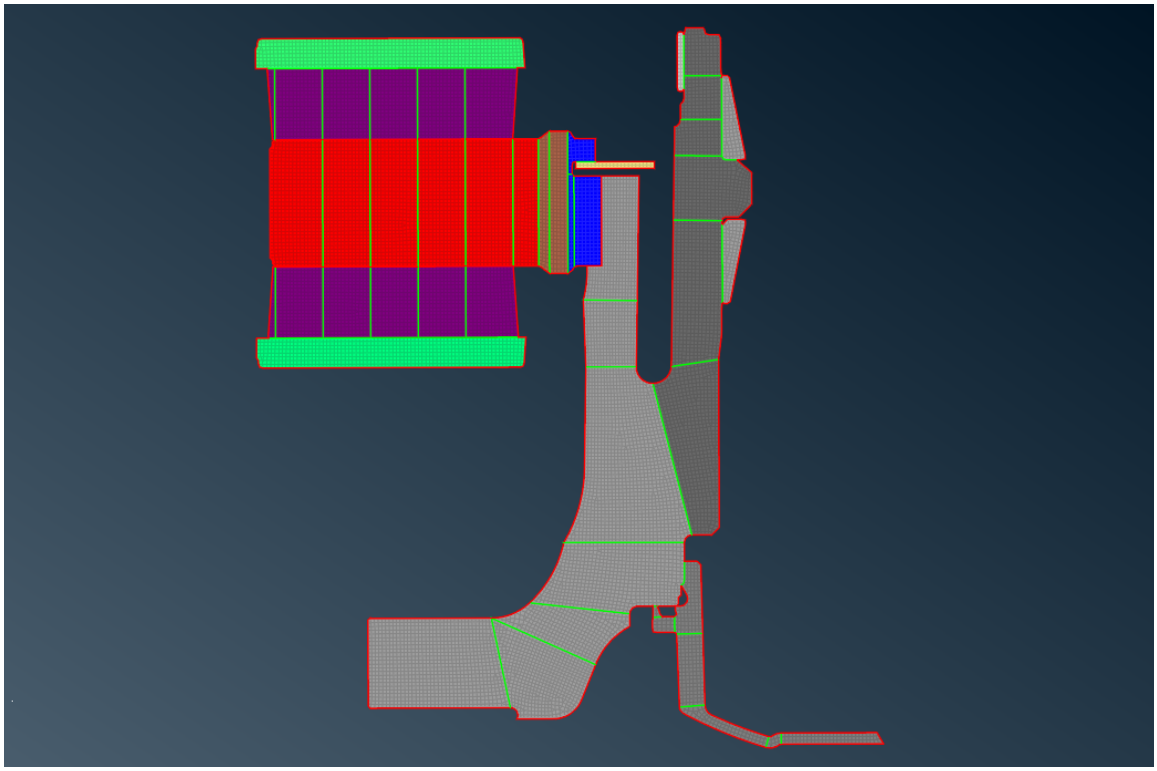

Figure 3.2: *The PIDs of the full thermal axisymmetric model of a D33 disc with wheel hub included, and with a* 1 mm *target size mesh. The green parts are the backing plates, the purple are the pad linings, the red, brown and blue together form the disc and splines, the khaki-coloured part is a ring-spring, and the grey parts form the hub.*

In Figure 3.2 we see both pads and also the hub. Note that the pad that is further up in the picture is the inboard pad and that the one further down is the outboard pad.

Figure 3.2 shows the different PIDs of the thermal axisymmetric hub model. The wheel hub parts were assigned the material nodular iron, for which the material properties were known since previous work at Volvo.

In these models, the most important thing to keep in mind is that the energy involved should match the energy of an equivalent 3D-model. The disc and pads were assumed to be rings, when in reality the pads only cover an angle ϕ_0 of the revolution.

To account for this implicit assumption, the parameters and inputs of the axisymmetric models had to be adjusted accordingly. To illustrate this point, the density ρ_p, mass and internal energy of the pads are considered. Suppose that the entire pad lining have the same temperature T, the internal energy in reality is then equal to $\rho_{p,\mathrm{3D}} V_{p,\mathrm{3D}} c_{p,p} T$, whilst it would be calculated as $\rho_{p,\mathrm{axi}} V_{p,\mathrm{axi}} c_{p,p} T$ in the axisymmetric models. For consistent energy formulations these two values should be equal and thus

$$\rho_{p,\mathrm{3D}} V_{p,\mathrm{3D}} = \rho_{p,\mathrm{axi}} V_{p,\mathrm{axi}}, \tag{3.5}$$

which is equivalent to saying that the mass should be the same. Since $V_{p,\mathrm{3D}}/V_{p,\mathrm{axi}} \approx \phi_0/(2\pi)$,

$$\rho_{p,\mathrm{axi}} = \frac{\phi_0}{2\pi} \rho_{p,\mathrm{3D}}, \tag{3.6}$$

i.e. the density of the pad should be adjusted by a factor $\frac{\phi_0}{2\pi}$ for the axisymmetric models. By the same arguments

$$\rho_{s,\mathrm{axi}} = \frac{\phi_0}{2\pi} \rho_{s,\mathrm{3D}}, \tag{3.7}$$

for the backing plate. This adjustment of densities was also done in [35].

A mistake was made in this part of the modelling. For this kind of simulation the thermal conductivity should have also been adjusted for the pad [35]. Adjusting the density does ensure that the internal energy is correct, but it also increases the thermal diffusivity $k_t/(\rho c_p)$ of the pad and backing plate, which increases how fast the heat spreads throughout the pad. To account for this the conductivity would have to be lowered by a factor of $\phi_0/(2\pi)$, which would mean higher temperatures on the pad contact surface and thus likely higher wear. This error was only realised late on in the project, therefore it was not possible to redo all simulations and the effect on the results is only commented on briefly in Sections 4.1.5 and 4.2.4.

Further details on the thermal axisymmetric modelling can be found in Appendix B.2. Overall, the main principles were that applied radiation and convection boundary conditions, as well as heat fluxes, were adjusted, the contact surfaces were divided into partitions to be able to apply radially dependent heat flux, and that the initial temperature was applied as 50 °C. It was also assumed that the top surface of the backing plate had a constant temperature of 50 °C.

3.5 Thermomechanical Models

In this section the set-up of the thermomechanical models is described.

3.5.1 Axisymmetric Models

Several aspects of the thermomechanical axisymmetric models matched the thermal axisymmetric ones. Properties such as the density of the pads, heat transfer coefficients of convections, radiation and contact conductance were adjusted (and the thermal conductivity should have been adjusted but was not). The surface and node sets were the same, as was the underlying geometry. What was changed was how the heat generation was modelled, and that it was no longer only the temperature that was solved for, but also

the displacements.

Instead of applying heat fluxes on the pad and disc surfaces, the heat is generated as part of the contact pair between pad and disc surfaces. All energy created was considered to be converted to thermal energy and the heat partition was as previously set such that 96% goes to the disc and 4% to the pad.

An additional change compared to the thermal models was that the gap conductance was made pressure dependent. By combining (B.18) and (B.22) a formula was obtained, that is in part pressure dependent and, through the effective conductivity, in part temperature dependent. The gap conductance was still reduced by a factor of $\phi_0/(2\pi)$ for the thermomechanical axisymmetric models from the values used in the 3D-simulations, and is related in the input file to the reduced axisymmetric contact pressure.

Table 3.2: Normalised gap conductance values for the axisymmetric pad-disc contact that are temperature and pressure dependent.

T [°C]	p_{3D} [MPa]	p_{axi} [MPa]	$\left(\hat{h}_{s,axi} + \hat{h}_{g,axi}\right)/k_t^*$ [mW/(mm^{2}K)]
100	0.0	0.0	0.00
100	0.5	0.111	0.643
100	1.0	0.222	0.997
100	1.5	0.333	1.34
100	2.0	0.444	1.66
100	2.5	0.555	1.99
200	0.0	0.0	0.00
200	0.5	0.111	0.577
200	1.0	0.222	0.870
200	1.5	0.333	1.15
200	2.0	0.444	1.42
200	2.5	0.555	1.68

Table 3.2 shows the normalised values of the gap conductance that is prescribed, and are calculated from equation (3.3).

In the thermomechanical models we also accounted for wear. The wear scaling factors were calculated in 3D as listed in Tables B.1 and B.2. In the axisymmetric model the contact pressure were lowered by a factor $\phi_0/(2\pi)$, and as the wear is proportional to the contact pressure, that would cause less wear for the pads than in the 3D-model, if the same wear scaling factors were used. To counter-act this the wear scaling factor for the pad was increased, $k_{w,p,axi} = \frac{2\pi}{\phi_0} k_{w,p,3D}$, whilst the wear scaling factor for the disc was the same, $k_{w,d,axi} = k_{w,d,3D}$. The reason why $k_{w,d}$ was unchanged was because, whilst the pressure was lowered, only $\phi_0/(2\pi)$ of the disc contact surface was in contact at any given time, but in the axisymmetric model it was the whole surface.

For these thermomechanical simulations, axisymmetric thermally coupled quadrilateral, bilinear displacement and temperature elements (CAXT) or generalized axisymmetric thermally coupled quadrilateral, bilinear displacement and temperature, twist (CGAXT) elements have to be used. These elements are axisymmetric coupled temperature-displacement

elements, with the difference that the latter also has the twist angle as a degree of freedom [24]. This difference gives us two options for modelling the rotation, and thus how to implement the heat generation in the contact. Either CGAXT elements can be used and the rotation of the disc can be prescribed with the correct angular velocity, or CAXT elements can be used and the rotation is prescribed as a slip distance in the Abaqus user subroutine *FRIC* that allows for extended modeling by Fortran programming. The former is the preferable choice when simulating only one cycle, the latter was necessary when simulating extreme wear with the *UMESHMOTION* subroutine. The advantage with the subroutine is that interior nodes can be moved in a controlled way so that no elements are distorted, and geometry is preserved, which is useful when the wear depth is significant when compared to the original element depth [36].

For the first type of model, the wear was introduced via the built-in wear routine in Abaqus, the accumulative wear output CWEAR. CWEAR is accumulated wear depth, i.e. h_w and not dh_w/dt, that can be extracted as an output from surfaces. That depth is prescribed as a nodal displacement on the nodes of the contact surfaces. This is done practically by adding the wear scaling factors as wear surface properties that are set as not friction coefficient dependent and as not unitless (since the variant of Archard's law used does not include μ and we calculate k_w not k). As noted before the wear scaling factor for the pads is increased compared to 3D, whilst it is kept the same for the disc.

If it is possible to also implement multiple cycles and extreme wear with the built-in Abaqus functionality for wear was not explored as part of this project.

3.5.1.1 Single Cycle

As mentioned above, this model used CGAXT elements for simulating the coupled temperature-displacement problem with the rotation being a degree of freedom.

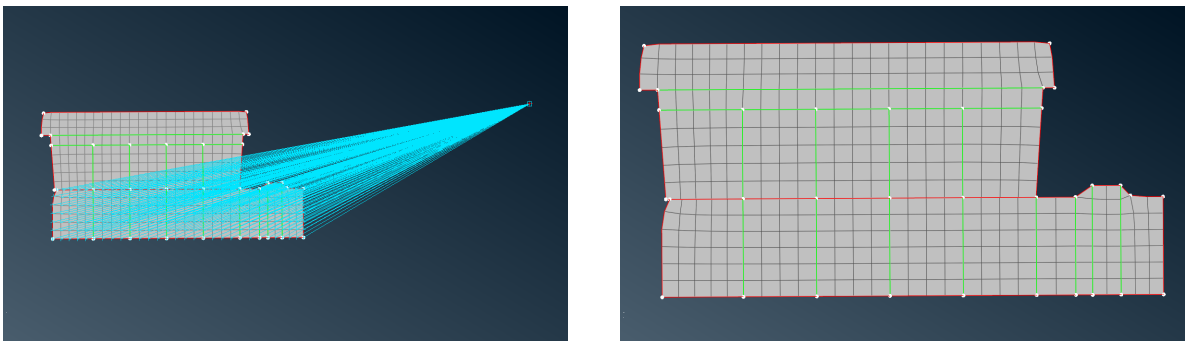

(a) *Model with coupling visible.* (b) *Model with coupling invisible.*

Figure 3.3: *The half-disc thermomechanical axisymmetric model of a D33 disc, pictured here with a mesh with a target size of* 3 mm.

The rotation of the disc was added by making a kinematic coupling for the rotation around the z-axis between the nodes of the disc and a reference node placed in origo, as pictured in Figure 3.3a. The reference node was prescribed an angular velocity of 59 rad/s. This imposed rotation was mainly used here for calculation of friction heating in our model.

Other displacement boundary conditions for the disc was that the spline edge of the disc was fixed in the radial direction and that symmetry boundary conditions were applied to the centreline of the disc. On the end of the backing plate the surface was fixed in the radial direction and in rotation.

Furthermore, the clamp force of 14.8 kN was accounted for by adding a pressure load on the top end of the backing plate.

Of note here was that a lower pressure was applied on the backing plate than in 3D, which means a proportionally lower contact pressure in the disc-pad interface. If thermal expansion were to be disregarded, this would be of little consequence. But, with thermal expansion parts of the pad and disc expands and with a lower contact pressure the indentation of that contact area would be smaller. This would lead to extreme hot-banding since the contact would become more localised. To counter-act this and keep the indentation the same, the Young's modulus, E, of all materials was lowered by the factor of $\phi_0/(2\pi)$ for all axisymmetric thermomechanical models. In [35] only the pad materials Young's modulus was lowered, however both should affect the indentation depth.

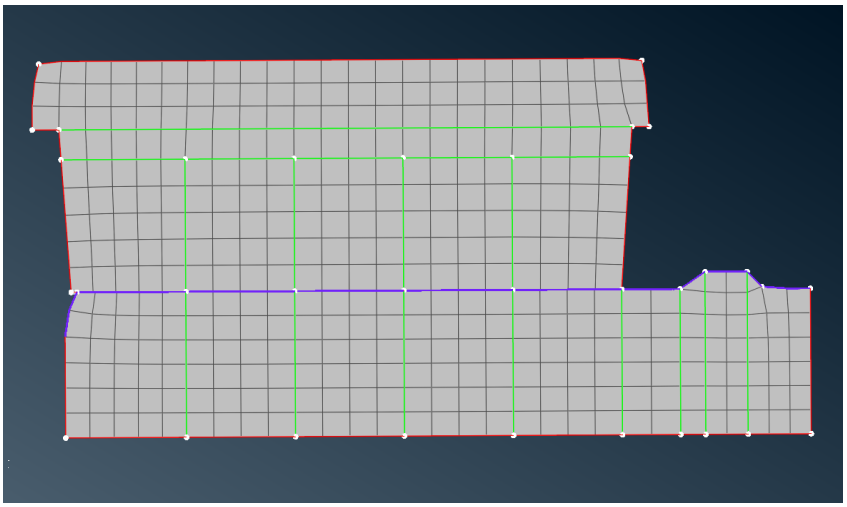

(a) *Contact surface of the disc.*

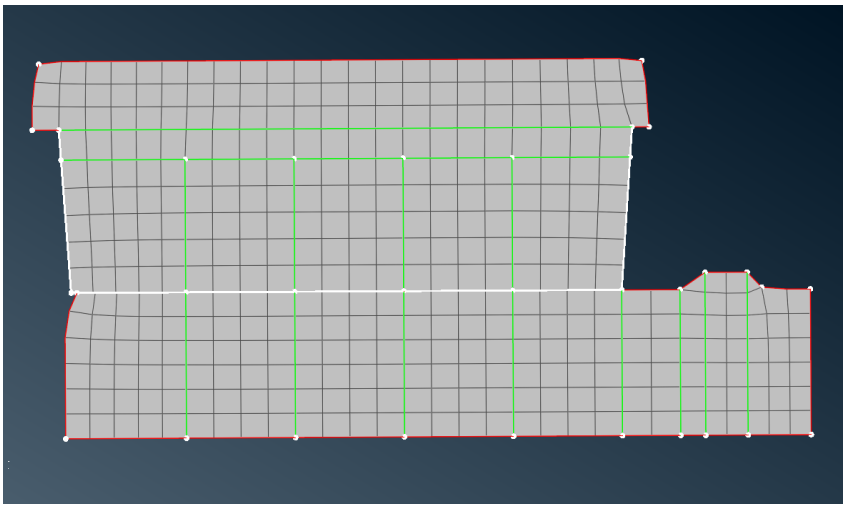

(b) *Contact surface of the pad.*

Figure 3.4: *Contact surfaces of pad and disc for the half-disc thermomechanical model, pictured here with a mesh target size of* 3 mm.

The values and surfaces of the convection and radiation were the same as in the thermal model, see Figure B.4. However, to prevent accidental penetration, the contact surfaces on pad and disc were extended to cover more of the sides, see Figure 3.4. Note however that the ambient convection and radiation that was applied to the disc contact surface must not be applied on this extended disc contact surface pictured in Figure 3.4a. Instead it must be applied to the same surface as in the thermal model. This is to not have double convection and radiation conditions on some edges, as there are overlap between the surface in Figure 3.4a and those in Figure B.4.

Extending the contact surfaces to the side had an unexpected side effect, any edges on the sides then accumulated wear in the out-of-plane direction, i.e. in the angular direction, even though they were not subject to any contact pressure. As a test, a version was tested where the surfaces were not extended. This only gave negligible changes of the results.

3.5.1.2 Multiple Cycles

When simulating wear and the final wear depth is equal to or greater than the length scale of the elements it is necessary to modify the underlying mesh in accordance to the wear. This is done by utilising the Abaqus functionality of Arbitrary Lagrangian-Eulerian (ALE) adaptive meshing, see Section 2.9. That per default moves nodes to fix elements assigned to the adaptive mesh domain. However, with the user subroutine *UMESHMOTION* one can control a specific node movement. Inside the subroutine, one can extract the temperature, contact pressure and coordinates of the node, and then prescribe a motion in accordance with Archard's law for the underlying geometry. This can be done, and has been done, in various different applications; for example Arjmandi et al. [37] used *UMESHMOTION* to simulate wear of 3D woven textiles.

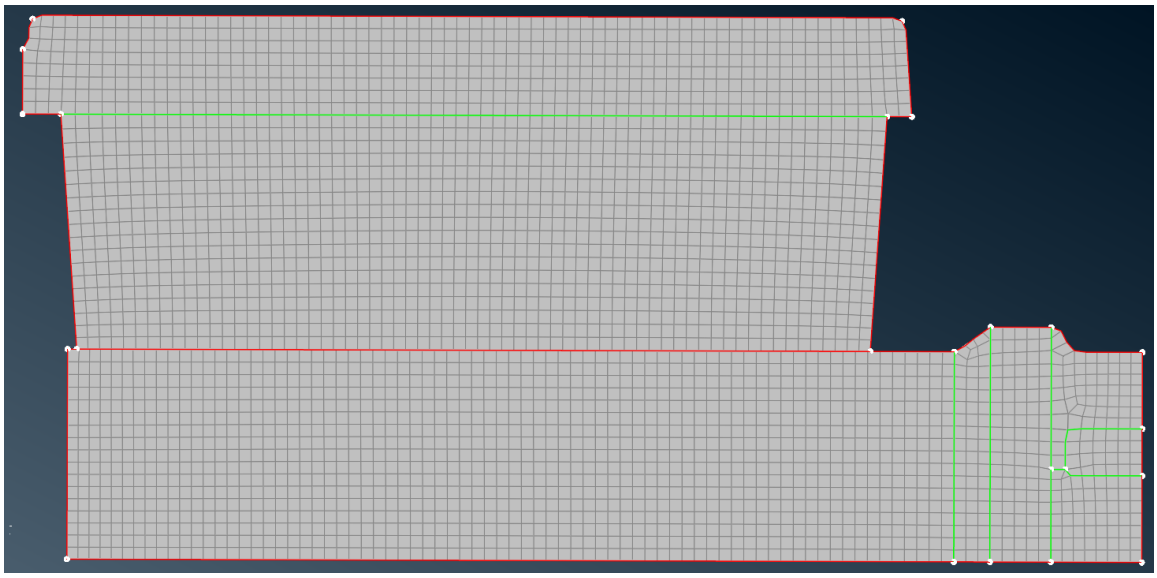

Figure 3.5: *The multiple cycles half-disc thermomechanical model with subroutines in this work also denoted the ultimate model, pictured here with a mesh target size of* 1 mm.

Figure 3.5 shows this half-disc thermomechanical model which is used with the user subroutines *UMESHMOTION* and *FRIC*. This model is in this project sometimes called the "ultimate" model as it includes everything investigated in this study (wear, thermal expansion, etc.) whilst being capable of simulating several cycles. Observe that slight changes have been made to the disc geometry, compare Figure 3.5 with Figure 3.3b, with a previously chamfered corner of the disc being changed to right angled corner. This change of the disc was partially done because the model had issue handling it when wear was included as it could easily cause distorted elements on the pad, and partially it was done to make it easier to mesh with only quadratic elements. Triangular elements were not supported by the adaptive meshing, thus it was ensured that the pad lining and the outer-most part of the disc were only meshed with quadratic elements. Some triangular elements still existed in the disc, but at the splines, which are not susceptible to wear due to the pads and therefore did not need to be included in the adaptive mesh.

Further details on how the subroutines work to apply the wear, and how multiple steps is applied, is included in Appendix B.3.1.

3.5.2 3D-Models

Simulating 3D-models makes it possible to capture circumferentially out-of-plane effects of the brake that does not show up in an axisymmetric model. Simulating 3D-models also makes it possible to validate axisymmetric assumptions. However, 3D-models are limited by the computational cost that comes with the number of elements and DOFs in a full 3D-representation. Due to the symmetry of the brake, it was determined that it would be sufficient to only simulate half the brake, and a half-model was therefore developed consisting of only one pad, one backplate and a half-disc.

Since the model contained complex geometry, it was determined that these areas could be simplified to further reduce the computational cost of the model. The splines and edges of the disc, as well as the backing plate, were modified using ANSA version 25.1.0. The geometry of the disc contact surface, as well as the entire pad, remained unaltered. The simplified geometry is pictured in Figure 3.6.

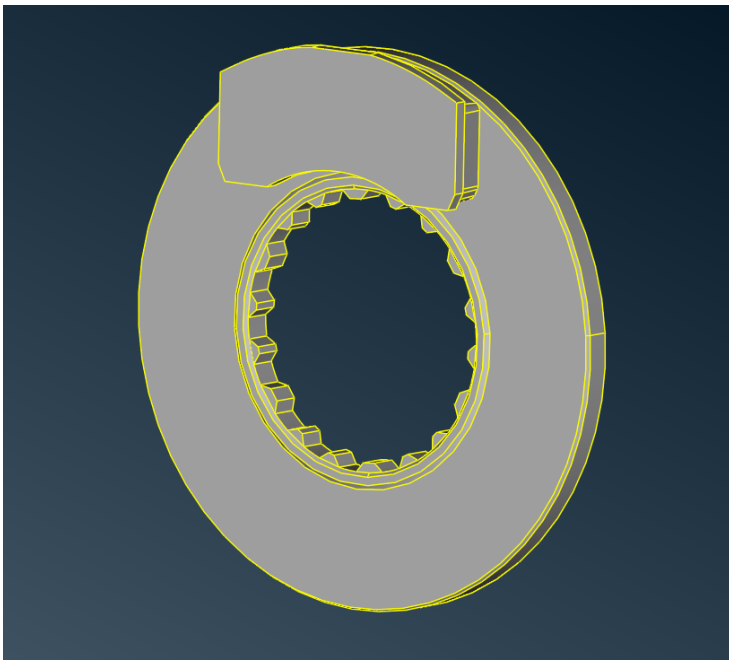

Figure 3.6: *The simplified half-disc 3D geometry of the D33 disc brake.*

Meshing in ANSA often results in simplifications to the geometry that effectively reach the number of DOFs. However, this was found to also affect the smoothness of the contacting surfaces, causing convergence issues with contact formulations and unreasonably large hot-spotting. This can be avoided using ANSA but would require a large effort and software knowledge to ensure that the geometry of the contacting surfaces stays unaltered. The geometry of the model was therefore cleaned using ANSA, with meshing done in Abaqus. This ensured that contact surfaces stayed smooth after meshing. Meshing was done entirely with 4-node linear displacement and temperature elements (C3D4T).

3.5.2.1 Single Cycle

The contact between the pad and the disc was established through a contact pair using linear penalty stiffness as in the axisymmetric model, with default values of extension zone

set to 0.2 and surface smoothening set to 0.1. Gap heat generation and gap radiation was specified as in the axisymmetric model while the gap conductance was adjusted to account for the entire disc and pad, see Table 3.3.

Table 3.3: Normalised gap conductance values for the 3D pad-disc contact that are temperature and pressure dependent.

T [°C]	p_{3D} [MPa]	p_{axi} [MPa]	$\left(\hat{h}_{s,3D} + \hat{h}_{g,3D}\right) / k_t^*$ [mW/(mm^{2}K)]
100	0.0	0.0	0.0
100	0.5	0.111	2.89
100	1.0	0.222	4.50
100	1.5	0.333	6.00
100	2.0	0.444	7.50
100	2.5	0.555	8.93
200	0.0	0.0	0.0
200	0.5	0.111	2.59
200	1.0	0.222	3.90
200	1.5	0.333	5.17
200	2.0	0.444	6.37
200	2.5	0.555	7.57

The contact surfaces between the pad and the backing plate were constrained using a tie constraint that allows them to move together as a single bonded entity. Since the mounting ring was not included in the half-model, a kinematic coupling was established between the spline nodes and a central reference point. The rotations and displacements of the disc were then applied directly to the disc reference point. The displacement of the discs symmetry surface was constrained in the axial direction while the rotation of the disc was constrained to only mimic wheel rotation. From the brake assembly it was determined that the backplate was only allowed to translate in the direction in which the force is applied and all other DOFs were therefore constrained.

Similarly to the axisymmetric model, a temperature boundary condition of 50 °C was applied on the surface of the backing plate on which the force is applied. An initial temperature of 50 °C was also applied to the disc, pad and backplate.

An instantaneous and constant positive rotational velocity of 59 rad/s was applied to the disc reference point to simulate disc rotation. An instantaneous and constant pressure was applied to the back of the backing plate to simulate the brake force. The area of the simplified backplate is 12750 mm^2. For a brake force of 14.8 kN the corresponding backplate pressure was calculated as

$$p = \frac{14800 \text{ N}}{12750 \text{ mm}^2} \approx 1.161 \text{ MPa} \tag{3.8}$$

Wear was applied using the built-in Abaqus CWEAR functionality, as in the axisymmetric model in Section 3.5.1.1. The wear scaling factors can be found in Tables B.1 and B.2.

To be able to extract results in the thickness of the disc and pad, and compare them with the thermocouple readings from the disc crack test (see 3.2.1), parametric points were

positioned at the effective radius in the disc and the pad. In Figure 3.7 the positions of the parametric points are shown.

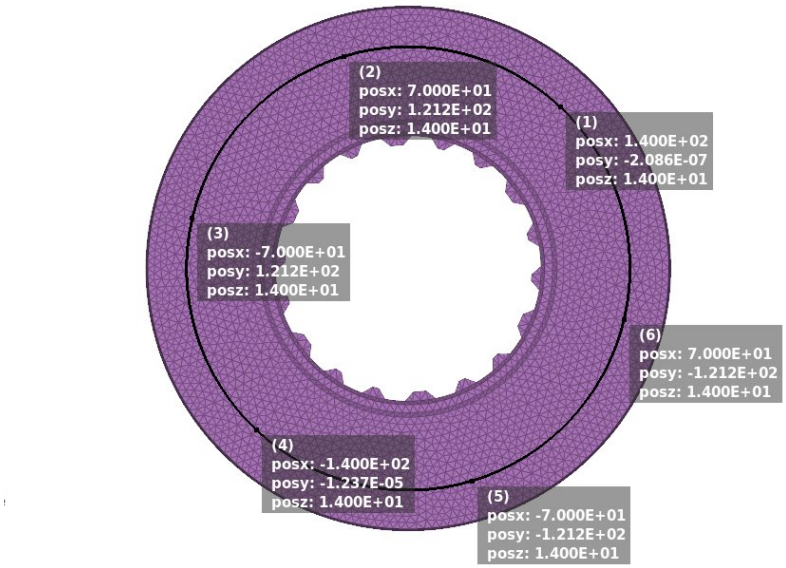

(a) *In the disc.*

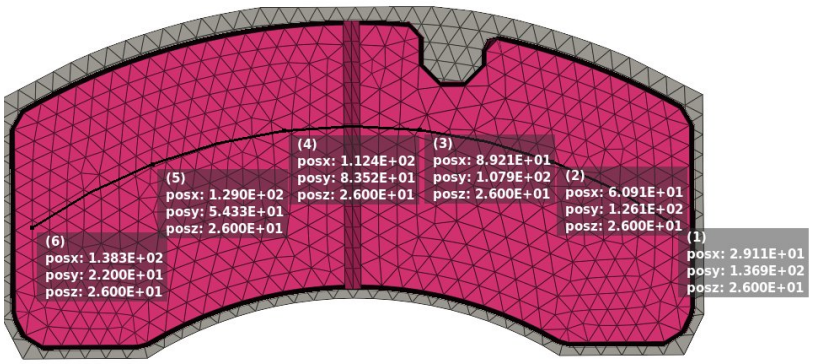

(b) *In the pad.*

Figure 3.7: *Picture of the parametric points located in the 3D-model.*

Six points are located in the disc and six points are located in the pad. In Figure 3.7a the names of the points are as follows:

(1) Point 1
(2) Point 2
(3) Point 3
(4) Point 4

(5) Point 5
(6) Point 6

In 3.7b the names of the points are as follows:

(1) Trailing Edge
(2) Middle, Trailing Side
(3) Central, Trailing Side
(4) Central, Leading Side
(5) Middle, Leading Side
(6) Leading Edge

Further, to compare with the axisymmetric model, three through-thickness sections were made of the disc, pad and backplate. These sections consisted of one through the leading end of the pad, one through the trailing end of the pad and one through the central part of the pad. Note that the central section had to be placed to the side of the groove in the pad.

The field output request frequency for the 3D-model was limited to save on computer storage. The frequency was set at 10 Hz which aligns closely with the frequency of the thermocouples in the disc crack tests.

3.6 Mesh Studies

To test the sensitivity and convergence of results, mesh studies were performed for the different models. The results of those mesh studies can be found in Appendix B.4. The mesh studies centred around the final maximum and mean temperatures, and results on wear predicted by CWEAR, on the disc and pad contact surfaces. To this end, the axisymmetric models converged around a mesh target size of 1 mm to 1.5 mm. The 3D-model did not fully converge for the mesh target sizes which could be simulated within a reasonable time-frame.

3.7 PINN

A proposed method to determine the material parameters of the brake pad and their temperature dependence was to use a PINN (physics-informed neural network) to fit them using the heat equation, boundary conditions and test data.

That method was however abandoned due to the limited time frame of this project and computational resources for it, and it was instead replaced with using the modeFRONTIER software, see 3.8. The PINN-method should work if enough time and resources is invested in it. It is outlined, along with relevant theory in Appendix E.

3.8 modeFRONTIER

In the work to determine the material parameters and other parameters of the model the optimisation software modeFRONTIER was used. It is a design optimisation software that can integrate CAD and CAE software, and it automates an evaluation of different designs made from input parameters on the basis of objectives that are taken from the

outputs of the process [38]. These objectives can both be design constraints, but also, as in our case, minimising error when comparing to data.

The optimisation included both the thermal material properties of the pad friction material, and the scaling factors were fitted. The details of these optimisation projects are included in Appendix B.5.

Two variants of the thermal material properties were included, one where the force (and heat fluxes) was constant and one where it varied linearly to a lower final value. Input parameters of these projects are values of the properties at $T = 20$ °C, and of the slope of the properties. For example, *k0* is the thermal conductivity at room temperature, and *k1* is the change per °C. Note that in the tests the torque/heat flux was constant, see Section 3.2.1, and the linear variation of the force/heat fluxes for a thermal model was mostly included to see how it would affect the results.

For the wear scaling factors three different studies were performed. These were based on the following assumptions:

1. To have a constant $k_{w,p}$.
2. To scale up the values of $k_{w,p}(T)$ and $k_{w,d}(T)$ by a factor.
3. To fit a curve $k_{w,p}(T) = a + c \cdot b^{T/100}$.

This was done as the measured temperature dependent values of k_w was underestimating the pad wear in comparison with the disc crack tests, see Section 3.2.1. Note that these were done with the unadjusted value of $k_{t,p}$, which will have effects on the surface temperature. This makes the results of the temperature dependent studies more questionable, but is less likely to have affected the constant $k_{w,p}$ study.

4
Results

In this chapter the results of the FE-simulations are presented. The results from the modeFRONTIER projects are only summarised with them being presented fully in Appendix D. Unless otherwise specified, all units of the results are those used in the FE code, i.e. $°C$, MPa, s and mm.

Note that results presented in Figures have more significant figures than what is reasonable given the accuracy of the models.

4.1 FE-Simulations of One Cycle

This section includes the results of all simulations that only simulate one cycle. This includes thermal and thermomechanical axisymmetric models as well as the thermomechanical 3D-models.

Only the most relevant results are presented, with only a select few time points. The focus is therefore on how the temperature changes over time, especially on the pad and disc contact surfaces, as well as the evolution of contact pressure and wear.

The results for each type of model is mostly presented separately. In Section 4.1.4 temperatures from models, extracted from the corresponding depth and radial position, are compared with measurements of temperatures from tests, see Section 3.2.1.

Note that mean values are with regards to the mean of the nodes, they are not weighted means with regards to the radial position. Thus for the same mean temperature values on a surface, the energy may differ depending on the radial distribution. The ”contact” surface was also defined for a larger area for the 3D-model than for the axisymmetric model, with the 3D-model including not only the portion of the disc that is in contact with the pad but extending further inwards to the splines. This will mean that the mean values will inevitably differ between 3D- and axisymmetric models.

4.1.1 Thermal Axisymmetric Models

This subsection includes the results of the thermal axisymmetric models, see Section 3.4.1, including both the symmetry model of only a half-disc and the model with the hub included. Note that these results are with the unadjusted thermal conductivity.

4.1.1.1 Half-Disc

The following pictures and plots are the results of the thermal axisymmetric model with half the disc. Results are presented for the finest mesh tested, the 0.5 mm mesh, in Section B.4.1.1.

Figure 4.1 shows the nodal temperature for the model at $t = 10$ s and $t = 40$ s. Note that the temperature is higher at outer radii (to the right), where the heat flux is greater due to the constant pressure terms, see Section 3.4.1.

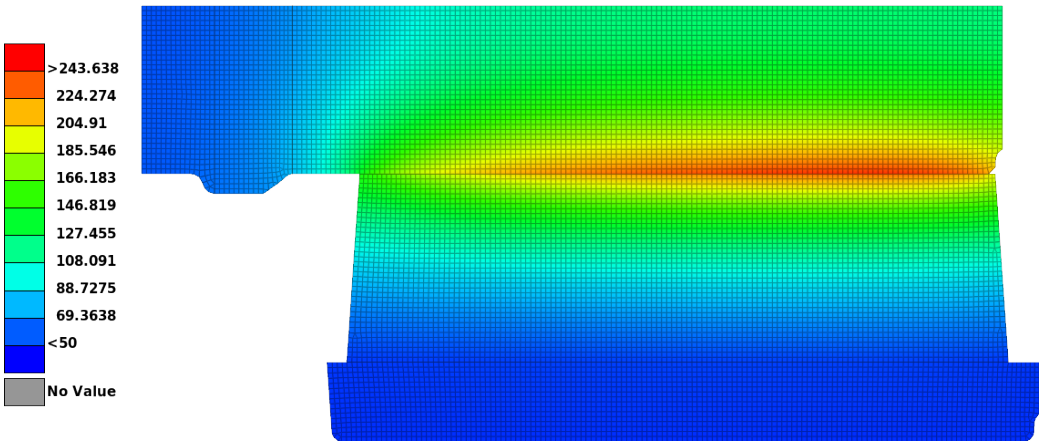

(a) *At* $t = 10$ s

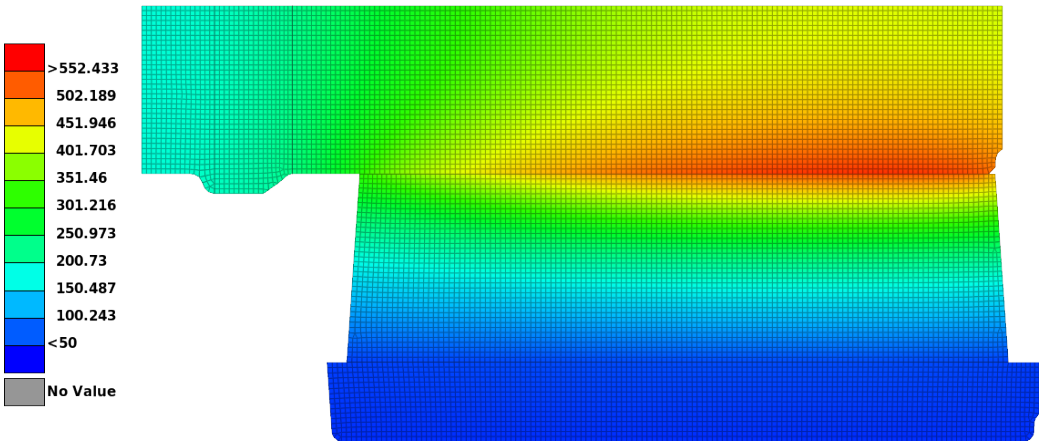

(b) *At* $t = 40$ s

Figure 4.1: *Picture of the nodal temperatures for the thermal axisymmetric half-disc model at selected time points.*

Figure 4.2 shows the maximum and mean nodal temperatures on the disc contact surface. The temperature difference between maximum and mean grows over time, but grows rather steadily, and is approximately 55 °C at the end of the cycle.

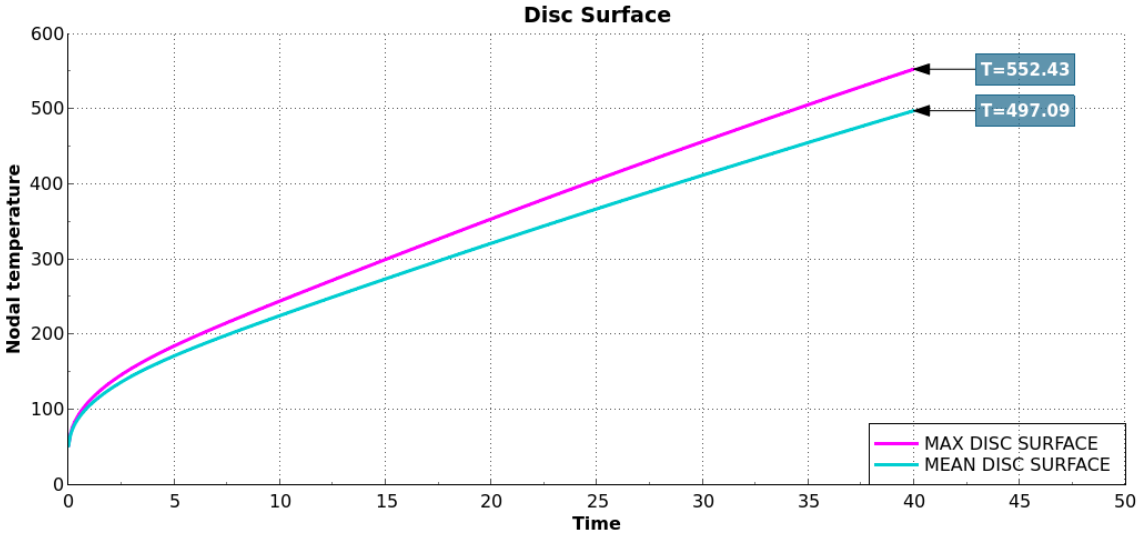

Figure 4.2: *The mean and maximum temperature on the disc contact surface over time for the thermal half-disc model.*

Figure 4.3 shows the change of the maximum and mean temperatures on the pad contact surface. Note that in comparison with the disc surface, Figure 4.2, the final temperature difference is approximately the same between maximum and mean. The final temperature difference between maximum pad temperature and maximum disc temperature is approximately equal to 17.6 °C, with the difference between the means being 16.9 °C.

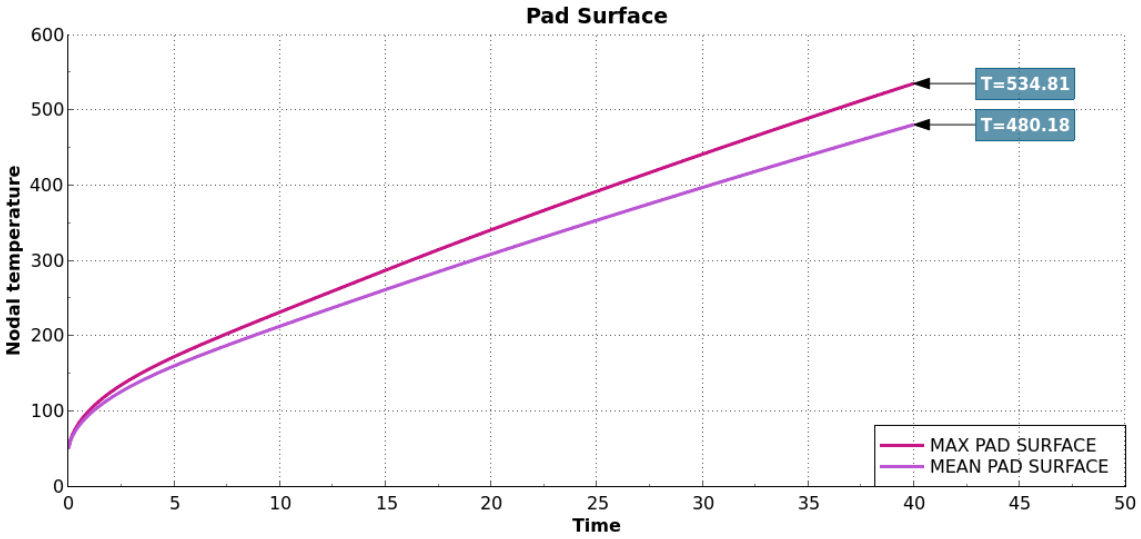

Figure 4.3: *The temperature on the pad contact surface over time for the thermal half-disc model.*

Figure 4.4 shows predictions of the accumulated wear depths of pad and disc using the procedure in Appendix B.1.1, and with temperature dependent k_w values. The temperatures used for the predictions was the mean surface temperatures over time in Figures 4.2 and 4.3. Note that the pad wear increases exponentially whilst the wear of the disc increases almost linearly, which is due to the difference in temperature dependence of the wear scaling factors $k_{w,p}$ and $k_{w,d}$.

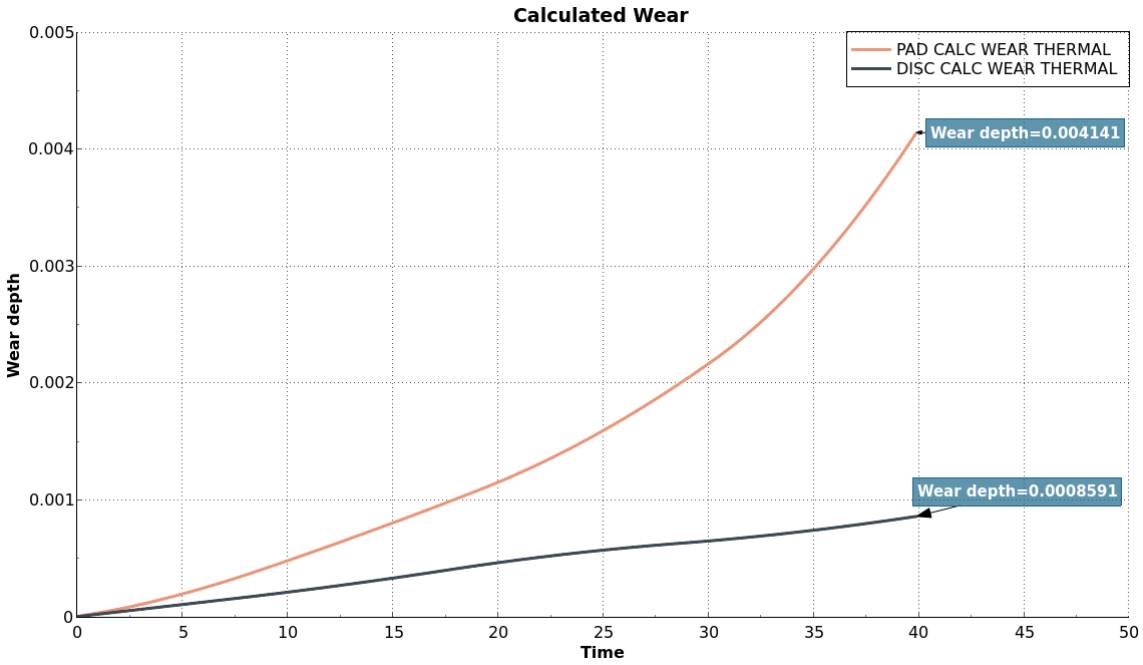

Figure 4.4: *Calculated wear depth on pad and disc for the thermal half-disc axisymmetric model.*

4.1.1.2 With Hub

In this subsection the results from the thermal axisymmetric model that includes the hub, see Section 3.4.1, are discussed. In the simulation for this model the gap conductance for the surface interaction at the splines was set to 1.125 mW/(mm^{2}K).

The mesh used was the same as the one used for the modeFRONTIER thermal material projects, see Appendix B.5.1, i.e. a target size of 1 mm on the disc and pads, and a target size of 2 mm on the hub.

In regards to temperatures, the results almost replicated the ones of the half-disc model, besides slight changes to the maxima and the temperature at the splines. For the disc, the maximum and mean temperatures on the contact surface was changed by +0.3 °C and −1.3 °C respectively, whilst for the pad they changed by −4.9 °C and −5.6 °C.

Due to there being a finite gap conductance at the splines a temperature difference forms over the contact interface. At the disc side the temperature was ≈ 120 °C and at the hub side it was ≈ 80 °C. The temperature on the disc side is significantly lower than when that edge is insulated, see Figure 4.1b, for which it is ≈ 150 °C. The heat did not spread much throughout the hub, with only the part at the splines having significantly raised temperatures. The final minimum temperature in the wheel hub is even reduced to 47.0 °C due to convection and radiation.

At the end of braking, the maximum temperature on the disc surface was 554 °C, and the final mean was 496 °C. Comparing with the half-disc model, see Figure 4.2, we note that the final maximum temperature is increased by approximately 0.3 °C, whilst the mean is decreased by ≈ 1.3 °C.

The final maximum temperature on the pad surface was 530 °C, and the final mean was 475 °C. In comparison with the half-disc model, see Figure 4.3, the maximum temperature is decreased by ≈ 4.9 and the mean is decreased by ≈ 5.6 °C. The final temperature difference between pad and disc is thus ≈ 22.8 °C for the maximum and ≈ 21.3 °C for the mean temperature.

The calculated wear values only slightly differs when compared to the half-disc model. For the pad the accumulated wear depth was 4.018 µm, whilst for the disc it was 0.8582 µm. The reduced value for the pad is due to lower mean temperature on the pad surface.

4.1.1.3 With Cast Iron Backing Plate

Changing to a cast iron backing plate for the thermal half-disc model reduced the maximum temperature on the disc surface by 0.39 °C to 552 °C. On the pad surface it decreased the maximum 0.72 °C to 534 °C. The changes were thus negligible.

At the measurement point in the pad the final temperature decreased by about 4 °C to 219 °C.

4.1.2 Thermomechanical Axisymmetric Model

The following pictures and plots present the results from the thermomechanical axisymmetric model. The results are presented for the finest mesh studied, the 0.5 mm mesh. Note that these results are with the unadjusted thermal conductivity.

Figure 4.5 shows the temperature through pad and disc at $t \approx 10$ s and $t = 40$ s. At $t = 40$ s it is clear that a high temperature zone has formed at the middle of the contact surface, which means that there is a hot band. The hot band forms due to thermal expansion of already warm parts which propagates since it increases the contact pressure leading to higher local heat generation. Comparing with the results from the thermal model, see Figure 4.1, one can see that the difference between the two is not that great at $t = 10$ s when the hot band has not fully formed, but at $t = 40$ s the hot band has causes the results to differ greatly.

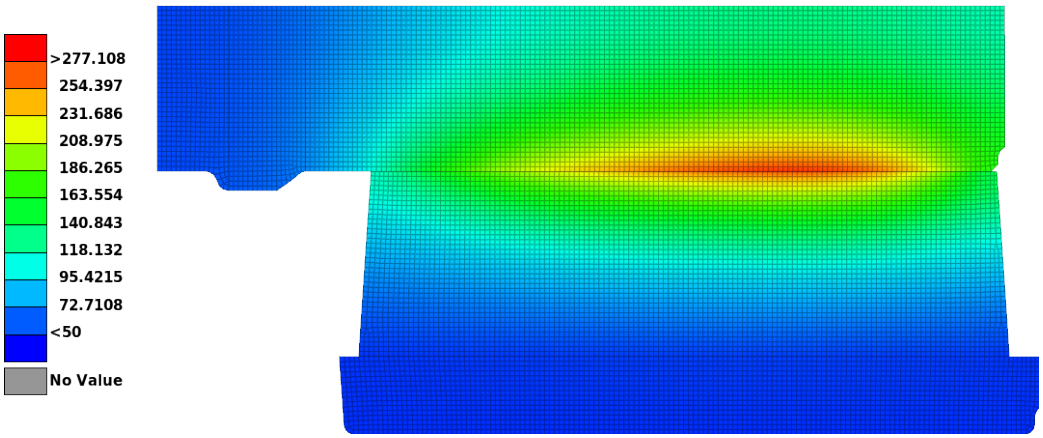

(a) *At* $t \approx 10$ s

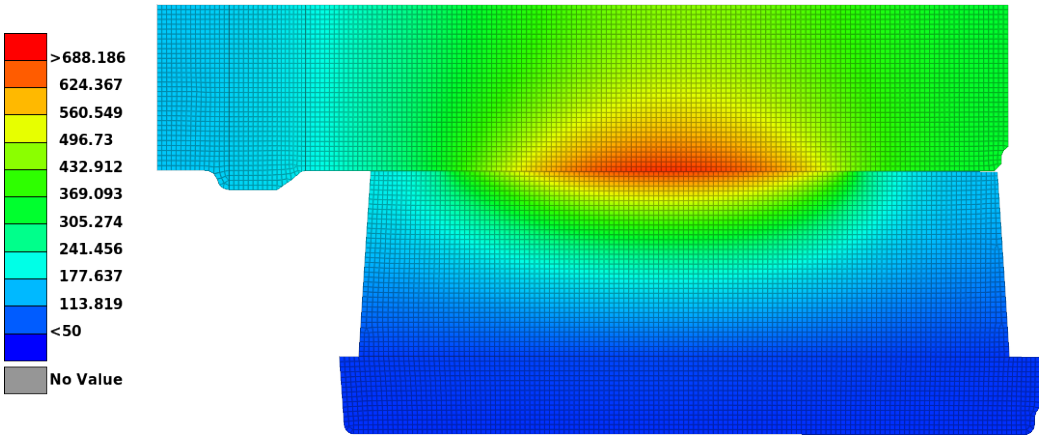

(b) *At* $t = 40$ s

Figure 4.5: *Picture of the nodal temperatures for the thermomechanical axisymmetric model at selected time points.*

Figure 4.6 shows the maximum and mean temperatures on the disc contact surface for this thermomechanical model. Notably the final difference between maximum and mean is substantially larger than for the thermal simulation, see Figure 4.2, with it being increased from approximately 55.3 °C to about 181 °C. This increase is due to the formation of the hot band, with the maximum temperature being 136 °C higher than in the thermal simulation. The final mean disc temperature is also higher, but only by about 10.1 °C.

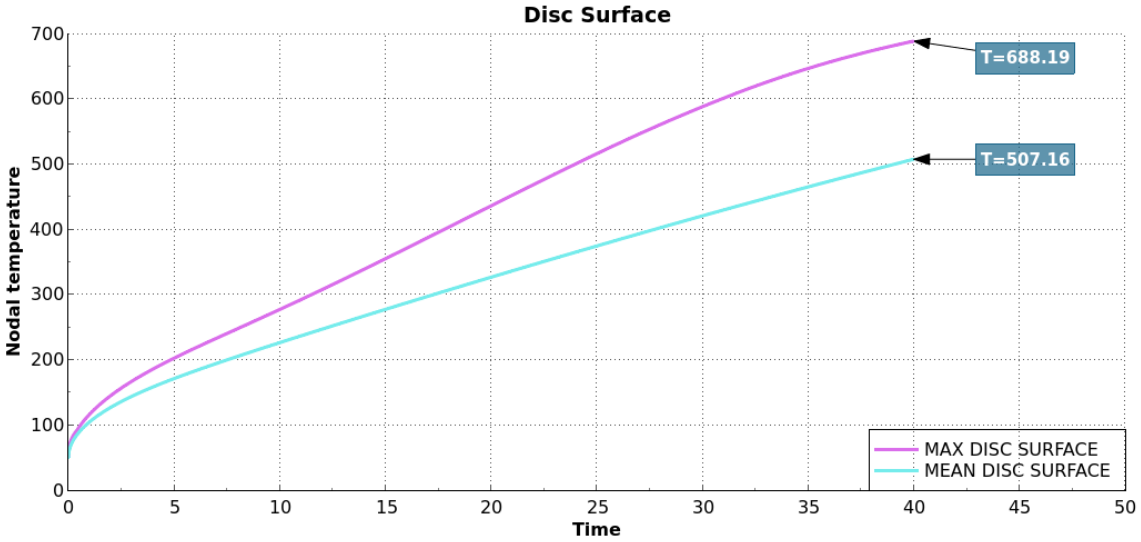

Figure 4.6: *The temperature on the disc contact surface over time for the thermomechanical axisymmetric model.*

Figure 4.7 shows the maximum and mean temperatures on the pad contact surface. Like for the disc the temperature difference is much greater than for the thermal simulation, see Figure 4.3, with an increase of 141 °C.

However, the mean temperature of the pad surface has decreased by approximately 36.8 °C compared to the thermal simulation. Also the temperature difference between maximum pad and disc temperatures is now lowered to 12.3 °C from 17.6 °C, whilst for the mean temperature it has increased from 16.9 °C to 63.8 °C. That the difference between maximum and mean surface temperature has increased greatly imply a larger temperature difference across the pad surface for the thermomechanical model; this can be seen in comparisons between Figures 4.1b and 4.5b.

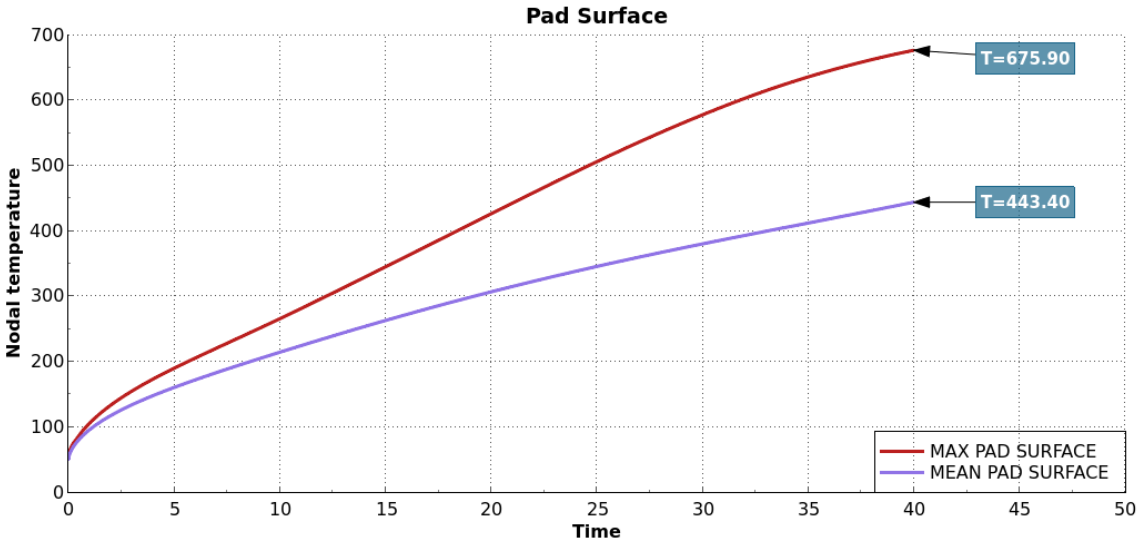

Figure 4.7: *The temperature on the pad contact surface over time for the thermomechanical axisymmetric model.*

In Figure 4.8, some snapshots of the contact pressure are shown. The pressure distribution

changes over time and one can see the pressure increase centrally that corresponds to the formation of the hot band. At $t \approx 0$ s, Figure 4.8a, the contact pressure is relatively constant, except for some spikes likely due to edge effects. At $t \approx 10$ s, Figure 4.8b, the contact pressure distribution has become uneven due to the thermal expansion, contrast the position of the the higher contact pressure with the position of the higher temperatures in Figure 4.5a, but most of the pad is still in contact with the disc. In the end, at $t = 40$ s, the contact has become localised with some parts of the pad not being in contact at all, a clear sign of the hot-banding that occurs.

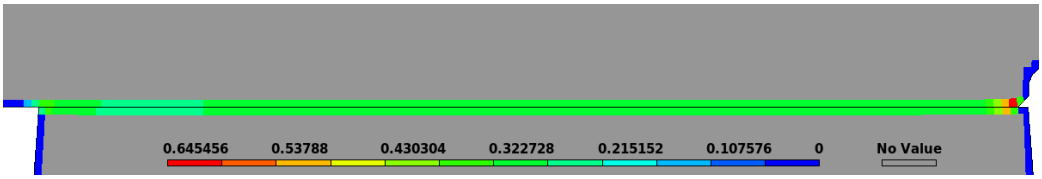

(a) *At* $t \approx 0$ s

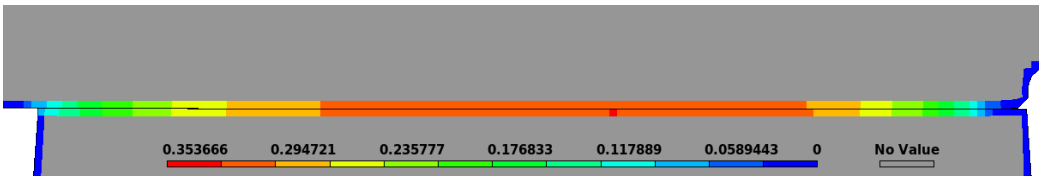

(b) *At* $t \approx 10$ s

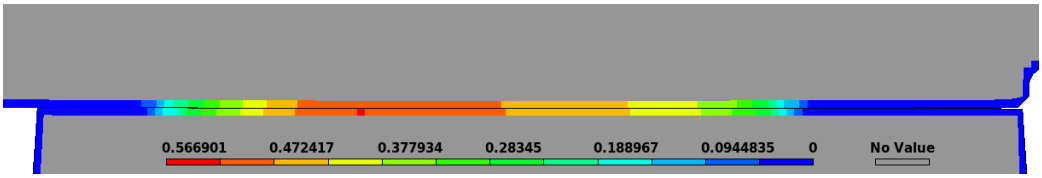

(c) *At* $t = 40$ s

Figure 4.8: *Picture of the contact pressure for the thermomechanical axisymmetric model at selected time points.*

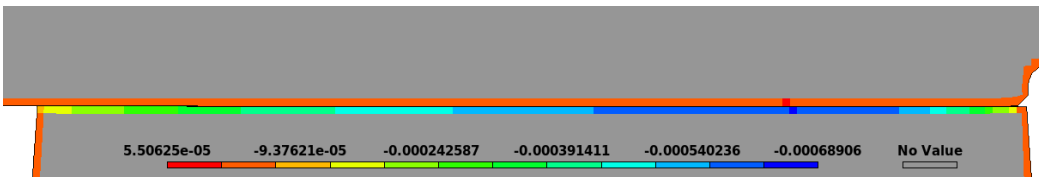

(a) *At* $t \approx 10$ s

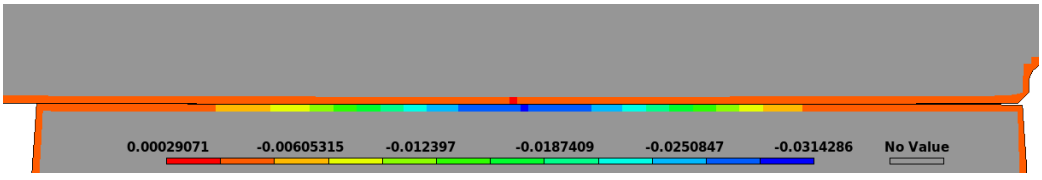

(b) *At* $t = 40$ s

Figure 4.9: *Picture of the accumulated wear for the thermomechanical axisymmetric model at selected time points.*

Figure 4.9 shows snapshots of the accumulated wear. Note that values on the pad are negative and they are positive on the disc, this is because of the wear occurring in opposite

directions.

It is important to consider when viewing the results of the accumulated wear in Figure 4.9 that those results are history dependent. For example when comparing Figures 4.8b and 4.9a it is clear that the position of the highest pressure is not the at the same position as that of the highest wear.

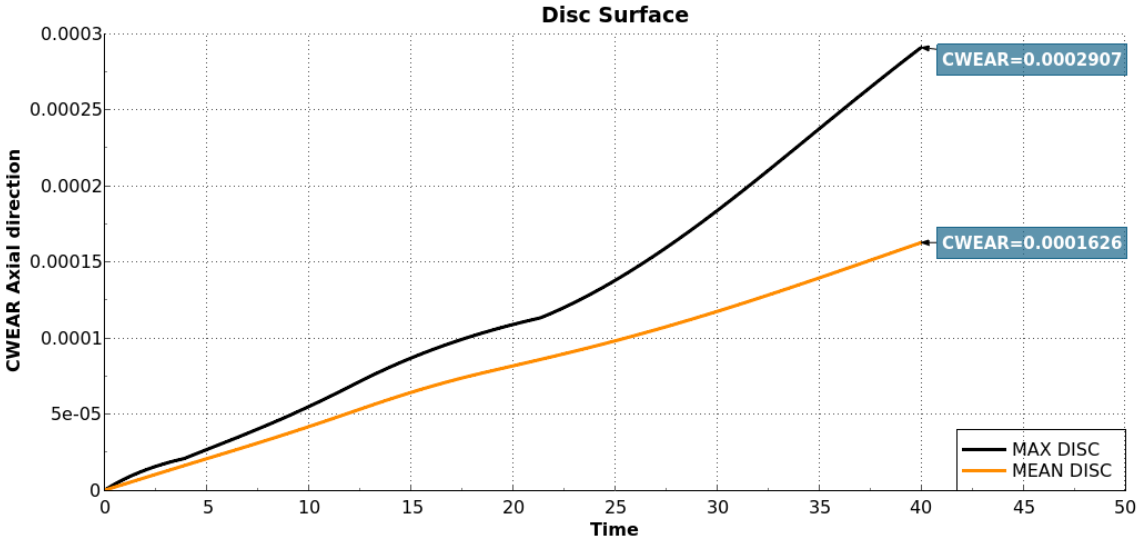

Figure 4.10: *The accumulated wear on the disc contact surface over time for the thermomechanical axisymmetric model.*

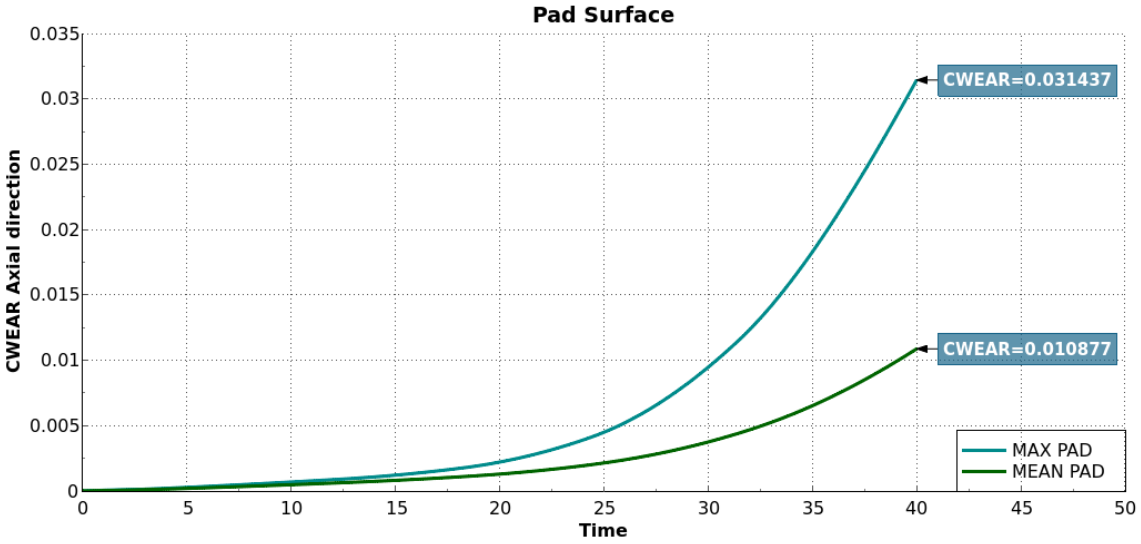

Figure 4.11: *The accumulated wear on the pad contact surface over time for the thermomechanical axisymmetric model.*

Figure 4.10 shows resulting accumulated wear on the disc surface and Figure 4.11 shows it on the pad surface.

4.1.2.1 Without Thermal Expansion and Wear

To allow further comparison with the thermal model, a thermomechanical simulation was performed where the thermal expansion and wear were disregarded.

This simulation gave a final maximum temperature of 582 °C on the disc and of 561 °C on the pad, with the temperature distribution being closer visually to what is seen in Figure 4.1b. The temperature was thus lower than in the thermomechanical model that accounts thermal expansion and wear, but for the disc the maximum temperature is ≈ 29.7 °C higher than in the thermal simulation, and for the pad it is ≈ 26.3 °C greater.

4.1.2.2 With Cast Iron Backing Plate

Changing to a cast iron backing plate instead of steel for this thermomechanical model, reduces the final maximum temperature from 688 °C on the disc surface, see Figure 4.6, to 685 °C. Similarly, on the pad surface it decreases from 676°C, see Figure 4.7, to 672 °C.

At the measurement point in the pad the final temperature increases from 244 °C to 248 °C.

4.1.3 Thermomechanical 3D-Model

Shown in Figure 4.12 are the nodal surface temperatures on the disc and pad at $t = 10$ s and $t = 40$ s for the thermomechanical 3D-model.

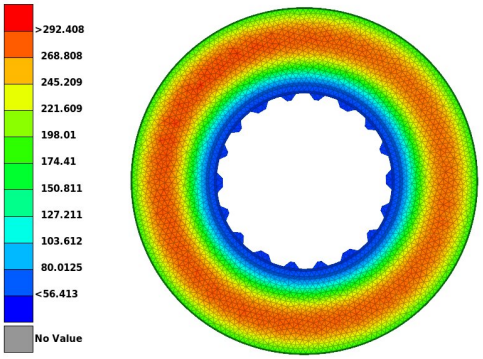

(a) *Disc at $t = 10$ s. Counter-clockwise rotation.*

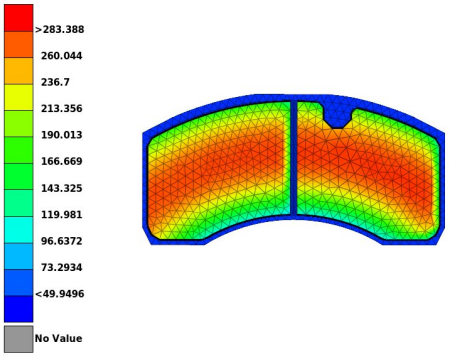

(b) *Pad at $t = 10$ s. Leading edge to the left.*

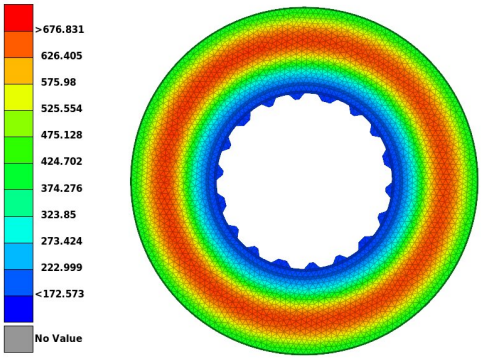

(c) *Disc at $t = 40$ s. Counter-clockwise rotation.*

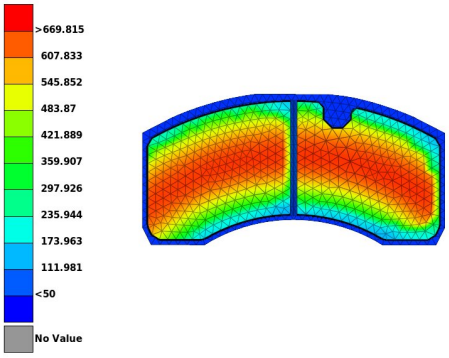

(d) *Pad at $t = 40$ s. Leading edge to the left.*

Figure 4.12: *Picture of the nodal surface temperatures for the thermomechanical 3D-model at selected time points.*

Wide bands of elevated temperatures form early on both the disc and the pad, and at the end of the simulation these hot bands become thinner and more concentrated. Temperatures are evenly distributed circumferentially on the disc with no large gradients. This is also mostly true for the pad, except for lower temperatures on the trailing edges. It should be noted that the highest calculated nodal temperature on the pad is found on the trailing side.

In Figures 4.13 and 4.14, the maximum and mean nodal surface temperatures of the disc and pad for the thermomechanical 3D-model are plotted over time.

As shown in Figure 4.13, the maximum nodal surface temperature for the disc is unsteady as the position of the maximum changes over time.

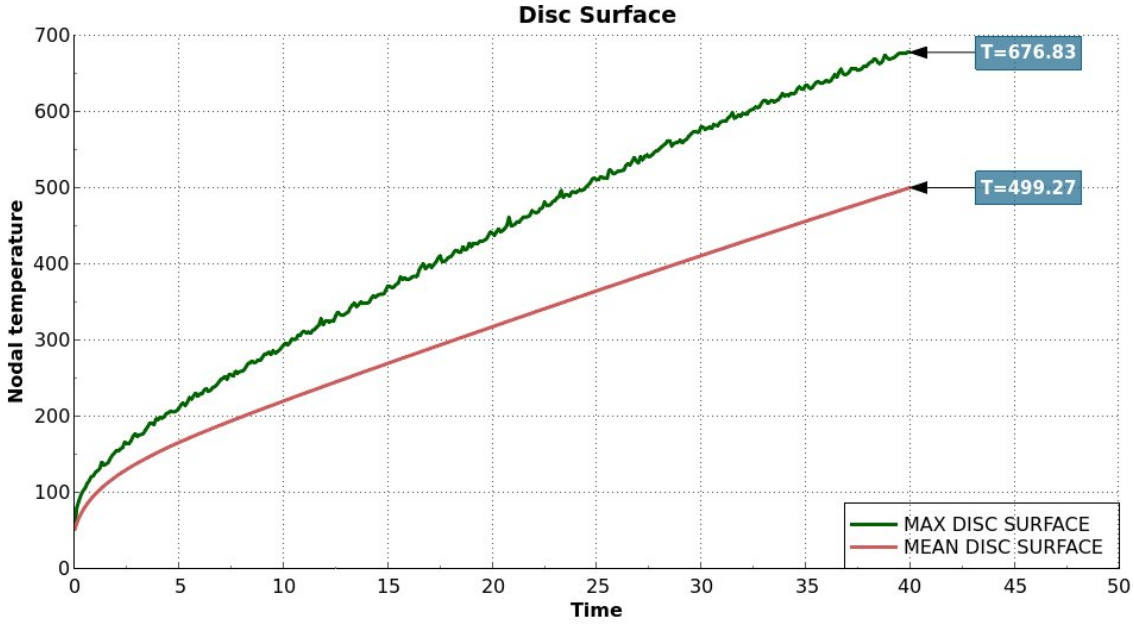

Figure 4.13: *The temperature on the disc contact surface over time for the thermomechanical 3D-model.*

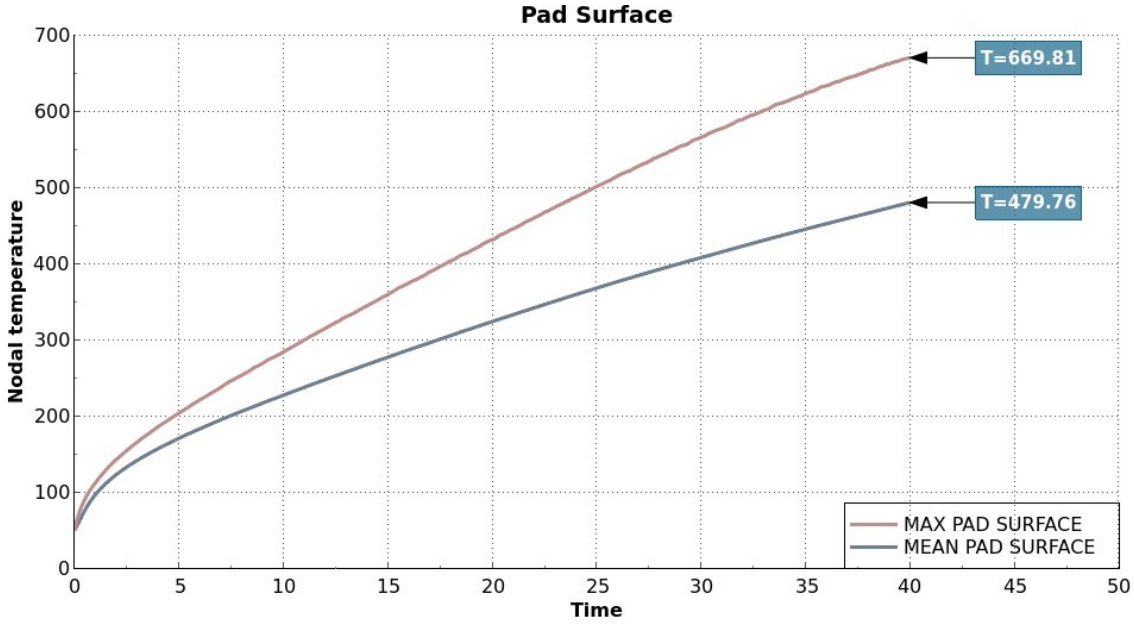

Figure 4.14: *The temperature on the pad contact surface over time for the thermomechanical 3D-model.*

The variation of the maximum nodal surface temperature for the pad in Figure 4.14 shows similar behaviour but at a much smaller scale.

In Figure 4.15 the nodal temperatures for the leading, central and trailing cross-sections are presented at $t = 10$ s and $t = 40$ s.

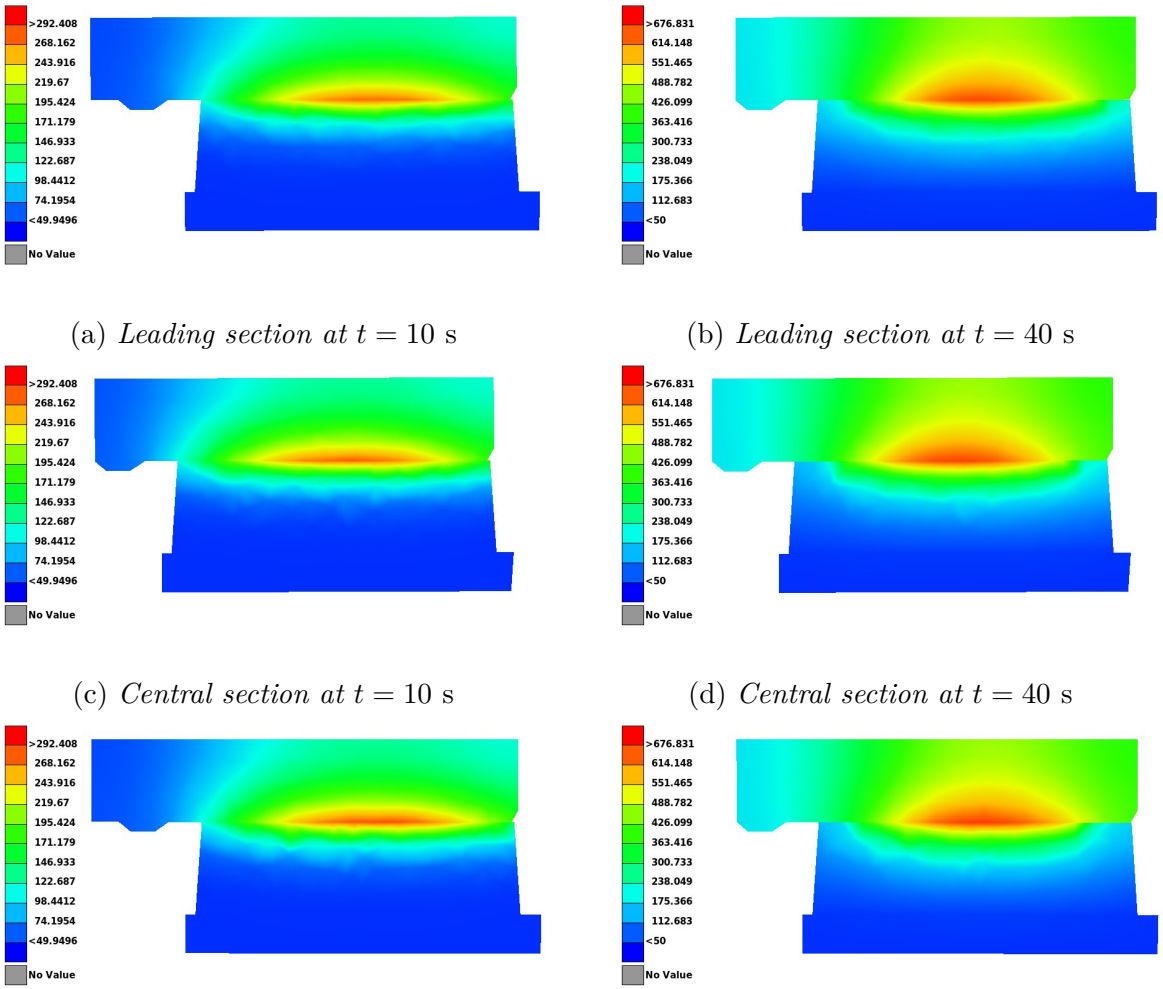

(a) *Leading section at* $t = 10$ s

(b) *Leading section at* $t = 40$ s

(c) *Central section at* $t = 10$ s

(d) *Central section at* $t = 40$ s

(e) *Trailing section at* $t = 10$ s

(f) *Trailing section at* $t = 40$ s

Figure 4.15: *Picture of the nodal temperatures for the thermomechanical 3D-model at selected time points and sections.*

The temperature distribution shows similar behaviour between each of the presented sections.

Shown in Figures 4.16 and 4.17 are the nodal temperatures of the parametric points located in the disc and pad over time (see Figure 3.7 for the location of the parametric points).

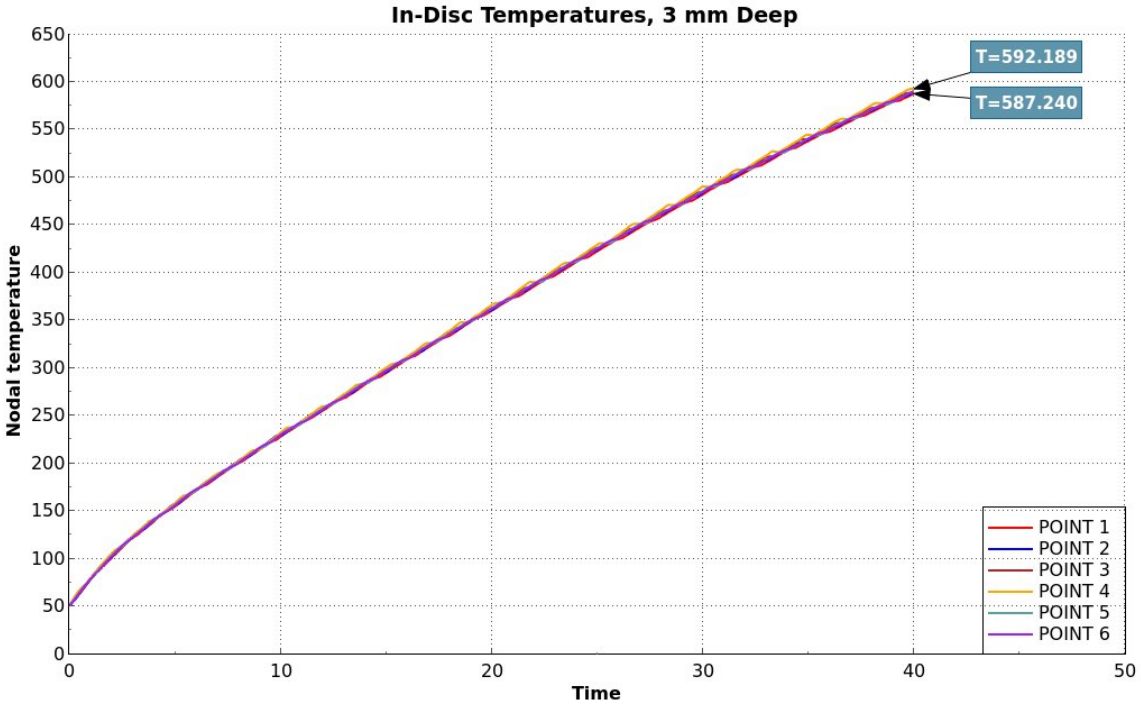

Figure 4.16: *Nodal temperatures of the parametric points in the disc of the thermomechanical 3D-model.*

As expected, the temperatures between the points in the disc differ only by a small amount and the parametric point showing the highest temperature constantly changes as the disc rotates. The maximum and minimum temperature of those points, at $t = 40$ s, is $T \approx 592$ °C and $T \approx 587$ °C respectively.

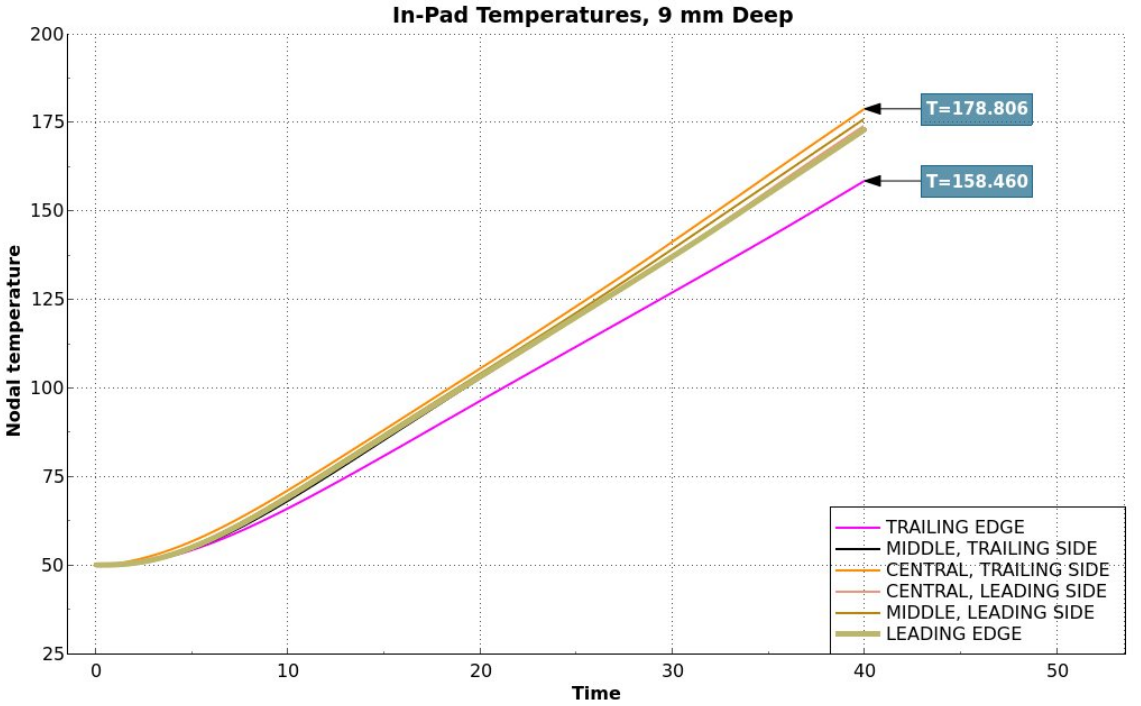

Figure 4.17: *Nodal temperatures of the parametric points in the pad of the thermomechanical 3D-model.*

The temperatures of the points in the pad differ more than the points in the disc and show a similar behaviour to Figure 4.14. Here, the maximum in-pad temperature is found at the point "Central, Trailing Side" while the minimum is found at the point "Trailing Edge". Their values are $T \approx 179$ °C and $T \approx 158$ °C respectively.

Shown in Figure 4.18 are the contact pressures on the pad surface at $t = 0$ s, $t = 10$ s and $t = 40$ s. Note that the contact pressure on the disc surface is not presented since the part of the disc surface that is in contact with the pad displays an identical contact pressure distribution as that of the pad.

At $t = 0$ s an even contact is established between the disc and pad without brake force being applied. At $t = 10$ s the inner and outer radial edges, as well as the trailing edges of the leading and trailing side of the pad, begin to lose contact with the disc as both the pad and disc thermally expands. Maximum contact pressures are found on the leading edges of the leading side and the trailing side. At $t = 40$ s the central hot band has fully developed and the contact pressure distribution is concentrated around the effective radius, with a broader distribution on the leading side and the maximum located on the trailing side.

Shown in Figure 4.19 is the magnitude of the accumulated wear on the disc and pad surfaces at $t = 10$ s and $t = 40$ s.

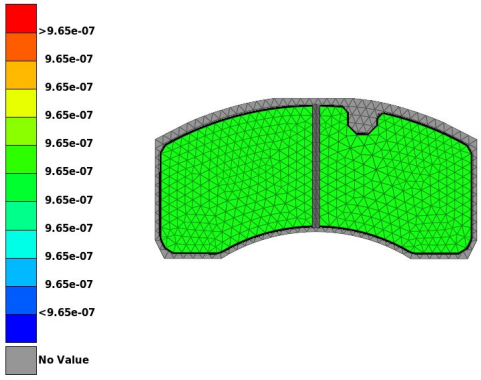

(a) *At* $t = 0$ s

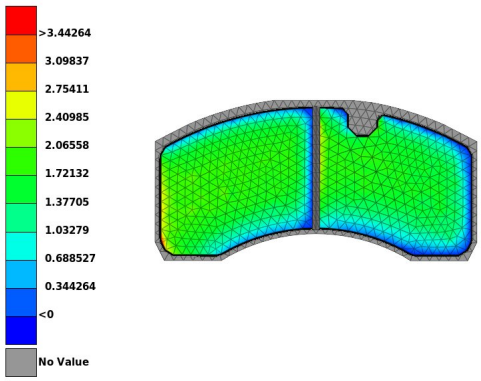

(b) *At* $t = 10$ s

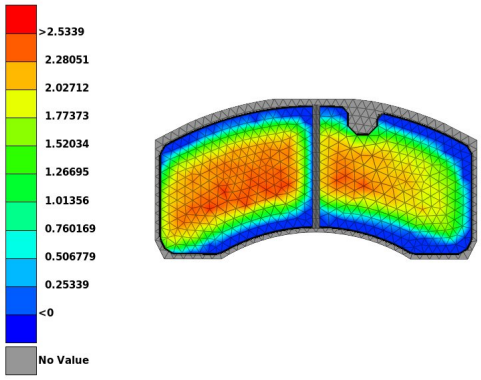

(c) *At* $t = 40$ s

Figure 4.18: *Pad contact pressure for the thermomechanical 3D-model at selected time points. Leading edge to the left.*

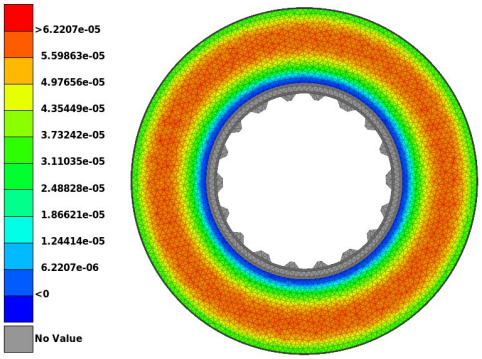

(a) *Disc at $t = 10$ s. Counter-clockwise rotation.*

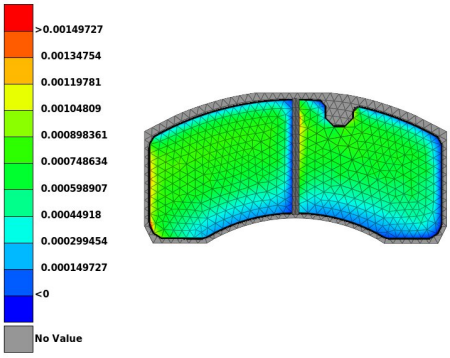

(b) *Pad at $t = 10$ s. Leading edge to the left.*

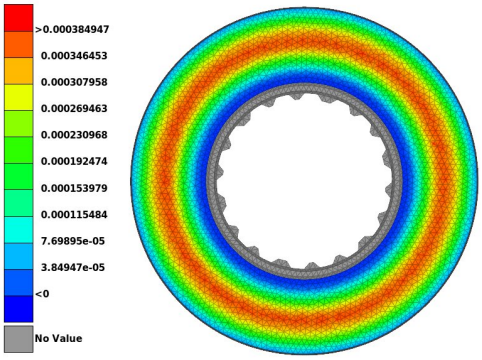

(c) *Disc at $t = 40$ s. Counter-clockwise rotation.*

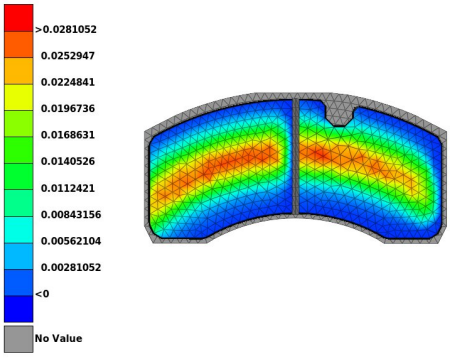

(d) *Pad at $t = 40$ s. Leading edge to the left.*

Figure 4.19: *Picture of accumulated wear magnitude for thermomechanical 3D-model at selected time points.*

The accumulated wear distribution closely follows the development of the hot band that forms at the effective radius over time. The pad shows larger values of wear at the central parts with the largest accumulated wear on the trailing side.

Figures 4.20 and 4.21 shows the magnitudes of the maximum and the mean accumulated wear of the disc and pad respectively. The maximum accumulated wear was 0.38 µm on the disc surface and 28 µm on the pad surface.

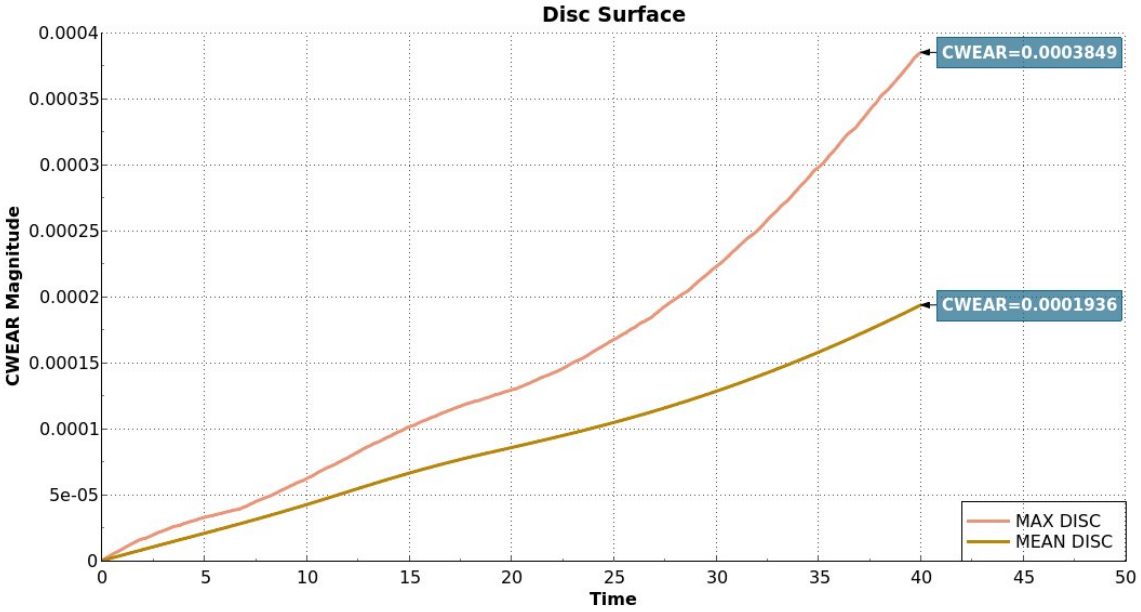

Figure 4.20: *Accumulated wear on disc contact surface over time for thermomechanical 3D-model.*

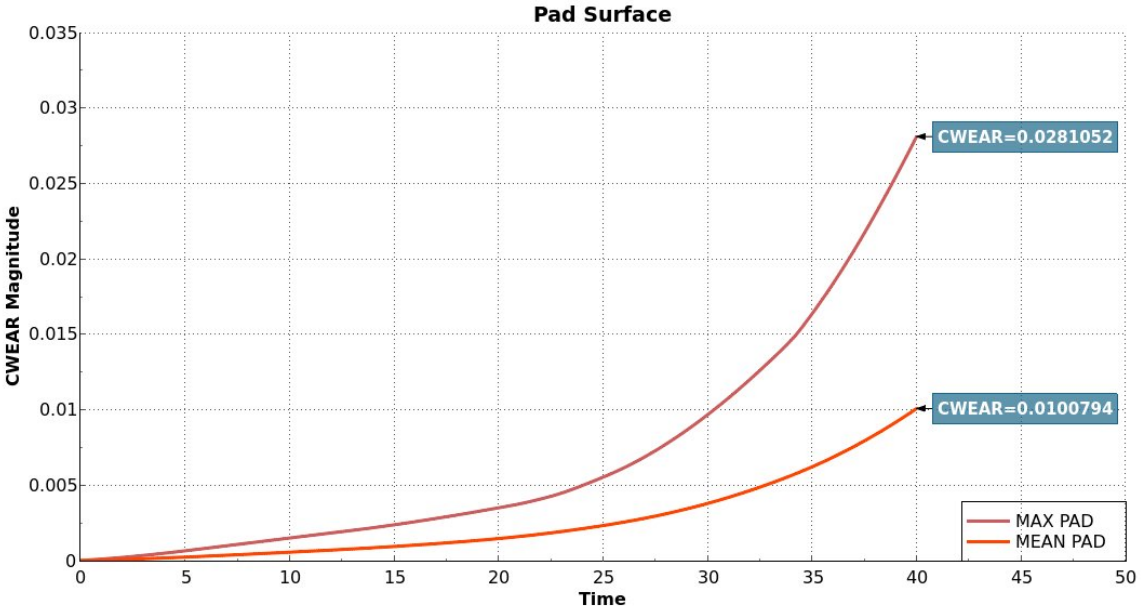

Figure 4.21: *Accumulated wear on pad contact surface over time for thermomechanical 3D-model.*

4.1.4 Comparison of Temperatures

In this subsection the results from the simulations are compared with the measured maximum and mean temperatures from the brake testing cycles. For the fairest comparison, only the early cycles, before cycle 100, were included so that the wear did not have a significant effect on the position of the measurement sensors. Note however that prior to these 100 cycles some wear will also have occurred as part of the bedding-in process; the simulations are for unworn pad geometry.

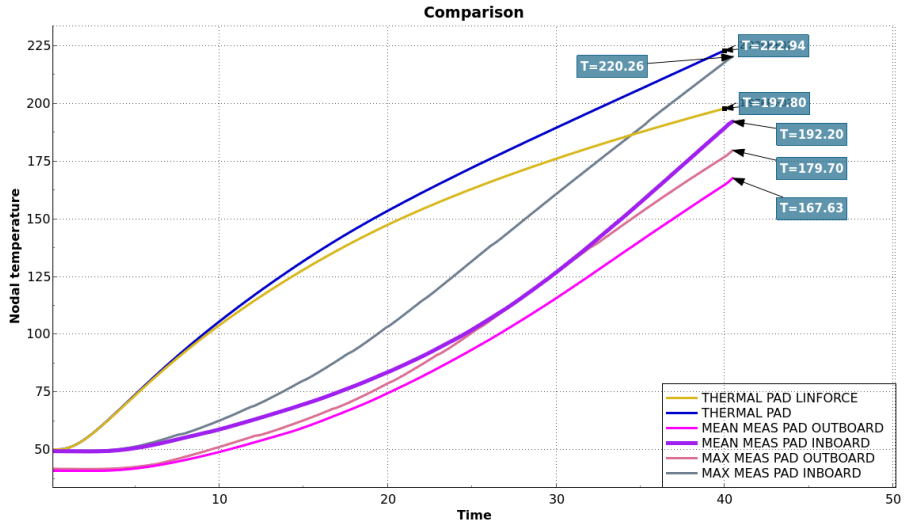

(a) *Thermal axisymmetric half-disc model. Both results with a constant clamp force of* 14.8 kN *and one linearly decreasing to* 10 kN *are presented.*

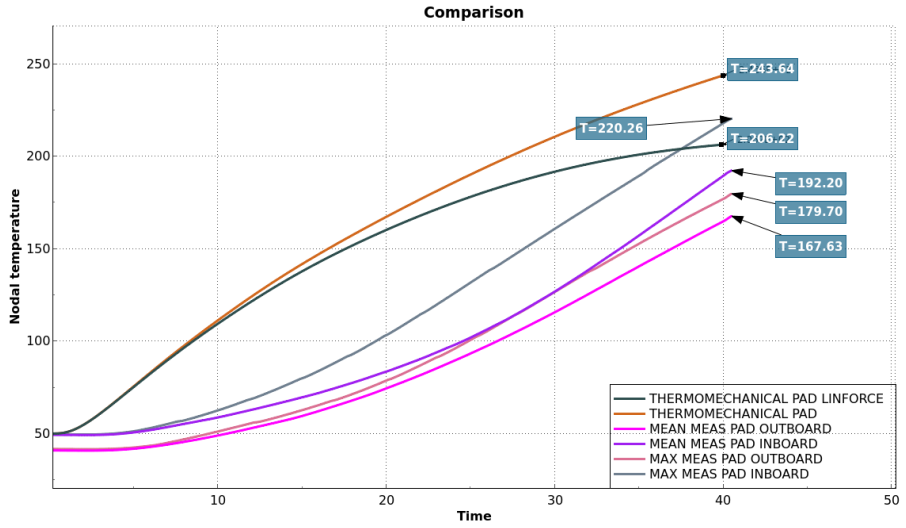

(b) *Thermomechanical model. Both results with a constant clamp force of* 14.8 kN *and one linearly decreasing to* 10 kN *are presented.*

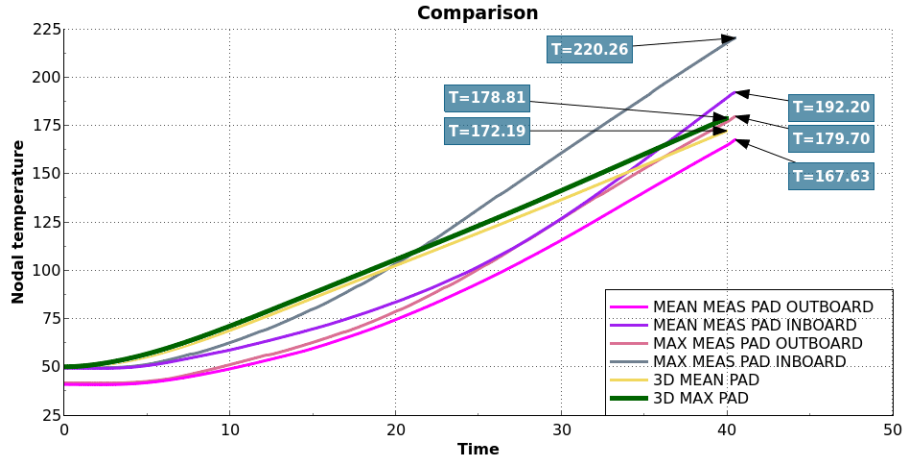

(c) *3D-model. Maximum and mean temperature of the parametric points at the correct depth and radii are presented, for constant clamp force.*

Figure 4.22: *Comparison of calculated results for the thermal axisymmetric half-disc, thermomechanical axisymmetric half-disc, and thermomechanical 3D half-disc models with the measured temperatures in the pads. In legends MEAS stands for measurement and LINFORCE for linear variation of force/heat flux.*

Figure 4.22 shows comparisons between temperature results for the three different simulation models along with the measured data of the pads. What is clear from Figure 4.22 is that the axisymmetric models overshot the temperature in the pads, especially if the constant clamp force assumption is used. For comparison simulations were done with the clamp force varying linearly from 14.8 kN to 10 kN (this value was a very rough guestimate and should not be assumed to be more correct), and from Figures 4.22a and 4.22b it is clear that the final temperature then becomes closer to the mean temperatures measured in the pad.

Comparing between Figures 4.22a and 4.22b it is clear that the thermomechanical model overestimates the temperature more than the thermal model. We can also note from Figure 4.22 that for all three models, especially the axisymmetric models, the temperature increases much more rapidly early in the brake application than it did in the measurements.

It is also clear from Figure 4.22 that for this 3D-model the temperature prediction in the pad has a much lower temperature than the axisymmetric models. When compared to the measurements, especially the outboard pad, the 3D-model seems more accurate. It is however worth noting that the outboard pad in the tests have a lower initial temperature of about ≈ 41 °C. Contrasted with the more comparable inboard pad measurements, the 3D-model instead undershoots the final temperature.

Note that the axisymmetric results are with the unadjusted thermal conductivity, hence the temperatures are likely higher than they should be.

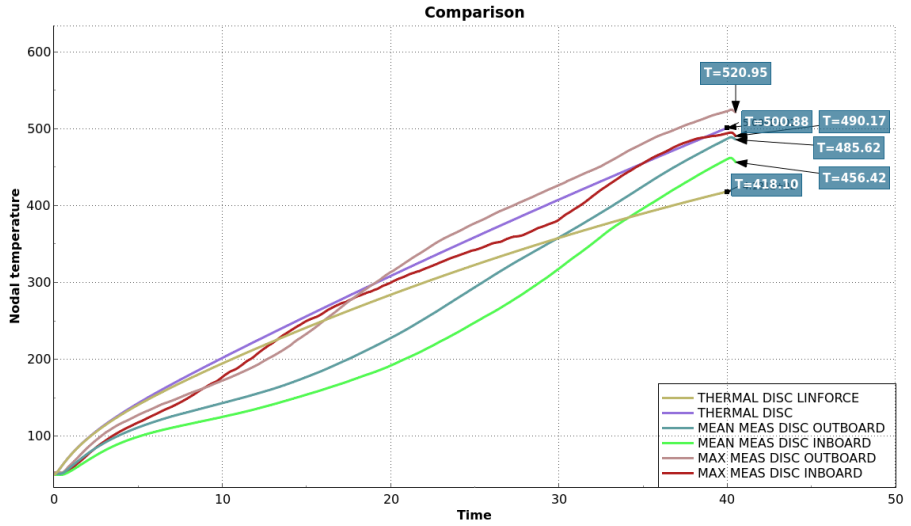

(a) *Thermal axisymmetric half-disc model. Both results with a constant clamp force of* 14.8 kN *and one linearly decreasing to* 10 kN *are presented.*

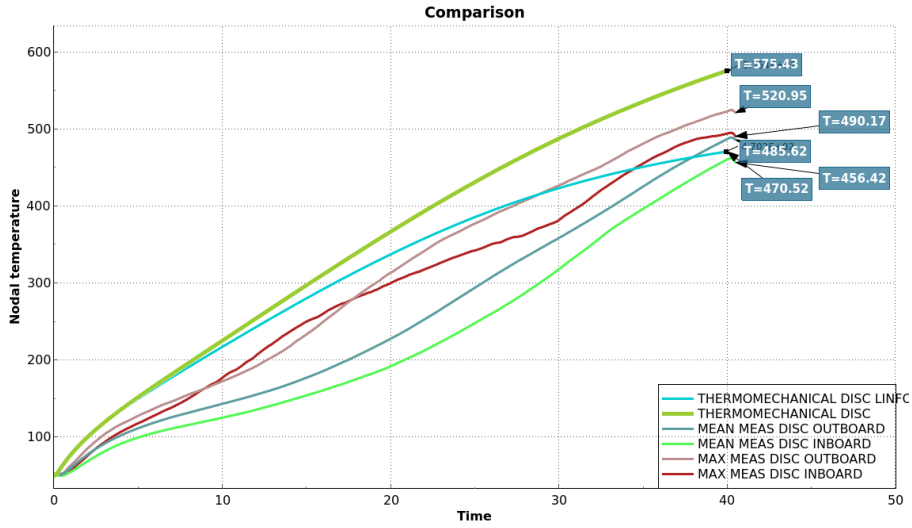

(b) *Thermomechanical model. Both results with a constant clamp force of* 14.8 kN *and one linearly decreasing to* 10 kN *are presented.*

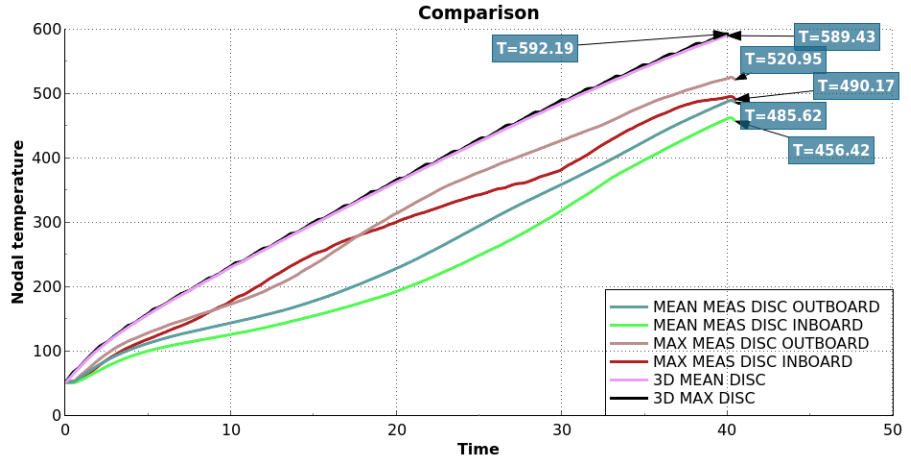

(c) *3D-model. The maximum and mean temperature of the parametric points are presented, for a constant clamp force of* 14.8 kN.

Figure 4.23: *Comparison of the thermal axisymmetric half-disc, thermomechanical axisymmetric half-disc, and thermomechanical 3D half-disc models with the measurements in the disc. In legends MEAS stands for measurement and LINFORCE for linear variation of force/heat flux.*

Figure 4.23 shows comparison between the results of the models and the measurement in the disc. All models with constant clamp force overestimates the measured data for the temperature at the end of the braking cycle. The axisymmetric models overshoot the temperature, in contrast with the pads the 3D-model also overshoots the temperature in the disc and does so more than the axisymmetric models.

Using a linearly decreasing clamp force of course lowers the temperatures, see Figures 4.23a and 4.23b, but in the case of the thermal model it causes an underestimation of the final temperature. This is however expected as in the measurements the torque and brake power is kept constant, and with this varying linear force that will become lower in the thermal model. This linear decrease is thus technically a qualitative model error as well.

As with the pads the temperatures increase more rapidly in the beginning of the cycle for the simulations than they did in the measurement, although the difference is less stark.

4.1.5 Correct Thermal Diffusivity for Axisymmetric Models

In this section the change of the results for the axisymmetric models if the pad and backing plates thermal conductivity is lowered by a factor of $\phi_0/(2\pi)$ is presented.

Table 4.1: Changes of final temperatures when comparing unadjusted pad and backing plate conductivity with adjusted values, and compared with 3D. The 3D values for the measurement points are for the mean of the parametric point values. All values are in °C

Model & Place	Change	Temp. adjusted	3D
Thermal max. disc surface	+30.5	583	-
Thermal mean. disc surface	+26.7	524	-
Thermal max. pad surface	+46.3	581	-
Thermal mean. pad surface	+40.1	520	-
Thermal disc meas. point	+6.59	528	-
Thermal pad meas. point	−46.9	176	-
Thermomec. max. disc surface	+5.98	649	677
Thermomec. mean. disc surface	+28.7	536	499
Thermomec. max. pad surface	+18.9	650	670
Thermomec. mean. pad surface	41.4	485	480
Thermomec. disc meas. point	+43.3	619	589
Thermomec. pad meas. point	−69.3	174	172

Table 4.1 shows the change of the temperatures for the thermal and thermomechanical axisymmetric models at different places when the pad conductivity is adjusted. The wear depths in the thermomechanical model also changed. For the disc the maximum accumulated wear depth was decreased by 0.042 µm to 0.2488 µm, whilst the mean decreased by 0.0051 µm to 0.1575 µm. The change was more substantial for the pad; the maximum was decreased by 3.11 µm to 28.83 µm, whilst the mean increased by 0.622 µm to 11.50 µm.

4.2 Multiple Cycles and Wear Estimations

In this section the results of the ultimate axisymmetric model with multiple cycles are presented.

Two simulation was performed using temperature dependent values of $k_{w,p}$ based on wear measurements, see Section B.1.1, one with the normal α value and the other with four times that value. The latter was performed as a test of more hot-banding could be induced, some results for this simulation can be found in Appendix C.2. Another simulation was performed with a constant value of $k_{w,p}$ determined with modeFRONTIER, see Section B.1.1, with the value used being $k_{w,p}/k^* \approx 12.32$, the one with the lowest error presented in Table D.13.

The primary focus of the results presented is on the values of temperature and wear at the end of each cycle, and not the results for $t < 40$ s. The wear for the cycles are presented separately from the other results in Section 4.2.3. Note that in Figures the word stop has been used, that is synonymous in this context with cycle.

4.2.1 Temperature Dependent Wear Scaling Factors

The following pictures and plots are the results for the simulation with temperature dependent $k_{w,p}$.

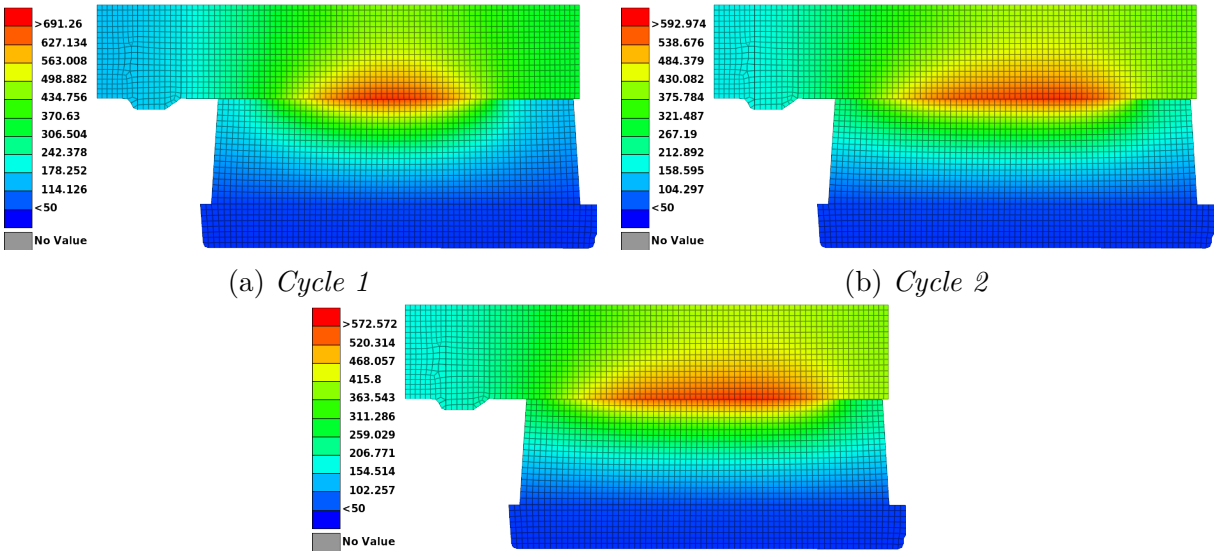

(a) *Cycle 1* (b) *Cycle 2*

(c) *Cycle 3*

Figure 4.24: *Temperature at the end of the three first cycles.*

Figure 4.24 shows the temperature at $t = 40$ s for the first three cycles. Note that the maximum temperature decreases rapidly for each cycle, from 691 °C in cycle 1 to 593 °C in cycle 2 and to 573 °C in cycle 3.

The maximum temperature of 691 °C in cycle 1, see Figure 4.24a, is slightly higher than the maximum temperature of the thermomechanical axisymmetric one-cycle model, see Figure 4.5b, of 688 °C. This is likely due to the slight difference in how $k_{w,p}(T)$ is

calculated for $T > 500$ in the built-in Abaqus wear routine and how it is calculated in the Fortran user subroutine, see Section B.1.1.

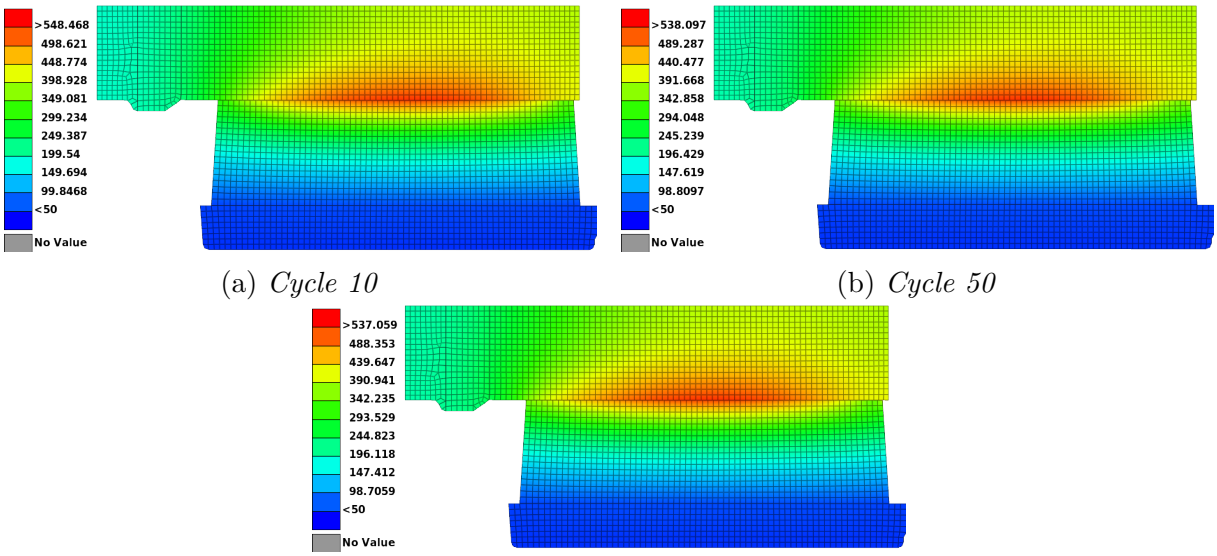

(a) *Cycle 10* (b) *Cycle 50*

(c) *Cycle 100*

Figure 4.25: *Temperature at the end of the "intermediary" cycles 10, 50 and 100.*

Figure 4.25 shows the temperature at $t = 40$ s for three intermediary cycles, cycles 10, 50 and 100. Between cycles 10 and 50 the maximum temperature decreases by approximately 10.3 °C from 548 °C to 538 °C. Between cycles 50 and 100 the reduction is much lower at only ≈ 1.04 °C when it is lowered to 537 °C in cycle 100.

Unlike in cycle 1, see Figure 4.24a, there is no now longer a clear observed hot band at the end.

At later cycles a steady-state is found. The maximum temperature is no longer decreasing, and is relatively constant, with an increase of ≈ 1 °C each from cycles 300 to 400 and 400 to 500.

Figure 4.26 shows the calculated maximum and mean temperature on the disc contact surface at $t = 40$ s for each cycle. This shows what could be observed in Figures 4.24 and 4.25. The maximum temperature decreases rapidly with the hot band being worn in, with the difference between maximum and mean temperature being reduced compared to the first step.

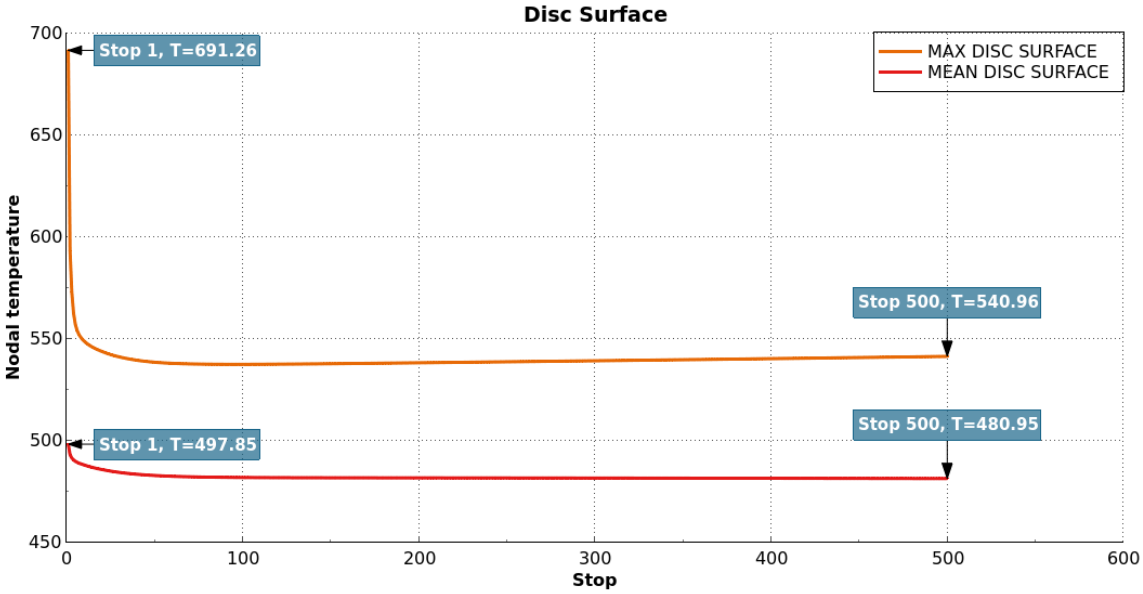

Figure 4.26: *Final maximum and mean nodal temperature on the disc surface.*

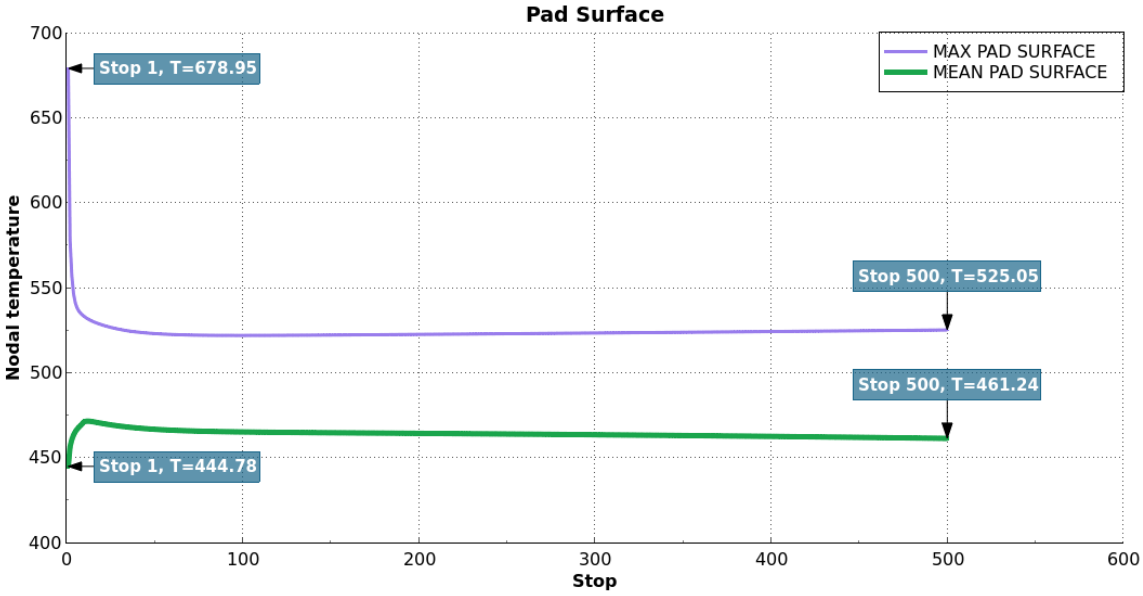

Figure 4.27: *Final maximum and mean nodal temperature on the pad surface.*

Figure 4.27 shows the maximum and mean temperature on the pad contact surface at $t = 40$ s for each cycle. The maximum temperature follows the same trend as on the disc surface, see Figure 4.26. Unlike on the disc surface where the mean temperature slightly decreased as the hot band was dissolved, the mean temperature on the pad increases slightly. This is indicative of a more even contact between disc and pad.

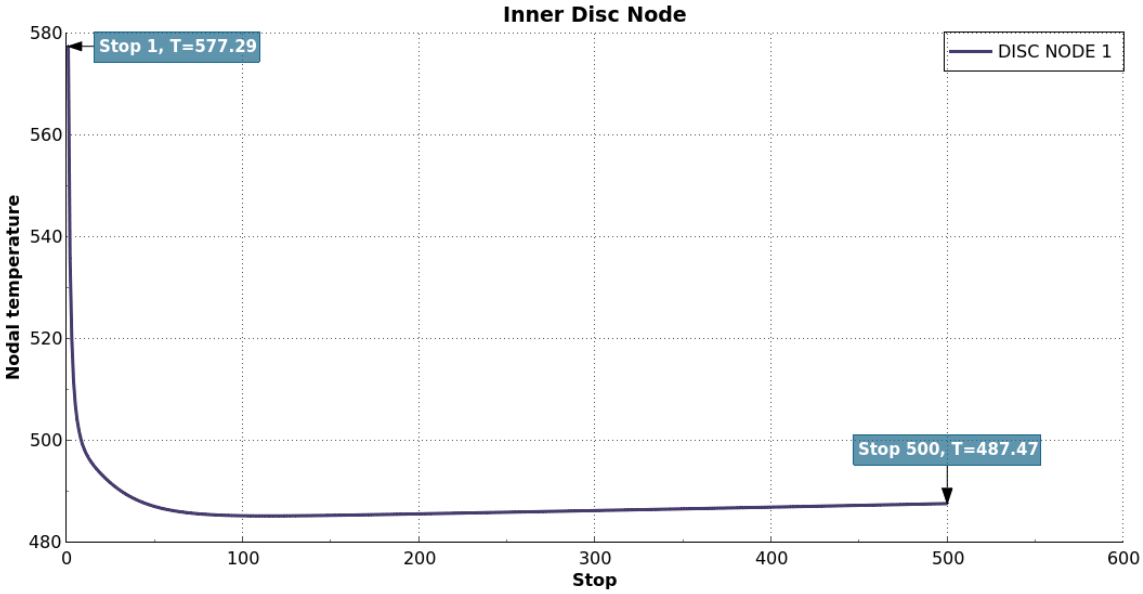

Figure 4.28: *Final maximum and mean nodal temperature on an inner disc node. The node is at the start of the simulation approximately in the same placement as the measurement probe.*

Figure 4.28 shows the temperature at $t = 40$ s for the node placed closest to the where the measurement probe was placed in the disc. As at the surface, the temperature decreases rapidly for the first cycles until it becomes relatively constant later on. Note especially that the final temperature of cycle 500 in this node is 487.47 °C, which is very close to the mean temperatures measured in the disc, see Figure 4.23 and Table 4.2.

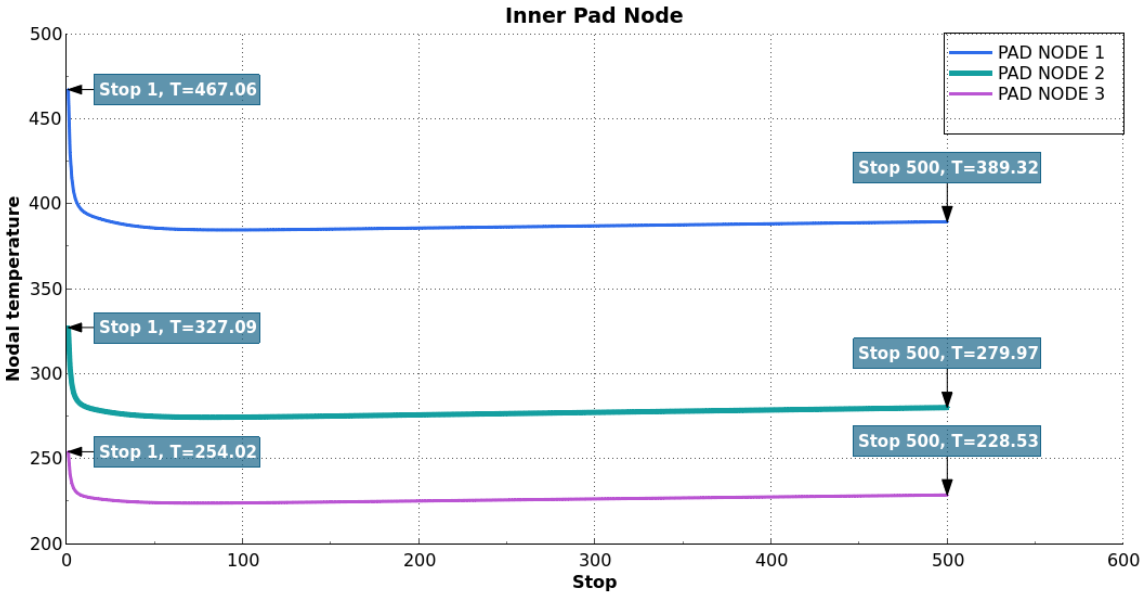

Figure 4.29: *Final maximum and mean nodal temperature on inner pad node. The nodes are at the start at approximately the effective radius, with roughly depths of 3, 6, and* 9 mm

Figure 4.29 shows the temperatures at $t = 40$ s for three nodes in the pad, placed at the effective radii at roughly depths of 3, 6 and 9 mm, with the latter being the node closest to the measurement probe in the pad at the start. As on the surface, the temperature

decreases by substantially during the first few cycles, and after a while they are somewhat constant (at least with this temperature scale).

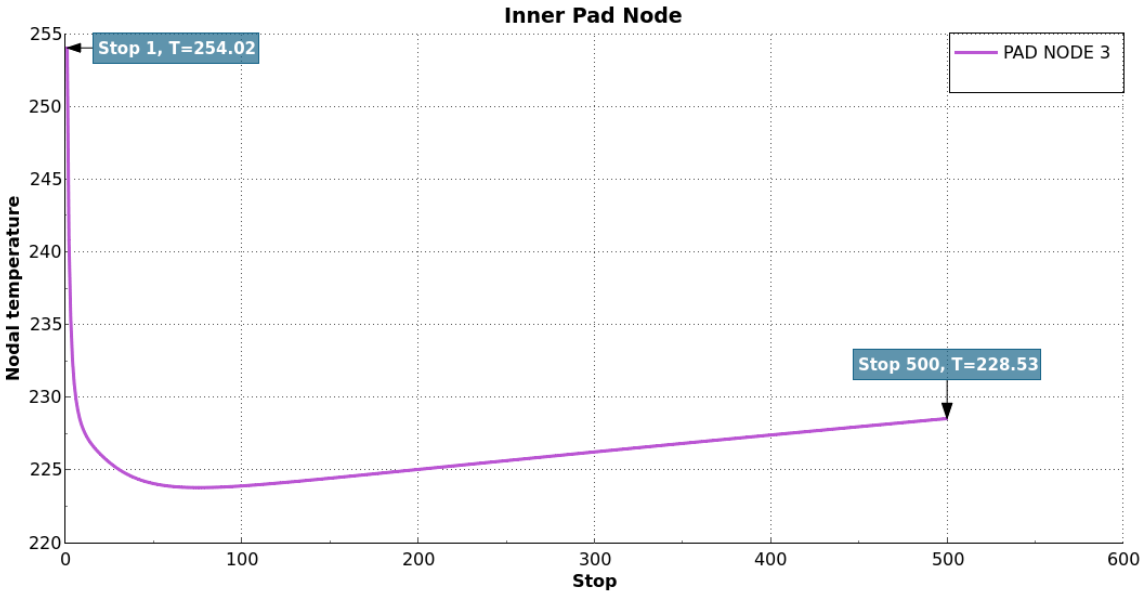

Figure 4.30: *Final maximum and mean nodal temperature on inner pad node 3, the node originally closest to the measurement point*

Figure 4.30 shows the temperature only for pad node 3, the one originally closest to the placement of the measurement probe. With this temperature scale it is now clear that the temperature increases for later cycles.

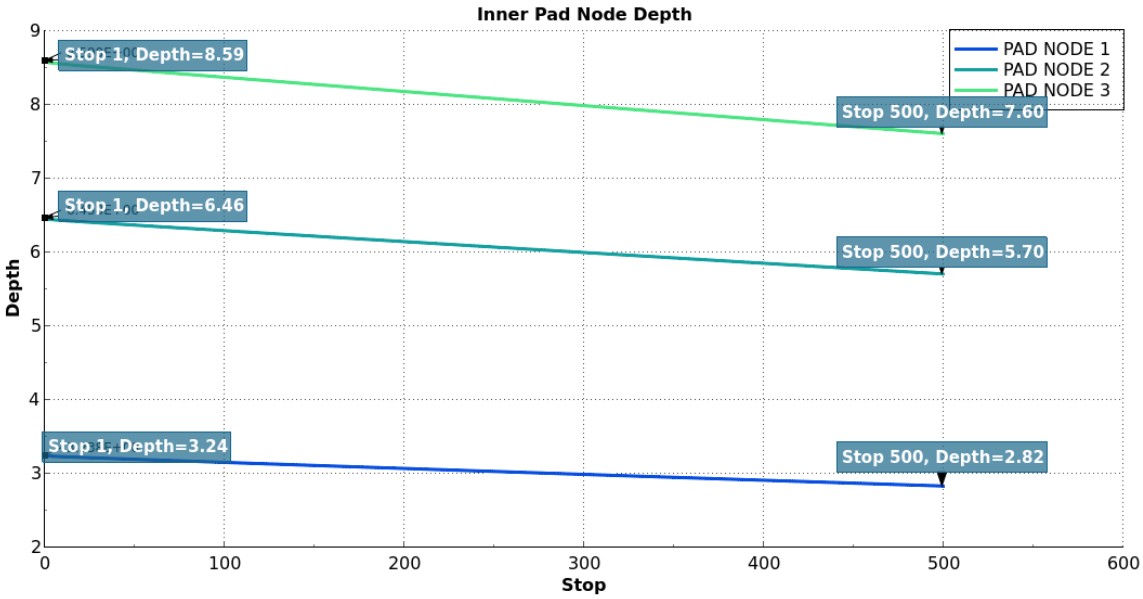

Figure 4.31: *The depth of the nodes in the pads from which the results are extracted, and how that depth changes with number of simulated braking applications.*

Figure 4.31 shows the change of depth from the friction surface for the nodes. Note that due to the scaling factor s that control node movement inside the pad volume in *UMESHMOTION*, see Appendix B.3.1, the nodes will not move a distance equal to the wear depth

closer to the surface but the movement will instead be smaller. This is clear from the node closest to the surface only moving a distance of 0.42 mm closer to the surface whilst the node 3 moves a distance of 0.99 mm. This also means that whilst node 3 is close to the measurement probe at the start it will not be at the end if the pad has worn non-negligibly.

The results from Figures 4.29 and 4.30 can thus not be easily compared with the measurements. Considering that node 3 will be at a greater or equal depth than the measurement probe at the end of the simulation, we can still conclude that since the minimum final temp of that node is ≈ 224 °C, and that is higher than the temperatures measured in the pad measurement probe, that the results of the model are still too warm in the pad.

Table 4.2: Comparison of final temperatures with measurements cycles before number 100. All temperatures are in °C.

Placement	Measured mean	Measured max	Measured min	Simulation
Disc inboard	456	490	350	478
Disc outboard	486	521	383	478
Pad inboard	192	220	166	> 224
Pad outboard	168	180	157	> 224

Table 4.2 shows a summarised comparison between the final values of the temperature in the measurements and those in Figures 4.28, 4.29 and 4.30. Note that the reason why the pad simulation value is denoted with ">" is both because that it is simply the minimum value it has, and that as stated earlier that node 3 will likely be further from the friction surface than the measurement sensor.

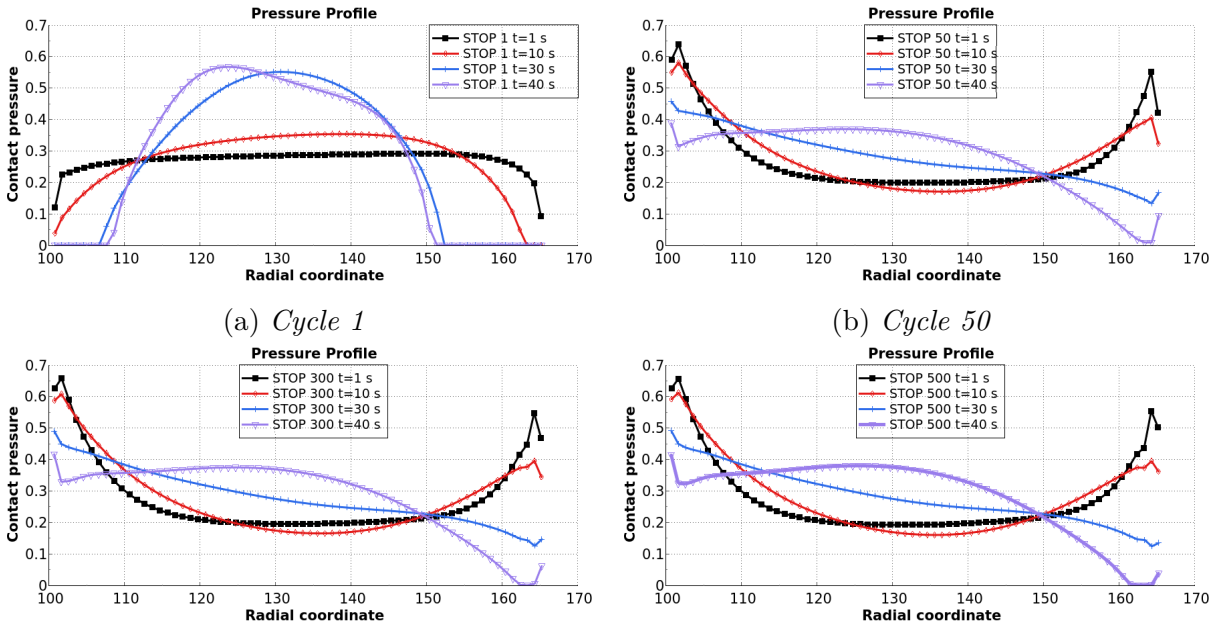

(a) *Cycle 1* (b) *Cycle 50*

(c) *Cycle 300* (d) *Cycle 500*

Figure 4.32: *The contact pressure profiles at selected times for a few selected cycles. The contact pressure is extracted from the pad surface.*

Figure 4.32 shows how the contact pressure distribution changes along disc radial coordinate with time for cycles 1, 50, 300 and 500. The contact pressure distribution at $t = 1$ s

gives us information about how different parts of the pad (and disc) contact surface has been worn from previous braking. High local contact pressure at that time means that the local wear has been low, and therefore higher contact pressure results when the pad is pressed against the disc. For the other selected time points, the contact pressure distribution gives information on how the temperature, and thermal expansion, changes on the surface.

In Figure 4.32a we see that the contact pressure distribution is near constant at $t = 1$ s due to the little wear that has occurred. As t increases we can see how the hot band forms gradually with a more and more localised contact pressure distribution, which is due to the thermal expansion of pad and disc.

In Figures 4.32b, 4.32c and 4.32d, the distribution at $t = 1$ s is nearly the same for all three cycles, and a valley has formed in the middle of the pad, where the hot-banding occurs. The relative little change is indicative of the change in wear depth being relatively constant over the surface, when looking at an entire cycle. At $t = 10$ s there are increases, relative to $t = 1$ s, at roughly 105 mm $\leq r \leq$ 125 mm and at 150 mm $\leq r \leq$ 160 mm, which means that the temperature has increased there. This then changes to an increase in the middle of the surface, which becomes more pronounced with time, although it never becomes as great as in the first cycle.

From Figure 4.32 we can thus see how the wear is distributed, how at later cycles the wear depth changes near constantly across the surface, and two ”hot” bands develop at the inner and outer radii which then intersect and form a less pronounced hot band in the middle.

4.2.2 Constant Wear Scaling Factor

The temperature results for constant $k_{w,p}$ can be found in Appendix C.1. The main difference found, with regards to temperature, was that no steady-state was formed at later cycles. Instead the maximum surface temperature increases once again at later cycles, indicating that the hot band reforms.

4.2.3 Comparison of Wear

In this subsection the wear for the two different simulations of 500 cycles is presented.

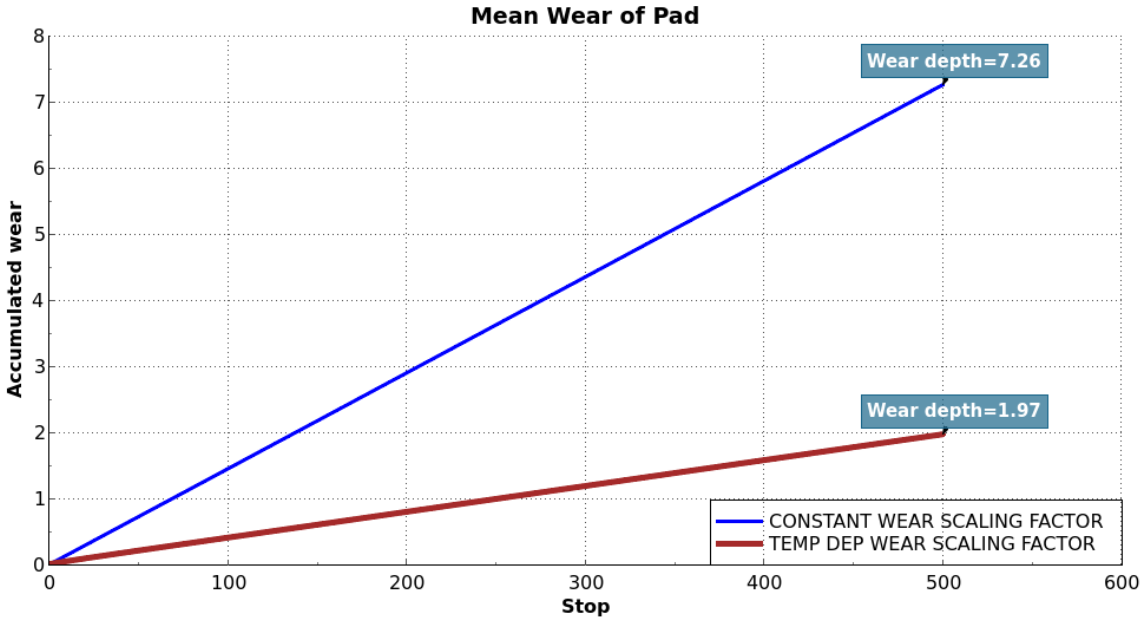

Figure 4.33: *Mean accumulated pad wear at the end of each cycle, presented for both constant and temperature dependent $k_{w,p}$.*

Figure 4.33 shows the mean accumulated wear depth on the pad surface for each cycle, for both temperature dependent and constant $k_{w,p}$.

Whilst the constant $k_{w,p}$ gives a wear depth that is nearly that of the measurements the temperature dependent $k_{w,p}$ gives much less wear, with the latter only giving a wear depth that is 27.13% of the one that the former gives.

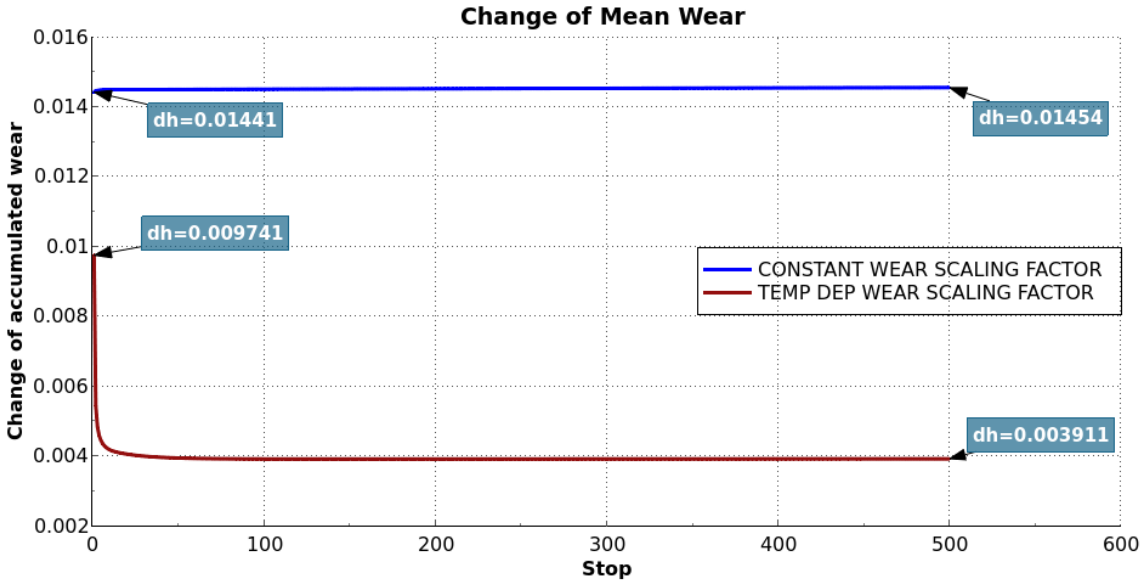

Figure 4.34: *Change of the mean accumulated pad wear for each cycle, presented for both constant and temperature dependent $k_{w,p}$.*

Figure 4.34 shows how much the accumulated mean wear on the pad changes for each cycle. For the constant $k_{w,p}$, the change is relatively constant for each cycle. Meanwhile for the temperature dependent $k_{w,p}$ it is much larger for the initial cycles, where we have

greater pad surface maximum temperature bands, than at later cycles, for which the wear is relatively constant, a result of that the surface temperature are relatively constant over those cycles.

Note in Figure 4.34 that even when the hot-banding is very pronounced, i.e. cycle 1, the value of Δh_{av} for temperature dependent $k_{w,p}$ is still less than it is for the constant $k_{w,p}$. Thus, even if the same hot band had formed for each cycle the temperature dependent $k_{w,p}$ would still have underestimated the total wear depth.

The maximum wear depth on the disc at the end of cycle 500 is ≈ 0.1408 mm for temperature dependent $k_{w,p}$, and ≈ 1.085 mm for constant $k_{w,p}$.

4.2.4 Correct Thermal Diffusivity

If correctly adjusted thermal conductivity values are used for the pads the temperature on the contact surface will change and thus the wear. In this subsection the changes of results for $k_{t,p}$ reduced by $\phi_0/(2\pi)$, with temperature dependent $k_{w,p}$, is briefly presented.

Compared with the results in Section 4.2.1 the overall trends are the same albeit the the values differ.

On the contact surfaces the maximum and mean temperature at the end of each cycle plateau in the same manner. For the disc contact surface at the first cycle final maximum temperature is increased by about 3.9 ° and the mean is increased by about 30.3 °C. At cycle 500 the increases are 12.8 °C and 24.6 °C respectively. On the pad contact surface the maximum temperature at the end of the first cycle is increased by 16.8 °C and the mean is increased by 41.0 °C. At cycle 500 the increases are 27.0 °C and 44.4 °C respectively.

At node 3 in the pad the temperature at the end of cycle 1 is 184 °C and at the end of it is 173 °C. At the measurement point in the disc it changes to 619 °C in the first cycle and to 503.5 °C in the final cycle.

The accumulated mean pad wear depth is 2.36 mm, so it has increased slightly, by ≈ 0.39 mm or 19.8%, compared to the with the wrong conductivity value, but is still significantly less than for constant $k_{w,p}$.

4.3 modeFRONTIER

The results for the modeFRONTIER projects can be found in full in Appendix D.

For comparison the normalised value of the thermal conductivity of the pad friction material as determined by the supplier at $T = 99$ °C is $k_{t,p}/k_t^* \approx 1.28$ (k_t^* is the normalisation factor for the conductivity). Important results are that $k_t/k_t^* \approx 0.802$ at $T = 99$ °C with the constant clamp force, and $k_t/k_t^* \approx 0.953$ for the linear clamp force. This is the values that then should be applied in the model, the true values will be $2\pi/\phi_0 = 4.5$ times larger.

From the study on constant $k_{w,p}$ it was determined that $k_{w,p}/k^* = 12.32 \cdot 10^{-8}$ MPa^{-1}. This value was used in the simulation presented in Appendix C.1. Note that in the handbook calculation in Appendix B.1.1 the constant value was determined to be $\bar{k}_{w,p}/k^* \approx 11.582 \cdot 10^{-8}$ MPa^{-1}. The difference in value is likely due to approximate/effective values of the pressure and radius being used in the handbook calculation.

5
Discussion

In this chapter the results and methodology of this MSc thesis work are discussed. Possible sources of errors and improvements are presented.

5.1 Discussion of Results

Differences and similarities between the different types of simulation models and the comparisons with measurements are discussed.

5.1.1 Temperatures in Models Compared to Measurements

The overarching conclusion from the temperature results presented in Section 4.1 is that in the simulations of one cycle the temperatures in the models get higher in the measurement points than the temperatures recorded in the tests. At least for when the pad thermal conductivity was not properly adjusted.

Despite that only the first 100 cycles are extracted, the wear of the pads will cause the sensors to move closer to the surface thus leading to higher temperatures. Hence, with the models of one stop with a new pad we would expect the temperatures to be less or equal to the mean values, not greater than them and certainly not greater than the maximum.

Overall, the thermal models compared better with the measurements than the one cycle thermomechanical models. One reason for this may simply be that in the one cycle thermomechanical models a hot band forms close to the measurement points. With the wear of pad and disc we expect that the hot band would form at a different radius, or not form at all, for different cycles, based on the variation of final brake temperature values from the measurements. Therefore, simulating simply one cycle with a thermomechanical model may be unideal if one wants to capture only the temperature in a specific point of the disc or pad.

The 3D-model gave a much more accurate temperature prediction in the pads than the other models, despite it being a thermomechanical model, and despite the surface temperature being roughly the same as for the thermomechanical axisymmetric model. A partial reason for this may be due to the mesh. As covered in Appendix B.4.2 the increase in computational time made the finest mesh tested, which was also used, to only have a mesh target length of 5 mm, even though the results were not fully converged. Furthermore, such a coarse mesh also means that the parametric point will be further from any nodes, and the interpolation may thus cause an underestimation of the temperature under the surface. This is also likely the reason for the disc temperature being greater than for the

other models.

The real reason for the discrepancy for the axisymmetric models is likely the mistake that when the density was lowered for the pads, the thermal conductivity was not adjusted as well. The final temperatures at the measurement point in the pad is 176.0 °C and 174.3 °C for the thermal and thermomechanical model, respectively, see Section 4.1.5, if $k_{t,p}$ is adjusted. This compares much better with the measurements and the 3D-model, see Figure 4.22, than with the unadjusted conductivity.

A partial reasons for the overestimation of the disc temperature for the 3D-model in Figure 4.23c may be that the constant clamp force assumptions can for a thermomechanical model lead to the torque/heat generation not being constant as in the tests. Figure 4.23b shows how varying the clamp force could possibly lead to more accurate predictions, although that was for unadjusted values of $k_{t,p}$.

Even though the brake energy may have been overestimated, the initial clamp force should have been correct. Therefore, that the initial increase of the temperature in the pads is much more rapid for the (axisymmetric) models than they are in the measurements, see Figures 4.22a and 4.22b, was initially surprising. It should also be noted that the initial increase in the disc is much more comparable, see Figures 4.23a and 4.23b, especially if one takes into account that there is about a 0.5 s delay until the torque has reached 1200 Nm in the tests.

This high initial increase in temperature in the pads may thus be an indication that the thermal diffusivity of the pad material for low temperatures was too great in the models, i.e. that $k_{t,p}/(c_{p,p}\rho_p)$ was too large. This was found to be true with the realisation that the pads thermal conductivity should have been reduced for the axisymmetric models.

The differences may also be due to how the measurements are taken. The question is, do the sensors instantly capture the correct temperatures? The thermocouples themselves will not have a perfect thermal contact with the pad material and may therefore give a delayed response and hence an underestimation of the temperature at transient conditions. The thermocouples may also not be placed at the specified depth of 9 mm, but rather within a certain tolerance.

5.1.2 Thermal vs. Thermomechanical

As previously noted the thermal axisymmetric model gives lower temperatures on both contact surfaces, and measurement points, than the thermomechanical axisymmetric model does.

A partial reason for the lower temperatures in the thermal models is likely the presumed mix between constant pressure and constant wear for the heat flux, see Sections 3.3.1 and 3.4.1. To be specific it is that the clamp force was calculated from the brake torque with a constant pressure assumption, and then the contact pressure for the constant wear, p_2, was calculated from that clamp force. This will mean that the brake torque, and thus the brake energy, from the constant wear part will be lower than that from the constant

pressure part, i.e.

$$\tau_1 = 2\int_{r_2}^{r_3} \mu p_1 r^2 \,\mathrm{d}r > \tau_2 = 2\int_{r_2}^{r_3} \mu p_2 r_2 r \,\mathrm{d}r. \tag{5.1}$$

Thus, the total energy will be less and the temperature lower. A counter argument is that the difference will not be very large ($\tau_1/\tau_2 \approx 1.019$), and that in the modeFRONTIER projects, see Appendix D.1, the correlation coefficient for ζ was low, which means that the mix of constant pressure or constant wear was not very important for the results. That there is a difference is however supported by the results in Section 4.1.2.1, in which the thermomechanical model was employed when disregarding thermal expansion and wear (which will give a constant pressure distribution), and still gave significantly higher maximum temperatures than the thermal model, although at the surface.

The most important distinction between the thermal and thermomechanical models is the possibility for hot-banding to form in the latter, and the effect this has on the generation and distribution of the heat.

An interesting side-effect of the localisation of the contact pressure, and thus heat generation with hot-banding is how it affects the transfer of heat on the pad contact surface. As touched upon in Section 4.1.2 in regards to Figures 4.3 and 4.7, the mean temperature on the pad surface is lower for the thermomechanical model than the thermal model, despite the maximum being significantly higher. The reason for this is how the contact conductance is affected by the hot-banding.

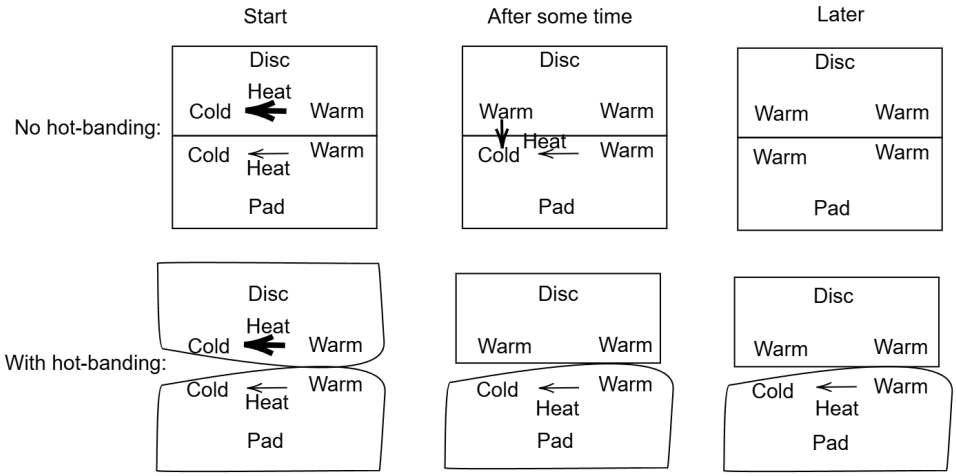

Figure 5.1: *Sketch of how hot-banding/hot-spotting and the contact conductance creates differences in the temperature distribution on the pad contact surface.*

This effect is explained visually in Figure 5.1. The heat will flow much faster from the warm parts of the disc, and thus spread more evenly, due to the higher thermal conductivity of the cast iron, whilst it spreads more slowly from warm to cold parts in the pad. However, without thermal expansion, we have full contact across the pad surface. This means that we will also have a contact conductance which partitions heat from the now warm parts of the disc surface to the still cold parts of the pad (middle picture on top row) which then gives an even temperature distribution on the pad surface as well. In

a thermomechanical model the gap conductance is however calculated as a function of the contact pressure, and with hot-spotting the cool parts will go entirely out of contact meaning that the gap conductance will be zero. Therefore, the heat will not spread that well across the pad surface for a thermomechanical model when there is hot-spotting.

Lastly, it is worth noting that using the temperature values of the surfaces from the thermal model and calculating the wear gives a severe underestimation of it, see Figures 4.4. This is simply due to that the thermal models can not replicate hot-banding, hence the maximum temperatures are lower, and with temperature dependent $k_{w,p}$, which increases exponentially with temperature, this will cause a significant difference in the predicted wear.

5.1.3 Thermoelastic Effects

One of the main purposes of the thermomechanical 3D-model was to study out-of-plane thermoelastic effects such as hot-spotting. Axisymmetric modelling and assumptions limit the types of thermoelastic effects to only one plane and thus hot-banding is the only form of hot-spotting that can be modelled. With 3D-modelling, it would be possible to capture other forms of hot-spotting as well, such as gradients on hot bands and macroscopic hot spots.

However, in the thermomechanical 3D-model the only type of hot-spotting observed was the formation of hot bands. As discussed in 2.8, Panier, Dufrénoy, and Weichert [30] found, in their experimental investigation of hot spots in railway disc brakes, that temperature gradients on hot bands, arising from frictionally excited thermoelastic instabilities, develop under prolonged braking. In their tests, they simulated braking sequences lasting between 83 seconds and 403 seconds, whereas the simulated test in this study lasted only 40 seconds. It is therefore reasonable to assume that insufficient time was available for such gradients to develop during the brake cycle here studied.

Furthermore, given the delimitations concerning plastic and metallurgical effects, as well as the simplifications made to the simulated geometry, it is reasonable to assume that the buckling modes required for macroscopic hot-spotting to develop cannot be captured using the here employed models.

5.1.4 Axisymmetric vs. 3D

Although the axisymmetric assumption works well for studies of the disc, the same can not entirely be said about the pad. The pad itself is split into two parts by a groove where one of the parts contains a cut-out, see Figure 3.7b. Also, since the pad is not shaped as a perfect circular arc, the axisymmetric scaling may overestimate or underestimate the material properties of the pad depending on how the pad angle ϕ_0 is determined, see Section 2.2. Further, as previously discussed in Section 2.7, the contact pressure of the 3D-model varies with angular position and is often higher on the trailing side of the pad compared to the leading side, as can be seen in Figure 4.18c. This contributes to different temperatures, contact pressures and wear depending on where in the pad the readings are taken from.

As previously stated, the finest mesh size that was achievable for the 3D-model was 5 mm which was also the mesh size that was used in the simulations of the final model. This mesh was not considered to have converged and may thus have contributed to inaccurate results. The finer mesh used for the axisymmetric model was considered to have converged, making the results from those models more trustworthy in that respect.

Most of the deviation between axisymmetric and 3D model results can be explained by the error that $k_{t,p}$ was not reduced for the initial simulations of the axisymmetric model. The results in Section 4.1.5 are closer to those observed for the 3D model in Section 4.1.3.

Mean values on the disc surface also differs, even when adjusting $k_{t,p}$, with lower values for the 3D, see Table 4.1. The reason why is because when extracting results from the disc surface nodes closer to the splines were included, which are colder and have less wear, in comparison with the axisymmetric model for which only nodes that had actually been in contact where included in the extraction.

5.1.5 One Cycle vs. 500 Cycles

In the thermomechanical axisymmetric and 3D model of one cycle a very warm hot band develops around the brake disc. When the temperatures from these simulations were compared with measurements, it was clear that the calculated temperature was too high. The weakness of the one cycle models is that they do not take into account any history effects, and that the TEIs that may form are not necessarily representative of all cycles. If the hot bands form, and the where they form, may vary from cycle to cycle.

The main strength of the thermomechanical axisymmetric model is its ability to use Fortran subroutines to update the mesh according to wear. This makes it possible to simulate multiple cycles with extreme wear and better assess how the results change over time. In simulating multiple cycles, it was found that this initial hot band quickly wears away, lowering the maximum temperature on the surface. In the case of a temperature dependent $k_{w,p}$ the temperature evolution on the surface can be seen to repeat for every brake application, and the temperature in the disc becomes more accurate when compared to the measurements. With a constant value of $k_{w,p}$ the temperature on the surface increases again for later cycles, indicating greater hot-banding.

The one-cycle models, will due to the hot-banding be unlikely to give a generally correct accurate wear prediction, due to the destruction and reformation of hot spots. This problem is further amplified by uncertainty with the measured values of $k_{w,p}(T)$. However, with careful tuning, temperatures could be captured for single experimentally studied events.

With the multiple cycles model it was not possible to get an accurate total wear prediction with the measured values of $k_{w,p}$. A partial reason for this could be that the hot-banding was less pronounced after the first cycles. However, it is worth noting that since the wear depth from cycle 1, despite the hot band, is below what would have been required to match the total wear, if it was the change for all 500 cycles, see Figure 4.34. Therefore, the lack of further hot-banding can only be a partial explanation.

In the measurements, there is also a large variance in the final measured temperatures in the disc and pads, indicating that hot spots form that vary in position. This is not captured in this multiple cycles model for the standard parameter settings, in which the calculated temperature at the nodes vary due to the wear, but they do not oscillate in the same manner as measured in the tests. The same manner of hot-banding is not captured in as in the tests, but only an aggregate.

It seems that the here modelled strong temperature dependence of $k_{w,p}$ is not capturing the entire spread of the surface temperatures. This will effectively prevent any possibility of accurately modelling the wear of the pads. It is therefore essential for future modelling that this is further investigated.

It is possible that the penalty contact formulation used in the model is too generous in the amount of penetration it allows, and that the contact gets too ”spread out”. It may also be so that the thermal expansion coefficient and/or the Young's modulus of the pad friction material is too low, which would cause a larger contact zone, and less hot-spotting. That increasing the thermal expansion coefficient α introduced variance in the final temperatures in the disc measurement point, and increased the mean wear depth, see Appendix C.2, indicates that this is a plausible explanation. That a constant value of Young's modulus was used for the pad and not temperature dependent values may also contribute. It should be reiterated that simply modifying parameters such as the thermal expansion coefficient and Young's modulus until the results match the measurements may simply be introducing qualitative errors.

Another possible issue is numerical errors made by the *UMESHMOTION* subroutine and the adaptive meshing. For example, late on in the study it was realised that the way that the wear update is disabled in the reset step, see Appendix B.3.1, might enable normal adaptive meshing to occur instead. Then the nodes at the contacts might be moved slightly during the reset step, and whilst the movement in of it self is likely to be slight such errors might propagate. Further investigation on the effect this has on the results is required, and initializing the mesh movement to zero before the wear update might be preferable.

The fact that an axisymmetric model can only capture the formation of a hot band, may be affecting the results of the simulation. Any angular variation of the temperature will be smeared out across the surfaces of the pad and disc. This means that the temperature at any given radii in the axisymmetric models will be the aggregate of the temperatures at that radii.

That the axisymmetric models are incapable of capturing other TEIs is a weakness when simulating load cases where those are expected. For example if macroscopic hot-spotting occurs on the disc the models would not be able to capture them, and thus not capture the effect they have on the pad.

Lastly, whilst it was possible to use modeFRONTIER to determine a constant value of $k_{w,p}$, for which the total wear depth becomes more correct when compared to the measurement, this method has some downsides. Most acutely, the constant value of $k_{w,p}$ will be dependent on the temperature and load history, and thus it will not be applicable

on another case. To determine the constant value one must also know the total wear, or the accumulated wear for a representative portion. If we already know the wear for the load case there is also very little point to simulate it using a constant $k_{w,p}$, since we already know what the total wear will be, the values of $\mathrm{d}h/\mathrm{d}t(t,r)$ will not be accurate, and the temperature will also be affected (primarily with greater maximum surface temperatures).

5.1.6 Other Observations

From the results with a cast iron backing plate, see Sections 4.1.1.3 and 4.1.2.2, it is clear that modelling choices regarding the backing plate had little effect on the overall results for the models in this thesis. However, this may not be true for certain load cases. For longer brake cycles, where the heat will spread throughout the pad lining and into the backing plate, the thermal material properties of a cast iron backing plate may affect the results more. In addition, if the brake force were to be applied with a point force or with contact from a brake piston instead of an evenly distributed pressure, the pressure distribution on the pad could be influenced by the material properties of the backing plate.

The assumption that the end of the backing plate is kept at a constant temperature of 50 °C had little influence on the results for the here-in studied rather short brake application when compared to an insulated end of the backing plate. However, when the pad lining wears down for multiple cycles we would expect more heat to reach the backing plate, which means that the difference in results will be greater. Further, during longer brake cycles, where more of the trapped heat in the pad will diffuse into the backing plate, the boundary conditions of the backing plate will have a greater influence on the outcome of the result. Of course, the truth lies somewhere in-between, with the backing plate becoming warmer, but with some heat being transferred from it to other parts of the brake assembly.

5.2 Parameter Tuning

The parameter optimisation done in modeFRONTIER had mixed results. Overall, the results presented for the thermal material properties, presented in Appendix D.1, show that the thermal conductivity is underestimated when compared to the measured value of the conductivity. At 99 °C the measured (normalised) conductivity was $k_t/k_t^* \approx 1.28$. The mean normalised values obtained were 0.802 and 0.793 for the two runs with constant force, and 0.953 for the linear variation of force. The modeFRONTIER values are however the adjusted values, i.e. the true conductivity values should be 4.5 times greater, the value that would have been correct would have been $1.28/4.5 \approx 0.284$. Hence both are overestimations of the conductivity, and lowering the total heat flux by giving a linear variation of the force gave an even greater overestimation.

From looking at these results, it is easy to assume that an increase in the heat flux over time would instead generate a correct result. However, it is more reasonable to assume that in order to determine one parameter, the rest of the parameters must be known. These two different conclusions form the cornerstones of the dilemma with the parameter tuning, qualitative versus quantitive errors.

5.2.1 Qualitative Versus Quantitive Errors

In the modeFRONTIER projects in this report, the premise has been consistent. We set up our FE-model, we allow certain input parameters to be varied, and then we compare with data to see what the error was with regard to the temperature. The output mean square error is what would be called a quantitative error; we can assign a value of it with zero being no error and a high value meaning a high error. The conclusion one would draw is that if the quantitive error is low the model is more accurate.

In a sense it is correct that a low quantitative error means a more accurate model, at least with regards to what we can measure. If the comparison between our final models and the measurements, see Section 4.1.4, had a low quantitative error, we would probably conclude that the model was accurate. However, in the modeFRONTIER projects, a different type of study has been performed. We have several inputs causing a multitude of possible "solutions", all of which are equally accurate with regards to the quantitative error. Most importantly the FE-model has, implicitly and explicitly, assumptions built in to them. These assumptions, depending on their validity, can then lead to qualitative errors, i.e. errors in what is simulated. A model with high qualitative errors may, or may not, have high quantitative errors. Sometimes faulty modelling choices add up, and sometimes one qualitative error may reduce the quantitative effect of another qualitative error.

It is reasonable to assume that the FE-models used in the modeFRONTIER projects are imperfect. Assumptions have been made that we know are not entirely accurate, for example the constant force assumption or that a thermal model is used when the problem is thermomechanical. What happens is then that when we are trying to get accurate values of the thermal conductivity of the pad $k_{t,p}$, i.e. minimising a certain qualitative error, it is instead adapting to a quantitive error, which may be lower with a greater qualitative error.

Consider the specific heat capacity for the pad $c_{p,p}$. The values used in the modeFRONTIER projects for $c_{p,p}$ was far greater than the values later obtained from suppliers, and differed by as much as 60 %, see Appendix B.1.4. Using these values then represents a qualitative error, something that is compensated for by changing k_t. It stands to reason that if the lower c_p values had been used, lower, more accurate thermal conductivity values would have been obtained.

Another issue is that in the thermal material property studies the same value of thermal conductivity of the pad $k_{t,p}$ was applied as a material property as was used for calculating the gap conductance. Since the former should have been an adjusted value and the latter calculated with the true 3D-value, there will be a discrepancy in the model. In short, for a prescribed value of the conductivity, the gap conductance should have been greater in these studies.

It should be noted that for a thermal model the decrease in clamp force that is tested is only semi-accurate. Unless we change the shape of the contact pressure distribution, for example with non-constant $\zeta(t)$, a constant clamp force and a constant brake torque (and thus heat flux) is the same thing. This reduction is thus in fact another qualitative error with a thermal model (but would not be one with a thermomechanical model).

Another form of qualitative error comes in the form of prior, assumed, knowledge. The range values of the thermal conductivity was set in part from what ranges gave accurate results in earlier iterations of the modeFRONTIER studies, but also from inferable knowledge of what the thermal conductivity of an OC-pad is approximately, see [10] and [7]. This was done before it was realised that $k_{t,p}$ should have been reduced by $\phi_0/(2\pi)$, thus those ranges may have been wrong and hindering finding the correct $k_{t,p}$-value.

It was observed that in the second wear project, the scaling up of $k_{w,p}$, was motivated by the possibility that a pressure value was slightly off, see Appendix B.5.2. The result given in Appendix D.2.2, with a scaling factor of 3.85, is too large to be caused by a calculation error, so it is likely only introducing a new qualitative error.

The solution to this type of problem is as stated earlier that to determine one parameter correctly, we must know the rest. The solution is more knowledge, either in terms of knowledge of other parameters or in terms of more, and different types, of data.

If we knew other inputs, such as c_p, of the model with certainty, before the start of the modeFRONTIER projects, we would likely have gotten less variance in the solutions of k_t. It would however likely still been several combinations of *k0* and *k1* that would have given the same MSE values.

More data in this case does not refer to more cycles included in the fitting. Instead more data could have been to have additional measurement probes in the pad, which ideally would have been placed at different depths, thus giving a good indication of the thermal diffusivity of the pad material.

An idea which could have been tested with modeFRONTIER would have been to use an additional node at a lesser depth in the pad, and compare it to later cycles in the model where the measurement probe would have been at that depth. This would have artificially given us an additional measurement probe. This was not tested in part due to time constraints, but also because it would not have been entirely accurate since, whilst it may have been at the correct depth, the total thickness of the pad would have been incorrect compared to those later cycles.

Larger amounts of data could also mean a more varied data set. Consider the modeFRONTIER projects in which the objective was to determine $k_{w,p}$ as a function of temperature. In this thesis work only one value of the wear depth was available to fit against, with one load case. Considering that the accumulated wear is dependent on the entire history of temperature and contact pressure on the surface this will disguise a lot of information, which makes it difficult to predict the wear behaviour. Now if instead different load cases, some which reach high temperatures and some which do not, were tested, they all could have been simulated and compared to, which likely would have given a better indication of the temperature dependence.

5.2.2 The Positives

It is worth noting that not everything went wrong with the modeFRONTIER projects, even though it may seem like it from what is stated above.

In the wear projects, especially the constant $k_{w,p}$, it was shown that if the number of inputs were more limited we can get more elaborated answers on what inputs should be used to get the best quantitative prediction of the outputs.

Even the studies on thermal material properties had some positives. The conductivity was still determined to the correct order of magnitude, it was not predicted that the pad was a near-perfect insulator nor that it was a good conductor. A way of working was created to fit the parameters so that the quantitative error can be minimised; the next step is to develop the work in such a way so that the qualitative errors are minimised as well.

Although not all of the attempts were satisfactory, the relevant goal of this thesis, see Section 1.4, "To explore methods of fitting parameters of FE-models (thermal conductivity, specific heat, clamp force, etc.) such that errors of models are minimised", was fulfilled.

5.3 Discussion of Methodology

In his 1976 paper, George E. P. Box used the phrase "all models are wrong" to describe the limitations of models and how no model is ever completely accurate [39, p. 792]. However, with this he meant that despite failing to perfectly capture empirical phenomena, models still serve as useful approximations and can provide valuable insights if applied cautiously [39]. George E. P. Box and Norman R. Draper extend on the famous phrase in the book "The Use of Approximating Functions,":

> "Essentially, all models are wrong, but some are useful."[40, p. 424].

Due to the time frame and the resources available, simplifications and assumptions had to be made in the development of the models to solely focus on capturing the phenomena relevant to the study. This may have caused the outcome of the simulated results to not perfectly include all the natural phenomena that occurs during a disc brake cycle.

Firstly, to minimise the computational cost of the models used in this project, and to enable the use of certain element types, simplifications to the geometry had to be made. These simplifications may have added or removed material in a model which may have slightly affected the outcome of the results. Most of the models used in this project also only consisted of one pad, one backplate and half a disc. The behaviour of the disc brake was then assumed to be symmetrical on both sides of the disc. Although this is a common practice when simulating disc brakes it fails to capture antisymmetric behaviour.

The inboard and outboard pad are anti-symmetrical to each other and could slightly affect the contact pressure distribution during thermal expansion. Asymmetry in the ring-spring geometry and mounting location may also give rise to asymmetric behaviour between the two disc sides, affecting contact pressure, heat generation, thermal expansion and wear. This can not be captured with a model that presumes symmetry. Further, the symmetric assumption does not allow the symmetry-plane of the disc to translate in the axial direction, which in turn restricts elastic buckling in the disc which may give rise to

macroscopic hot-spotting [30].

The penalty formulation was employed in the contact pairs between the pad and disc. The penalty formulation is a common contact formulation as contact is easily established, helping with solution convergence. However, depending on the parameters used, the influence of surface perturbations that may contribute to the early development of gradients on hot bands may be reduced or removed. In this project, the default Abaqus settings were used, with the extension zone set to 0.2 and the surface smoothening set to 0.1. Due to the time frame of this project, it was not possible to do a parameter study on these contact parameters.

All thermomechanical models developed in this project employed a constant coefficient of friction (COF) of $\mu = 0.3$, which was motivated mainly by the project time frame, as the development of a dynamic description of the COF would require extensive testing and modelling. As discussed in 2.6, the COF may vary depending on several factors, such as temperature, contact pressure, wear history and sliding velocity. As temperature and contact pressure increase, the COF tends to decrease [19, 28]. However, severe frictional heating may also lead to increased wear and local melting, thereby altering the contact interface and further modifying the COF. The birth and death of contact patches due to wear particles have also been shown to play a direct role in determining COF [28]. Owing to the many dynamic factors involved in the complex tribological mechanisms governing the COF, it is difficult to assess how the use of a constant COF may have influenced the results obtained in this project.

In the rig-tests, the brake torque is kept constant by varying the force that is applied to the pads. However, in this project, all the thermomechanical models developed simulated brake force by applying a constant and evenly distributed pressure to the backing plate. This may have led to the models having a higher or lower contact pressure at the interfaces of the pad and disc depending on the location of the hot band, which in turn may have influenced temperature development and wear.

Lastly, it should be noted that $\phi_0 = 80°$ that was used for the axisymmetric models was based on a rough measurement of the geometry. The pad is not shaped as a perfect circular arc which may lead to an overestimation or underestimation of the material properties of the pad, as previously mentioned in Section 5.1.4. The assumed pad angle of $\phi_0 = 80°$ may therefore have overestimated the "mass" of the pad closest to the outer radius of the disc. Future axisymmetric modelling should therefore consider the mass conservation of the pad in the determination of ϕ_0 or divide the pad into different radial sections with different densities.

5.4 Future Work

This section covers possible and recommended follow-up studies based on this MSc thesis work.

5.4.1 Representative Driving Cycles

The disc crack test was considered to be a good starting point in order to compare our modelling capabilities since the test cause extreme wear and temperature development in the brake. This gave a good indication of the viability of our FE-modelling. However, it is not a realistic braking cycle and is purely used for testing.

The next step in using FE-modelling of temperature and wear in disc brakes is to model a representative driving cycle, which mimics real driving conditions. This may give a better understanding of what type of driving behaviours do, or do not, cause large amounts of wear.

The focus of any such modelling would naturally be on the Euro 7 test cycle, with the modelling used both as complement and comparison with rig-testing, but also to be used to predict how any design changes would change the amount of wear of brake disc and pad. It could thus be an important tool to ensure compliance with Euro 7 emission limits.

However, the modelling work does not need to cycle at Euro 7 testing. It could also be used to test other driving cycles, both extreme and standard ones, to get a fuller picture of the wear of the disc brakes.

Hot-spotting such as gradients on hot bands and macroscopic hot spots are considered some of the more damaging thermal gradients and usually develop under prolonged braking, as discussed in Section 2.8. By simulating and testing longer brake cycles, the here presented models could be extended to consider these types of thermoelastic effects and give more insight into the effects they have on the wear of pad and disc.

5.4.2 Plastic and Metallurgical Effects

For this project, all materials were assumed to behave isotropically, and their response was assumed to be thermoelastic. As discussed in 2.8, the transition from gradients on hot bands to macroscopic hot spots is usually explained by elastic or plastic buckling of the brake disc. Experimental studies have found that the distribution of macroscopic hot spots between the two sides of the disc has shown signs of a circumferentially ”buckled” deformation pattern caused by plastic flow and metallurgical transformations at high temperatures [30]. In order to model macroscopic hot spots it is therefore necessary to account for plastic flow and metallurgic transformations.

5.4.3 Full 3D-Modelling

In this work, computational resources were a limiting factor on the number of DOFs that could be simulated. Due to this, only a half-model of the disc brake could be simulated under the assumption of symmetrical behaviour between the two sides of the disc. This assumption will not allow for capturing antisymmetric behaviour between the two sides of the disc that develops from hub inertia, buckling and asymmetry in contact areas. To more accurately capture these effects, a full model, or possibly a pie-slice model, would need to be modelled.

5.4.4 Contact Formulations

In addition to a parameter study on the contact parameters in the penalty method, further exploration of different contact formulations is encouraged. Grzes and Kuciej [10] used the Arbitrary Lagrangian Method (ALM) as the contact formulation between disc and pad, which is more precise but may also require additional iterations to converge. With user subroutines it is also possible to employ other contact formulations than the default ones in Abaqus. The transient dynamic contact methodology used by Dufrenoy [25] could then be applied to capture thermoelastic instabilities more accurately. However, it is important to mention that running user subroutines will substantially increase the computational cost of a model, especially if friction and contact are user-defined. Great effort would therefore be required in the optimisation of these subroutines with iteration reduction, memory allocation, vectorisation and more.

5.4.5 Measurements of Wear

The methodologies for determining wear scaling factors k_w in this thesis project has, as established, its disadvantages. The calculation of the temperature dependent values, see Appendix B.1.1, is wrought with assumptions and idealisations. An average contact pressure is assumed, an effective radius must be assumed, and most importantly, it is implicitly assumed that the temperature of the surface does not change much during the brake applications of those tests.

These imperfections, together with the results of the wear simulations studies, makes improving the testing of k_w a priority moving forward.

The ideal test procedure would be one where the temperature of the material is kept exactly constant, with known contact pressure and sliding velocity. This is not really possible, but what can be done is pin-on-disc tests, see Section 2.7, in which the temperature can be measured and the rest is known. Alternatively, the measurements of wear can still be done with full-scale testing on disc and pads, with some alterations. A suggestion is to take a cycle, such as for example the crack test, and divide into different time-portions. For example, using the same load and angular velocity, one repeats the tests for four different sets of pads, with the difference for each set being the duration of each cycle. For one set each cycle could last for 10 s, for another for 20 s, for another for 30 s, and lastly for 40 s. Having different durations of the cycles would allow us to gain more knowledge of how much wear occurs for different temperatures, as the shorter cycles would not reach as high temperatures as the longer ones. From the temperature and wear results of such full-scale tests one could either do some hand-calculations, as done in Appendix B.1.1, or one could do a more expansive fitting of the wear scaling factors than what was done in Appendix B.5.2.

Another idea which was suggested to us was to correlate the wear with particle measurements over time, from for example the Euro 7 test cycle. Although since both disc and pads are subject to wear, the fraction of particles coming from which source would vary with time (and temperature). To address this one would have to do a chemical analysis of the particles emitted to determine their sources.

5.4.6 Adaptive Meshing with Wear and Multiple Cycles in 3D

Arbitrary Lagrangian Eularian (ALE) adaptive meshing with wear modes was only considered for the axisymmetric model. Both user subroutines and ALE adaptive meshing increase the computational cost of a model and during the development of the user subroutine with adaptive meshing it was found that the wall clock simulation time for the 3D-model greatly increased. Due to the time frame and the resources provided for this work, this method was ultimately abandoned and wear modelling with the built-in CWEAR functionality in Abaqus was used instead. This did not prove to be a big limitation since only one cycle was simulated.

The built-in CWEAR functionality in Abaqus is limited to the contact nodes, and will cause elements to distort and invert when wear distances becomes significant relative to element dimensions. ALE adaptive meshing would therefore need to be employed if multiple cycles are to be studied using the 3D-model. ALE adaptive meshing can be combined with wear calculations using *UMESHMOTION* as was done in the axisymmetric model in this project. However, if Abaqus/Explicit were to be used for the analysis, it would enable ALE adaptive meshing using the built-in CWEAR functionality in Abaqus, effectively eliminating the need for a user defined subroutine, and thus allowing for quicker analyses.

5.4.7 Increase Model Accuracy

There are several manners in which the accuracy of the models could be improved upon.

Introducing a dynamic description of the coefficient of friction (COF) could substantially improve the accuracy of the models compared with the constant COF used in this project. This may be achieved, in part, through the development of a mathematical formulation for the instantaneous COF as a function of temperature, contact pressure, and sliding velocity. It may also be achieved through a state variable type description that accounts for wear history and the current state of the interface.

Another matter is whether or not to simulate all phenomena occurring in the test or not. In the multiple cycles model that has been used in this project we start right on cycle 1, and between each cycle the temperature is reset to our initial temperature of 50 °C across disc and pad. This modelling choice does however disregard both the bedding-in process of new pads, which is done before the tests, as well as the cooling process in between cycles. Simulating both of these additional processes would however increase the computational time substantially. With regards to the cooling process it would allow for a more accurate initial temperature field in the components at initiation of braking, but it would also require efforts on determining the heat transfer coefficients of convection and emissivity values, which are important for the cooling.

One topic of debate is the gap conductance in the contact between the disc and the wheel hub. The values used in the model with the hub have a great uncertainty with them. Ideally, this would be addressed by fitting the value of the gap conductance so that the temperatures in the wheel hub were accurate. However, for this thesis work and these tests no temperature values were available which made such a fit impossible. The accuracy of that gap conductance will however, likely only have a great effect on simulations

of longer brake applications than the ones studied in this work.

Lastly, if simulations are to be done with axisymmetric models on load cases where there is macroscopic hot-spotting, or large variations in temperature in the angular direction, one would need to re-assess the wear behaviour. As alluded to in Section 5.1.5 any angular variation of the temperature would be smeared out across the surface, which would affect the wear calculation.

5.4.8 Parameter Fitting

As noted in Section 5.2.1 there is a lot of work to be done in the fitting of the parameters in such a way so that both qualitative and quantitative errors are reduced. This may be done, as noted previously, by raising the fidelity of the model, by diversifying the types of data available, and by gaining more a-priori knowledge of the model parameters, either in form of values or as ranges.

6
Conclusion

The purpose of this project was to study the wear and temperature development in disc brakes through the development of FE-models, validation using rig-test data and material parameter calibration. This was accomplished by establishing thermal and thermomechanical axisymmetric and 3D-models, together with parameter fitting using modeFRONTIER.

The study showed that thermal axisymmetric models are useful for fast calculations and allow for parameter fitting, but they fail to capture banded contact and contact pressure redistribution. Thermomechanical models were able to represent these effects and showed strong local temperature peaks and non-uniform wear, but they also tended to predict higher temperatures than rig-test data. The thermomechanical 3D-model provided a more detailed representation of the pad temperature field and showed the importance of circumferential variations, but its computational cost limited mesh refinement and studies of longer braking durations and multiple brake cycles.

For the multiple-cycle simulations with a temperature dependent wear scaling factor, the effects of the initial hot band that formed during the first cycle were reduced by wear effects over time, after which the disc temperature stabilised. This produced a temperature development that was closer to the rig-test data than with a constant wear scaling factor, where the hot band reformed over time. However, in the case of wear, the simulations with a constant wear scaling factor were closer to the rig-test data than with a temperature dependent wear scaling factor, although total wear was still underestimated. This indicates that accurate wear modelling requires both reliable temperature prediction and better experimental data for wear coefficients.

The parameter calibration work showed that modeFRONTIER can be used to fit thermal material properties and wear parameters, but the results also demonstrated that low numerical error does not necessarily imply physically correct parameters. In particular, the fitted thermal conductivity values deviated from the supplier data, implying that model simplifications can be compensated for by parameter adjustment. Therefore, the calibration results should be interpreted with caution.

Overall, the project demonstrates that FE-modelling is a valuable tool for studying wear and temperature development in disc brakes but that model accuracy, contact formulation, material parameters and loading assumptions all have a major impact on the results. Future work should focus on increasing model accuracy, further parameter calibration, improving the representation of contact conditions, using more representative driving cycles and extending the models to capture full 3D behaviour more accurately.

Bibliography

[1] Z. C. Samaras et al. “A European regulatory perspective towards a Euro 7 proposal”. In: *SAE International Journal of Advances and Current Practices in Mobility* 5.2022-37-0032 (2022), pp. 998–1011.

[2] J. Dornoff and F. Rodríguez. “Euro 7: The new emission standard for light-and heavy-duty vehicles in the European Union”. In: *International Council on Clean Transportation* (2024).

[3] M. L. Feo et al. “Laboratory and on-road testing for brake wear particle emissions: a review”. In: *Environmental Science and Pollution Research* 30.45 (2023), pp. 100282–100300.

[4] M. Mägi, K. Melkersson, and M. Evertsson. *Maskinelement*. Studentlitteratur, 2017.

[5] R. Limpert. *Brake design and safety*. SAE international, 2011.

[6] A. Alami Alamdari and B. Fozzati. “Virtual sensor-AI model training using VOLVO Brake temperatures”. In: (2025).

[7] G. Le Gigan. *On improvement of cast iron brake discs for heavy vehicles: Laboratory experiments, material modelling and fatigue life assessment*. Chalmers Tekniska Hogskola (Sweden), 2015.

[8] T. Okamura and H. Yumoto. “Fundamental study on thermal behavior of brake discs”. In: *SAE Transactions* (2006), pp. 1731–1746.

[9] F. Talati and S. Jalalifar. “Analysis of heat conduction in a disk brake system”. In: *Heat and mass transfer* 45.8 (2009), pp. 1047–1059.

[10] P. Grzes and M. Kuciej. “FE analysis of the brake pad and brake disc wear with thermal-structure interaction”. In: *Wear* (2025), p. 206331.

[11] J. Reddy. *An introduction to continuum mechanics*. Cambridge University Press, 2008.

[12] H. A. Abdel-Aal. “Flash Temperature Theory”. In: *Encyclopedia of Tribology*. Ed. by Q. J. Wang and Y.-W. Chung. Boston, MA: Springer US, 2013, pp. 1182–1194. ISBN: 978-0-387-92897-5. DOI: 10.1007/978-0-387-92897-5_1312. URL: https://doi.org/10.1007/978-0-387-92897-5_1312.

[13] A. Loizou, H. Sheng Qi, and A. J. Day. “A fundamental study on the heat partition ratio of vehicle disk brakes”. In: *Journal of heat transfer* 135.12 (2013), p. 121302.

[14] M. Eriksson, F. Bergman, and S. Jacobson. “On the nature of tribological contact in automotive brakes”. In: *Wear* 252.1 (2002), pp. 26–36. ISSN: 0043-1648. DOI: https://doi.org/10.1016/S0043-1648(01)00849-3. URL: https://www.sciencedirect.com/science/article/pii/S0043164801008493.

[15] J. R. Barber. “Thermoelastic instabilities in the sliding of conforming solids”. In: *Proceedings of the Royal Society of London. A. Mathematical and Physical Sciences* 312.1510 (Sept. 1969), pp. 381–394. ISSN: 0080-4630. DOI: 10.1098/rspa.1969.0165. eprint: https://royalsocietypublishing.org/rspa/article-pdf/312/

1510/381/58321/rspa.1969.0165.pdf. URL: https://doi.org/10.1098/rspa.1969.0165.

[16] M. Godet. "The third-body approach: a mechanical view of wear". In: *Wear* 100.1-3 (1984), pp. 437–452.

[17] C. V. Madhusudana. *Thermal contact conductance*. Vol. 79. Springer, 1996.

[18] T. Vernersson and R. Lundén. "Wear of brake blocks for in-service conditions—Influence of the level of modelling". In: *Wear* 314.1-2 (2014), pp. 125–131.

[19] J. Lemaitre. *Handbook of materials behavior models, three-volume set: nonlinear models and properties*. Academic Press, 2001.

[20] P. Wriggers. *Computational contact mechanics*. 2nd. Springer, 2006.

[21] D. V. Schroeder. *An Introduction to Thermal Physics*. Oxford University Press, Jan. 2021. ISBN: 9780192895547. DOI: 10.1093/oso/9780192895547.001.0001. URL: https://doi.org/10.1093/oso/9780192895547.001.0001.

[22] N. Ottosen and M. Ristinmaa. *The Mechanics of Constitutive Modeling*. Elsevier, July 2005. ISBN: 978-0-08-044606-6. DOI: 10.1016/B978-008044606-6/50000-X.

[23] X.-G. Lu, M. Selleby, and B. Sundman. "Theoretical modeling of molar volume and thermal expansion". In: *Acta materialia* 53.8 (2005), pp. 2259–2272.

[24] Dassault Systèmes Simulia Corporation. *Abaqus version 2024 documentation*. Accessed 2026-05-06. 2024. URL: https://docs.software.vt.edu/abaqusv2024/English/?show=SIMULIA_Established_FrontmatterMap/sim-r-DSDocAbaqus.htm.

[25] P. Dufrenoy. "Two-/three-dimensional hybrid model of the thermomechanical behaviour of disc brakes". In: *Proceedings of the Institution of Mechanical Engineers, Part F: Journal of Rail and Rapid Transit* 218.1 (2004), pp. 17–30.

[26] L. Jiang and R. J. Rogers. "Combined Lagrangian Multiplier and Penalty Function Finite Element Technique for Elastic Impact Analysis". In: *Computers & Structures* 30.6 (1988), pp. 1219–1229. DOI: 10.1016/0045-7949(88)90187-3. URL: https://scienceon.kisti.re.kr/srch/selectPORSrchArticle.do?cn=NART16482657.

[27] J. F. Archard. "Elastic deformation and the laws of friction". In: *Proceedings of the Royal Society of London. A. Mathematical and Physical Sciences* 243.1233 (Dec. 1957), pp. 190–205. ISSN: 0080-4630. DOI: 10.1098/rspa.1957.0214. eprint: https://royalsocietypublishing.org/rspa/article-pdf/243/1233/190/50608/rspa.1957.0214.pdf. URL: https://doi.org/10.1098/rspa.1957.0214.

[28] G. Ostermeyer. "On the dynamics of the friction coefficient". In: *Wear* 254.9 (2003). Papers presented at the 280th We-Hereaus Seminar Integrating Friction and Wear Research, pp. 852–858. ISSN: 0043-1648. DOI: https://doi.org/10.1016/S0043-1648(03)00235-7. URL: https://www.sciencedirect.com/science/article/pii/S0043164803002357.

[29] G. Ostermeyer. "Friction and wear of brake systems". In: *Forschung im Ingenieurwesen* 66.6 (2001), pp. 267–272. DOI: 10.1007/s100100100063. URL: https://link.springer.com/article/10.1007/s100100100063.

[30] S. Panier, P. Dufrénoy, and D. Weichert. "An experimental investigation of hot spots in railway disc brakes". In: *Wear* 256.7 (2004), pp. 764–773. ISSN: 0043-1648. DOI: https://doi.org/10.1016/S0043-1648(03)00459-9. URL: https://www.sciencedirect.com/science/article/pii/S0043164803004599.

[31] K. Lee and J. Barber. "An experimental investigation of frictionally-excited thermoelastic instability in automotive disk brakes under a drag brake application". In: (1994).

[32] N. Audebert, J. R. Barber, and P. Zagrodzki. “Buckling of Automatic Transmission Clutch Plates due to Thermoelastic/Plastic Residual Stresses”. In: *Journal of Thermal Stresses* 21 (Apr. 1998), pp. 309–326. DOI: 10.1080/01495739808956149.

[33] X. Fan and H. Lippmann. “Elastic-Plastic Buckling of Plates under Residual Stress”. In: *Advances in Engineering Plasticity and its Applications (aepa 1996)*. Ed. by T. Abe and T. Tsuta. Oxford: Pergamon, 1996, pp. 95–100. ISBN: 978-0-08-042824-6. DOI: https://doi.org/10.1016/B978-0-08-042824-6.50018-0. URL: https://www.sciencedirect.com/science/article/pii/B9780080428246500180.

[34] H. Yao. *Arbitrary Lagrangian–Eulerian (ALE) Formulation: Theory, Numerical Methods, and Applications*. Tech. rep. TR-2026-01. Chalmers University of Technology, Department of Mechanical Engineering, 2026. DOI: 10.63959/m2.techreport/2026.1.

[35] Dassault Systèmes Simulia Corporation. *Thermal-stress analysis of a disc brake*. Accessed 2026-06-01. 2024. URL: https://docs.software.vt.edu/abaqusv2025/English/SIMACAEEXARefMap/simaexa-c-discbrake.htm.

[36] Dassault Systèmes Simulia Corporation. *Contact Wear*. Accessed 2026-06-01. 2024. URL: https://docs.software.vt.edu/abaqusv2025/English/SIMACAEITNRefMap/simaitn-c-contactwear.htm.

[37] M. Arjmandi et al. “Finite element modelling of sliding wear in three-dimensional woven textiles”. In: *Tribology International* 115 (2017), pp. 452–460. ISSN: 0301-679X. DOI: https://doi.org/10.1016/j.triboint.2017.06.015. URL: https://www.sciencedirect.com/science/article/pii/S0301679X17303031.

[38] ESTECO Engineering. *modeFRONTIER*. Accessed 2026-06-01. 2026. URL: https://engineering.esteco.com/modefrontier/.

[39] G. E. P. Box. “Science and Statistics”. In: *Journal of the American Statistical Association* 71 (1976), pp. 791–799. URL: https://api.semanticscholar.org/CorpusID:3906689.

[40] G. E. P. Box and N. R. Draper. *Empirical model-building and response surfaces*. New York: Wiley, 1987.

[41] Z. Olesiak, Y. Pyryev, and A. Yevtushenko. “Determination of temperature and wear during braking”. In: *Wear* 210.1-2 (1997), pp. 120–126.

[42] T. Vernersson et al. “Wear of railway brake block materials at elevated temperatures: pin-on-disc experiments”. In: *Eurobrake 2012*. 2012.

[43] C. Fang. *An introduction to fluid mechanics*. Vol. 935. Springer, 2019.

[44] A. Belhocine and O. I. Abdullah. “Thermomechanical model for the analysis of disc brake using the finite element method in frictional contact”. In: *Multiscale Science and Engineering* 2.1 (2020), pp. 27–41.

[45] P. Grzes. “Finite element solution of the three-dimensional system of equations of heat dynamics of friction and wear during single braking”. In: *Advances in Mechanical Engineering* 10.11 (2018), p. 1687814018808643.

[46] M. Eriksson and S. Jacobson. “Tribological surfaces of organic brake pads”. In: *Tribology international* 33.12 (2000), pp. 817–827.

[47] D. Bettge and J. Starcevic. “Topographic properties of the contact zones of wear surfaces in disc brakes”. In: *Wear* 254.3-4 (2003), pp. 195–202.

[48] N. Suresh. Private communication. Chalmers University of Technology, Mar. 24, 2026.

[49] Dassault Systèmes Simulia Corporation. *UMESHMOTION*. Accessed 2026-06-11. 2024. URL: https://docs.software.vt.edu/abaqusv2024/English/?show=SIMACAESUBRefMap/simasub-c-umeshmotion.htm.

[50] E. Haghighat et al. "A deep learning framework for solution and discovery in solid mechanics". In: *arXiv preprint arXiv:2003.02751* (2020).

[51] S. Cuomo et al. "Scientific machine learning through physics–informed neural networks: Where we are and what's next". In: *Journal of Scientific Computing* 92.3 (2022), p. 88.

[52] C. Forssén. *TIF385 Bayesian inference and machine learning*. This work is licensed under the Creative Commons BY-NC license. Online; accessed February 3, 2026. 2022. URL: https://cforssen.gitlab.io/tif385-book/content/MachineLearning/ModelValidation.html.

r

A

Additional Theory

In this appendix additional theory to supplement that in Section 2 is included, which is informative, but not strictly necessary to understand this study.

A.1 Material Time Derivative

The material time derivative of a variable ϕ is defined as [11]

$$\frac{D\phi}{Dt} = \left(\frac{\partial\phi}{\partial t}\right)_{\boldsymbol{X}=\text{constant}} = \left(\frac{\partial\phi}{\partial t}\right)_{\boldsymbol{x}=\text{constant}} + \left(\frac{\partial x_i}{\partial t}\right)_{\boldsymbol{x}=\text{constant}} \frac{\partial\phi}{\partial x_i}, \tag{A.1}$$

where $\boldsymbol{X}$ is the Lagrangian description and $\boldsymbol{x}$ is the Eulerian, the operator is

$$\frac{D}{Dt} = \left(\frac{\partial\phi}{\partial t}\right)_{\boldsymbol{x}=\text{constant}} + \left(\frac{\partial x_i}{\partial t}\right)_{\boldsymbol{x}=\text{constant}} \frac{\partial\phi}{\partial x_i} + \boldsymbol{v}\cdot\nabla. \tag{A.2}$$

We observe that if the disc is not subjected to large transient deformations, the velocity term will be dominated by the rigid body motion (the rotation of the disc) so in the cylindrical coordinate system

$$\frac{D\phi}{Dt} = \left(\frac{\partial\phi}{\partial t}\right)_{\boldsymbol{x}=\text{constant}} + \omega\frac{\partial\phi}{\partial\theta}, \tag{A.3}$$

in the disc. For the static pads however

$$\frac{D\phi}{Dt} = \left(\frac{\partial\phi}{\partial t}\right)_{\boldsymbol{x}=\text{constant}}. \tag{A.4}$$

A.2 Proof of Relationship Between Volumetric and Linear Thermal Expansion Coefficients

That $\beta_v \approx 3\alpha$ can be proven by considering a the thermal expansion of a small volume $\mathrm{d}V = \mathrm{d}x\mathrm{d}y\mathrm{d}z$ as

$$\begin{aligned}
\beta_v\left(T-T_0\right)\mathrm{d}V &= \left(1+\alpha\left(T-T_0\right)\right)^3\mathrm{d}x\mathrm{d}y\mathrm{d}z - \mathrm{d}x\mathrm{d}y\mathrm{d}z \\
&= \left(3\alpha\left(T-T_0\right) + 3\alpha^2\left(T-T_0\right)^2 + \alpha^3\left(T-T_0\right)^3\right)\mathrm{d}x\mathrm{d}y\mathrm{d}z \\
&= \{\alpha \text{ is small}\} \approx 3\alpha\left(T-T_0\right)\mathrm{d}V.
\end{aligned} \tag{A.5}$$

B
Details on Methodology

This appendix contains details on information about the models that is not covered fully in Chapter 3. This includes for example details on model parameters, how convection and radiation, subroutines, mesh studies and modeFRONTIER.

B.1 Model Parameters

B.1.1 Wear Scaling Factor

The wear scaling factor k, or rather $k_w = k/H$, was fitted to experimental values of the wear. As previously explained, the wear rate for the brake pads at simulation depends both on the radius r as well as the contact pressure p and the angular velocity ω, which generally vary with time. This means that the exact value of the wear depth over time is complex to determine as it would require knowing how the contact pressure distribution varies with space and time. Grzes and Kuciej [10] proposed calculating an average wear depth

$$h_{av}(t) = k_w r_{eq} \int_0^t p(\tau)\omega(\tau)\,\mathrm{d}\tau, \tag{B.1}$$

where r_{eq} is an equivalent (effective) radius, and p is the average pressure. We note that a more general solution, that does not disregard that the wear depth will vary with r is

$$h_w(r,t) = k_w \int_0^t p(r,\tau)\omega(\tau) r\,\mathrm{d}\tau, \tag{B.2}$$

and that the wear volume will thus vary with time as

$$W(t) = k_w \phi_0 \int_{r_2}^{r_3} \int_0^t p(r,\tau)\omega(\tau) r^2\,\mathrm{d}\tau\,\mathrm{d}r. \tag{B.3}$$

where all is known except for k/H. The measurement values of the wear will be in terms of mass lost through wear. Assuming constant density ρ_p of the brake pads we have that

$$\rho_p W(t) = m_p(0) - m_p(t), \tag{B.4}$$

and thus k_w can be obtained by scaling the integral in equation (B.3) so that it fits the measurements values of the mass, or by scaling equation (B.1) or (B.2) to measurement values of the change of thickness.

Note that an implicit simplification has been done in the derivation above, and that is that k_w is constant. In truth the wear rate is temperature dependent [41], and will thus

vary with time during a braking event. In [41] the temperature dependence is modelled as

$$k_w = K_{w0}\left(d_0 + d_1 T(t) + \frac{d_2}{\left(d_3\left(T_{w1} - T(t)\right)\right)^2 + 1} + \frac{d_4}{\left(d_5\left(T_{w2} - T(t)\right)\right)^2 + 1}\right), \tag{B.5}$$

which gives a total of 8 parameters (K_{w0}, d_{1-5} and T_{w1-2}) that needs to be fitted to. To use such a model would thus require inserting k_w into the integral and using measurement data of the brake pads' temperature and the mass loss to determine any parameters. The issue is that in practice the mass loss of the brake pads can only be measured before and after a braking cycle, not during. This means that any model of k_w that has multiple parameters requires several different measurement series. Typically, the wear rate increases with temperature, with the wear rate for organic composites increasing rapidly as they approach a critical temperature of approximately 500 °C, see [42], [18]. Any estimate of the wear rate as constant will thus depend heavily on the brake cycle used in the tests, and will at best work as a time-averaged wear rate for that specific brake cycle. The constant wear rate will be an overestimate of the wear rate at the start of a cycle (low temperature), and an underestimate of the wear rate at the end (high temperature).

For this project we had two options. Either to use constant values for the wear scaling factors or to use temperature dependent values obtained from limited testing, see Section 3.2.2.

For the former using equation (B.1), that for all the 500 cycles we obtain the mean wear depth per cycle is

$$h_{av,p} = p\bar{k}_{w,p} r_{eq,D33} \cdot 59 \text{ rad/s} \cdot 40 \text{ s} = \frac{\text{Final mean wear depth}}{500}, \tag{B.6}$$

where $h_{av,p}$ is the average wear per cycle for the disc crack tests, see Section 3.2.1, and p is the contact pressure in those tests. Then we have that $\bar{k}_{w,p}/k^* \approx 11.582 \cdot 10^{-8}$ MPa^{-1}, where k^* is a unit-less normalisation factor for the wear scaling factors.

The temperature dependent values are obtained from measurement values of wear depth from wear tests, see Section 3.2.2. With the assumption that the temperature does not increase substantially from the initial brake temperature in those tests we can use equation (B.1) and obtain that for each temperature the value will be given by

$$\begin{aligned} \Delta h_{av,p}(T) &= p k_{w,p}(T) r_{eq,D37} \omega_0^2 \frac{J}{2\tau} = \frac{\text{Mean change of pad thickness for } T}{\text{Number of cycles for } T} \\ \Delta h_{av,d}(T) &= \frac{\phi_0}{2\pi} p k_{w,d}(T) r_{eq,D37} \omega_0^2 \frac{J}{2\tau} = \frac{\text{Mean change of disc thickness for } T}{2 \cdot \text{Number of cycles for } T}. \end{aligned} \tag{B.7}$$

The reason for the factor $\frac{\phi_0}{2\pi}$ is because that is the fraction of the disc contact surface that is in contact at any given time. That the mean change of the disc thickness is divided by 2 is because the wear occurs on both surfaces of the disc. Note that both p and $r_{eq,D37}$ are specific to the the wear test and the D37-disc.

Table B.1: Normalised temperature dependent wear scaling factors of the pad and disc.

T [°C]	$k_{w,p}/k^*$ [$\cdot 10^{-8}$ MPa^{-1}]	$k_{w,d}/k^*$ [$\cdot 10^{-8}$ MPa^{-1}]
100	1.00	0.675
200	2.00	0.675
300	2.30	0.900
400	4.20	0.450
500	10.2	0.900

Table B.1 shows Normalised temperature dependent values of the wear scaling factors. Note that the temperature of the pad and disc will not in fact be these constant values during the wear tests, therefore as discussed above these values are only approximate.

It is worth noting that in Table B.1 $k_{w,p}$ increases exponentially whilst $k_{w,d}$ remains relatively constant. To accurately model wear at temperature higher than 500 °C we will need to extrapolate the values of $k_{w,p}$ and $k_{w,d}$. The choice made was to extrapolate using the two last values, 400 and 500 °C, and let that extrapolation be exponential for the pad and linear for the disc, i.e.

$$\begin{aligned} k_{w,p}(T) &= k_{w,p}(500) \cdot \left(\frac{k_{w,p}(500)}{k_{w,p}(400)} \right)^{\left(\frac{T-500}{100}\right)}, \text{ if } T > 500 \\ k_{w,d}(T) &= k_{w,d}(500) + (k_{w,d}(500) - k_{w,d}(400)) \cdot \frac{T-500}{100}, \text{ if } T > 500. \end{aligned} \tag{B.8}$$

In the input files the extrapolated values were then added at 600, 700 and 800 °C. In the multiple cycles model, see Section 3.5.1.2, the extrapolation is added as part of a function.

Table B.2: Extrapolated normalised temperature dependent wear scaling factors of the pad and disc.

T [°C]	$k_{w,p}/k^*$ [$\cdot 10^{-8}$ MPa^{-1}]	$k_{w,d}/k^*$ [$\cdot 10^{-8}$ MPa^{-1}]
600	25.1	1.35
700	60.2	1.80
800	146	2.25

Table B.2 shows the extrapolated values of the wear scaling factors at 600, 700 and 800 °C. It is worth noting that when specifying the values in Tables B.1 and B.2 as properties in Abaqus it will interpolate between them linearly.

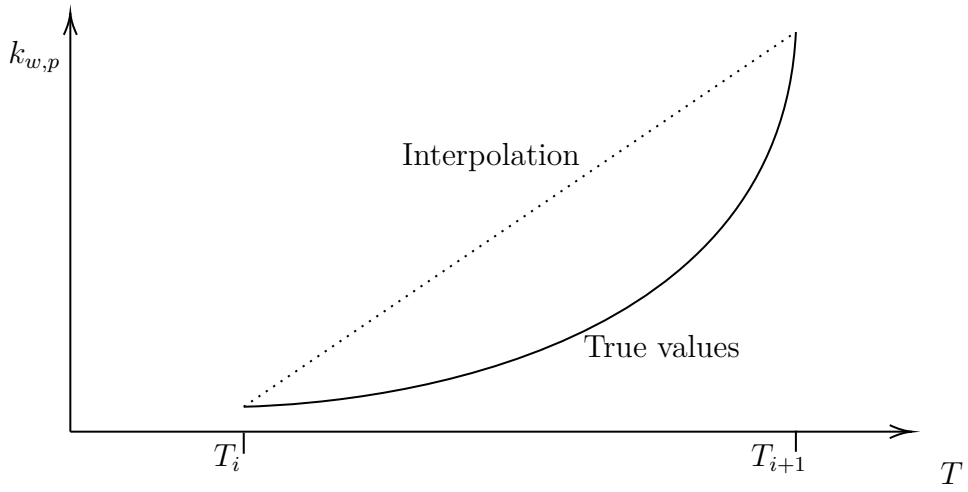

Figure B.1: *Sketch of how the interpolation affects the intermediary values of $k_{w,p}$ in the range $T_i < T < T_{i+1}$ if $k_{w,p}$ is a convex function.*

Figure B.1 shows how the linear interpolation would affect the values of $k_{w,p}$ in between our measured values, and it is clear from the graph that for a convex function such as $k_{w,p}(T)$ the linear interpolation in Abaqus will give an overestimation of the wear scaling factor in the intermediary ranges.

B.1.2 Heat Transfer Coefficient of Convection

The convective heat transfer coefficient h was estimated using empirical formulas for brake discs that depends on the air flow.

The value of the convective heat transfer coefficient will depend on the nature of the flow around the disc. The flow can be characterised by the Reynolds number

$$\mathrm{Re} = \frac{\rho_a v_a L}{\mu_a}, \tag{B.9}$$

where v_a is the speed of the fluid/air, L is a characteristic length which for the disc would be the diameter, μ_a is the viscosity of the air and ρ_a is the air density. Another number needed is the Prandtl number

$$\mathrm{Pr} = \frac{\mu_a}{\rho_a \lambda_{th,a}}, \tag{B.10}$$

where $\lambda_{t,a} = k_{t,a}/(\rho_a c_{p,a})$ is the thermal diffusivity of the air [43], [5].

Per Limpert [5] for a given airflow the heat transfer coefficient of convection for a solid disc can be calculated for laminar flows ($\mathrm{Re} < 2.4 \cdot 10^5$) as,

$$h_d = 0.70 \frac{k_{t,a}}{D} \mathrm{Re}^{0.55}, \tag{B.11}$$

with D being the disc diameter. Whilst for turbulent flows ($\mathrm{Re} > 2.4 \cdot 10^5$) it will be [5]

$$h_d = 0.40 \frac{k_{t,a}}{D} \mathrm{Re}^{0.8}. \tag{B.12}$$

The formulations above are only for brake discs and not brake pads. In other studies such as [10] and [44], similar expressions were used for the heat transfer coefficient of the disc, or it was calculated using a computation fluid dynamics (CFD) software, whilst constant values were used for the brake pads outer surfaces. In [45] it was assumed that it was equal to 7 W/(m^{2}K), and in [44] it was assumed to be 5 W/(m^{2}K).

Table B.3: Thermal properties of air at 1 atm and 300 K, [17], except for the density which is at 20 °C [43].

$k_{t,a}$ [W/(m^{2}K)]	c_p/c_v [-]	μ_a [$\cdot 10^{-6}$ kg/(ms)]	c_v [J/(kgK)]	λ [$\cdot 10^{-6}$ m]	ρ_a [kg/m^3]
0.0262	1.40	18.5	718	0.064	1.204

In Table B.3 thermal properties of air is listed. From these values we obtain that Pr $\approx$ 0.7098.

B.1.3 Thermal Contact Conductance

To estimate the thermal contact conductance empirical formulas are used to estimate it based on the material properties of the bodies.

B.1.3.1 Spot Conductance

Madhusudana [17] presents two formulas to calculate the spot conductance, one for elastic and one for plastic deformation at the contact,

$$\begin{aligned} \text{Elastic: } \hat{h}_s &= 1.55 \left(\frac{k_t' \tan\theta}{\sigma}\right) \left(\frac{p\sqrt{2}}{E' \tan\theta}\right)^{0.94} \\ \text{Plastic: } \hat{h}_s &= 1.13 \left(\frac{k_t' \tan\theta}{\sigma}\right) \left(\frac{p}{H}\right)^{0.94}, \end{aligned} \tag{B.13}$$

where k_t' is the effective thermal conductance, E' is the effective Young's modulus, $\tan\theta$ is the mean absolute slope of the profiles, H is the hardness of the softer material and σ is the effective roughness of the surfaces [17].

Whether or not elastic or plastic deformation happens is determined by the plasticity index,

$$\psi = \left(\frac{E'}{H}\right) \tan\theta, \tag{B.14}$$

with $\psi > 1$ indicating plasticity [17].

For the materials in question

$$E' = \frac{2}{\frac{1-\nu_d^2}{E_d} + \frac{1-\nu_p^2}{E_p}} = 859.9 \text{ MPa}, \tag{B.15}$$

per values from Volvo and suppliers. For OC-friction materials it was found by Eriksson and Jacobson [46] that the hardness varies between 200 MPa and 4 GPa depending on the indentation depth. For the cast iron the hardness value was found to be 170. Mistakenly this was assumed to be in MPa, but later it was discovered to be the Brinnell hardness.

In the following calculations the value of H used was thus 170 MPa when it should have been 200 MPa, or an even higher value. We note however that with a higher value of the hardness we would only have gotten the same conclusion with regards to plasticity contra elasticity, and thus the same conductance.

Therefore, for elasticity it would be required that

$$\tan\theta \leq \frac{H}{E'} = 0.1978 \Longrightarrow \theta \leq 11.19°. \tag{B.16}$$

In a study by Bettge and Starcevic [47] the tilting of the contact surface for disc brakes, among other things, was studied with quantitative microscopy. This was measured in both the perpendicular and parallel direction to the direction of the sliding direction. This was done for several specimens and the largest mean absolute value was for one pad specimen where it was 1.93° in the parallel direction, and 0.36° for the disc [47]. In this study it is therefore assumed that $\tan\theta \leq 0.1978$ is reasonable for disc brakes, and thus that the formula for elastic deformation should be used when estimating the spot conductance. We note that in the formula for elastic deformation the spot conductance is proportional to $(\tan\theta)^{0.06}$, one approximation would be to say that this is approximately equal to 1, but we note that $0.1978^{0.06} \approx 0.907$. The exact value of $\tan\theta$ is unknown, but since $(\tan\theta)^{0.06}$ is relatively constant within the possible span of angles we can set $(\tan\theta)^{0.06} = 0.9$, however it will likely lead to a slight overestimation of the spot conductance.

Eriksson and Jacobson [46] found that depending on the direction, perpendicular or parallel to the sliding direction, the roughness of a cast iron brake disc was $R_a = 0.1$ µm and $R_a = 0.3$ µm respectively, whilst for the an OC-pad it was $R_a = 2$ µm (not any particular direction). If we assume that these values are representative for cast iron discs and friction materials in brake pads, and use the average value for the brake disc, we get that the effective roughness of the contact [17] is

$$\sigma = 1.25\sqrt{0.2^2 + 2^2}\ \text{µm} = 2.51\ \text{µm}. \tag{B.17}$$

Applying the elastic formula in equation (B.13) and inserting our values we obtain that

$$\begin{aligned}\hat{h}_s &= 1.55\left(\frac{k_t' \tan\theta}{\sigma}\right)\left(\frac{p\sqrt{2}}{E'\tan\theta}\right)^{0.94} = 1.55 \cdot \frac{0.9}{2.51\cdot 10^{-3}}\left(\frac{\sqrt{2}}{859.9}\right)^{0.94} k_t' p^{0.94} \\ &= 1.3428 k_t' p^{0.94},\end{aligned} \tag{B.18}$$

where we have that with k' in mW/(mmK) and p in MPa the unit of $\hat{h}_s$ is mW/(mm^{2}K). The effective conductivity is defined as

$$k_t' = \frac{2k_{t,p}k_{t,d}}{k_{t,p} + k_{t,d}}, \tag{B.19}$$

[17], therefore it will be dominated by the material with lower thermal conductivity, i.e. the friction material. For example, if $k_{t,p} = 2$ W/(mK) and $k_{t,d} = 50$ W/(mK) we would get $k_t' \approx 3.85$ W/(mK).

B.1.3.2 Gas Conductance

The mean separation between two rough surfaces can be calculated as

$$\delta = 1.53\sigma \left(\frac{p}{H}\right)^{-0.097}, \tag{B.20}$$

if they follow a Gaussian height distribution [17, p. 65]. Four our case $\delta \approx 6.326p^{-0.097}$ in µm with p in MPa. Note that this was erroneously calculated with $H = 170$ MPa, but this should only give a small difference compared with 200 MPa. The temperature jump distance is

$$g = \left(\frac{2-\alpha}{\alpha}\right)\left(\frac{2}{c_p/c_v+1}\right)\left(\frac{k_g}{\mu_a c_v}\right)\lambda, \tag{B.21}$$

with α being the accommodation coefficient and λ being the mean free path. For air we have that $g_a = 0.1286$ µm [17, p. 66]. Then the gas conductance is given by [17]

$$\hat{h}_g = \frac{k_{t,a}}{\delta + 2g_a} \approx \frac{0.0262 \text{ W/(mK)}}{(6.326p^{-0.097} + 2 \cdot 0.1286) \cdot 10^{-6} \text{ m}} = \frac{26.2p^{0.097}}{6.326 + 0.2572p^{0.097}} \text{ mW/(mm}^2\text{K)}, \tag{B.22}$$

with p in MPa.

B.1.4 Thermal Material Parameters

The thermal material parameters of the disc and pads that govern the heat flow, i.e. k_t, ρ and c_p, are here considered to be temperature dependent.

Originally, the plan was to determine the values of the properties for the cast iron disc and the pad friction material by using a physics-informed neural network (PINN), see Section 3.7. However, this approach was used only for study of the pad material, since the properties of the cast iron was already well known at Volvo, and it was also decided to not use a PINN due to several reasons, see Section 3.7. Instead the optimisation software modeFRONTIER was used, see Section 3.8, to try to fit the material parameters of the pad friction material so that the simulations matched the available data.

The data used to fit the thermal material properties is the measured temperature values from the disc crack tests, see Section 3.2.1. That data set is however limited in the sense that there is only one thermocouple per pad. Therefore any model of the temperature dependence of the parameters has to be relatively simple, otherwise any fit could be prone to overfitting and/or to give unphysical values. Therefore, it was assumed that k_t and c_p varied linearly, whilst it was assumed that $\rho = \rho_0/\left(1 + \rho_1\left(T - 20\ ^\circ\text{C}\right)\right)$. The latter to have a simple expression for ρ_0 that gave a thermal expansion that varied with temperature. Using equation (2.26) we get that $\alpha = \rho_1/\left(3 + 3\left(T - 20\ ^\circ\text{C}\right)\right)$.

At a later stage of the project some experimental values became available for the thermal material properties of the pad as well. A differential scanning calorimetry test was performed by a doctoral student at Chalmers which gave $c_p(T)$ values up to about $T = 140\ ^\circ$C [48]. From supplier values of k_t in the range $100\ ^\circ\text{C} \leq T \leq 300\ ^\circ$C were provided, as well as other measurements of c_p up to 250 °C, of ρ at room temperature and of α.

Instead of using the values of the thermal material properties obtained in the mode-FRONTIER optimisation, see Section B.5.1, the experimental values were used for other simulations. The reasons for why this was done were that it was deemed that we should not introduce qualitative errors to the model just to lower the quantitative errors, see Section 5.2.1.

The values of the material properties as determined by the supplier was not available, for the pad material used in the tests, when the mesh study was started, see Section B.4. However, those of a similar pad material from the same supplier was available. For the mesh study a combination of the conductivity and thermal expansion from that material, specific heat as determined by the doctoral student, and the density per the suppliers was used.

Later, when all properties were available from the supplier for the correct pad material, it was discovered that the specific heat values of the measurement from Chalmers differed from these substantially. At around 150 °C, c_p was overestimated by approximately 60% in the measurement from Chalmers. In the end we choose to use the values obtained in tests by the suppliers for all thermal material properties.

The properties of steel for the backing plate are taken from literature, to be specific from [10], although some properties of the steel were altered based on information from suppliers.

B.1.5 Others

The remainder of the parameters, such as $\sigma,\ \mu,\ T_e,\ F_{dp},\ \epsilon,$ and the properties of the air, are assumed to be constant.

The heat partition coefficient between pad and disc was assumed to be 0.96, i.e. 96% of the heat generation goes to the disc and 4% to the pad. In [9] the heat partition coefficient is given as

$$\sigma = \frac{\sqrt{k_{t,d}c_{p,d}\rho_d}S_d}{\sqrt{k_{t,d}c_{p,d}\rho_d}S_d + \sqrt{k_{t,p}c_{p,p}\rho_p}S_p}. \tag{B.23}$$

This expression can be used only for short durations of brake application, when the bodies may be assumed to be semi-infinite solids [5, p- 70]. From a rough calculation based on the obtained values of the material parameters equation (B.23) gives $\sigma = 0.95$.

As remarked upon in Section 2.6 the coefficient of friction μ is in fact not constant for most applications, but rather dependent on a multitude of factors. Accurately determining those dependencies were judged to be outside of the scope of the present study, and thus it is approximated as constant. The value of μ used in the simulations was 0.3.

B.2 Details on Axisymmetric Modelling

In this section details of the axisymmetric modelling is covered, including convection and radiation details as well as applied heat fluxes.

Changing the density can also be done to make it possible to do axisymmetric models of ventilated discs. This was done in previous work at Volvo, ER-613440, for thermo-mechanical simulations of a ventilated brake disc. The argument then is that mass (and internal energy) should be conserved so the "vanes" would be solid but with decreased density. Note that for accuracy this reduced density should only be applied in the portion of the disc where the vanes would be, and that the remainder of the disc should have the normal density of cast iron.

It is also important that the total heat that is put into the system is consistent with 3D-simulations and with reality, and this was done by adjusting the heat flux to disc and pad. In the axisymmetric simulations Abaqus would calculate the energy input as if the heat flux was applied to the surface across the entire revolution, whilst in reality the heat flux is only applied to a fraction of $\phi_0/(2\pi)$ of that area. Thus the heat fluxes to both pad and disc were adjusted so that in the axisymmetric models they are

$$\begin{aligned} q_{d,\text{axi}} &= \frac{\phi_0}{2\pi}\sigma\mu p\omega r \\ q_{p,\text{axi}} &= \frac{\phi_0}{2\pi}\left(1-\sigma\right)\mu p\omega r. \end{aligned} \tag{B.24}$$

With the addition of the parametrisation $p = p_1\left(1-\zeta(t)\right) + p_2\frac{r_2}{r}\zeta(t)$ it becomes

$$\begin{aligned} q_{d,1,\text{axi}} &= \frac{\phi_0}{2\pi}\sigma\mu\omega p_1 r\left(1-\zeta(t)\right) \\ q_{d,2,\text{axi}} &= \frac{\phi_0}{2\pi}\sigma\mu\omega p_2 r_2\zeta(t) \\ q_{p,1,\text{axi}} &= \frac{\phi_0}{2\pi}\left(1-\sigma\right)\mu\omega p_1 r\left(1-\zeta(t)\right) \\ q_{p,2,\text{axi}} &= \frac{\phi_0}{2\pi}\left(1-\sigma\right)\mu\omega p_2 r_2\zeta(t). \end{aligned} \tag{B.25}$$

Note that for most cases it would be straight-forward to calculate the terms $\frac{\phi_0}{2\pi}\sigma\mu\omega$ and $\frac{\phi_0}{2\pi}\left(1-\sigma\right)\mu\omega$ and assuming that μ is constant they would only vary with time. These terms were then added as amplitudes in Abaqus, with

$$\begin{aligned} &\text{Amplitude of constant pressure term for disc: } \frac{\phi_0}{2\pi}\sigma\mu\omega(t)\hat{p}_1\left(1-\zeta(t)\right) \\ &\text{Amplitude of constant wear term for disc: } \frac{\phi_0}{2\pi}\sigma\mu\omega(t)\hat{p}_2\zeta(t) \\ &\text{Amplitude of constant pressure term for pad: } \frac{\phi_0}{2\pi}\left(1-\sigma\right)\mu\omega(t)\hat{p}_1\left(1-\zeta(t)\right) \\ &\text{Amplitude of constant wear term for pad: } \frac{\phi_0}{2\pi}\left(1-\sigma\right)\mu\omega(t)\hat{p}_2\zeta(t). \end{aligned} \tag{B.26}$$

Here $\hat{p_1}$ and $\hat{p_2}$ were the pressures in MPa that it would take for the clamp force to be 1 N, which for the D33 brake disc were

$$\begin{aligned} \hat{p}_1 &= \frac{2\cdot 1\text{ N}}{\phi_0\left(r_3^2-r_2^2\right)} \approx 8.49\cdot 10^{-5}\text{ MPa} \\ \hat{p}_2 &= \frac{1\text{ N}}{\phi_0 r_2\left(r_3-r_2\right)} \approx 1.12\cdot 10^{-4}\text{ MPa}. \end{aligned} \tag{B.27}$$

To end up with the correct heat fluxes these were amplitudes were multiplied by the clamp force in N.

The remaining part of the heat flux expressions in equation (B.25) were radii r and r_2, linear and constant. To capture the linear variation of the heat flux it is possible to either construct a subroutine or to partition the surface into segments with different prescribed heat fluxes, the latter is something that has been done in previous work at Volvo, ER-613440. The latter alternative was chosen, however it should be noted that the heat flux was then only approximate and that the accuracy depends on the number of segments. The heat flux prescribed to each segment should be such that the real heat flux would give the same heat as the prescribed one, i.e for segment i

$$\hat{q}_{1,i}A_i = \phi_0 \int_{r_i}^{r_{i+1}} r^2 \,\mathrm{d}r \implies \hat{q}_i = \frac{1}{A_i}\phi_0 \frac{r_{i+1}^3 - r_i^3}{3} = \frac{2\left(r_{i+1}^3 - r_i^3\right)}{3\left(r_{i+1}^2 - r_i^2\right)}, \tag{B.28}$$

whilst for the constant heat flux the same "heat flux" can be prescribed across the entire surface and it was

$$\hat{q}_2 A_{tot} = \int_{A_{tot}} r_2 \,\mathrm{d}A \implies \hat{q}_2 = r_2. \tag{B.29}$$

Note that the heat fluxes were "radii", which is an artifact of that we have amplitudes that are not unitless. This is fine as long as one is consistent with the units in Abaqus, for example if the length unit is mm then the pressure should be in MPa.

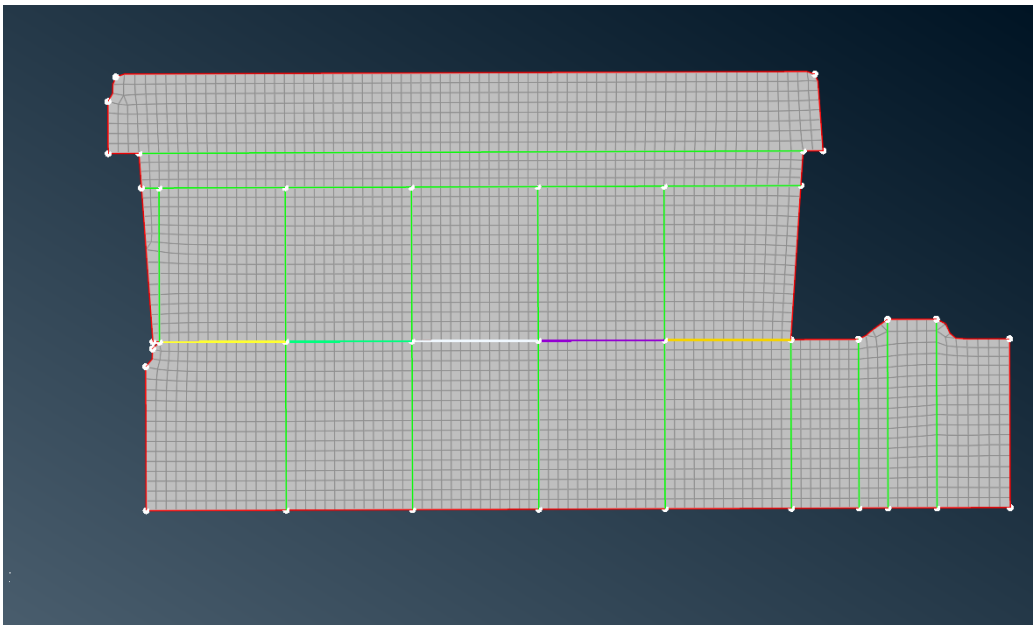

Figure B.2: *The thermal axisymmetric half-disc model with a* 1 mm *target size mesh. The contact surfaces/segments 1 through 5 are highlighted with orange, purple, white, turquoise, and yellow colours respectively.*

The surface was partitioned into five evenly long segments, see Figure B.2. For the pads used and the D33 disc these segment where approximately 12.72 mm long.

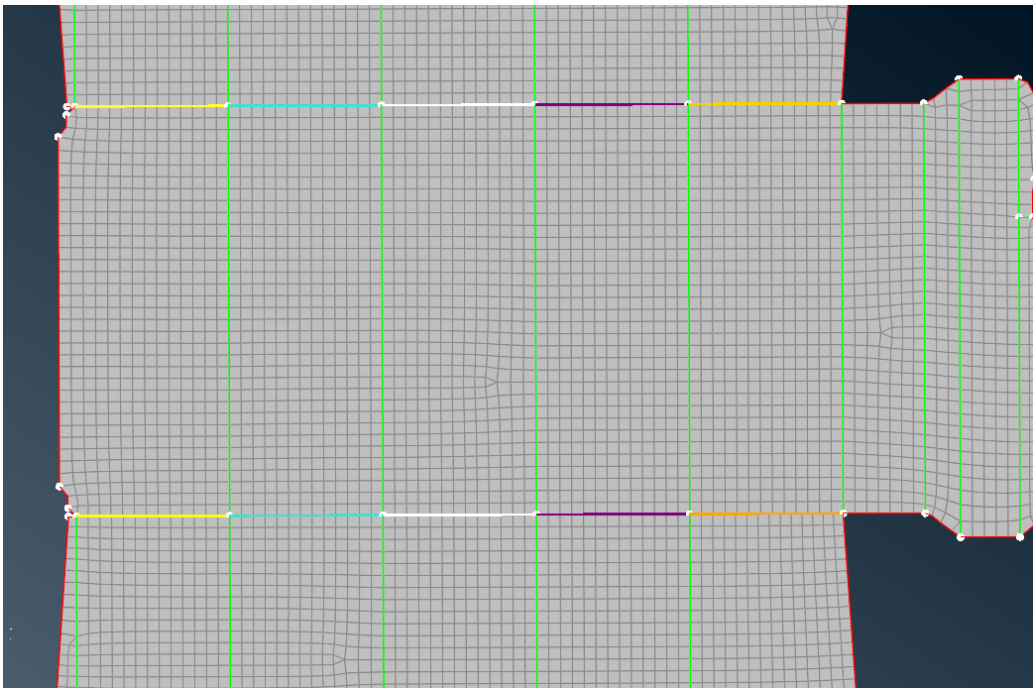

Figure B.3: *The thermal axisymmetric full hub model with a* 1 mm *target size mesh. The contact surfaces/segments 1 through 5 are highlighted with orange, purple, white, turquoise, and yellow colours respectively.*

Figure B.3 shows the segments on the full model that includes the hub.

Table B.4: Heat flux parameters for the constant pressure term applied on segments of the contact surfaces. Segment 1 is the inner-most segment, and the segments are numbered in order so that the radii are increasing order.

Segment	$\hat{q}_{1,i}$ [mW/mm^2]
1	107.3
2	120.0
3	132.7
4	145.4
5	158.1

Note that the values of the parameters in Table B.4 had to be multiplied by the clamp force in N. This is done in the Abaqus input file by adding a parameter for the force, the heat fluxes are then added as expressions of $\hat{q}_{j,i}F_{clamp}$, $j = 1, 2$ and $i = 1, ..., 5$.

By the same principal as for the heat fluxes the heat transfer coefficients of convection, and the emissivity, had to be adjusted to account for the differences in modelled surface area. These boundary conditions were applied on seven surfaces: the outer and inner parts of the disc (not in contact), the contact surface of the disc, the outer and inner parts of the pads (not in contact), and (if included) the inner and outer parts of the hub. The values of h and ϵ of the disc contact surface needed to be adjusted by a factor $(1-\frac{\phi_0}{2\pi})$, since convective cooling only occurs when there is no contact. The values for the pads needed to be adjusted by the factor $\frac{\phi_0}{2\pi}$. The remaining four surfaces do not have to have their values adjusted.

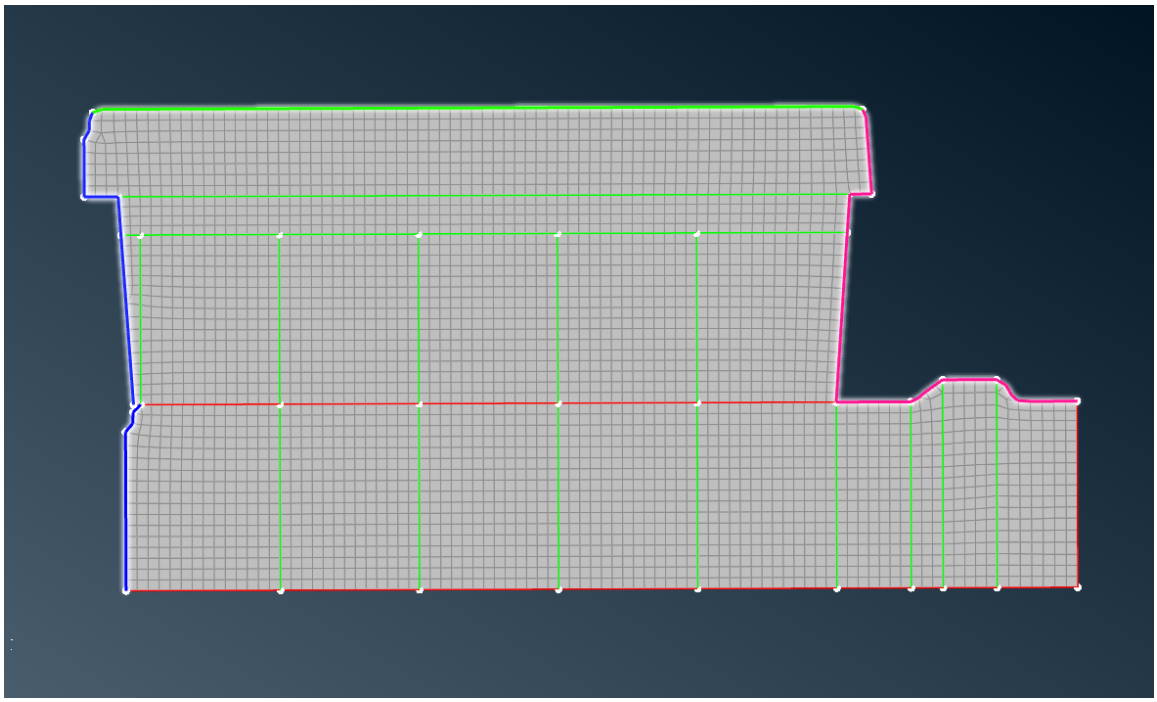

Figure B.4: *The thermal axisymmetric half-disc model with a* 1 mm *target size mesh. The highlighted blue edges form the "outer" surfaces, the pink form the "inner" and the green form the top end of the backing plate.*

Figure B.4 shows the division between these different types of surfaces for the axisymmetric half-disc model.

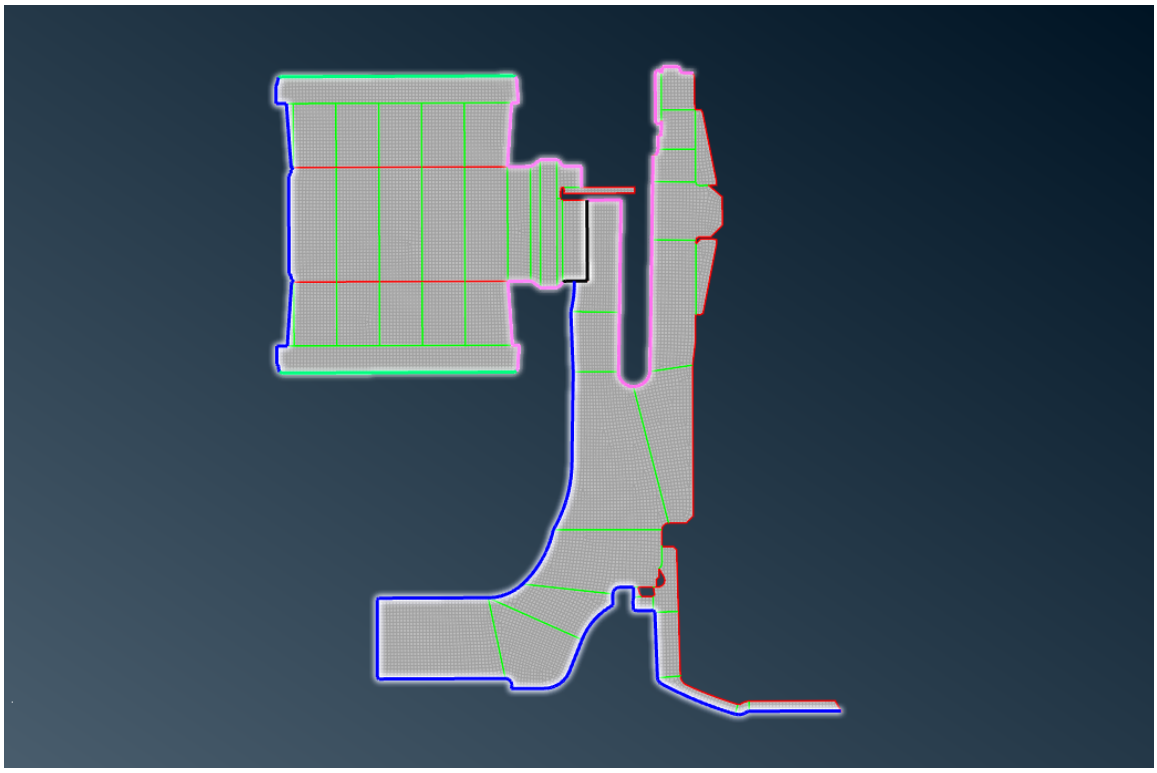

Figure B.5: *The thermal axisymmetric full hub model with a* 1 mm *target size mesh. The highlighted blue edges form the "outer" surfaces, the pink form the "inner" and the green form the top end of the backing plate. The black edges are the splines interface.*

Figure B.5 shows the division between these different types of surfaces for the axisymmetric model with the hub.

We assumed that the values of the heat transfer coefficient of convection was constant on these surfaces. The rotation of the disc was as previously stated approximately 59 rad/s, and the velocity of the air relative the surface differs with $v_a \pm \omega r$ at radial position r. At the outer part of the disc $\omega r_4 \approx 9.735$ m/s, whilst at the inner part of the disc $\omega r \approx \omega \left(\frac{r_2+r_1}{2}\right) \approx 5.298$ m/s. Note that whilst the heat transfer coefficient of convection may differ across the surface, the relative motion causes both an increase and decrease of the relative velocity, and which would be difficult to capture in a FE-simulation. Therefore the inlet velocity of the air v_a was used for calculations of the heat transfer coefficient of convection.

With $v_a = 40$ km/h, and using the equations and values stated in Section B.1.2 Re $\approx 2.38 \cdot 10^5$ was obtained, so the flow was laminar, and thus $h_d \approx 50.4$ W/(m^{2}K) $= 0.0504$ mW/(mm^{2}K). This value was prescribed to both inner and outer parts of the disc surface. The value on the contact surface of the brake disc was then $\left(1 - \frac{\phi_0}{2\pi}\right) h_d \approx 0.0392$ mW/(mm^{2}K).

For the hub values of h were applied as based on previous work at Volvo, ER-613440 on inner and outer surfaces, see Figure B.5. Any values of h for the pads from previous simulations could not be found, therefore it was assumed to be 0.006 mW/(mm^{2}K) on both outer and inner parts, i.e. consistent with other works, see Section B.1.2. However, that value should be for a full 3D-simulation, the value used in the axisymmetric model was $\frac{\phi_0}{2\pi} \cdot 0.006$ mW/(mm^{2}K) ≈ 0.00133 mW/(mm^{2}K).

The emissivity values are also assumed to be constant. In the test that were performed at Volvo an emissivity value that had been used for the brake disc, ER-686445. That value had been correlated with test data from the thermocouples, and is therefore used. The same emissivity is applied on the hub as on the disc. On the disc contact surface for the radiation to the environment an adjusted value of $\left(1 - \frac{\phi_0}{2\pi}\right) \epsilon_d$ is applied.

For the brake pads the value used in Grzes and Kuciej [10] of $\epsilon_p = 0.8$ was applied, but for the axisymmetric models it was changed to $0.8\frac{\phi_0}{2\pi} \approx 0.178$.

In the contact the gap radiation functionality is used in Abaqus. For the full 3D-model we assume that the clearance between pad and disc is so small that the view factor was $F_{dp} \approx 1$. In the axisymmetric model we instead set that $F_{dp} = \frac{\phi_0}{2\pi}$, to account for the area change. The emissivity values should be the same as for the full 3D-simulation. Note that there were thus two types of radiation on the disc contact surface, one that goes to pad and one to the environment, and that the values had been adjusted so that it was like $\phi_0/(2\pi)$ of the disc surface exchanges radiation with the pad, and $(1 - \phi_0/(2\pi))$ with the environment.

The contact conductance was also included in the models. To account for the spot and gas conductance effects a gap conductance was added to the contact formulation. The values of those conductances had to be adjusted for the axisymmetric models a factor $\frac{\phi_0}{2\pi}$. Using equation (B.18) and (B.22) and setting $p = p_1 = 1.2567$ MPa, the constant contact

pressure in 3D for $F_{clamp} = 14.8$ kN, we obtain that

$$\hat{h}_{s,\text{axi}} \approx \frac{\phi_0}{2\pi} 1.663 k_t' \approx 0.370 k_t' \text{ and } \hat{h}_{g,\text{axi}} \approx \frac{\phi_0}{2\pi} 4.068 \approx 0.904 \text{ mW/(mm}^2\text{K)}. \quad \text{(B.30)}$$

Note that due to conductivity the conductance is temperature dependent.

Table B.5: Normalised gap conductance values for the pad-disc contact that are temperature and clearance dependent.

T [°C]	$\left(\hat{h}_{s,3D} + \hat{h}_{g,3D}\right)/k_t^*$ [mW/(mm^{2}K)]	$\left(\hat{h}_{s,axi} + \hat{h}_{g,axi}\right)/k_t^*$ [mW/(mm^{2}K)]
100	5.17	1.15
200	4.57	1.02

In Table B.5 the gap conductance values that were prescribed in the model are listed as norms of k_t^*. Note that in thermal models this property was both temperature and clearance dependent. That the only temperature values were for 100 °C and 200 °C was because that was the only overlap in measured conductivity values for pad and disc.

If the hub was included in the simulation a gap conductance in the splines was introduced. In a previous work at Volvo, ER-618217, a value of 2.25 W/(m^{2}K) was used, but that was only for approximately 50% of the spline area. Thus for our formulation a value of 2.25/2 W/(m^{2}K) = 1.125 W/(m^{2}K) = 0.001125 mW/(mm^{2}K) was used. It was however noticed that such a small value gave an unphysical negligible increase of the temperature in the hub. It was therefore assumed that there had been a typo and we set 1.125 mW/(mm^{2}K). The exact value of the gap conductance for the splines should ideally be correlated with measurements of the temperature in the hub, such measurements were however not available in this thesis work.

The temperature on the top of the backplate was set at a constant value of 50 °C, i.e. any heat that flows through the pad lining all the way to the end of the backplate was assumed to be conducted away. The other possible boundary condition at that surface would be to have it be insulated. In some preliminary tests we found very little difference in the results between these two choices, even when insulated the temperature remains close to 50 °C. The reason for this is that the friction material in the pad lining is such a poor conductor that there is not much heat that flows all the way to the backplate for a short brake application.

B.3 Details on Subroutines

In this section details on subroutines and modelling employed for the "ultimate model", i.e. the axisymmetric model that allowed for study of multiple cycles, to work are provided, see Section 3.5.1.2. Details on the development of a subroutine for wear studies using the 3D-model are also presented.

B.3.1 Ultimate Model

When trying to use adaptive meshing on the CGAX elements there was an issue with the nodes becoming either under- or overconstrained. Changing to CAX elements solved

this issue, with the rotational dof being removed. Using CAX element with no rotation meant that the heat generation due to the rotation was lost. This was solved by manually introducing the sliding distance during an increment as $\omega r \Delta t$ in the *FRIC* subroutine, and calculating the dissipated frictional energy from that. This solution had been used by our supervisor in [18]. The *FRIC* subroutine is called by adding friction properties.

```
*FRICTION,USER,PROPERTIES=1, DEPVAR=0
 0.3
```

One important aspect of the *UMESHMOTION* subroutine is that it cannot identify the node set which is called, though it can identify the part name for which the node belongs. To prescribe the wear on both pad and disc it is therefore necessary to create two part instances in the input file. This was done by manually editing the .inp-file that was created from ANSA and separating the nodes and elements that belonged to pad and backing plate to one part, and those that belonged to the disc to another. Then the subroutine could identify if it is a pad or disc node and prescribe the correct wear scaling factor and mesh movement.

Some parts of the code was hard-coded for this specific case. For example the sliding velocity was calculated as 59 times the radial coordinate of the node, with 59 rad/s being the angular velocity. Other hard-coded parts concern the geometry and scaling factors.

The mesh movement of the pad nodes that are in contact is relatively simple. The contact pressure could be extracted and a movement was set for the mesh in accordance with Archard's law with the wear scaling factor times the contact pressure times the sliding distance as the displacement. One needs to be mindful to transform the movement to the nodes local coordinate system, but otherwise this was relatively straight forward. However, the interior nodes of the pads must also be moved in the same direction as the wear on the surfaces. If the interior nodes were not moved distorted elements would form when the wear is greater than the depth of the first layer of elements. An easy solution is to only apply the user subroutine on the nodes that will be in contact, whilst the other pad nodes are moved by "normal" adaptive meshing to prevent the element distortion. Below is how this would have been written in the .inp-file.

```
*ADAPTIVE MESH CONTROLS, name=Ada-1
0., 1.
*ADAPTIVE MESH, controls=Ada-1, elset=SET_ELEMS_PAD, FREQUENCY=1,
   MESHSWEEPS=1
*ADAPTIVE MESH CONSTRAINT, USER, TYPE=DISPLACEMENT
SET_NODES_PAD_CONTACT
*ADAPTIVE MESH CONSTRAINT, TYPE=DISPLACEMENT
SET_NODES_PAD_NOTCONTACT, 1, ,
```

However, this would not be an ideal solution. To add an adaptive mesh constraint on the inner nodes without a user subroutine the nodes must be constrained for one degree of freedom, either the radial or axial displacement. However there was a concern that this could lead to a geometry change. Therefore, this solution was not used, and we wanted to create a subroutine that worked for both contact nodes and interior nodes.

The adaptive mesh constraint for the user subroutine was added as type displacement, i.e. the wear was prescribed in the form of an incremental change of the wear depth, Δh_w. It is possible to change this to velocity type, then the wear would be prescribed

as $\mathrm{d}h_w/\mathrm{d}t$. Changing to velocity means that one uses the sliding velocity instead of the sliding distance. In tests we did not find that using either caused any noticeable difference in results, but as a matter of preference the wear was prescribed as a displacement in this project.

The approach for the pads was to calculate the accumulated wear for each node, determine the maximum accumulated wear of the nodes, and then move the inner nodes a distance $s \cdot (MAXW\_PAD - MAXWOLD\_PAD)$. $MAXW\_PAD$ was then the maximum accumulated wear of the previous increment, and $MAXWOLD\_PAD$ was that of the increment before that, whilst $0 \leq s \leq 1$ was a scaling factor determined by the geometry. $s = 0$ for a node at the end of the pad (at the interface to the backing plate), whilst $s \approx 1$ for a node close to the contact surface, and s was linearly dependent on the nodes depth in the pad. The reason for using maxima of accumulated wear from previous increments is that it is stable, easy to determine, and if properly implemented prevents element distortion. A possible issue would be if the wear was extremely uneven. Then if the maximum wear would be great it could excessively move inner nodes of the pad in parts that are not under any pressure. This should however only be a real issue if the pad surface is poorly aligned, or non-parallel, with the disc surface. Otherwise the difference in accumulated wear depth from node to node on the contact surface can not be to great, as those with more will go out of contact, and thus accumulate no more.

The easiest way to differentiate between contact and interior nodes is to check whether the node has the *CSTRESS* attribute available. However, the left and right edges of the pad lining had been added to the contact surface to prevent any possible penetration at the sides, meaning that those nodes whilst being ”interior” also have that attribute. To circumvent this issue we checked at the start of the first step which of the nodes that had a contact pressure greater than a tolerance value, and then those were identified as nodes at the top surface of the pad. If those nodes came out of contact, near zero contact pressure, due to wear or thermal expansion they were safeguarded from being moved. This safeguard was necessary to implement since otherwise we would have ”contact” nodes, temporarily out of contact due to thermal expansion, being moved as if they were an interior node.

For the disc a slightly different solution was necessary since for in Abaqus contact pairs, the contact pressure is only available on the secondary surface. For these simulations we had set that surface as the pad surface, meaning that when the subroutine was called for the disc it would not be able to extract any values of contact pressure. To solve this issue an interpolation function was added to the Fortran script, which based on common lists of the contact pressure and radii of the pad contact surface could find the two nearest neighbours of the disc node, and then linearly interpolates the contact pressure values of those neighbours. To make this functionality work it requires that the contact pressure and radii of the contact nodes of the pad are stored in each increment, and that the adaptive mesh is first applied on the pad, and then the disc so that current pressure values are used on the disc.

Since we for the disc had developed a function for the contact pressure as dependent on the radius the node movement could straightforwardly be applied as that stated by Archard’s law times a scaling factor s, for contact nodes we have that $s = 1$. The movement

of the interior nodes of the disc was thus not explicitly dependent on the accumulated wear. The scaling factor was because the remaining "thickness" of the disc adaptive mesh was determined by subtracting the maximum accumulated disc wear from the original thickness. I.e. if the disc adaptive mesh had an original thickness of 4 mm and the maximum disc wear depth at the end was 0.1 mm, then the remaining thickness, which is used to calculate s, is 3.9 mm.

```
1       UTEMP(1)=0.D0
2       UTEMP(2)=0.D0
3       UTEMP(3)=0.D0
4       IF (IS_PAD .EQ. 1) THEN
5             DH = 4.5D0*WCOEF * CPRESS * DSLIP !The factor 4.5 is 2pi/
                 phi0 and is there because the contact pressure has been
                 scaled down for the axisymmetric case
6
7     !Check if node is in contact
8
9             IF (CPRESS .GT. PTOL) THEN
10          ! treat as contact node
11                UTEMP(1) = 0
12                UTEMP(3) = 0
13                UTEMP(2) = DH
14                ACCWEAR_PAD_TEMP(LOCNUM)= DH
15            ELSE
16            ! treat as non-contact/interior node
17                PADT = ORIGINAL_PAD_ADAP_THICKNESS-MAXW_PAD !
                     ORIGINAL_PAD_ADAP_THICKNESS is the difference in z-
                     coordinate from the surface to the bottom layer of
                     nodes in the disc adaptive mesh
18                s = (COORDZ+MAXW_DISC-COORDZ_BOTTOM_OF_PAD_ADAP-COORDZ
                     -MAXW_PAD)/PADT !COORDZ_BOTTOM_OF_PAD_ADAP is the z
                     -coordinate of the bottom layer of nodes in the pad
                      adaptive mesh at the start.
19                IF (s .lt. 0.0D0) s = 0.0D0
20                IF (s .gt. 1.0D0) s = 1.0D0
21                IF (CONTACTNODE_PAD(LOCNUM) .EQ. 1.0D0) s = 0.0D0 !
                     prevents nodes that are on the contact surface from
                      being moved accidentally
22                UTEMP(2) = s*(MAXW_PAD-MAXWOLD_PAD)
23                UTEMP(1) = 0
24                UTEMP(3) = 0
25            ENDIF
26
27        ELSE
28    !Interpolate pressure values on pad to disc
29            CPRESS = CPRESSPAD_AT_R(COORDR)
30            DH = WCOEF * CPRESS * DSLIP
31            PADT = ORIGINAL_DISC_ADAP_THICKNESS-MAXW_DISC !
                 ORIGINAL_DISC_ADAP_THICKNESS is the difference in z-
                 coordinate from the surface to the bottom layer of nodes
                 in the disc adaptive mesh
32            s = (COORDZ_BOTTOM_OF_DISC_ADAP-COORDZ)/PADT !
                 COORDZ_BOTTOM_OF_DISC_ADAP is the z-coordinate of the
                 bottom layer of nodes in the disc adaptive mesh.
33            IF (s .lt. 0.0D0) s = 0.0D0
34            IF (s .gt. 1.0D0) s = 1.0D0
```

```
            ACCWEAR_DISC_TEMP(LOCNUM)= DH*s
            UTEMP(1) = 0
            UTEMP(3) = 0
            UTEMP(2) = -s*DH
      ENDIF
  !Coordinate transformation
      do kdim = 1, ndim
        do jdim = 1, ndim
            ULOCAL(kdim) = ULOCAL(kdim)-ALOCAL(jdim,kdim)*UTEMP(jdim)
        enddo
      enddo
```

The code snippet above was part of the *UMESHMOTION* subroutine, and it calculates the node movement. Note that some parts are more hard-coded, such as the coordinate inputs. Other parts, such as the direction that the wear should be applied in can also depend on the specifics of the geometry. It is important that the subroutine is properly tested. A reasonable change would be to set *ULOCAL* to zero before the last part, because ULOCAL will have non-zero values specified by normal adaptive meshing when entering the subroutine [49].

The subroutine was tested for extreme cases of wear. This was done by scaling up the *DH* values by large factors in the range of 1000 to 100000. We found that until the total wear is close to the depth of the adaptive mesh it was stable and worked as intended. Ergo, distorted elements was only an issue when the pad or disc was so worn down that the elements in the adaptive mesh became almost straight lines.

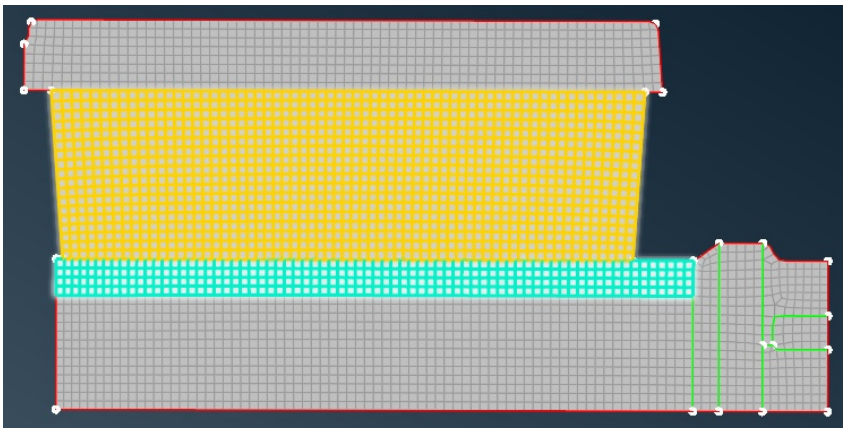

(a) *The element sets of the adaptive meshes in pad, yellow set, and in the disc, cyan set.*

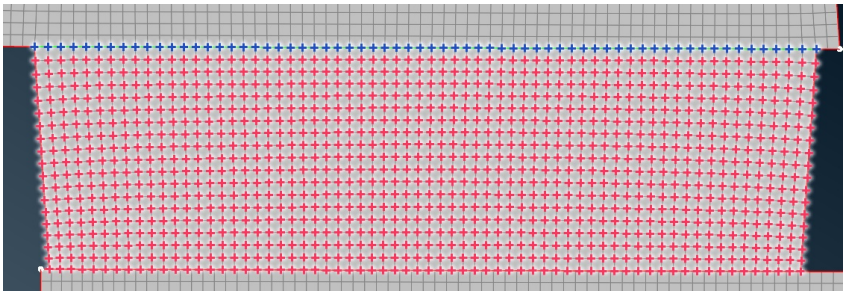

(b) *The node sets for the adaptive mesh in the pad. On the red set the subroutine is applied, on the blue it is not applied.*

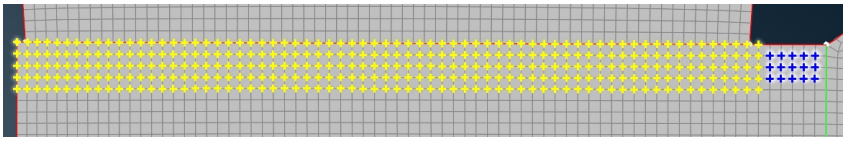

(c) *The node sets for the adaptive mesh in the disc. On the yellow set the subroutine is applied, on the blue it is not applied.*

Figure B.6: *The element and node sets on which adaptive meshing, with or without user UMESHMOTION subroutine, is applied.*

Figure B.6 shows the sets of elements and nodes that was used for the adaptive meshing. Note that there were two node sets for the disc, see Figure B.6c, one at the contact and one for inner nodes at the sides. For the former the user subroutine was applied as previously stated, for the latter a normal adaptive mesh was applied with the axial dof constrained. The reason for the second set was to prevent element distortion of the elements at the edge of the first node set when there was extreme disc wear. There are also two node sets at the pad, see Figure B.6b, one on which the wear was applied, and one which was the nodes at the end of the pad lining. The reason why the blue pad set *SET_NODES_PAD_END* was a separate node set was because it could cause abnormal node movement, if included in the other pad node set, which lead to element distortion. Adding a mesh constraint on that node set of the Lagrangian type ensured that those nodes followed the movement of the underlying material, and thus did not cause any issue. The snippet below shows the part of the Abaqus input file where the adaptive mesh was applied.

```
1 **INTRODUCE WEAR OF MATERIAL
2 *ADAPTIVE MESH CONTROLS, name=Ada-1
3 0., 1.
4 *ADAPTIVE MESH, controls=Ada-1, elset=SET_ELEMS_PAD, FREQUENCY=1,
```

```
   MESHSWEEPS=1
*ADAPTIVE MESH CONSTRAINT, USER, TYPE=DISPLACEMENT
SET_NODES_PAD
*ADAPTIVE MESH CONSTRAINT, CONSTRAINT TYPE=LAGRANGIAN
SET_NODES_PAD_END
*ADAPTIVE MESH, controls=Ada-1, elset=SET_ELEMS_DISC_WEAR, FREQUENCY=1,
   MESHSWEEPS=1
*ADAPTIVE MESH CONSTRAINT, USER, TYPE=DISPLACEMENT
SET_NODES_DISC_WEAR
*ADAPTIVE MESH CONSTRAINT, TYPE=DISPLACEMENT
SET_NODES_DISC_ADAPNOTUMESH, 2,
*PRINT, ADAPTIVE MESH=YES
```

In some early versions of the simulations it was dof 1 that was constrained for the second disc node set, and not dof 2. This was due to a misinterpretation of what that constraint meant. That difference did not cause any issue in the tests with one cycle and extreme wear, nor if one only simulated a few cycles. It did, in addition with an improper reset, however cause the nodes to move in the radial direction so much that elements were distorted, this happened around cycle 19. This slightly faulty version was used in the modeFRONTIER simulations outlined in Section B.5.2, since those simulations only ran for 10 cycles this is not considered to have be an issue.

To simulate multiple cycles multiple steps were defined. A step in Abaqus was the part of the input file in which the loads and boundary conditions are defined and applied. For each cycle firstly a step for the cycle itself was needed, but also it needed to be followed by a resetting step. This resetting step required two parts. Firstly, it needed to contain a ”boundary” condition applied on all nodes, which sets the temperature to the initial temperature of 50 °C. See the snippet below (dof 11 is the dof for temperature in Abaqus).

```
*BOUNDARY, TYPE=DISPLACEMENT
SET_NODES_ALL_DISC,          11,      ,         50.
SET_NODES_ALL_PAD,          11,      ,         50.
```

Secondly, it needed to temporarily turn of the *UMESHMOTION* subroutine. This was done by adding a return in the subroutine if the step number is an even number (which all reset steps will have). This return must be at the very start of the subroutine. See the snippet below.

```
IF (MOD(KSTEP, 2) .EQ. 0) RETURN
```

It is possible that the simple return above could cause adaptive meshing to occur during the reset steps as with a normal adaptive mesh, since *ULOCAL* is not changed. This could cause slight changes of the nodes placement in the reset steps. It is therefore recommended in future work to also specify that the mesh movement, *ULOCAL* should be zero in these steps. The prevention of the subroutine being applied in the reset steps can also be done by redefining the adaptive meshes in those steps to be of the Lagrangian types, and then reapply the adaptive mesh as above in all cycle steps.

In an early edition of the resetting a movement was also applied on the node set in the backplate to move the pad back from the disc and then back to it. This did however, for an unknown reason, also cause the nodes on the pad contact surface to form a flat surface again. This in turn caused the same nodes to again and again be the nodes which accumulates the most wear in each cycle, which in turn caused the relative movement

between those nodes and the first layer of the inner nodes to cause distortion.

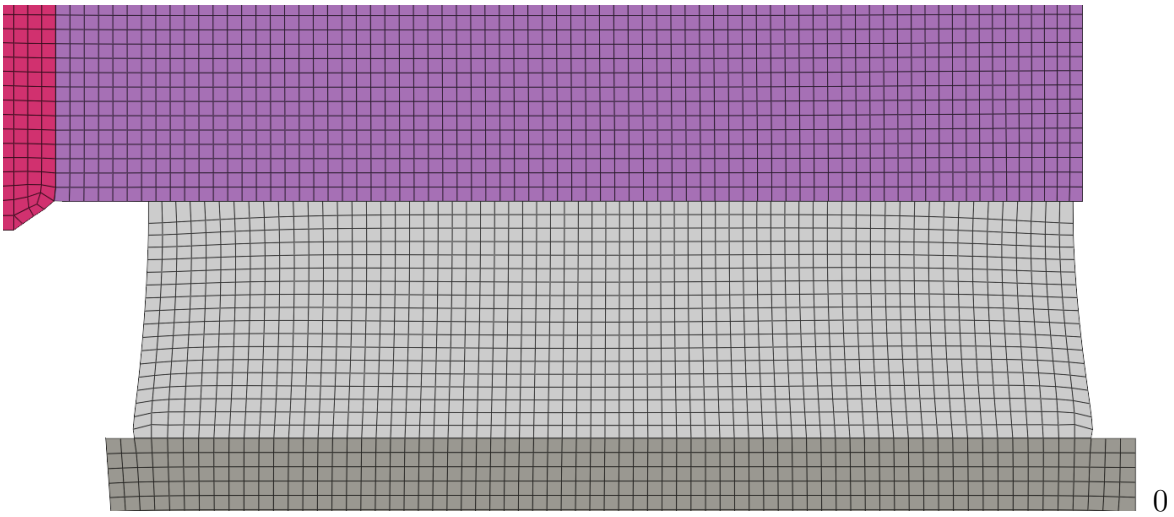

Figure B.7: *Distortion of the pad by resetting error. The distortion is noticeable in the first layer of elements for the pads. The picture is at the end of cycle 100, with a constant* $k_{w,p}$.

Figure B.7 shows the error mentioned above. This error can for little amounts of wears, or for few cycles, be unnoticeable in the results. It is easiest to observe for more cycles with slightly more wear. It is therefore recommended that one does such tests when constructing such subroutines. The easiest way to identify the error, besides simulating so long that it causes element distortion, is to look at the accumulated wear for each contact node in the pad and see if the difference grows gradually. If the error occurs it will grow more and more, whilst if the error does not occur we do not expect the accumulated wear to vary more than approximately 10 µm between different nodes.

B.3.2 Multiple Stops in 3D

ALE adaptive meshing only has support for certain element types. Arjmandi et al. [37] used 8-noded linear brick elements with reduced integration using hourglass control in their study of wear in three-dimensional woven textiles. 8-noded trilinear displacement and temperature elements with reduced integration using hourglass control (C3D8RT) was chosen for the adaptive mesh domain in order to include thermomechanical effects. Enhanced hourglassing was also enabled to solve zero-mode energy of deformed elements and thus enable the use of adaptive meshing [37]. Since wear only occurs on the disc and pad surfaces it was determined that the entire model did not have to consist of C3D8RT elements and that areas without wear and with more complex geometry could consist of 4-noded linear displacement and temperature elements (C3D4T).

During initial testing of the user subroutine it was found that the already long simulation time was increased greatly by the re-meshing routine. Further development of a *UMESH-MOTION* user subroutine for wear studies using the 3D-model was therefore abandoned because of the computational cost and time frame of the project. Wear was thus only simulated using the built-in CWEAR functionality in Abaqus.

B.4 Mesh Studies

This appendix includes the results of mesh studies for the employed models. To investigate the sensitivity of the results to the mesh size, a range of different mesh sizes are tested. The outputs which are extracted to investigate the sensitivity are the values of the maximum and mean nodal temperatures on the disc and pad contact areas in the final time increment. For thermomechanical models the mean and maximum wear were also extracted for the same nodes.

For some models different values of a fix time increment or values of DELTMX are tested. A DELTMX value is the allowed value of the maximum temperature change for an increment. For a thermomechanical analysis (a coupled temperature-displacement step) the time increment may also be lowered due to contact modelling iterations. The 3D-model was only tested with a DELTMX value of 10 °C since a smaller value would greatly increase the already long wall clock simulation time, limiting the mesh refinement that could be achieved.

Note that all meshes procured in this thesis project were checked using quality criteria, and if elements violated the quality criteria, those element and the adjacent regions were remeshed.

In these mesh studies the conductivity and thermal expansion values used are from a different pad friction material then the one used in the actual tests, see 3.2.1, but from the same manufacturer. At the time the mesh study started results for those properties were not available for the material used in the tests. Note that for the axisymmetric models the conductivity values has also not been adjusted properly.

B.4.1 Axisymmetric Models

This subsection contains the results of the mesh studies for the axisymmetric model. Note that there are no study specific for the axisymmetric thermomechanical model with multiple cycles, see Section 3.5.1.2. This is both because of time limitations, as that model takes longer time to set-up and simulate, but also because the results of the mesh study for the thermomechanical model with a single step, see Sections 3.5.1.1 and B.4.1.2 was deemed to sufficiently assess the mesh sensitivity for the axisymmetric thermomechanical model. That the ”ultimate model” used a fine enough mesh was judged by comparing the results after one cycle with that of the single cycle model.

B.4.1.1 Thermal Half-Disc

The results of the mesh study of the thermal axisymmetric half-disc model, see Section 3.4.1, can be seen below in Tables B.6 and B.7. For this model both a fixed time incrementation of 0.1 s and a DELTMX value of 1 °C were tested. For the former there will be 400 increments, for the latter the model takes between 635 and 655 increments.

Table B.6: Max temperature values for the mesh study of the axisymmetric thermal model. For each target element side length a simulation was done with a fixed time incrementation and one with a specified DELTMX value. The temperatures extracted to check convergence are the maximum nodal temperatures of pad and disc in the final time increment.

Target length [mm]	Time incr. [s]	DELTMX [°C]	Max disc temp. [°C]	Max pad temp. [°C]
0.5	0.1	-	536.923	511.728
0.5	-	1.0	536.936	511.767
0.75	0.1	-	536.913	511.730
0.75	-	1.0	536.954	511.770
1.0	0.1	-	536.826	511.606
1.0	-	1.0	536.867	511.646
1.5	0.1	-	536.595	511.346
1.5	-	1.0	536.636	511.386
2.0	0.1	-	536.019	511.333
2.0	-	1.0	536.060	511.372
3.0	0.1	-	536.670	511.015
3.0	-	1.0	536.718	511.055
5.0	0.1	-	545.746	518.433
5.0	-	1.0	545.792	518.480

Table B.6 shows the maximum temperatures for pad and disc. Note that the temperatures are nodal, which means that they are not averaged over the element.

Table B.7: Mean temperature values for the mesh study of the axisymmetric thermal model. For each target length a simulation was done with a fix time increment and one with a specified DELTMX value. The temperatures extracted to check convergence are the mean nodal temperatures of the contact surfaces on the pad and disc in the final time increment.

Target length [mm]	Time incr. [s]	DELTMX [°C]	Mean disc temp. [°C]	Mean pad temp. [°C]
0.5	0.1	-	483.755	460.022
0.5	-	1.0	483.785	460.051
0.75	0.1	-	483.444	460.683
0.75	-	1.0	483.473	460.712
1.0	0.1	-	483.043	460.240
1.0	-	1.0	483.072	460.269
1.5	0.1	-	481.340	459.437
1.5	-	1.0	481.370	459.466
2.0	0.1	-	482.465	455.727
2.0	-	1.0	482.495	455.756
3.0	0.1	-	482.439	459.331
3.0	-	1.0	482.469	459.360
5.0	0.1	-	482.468	450.770
5.0	-	1.0	482.501	450.802

Table B.7 shows the mean nodal temperatures of the pad and disc contact surface.

From the results in Tables B.6 and B.7 we can firstly note that the results did not differ greatly depending on if the fixed time incrementation or the DELTMX value was used.

We can also note that the maximum temperatures have more or less converged from a target length of 3 mm or less, whilst the mean temperatures have converged from a target length of 1 mm.

B.4.1.2 Thermomechanical

The results of the mesh study of the thermomechanical axisymmetric half-disc model of a single cycle, see Section 3.5.1.1, can be seen below in Tables B.8 and B.9 for the temperature and in Tables B.10 and B.11 for the wear depth. For this model two DELTMX values are tested, 1 °C and 10 °C, the former takes 426 to 428 increments and the latter takes 845 to 876 increments for analysis of the 40 s brake application.

Table B.8 shows the max nodal temperatures of the pad and disc, whilst Table B.9 shows the mean nodal temperatures of the contact surfaces.

Table B.10 shows the max wear depth of the pad and disc contact surface in the axial direction, whilst Table B.11 shows the mean wear depth of the contact surfaces in the axial direction.

Table B.8: Max temperature values for the mesh study of the axisymmetric thermomechanical model. The temperatures extracted to check convergence are the maximum nodal temperatures of pad and disc in the final time increment.

Target length [mm]	DELTMX [°C]	Max disc temp. [°C]	Max pad temp. [°C]
0.5	1.0	654.702	635.556
0.5	10.0	654.602	635.449
0.75	1.0	650.890	631.725
0.75	10.0	650.789	631.618
1.0	1.0	654.365	635.079
1.0	10.0	654.256	634.971
1.5	1.0	653.350	633.936
1.5	10.0	653.246	633.828
2.0	1.0	651.319	631.779
2.0	10.0	651.215	631.683
3.0	1.0	647.864	627.888
3.0	10.0	647.750	627.765
5.0	1.0	648.221	628.715
5.0	10.0	648.134	628.623

Table B.9: Mean temperature values for the mesh study of the axisymmetric thermomechanical model. The temperatures extracted to check convergence are the mean nodal temperatures of the contact surfaces on the pad and disc in the final time increment.

Target length [mm]	DELTMX [°C]	Mean disc temp. [°C]	Mean pad temp. [°C]
0.5	1.0	494.732	433.827
0.5	10.0	494.675	433.791
0.75	1.0	489.930	433.088
0.75	10.0	489.872	433.0478
1.0	1.0	492.074	435.235
1.0	10.0	492.0188	435.197
1.5	1.0	491.081	432.319
1.5	10.0	491.025	432.281
2.0	1.0	480.797	423.077
2.0	10.0	480.746	423.043
3.0	1.0	483.974	423.204
3.0	10.0	483.921	423.170
5.0	1.0	483.543	423.923
5.0	10.0	483.487	423.889

Table B.10: Maximum accumulated wear values for the mesh study of the axisymmetric thermomechanical model. The wear values are the maximum nodal CWEAR values in the axial direction of pad and disc in the final time increment.

Target length [mm]	DELTMX [°C]	Max disc wear [µm]	Max pad wear [µm]
0.5	1.0	0.247610	20.4306
0.5	10.0	0.247560	20.4367
0.75	1.0	0.279102	19.6425
0.75	10.0	0.279076	19.6478
1.0	1.0	0.299656	20.3195
1.0	10.0	0.299653	20.3257
1.5	1.0	0.314723	20.0660
1.5	10.0	0.314736	20.0724
2.0	1.0	0.323921	19.7039
2.0	10.0	0.323949	19.7106
3.0	1.0	0.325056	18.8098
3.0	10.0	0.325083	18.8815
5.0	1.0	0.342040	20.0064
5.0	10.0	0.342066	20.0119

Table B.11: Mean accumulated wear values for the mesh study of the axisymmetric thermomechanical model. The wear values are the mean nodal CWEAR values in the axial direction of the contact patches of pad and disc in the final time increment.

Target length [mm]	DELTMX [°C]	Mean disc wear [µm]	Mean pad wear [µm]
0.5	1.0	0.154243	7.86963
0.5	10.0	0.154205	7.87297
0.75	1.0	0.167707	7.64908
0.75	10.0	0.167683	7.65226
1.0	1.0	0.174915	7.86357
1.0	10.0	0.174902	7.86701
1.5	1.0	0.178283	7.69287
1.5	10.0	0.178282	7.69639
2.0	1.0	0.170947	7.23754
2.0	10.0	0.170944	7.24097
3.0	1.0	0.182580	7.02955
3.0	10.0	0.182583	7.03260
5.0	1.0	0.184634	7.38736
5.0	10.0	0.184642	7.39029

From Tables B.8, B.9, B.10, and B.11 we can see that again the change in the time incrementation/DELTMX value has little effect on the accuracy of the results (for this case). In terms of the mesh sensitivity we note relative convergence from 1.5 mm onwards, besides a little dip for 0.75 mm, whilst for the wear depth it does not converge completely (in relative terms) for the disc. The pad wear is relatively stable from 1 mm onwards besides a slight dip at 0.75 mm.

After one cycle, with the same parameters including wear scaling factors, the ultimate model with a target size of 1 mm has a maximum disc temperature of 657 °C and a maximum pad temperature of 637 °C. The mean disc temperature after one cycle is 490 °C, and for the pad it is 435 °C. The mean pad wear was approximately 6.97 µm, the max pad wear was 17.6 µm, and the max disc wear was 0.369 µm. The discrepancies in results compared to the single cycle model are likely due to the wear scaling factors being extrapolated exponentially for $T > 500$ °C for the ultimate model, whilst the single cycle model has linear interpolation between the extrapolated values which causes an overestimation, see Figure B.1 in Appendix B.1.1. If the single cycle model overestimates the wear for high temperatures that could lead to less pronounced hot-banding, and thus a lower maximum temperature than in the multiple cycle model.

B.4.1.3 modeFRONTIER Thermal Model

In this mesh study some parameters were different than previously stated. The gap conductance in the splines were set to 1 mW/(mm^{2}K). The values of the thermal conductivity, the specific heat and the density where all taken from [10].

The ”used” target length which is referred to in Tables B.12 and B.13 is the mesh that was used in the modeFRONTIER thermal projects, see Section B.5.1, which was meshed with a target length of 1 mm on disc and pads, and a target length of 2 mm on the hub.

For this mesh study a DELTMX value of 10 °C was used for all simulations.

Table B.12: Max temperature values for the mesh study of the thermal modeFRONTIER model. The temperatures extracted to check convergence are the mean nodal temperatures of the inboard and outboard contact surfaces on the pad and disc in the final time increment.

Target length [mm]	Inb. disc [°C]	Inb. pad [°C]	Outb. disc [°C]	Outb. pad [°C]
0.5	553.503	528.397	553.501	528.396
1.0	553.477	528.361	553.482	528.371
Used	553.477	528.361	553.482	528.371
1.5	553.441	528.277	553.692	528.567
2.0	552.748	527.870	552.804	528.454
5.0	566.334	539.391	608.127	576.729

Table B.12 shows the maximum temperatures for pad and disc on both the inboard and outboard sides.

Table B.13: Mean temperature values for the mesh study of the thermal modeFRONTIER model. The temperatures extracted to check convergence are the mean nodal temperatures of the inboard and outboard contact surfaces on the pad and disc in the final time increment.

Target length [mm]	Inb. disc [°C]	Inb. pad [°C]	Outb. disc [°C]	Outb. pad [°C]
0.5	497.931	475.074	497.811	474.956
1.0	497.356	475.534	497.111	473.679
Used	497.356	475.534	497.111	473.680
1.5	496.605	474.748	497.347	474.720
2.0	495.428	473.747	496.622	473.658
5.0	496.346	468.995	495.172	473.219

Table B.13 shows the mean nodal temperatures of the pad and disc contact surface on both the inboard and outboard sides.

The results of the mesh study presented in Tables B.12 and B.13 shows that the axisymmetric thermal model with the hub has converged from a target length of about 1.5 mm. It is also worth noting that the ”used” model and that of the target length of 1.0 mm has the same values for all investigated outputs. This is indicative of the hub, and its mesh, having little effect on the results for the studied case, especially when the results are temperature values on the contact surfaces, far from the splines and hub. Therefore it is advisable to have a coarser mesh on the hub if it is included so one saves on computational time.

B.4.2 3D-Models

B.4.2.1 Thermomechanical

The results of the mesh study of the thermomechanical 3D half-disc model of a single cycle, see Section 3.5.2.1, are can be seen below in Tables B.14, B.15, B.16 and B.17. As previously stated, this model was only tested using the DELTMX value of 10 °C.

Table B.14 shows the max nodal temperatures of the pad and disc, whilst Table B.15 shows the mean nodal temperatures of the contact surfaces. Table B.16 shows the max wear depth of the pad and disc, whilst Table B.17 shows the mean wear depth of the pad and disc. In Table B.18 the wall clock simulation time is listed for each target length.

Table B.14: Max temperature values for the mesh study of the thermomechanical 3D-model. The temperatures extracted to check convergence are the maximum nodal temperatures of pad and disc in the final time increment.

Target length [mm]	DELTMX [°C]	Max disc temp. [°C]	Max pad temp. [°C]
5.0	10.0	657.164	640.347
6.0	10.0	648.814	634.598
7.0	10.0	644.857	632.264
8.0	10.0	642.685	629.248
10.0	10.0	635.703	623.844
12.0	10.0	635.830	623.473
15.0	10.0	633.084	605.985

Table B.15: Mean temperature values for the mesh study of the thermomechanical 3D-model. The temperatures extracted to check convergence are the mean nodal temperatures of the contact surfaces on the pad and disc in the final time increment.

Target length [mm]	DELTMX [°C]	Mean disc temp. [°C]	Mean pad temp. [°C]
5.0	10.0	491.493	474.347
6.0	10.0	487.161	464.443
7.0	10.0	482.652	462.154
8.0	10.0	482.105	452.321
10.0	10.0	495.673	454.519
12.0	10.0	487.091	443.326
15.0	10.0	471.736	416.375

Table B.16: Maximum accumulated wear values for the mesh study of the thermomechanical 3D-model. The wear values are the maximum nodal CWEAR values in the axial direction of pad and disc in the final time increment.

Target length [mm]	DELTMX [°C]	Max disc wear [µm]	Max pad wear [µm]
5.0	10.0	0.350740	21.4072
6.0	10.0	0.375056	21.3803
7.0	10.0	0.348870	21.4724
8.0	10.0	0.368085	19.8623
10.0	10.0	0.325832	19.1539
12.0	10.0	0.332067	18.4660
15.0	10.0	0.310018	16.6443

Table B.17: Mean accumulated wear values for the mesh study of the thermomechanical 3D-model. The wear values are the mean nodal CWEAR values in the axial direction of the contact patches of pad and disc in the final time increment.

Target length [mm]	DELTMX [°C]	Mean disc wear [µm]	Mean pad wear [µm]
5.0	10.0	0.186963	8.42989
6.0	10.0	0.183244	7.92171
7.0	10.0	0.179958	7.61623
8.0	10.0	0.179546	7.22424
10.0	10.0	0.193044	7.05234
12.0	10.0	0.189566	6.54745
15.0	10.0	0.176217	5.59929

Table B.18: Wall clock simulation time for the mesh study of the thermomechanical 3D-model. All analyses were run remotely on a hpc-cluster using 4 CPUs.

Target length [mm]	Wall clock time [d-hh:mm:ss]
5.0	2-23:06:00
6.0	1-08:34:00
7.0	0-20:12:00
8.0	0-15:51:00
10.0	0-09:47:00
12.0	0-06:25:00
15.0	0-05:33:00

The results of the mesh study of the thermomechanical 3D-model shown in Tables B.14, B.15, B.16 and B.17 show that mesh convergence has not been met. Both the maximum and the mean temperatures in the disc and pad increase greatly as the mesh target size decreases. Both the maximum and mean accumulated pad wear seem to converge, but the maximum and mean accumulated disc wear fluctuate as the mesh target size decreases. All analyses were run remotely on a hpc-cluster using 4 CPUs, as discussed in Section 3.1. This relatively small number of CPUs imposed limitations on the the mesh study. Due to the considerable wall clock simulation time of the finer meshes, highlighted in Table B.18, it was not possible to continue the mesh study with refinements smaller than the tested target size of 5 mm. The analysis of the thermomechanical 3D-model was therefore simulated with a mesh seed target size of 5 mm.

B.5 modeFRONTIER

B.5.1 Thermal Material Properties

In our optimisation scheme we wanted to fit parameters using the thermal axisymmetric models. In early iterations the symmetric model with only half the disc and one pad was used. In the later iterations the version with the hub was used, see Figure 3.2.

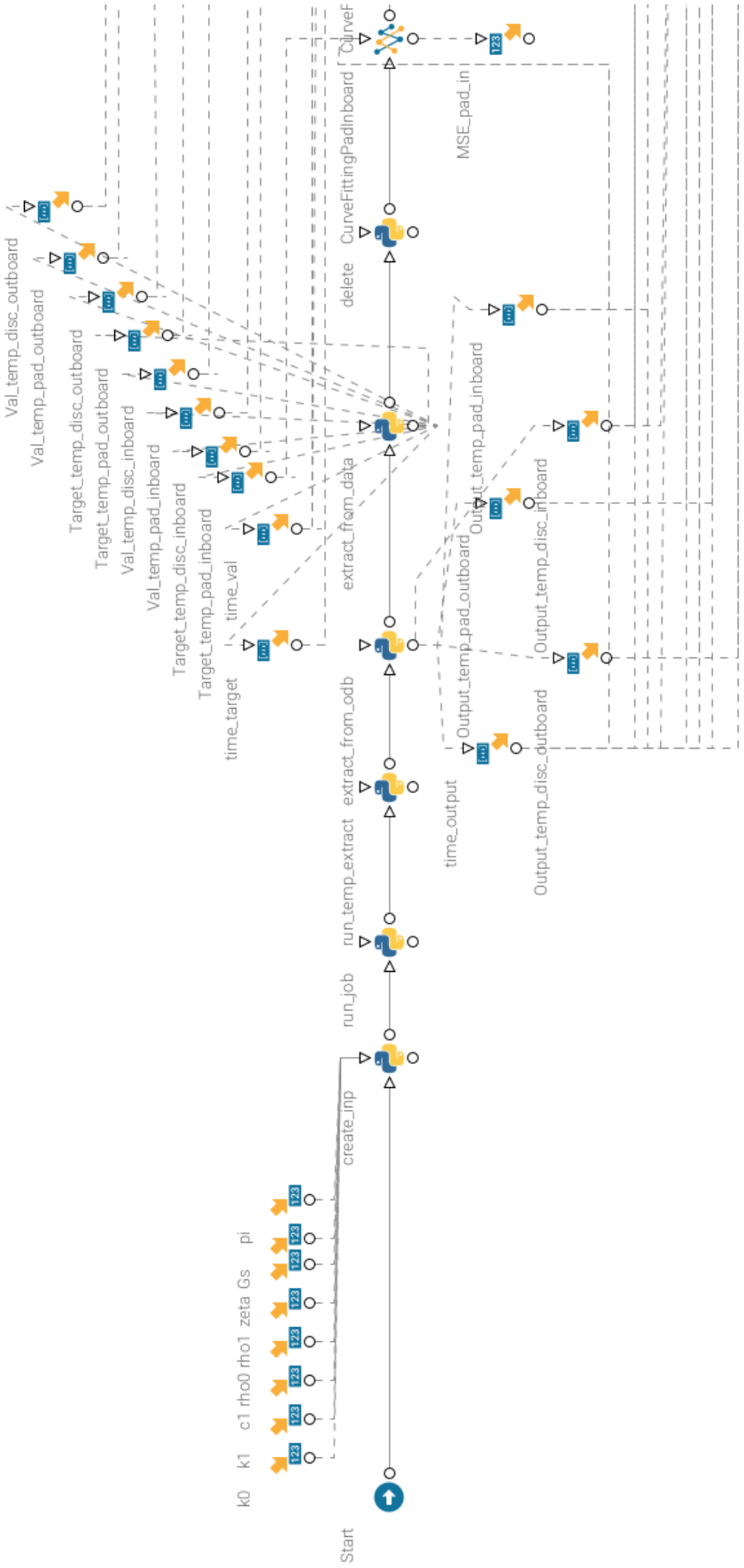

Figure B.8: *First half of the modeFRONTIER project with the thermal material properties.*

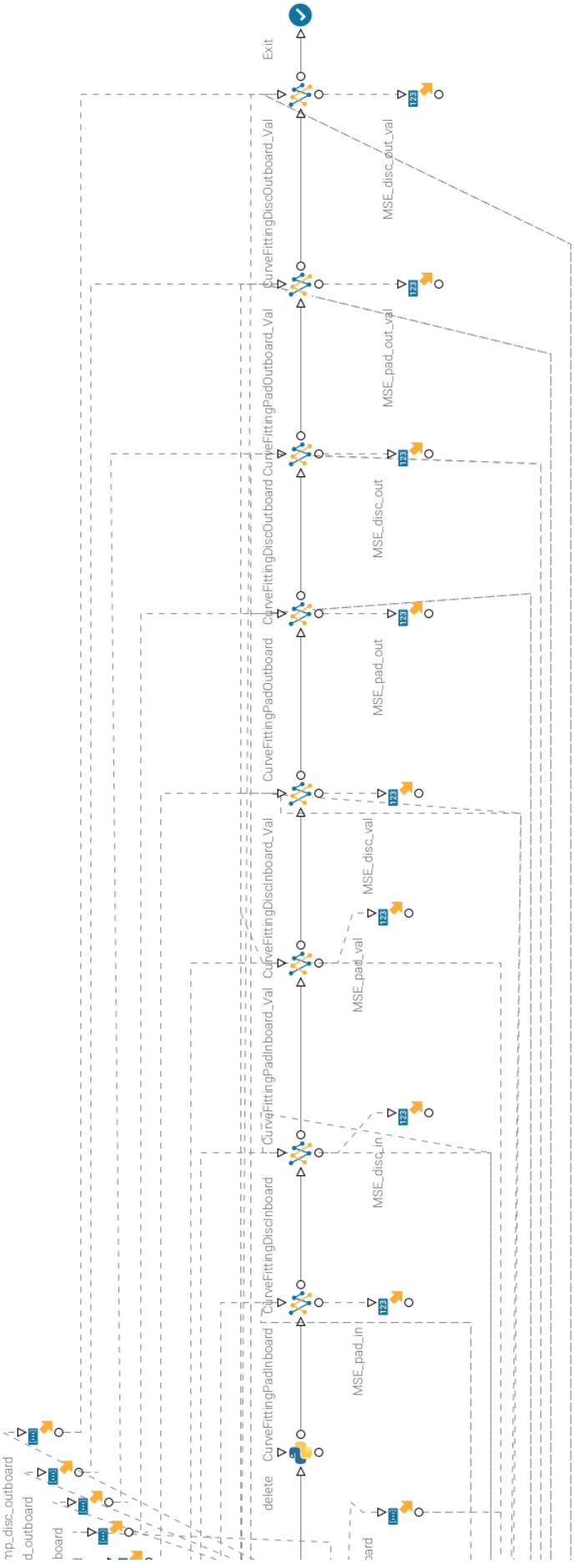

Figure B.9: *Second half of the modeFRONTIER project with the thermal material properties.*

The two final projects had a specific focus on the conductivity of the pads, with the error when comparing with temperature measurements in the pad being the objectives of the optimisation. The workflow for one of them can be seen in Figures B.8 and B.9. The inputs of this project are *k0*, *k1*, *c1*, *ρ0*, *ρ1*, *zeta*, *Gs* and *pi*. The thermal conductivity of the pad material is assumed to vary linearly with *k0* being the value at room temperature, whilst *k1* is the slope. This project was also set-up before it was realised that the conductivity should have been reduced in axisymmetric models, which affected the implementation. In this project measured values of c_p was available up to about 140 °C, see Section B.1.4, therefore those values were used and *c1* was added as the slope for higher temperatures. *ρ0* and *ρ1* were added as density properties, see Section B.1.4. *ρ0* was only varied between the maximum and minimum values of the density as given by the manufacturer. *zeta* is the parameter ζ that determines the mix between a constant pressure distribution and a constant wear distribution, see Section 3.3.1. *Gs* is the gap conductance at the splines, see Figure B.5, and *pi* was an adjustment factor that changed how much of the torque was added from the outboard or inboard side (i.e. if the clamp force/heat flux is greater on one side than the other). *Gs* and *pi* was parameters and not variables, meaning that they were not varied within a "run". *Gs* was either set to 0.001125 mW/(mm^{2}K) or 1.125 mW/(mm^{2}K), whilst *pi* was set to 1 (which corresponded to even force application). The other project had the same inputs, but had also added an input that the clamp force could decrease linearly with time, the additional input F is the clamp force at the end of the cycle.

The inputs were specified for certain ranges for example *c1* was only allowed to be positive and *k1* was only allowed to be negative. These are assumptions that may or may not be correct.

Note that varying the force also leads to a linear amplitude for the heat fluxes, but we know that for the disc crack tests that the heat fluxes should be constant since the torque is kept constant, see Section 3.2.1. Still the results from this study is interesting from an academic perspective.

In Section D.1 two runs of the former project with constant clamp force are presented, one with *Gs*= 0.001125 mW/(mm^{2}K) and one with *Gs*= 1.125 mW/(mm^{2}K). Additionally one run of the latter project with linearly varying clamp force/heat fluxes with *Gs*= 1.125 mW/(mm^{2}K) is presented.

Observe that for different values of *k0* and *k1*, and thus of $k_{t,p}(T)$, the value of the gap conductance between disc and pad was calculated per equation (B.30), and added to the surface interaction between pad and disc in the input file.

The workflow in modeFRONTIER, see Figures B.8 and B.9, was constructed using Python nodes which called on Python scripts. The first node always contained a script for creating the input file to Abaqus. That script added together parts of the original .inp-file created in ANSA with new lines that were dependent on the input parameters of the optimisation.

In the next Python node the .inp-file is sent to the cluster via a terminal, and it runs the command in the foreground. The Python node thereafter contains a script that runs another script in a terminal, which scans the .odb-file and picks out the nodes closest to

the measurement points and writes their temperature values to a .csv-file. The reason why it is a script that calls on another script is because reading the .odb-file requires Abaqus specific packages, and thus the extraction script needs to be ran in the terminal with *abaqus python*.

After this, there are two Python nodes which both contain scripts that reads .csv-files. The former reads the .csv-file that was just constructed from the FE-simulation, whilst the latter reads two .csv-files of the measurement data, with one being used as training data and one as validation data with a 90%/10%-split. The training and validation data is randomised, and taken from the measurements of the disc and pad inboard and outboard temperatures. The cycles that were included were 11-20, 51-60 and 91-100, see Section 3.2.1. The reason why no later cycles were included was because for later cycles the wear of the pads have caused a significant change of the position of the measurement points relative to the friction surface, thus they are incomparable with a thermal model.

The last Python node contained a script that deletes any file in the directory that we were not interested in keeping. After the Python nodes followed curve-fitting nodes for fitting our outputs from the FE-simulation to target data. There were eight different curve-fitting nodes, one for training and one for validation for each of the four measurement points. From these curve-fitting nodes we take out the mean square error (MSE) of the fit, and the objectives of the optimisation are then defined as minimising the MSE of the fits to the training data.

Note that we had a total of 30 cycles included. That means that for each thermocouple there are 30 different temperature values for each point in time, all of which will give an error when compared to the simulation. The minimum error which the modeFRONTIER studies can give is thus limited by the variance in the temperature measurements for the different cycles.

The optimisation will also be affected by simplifications, assumptions and errors in the modelling. The optimisation simulations required short simulation times, hence a thermal axisymmetric model was used. The mesh used had a target length of 1 mm on the pads and disc and 2 mm on the hub, and the maximum time increment allowed was 0.1 s with a maximum temperature change of 10 °C. It was verified that the mesh was sufficiently fine for our purpose, see Section B.4.1.3.

B.5.2 Wear

In early tests of the multiple cycles model, see Section 3.5.1.2, it was noted that when using the temperature dependent wear scaling factors the average wear was much less than what was expected when comparing to braking tests. When running a simulation of 10 cycles it was found that the accumulated pad wear was approximately 30 % of the measured wear.

Something worth noting is that these early tests were performed with material properties having preliminary values, see Section B.1.4. In particular the specific heat of the pad material was much greater than what it should have been, which in turn would cause

lower temperatures in the pad, and thus less wear. With the finally used properties the average wear after 10 cycles was 34% of the measured wear for 10 cycles.

To investigate this discrepancy a series of modeFRONTIER projects were initiated to see how changes of the wear scaling factors influences the average wear of the pad under the first 10 cycles of the test. The studies were:

I. To have a constant $k_{w,p}$.
II. To scale up the values of $k_{w,p}(T)$ and $k_{w,d}(T)$ by a factor.
III. To fit a curve $k_{w,p}(T) = a + c \cdot b^{T/100}$.

The reason why it is 10 cycles and not one or 500 are that we want to make sure that it is a sufficient number of cycles to be representative, if only one cycle is studied and a large hot band develops we can get a much larger wear value, whilst simulating more even more cycles would require more simulation time.

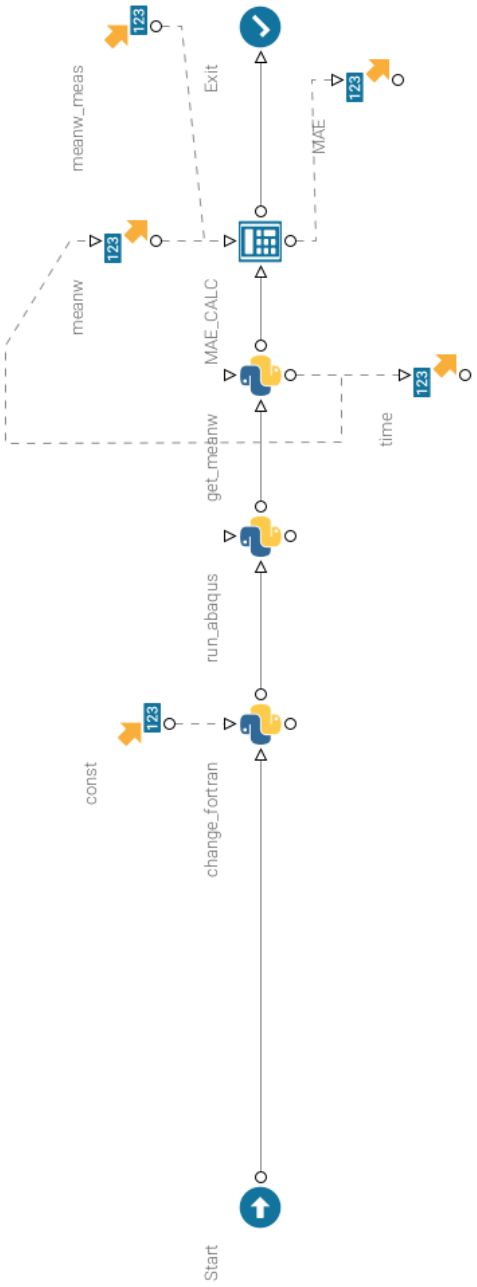

Figure B.10: *The workflow of the modeFRONTIER project with the constant wear scaling factor for the pads.*

The set-up in modeFRONTIER for these three different scenarios are very similar. Figure B.10 shows the workflow for the constant wear scaling factor project. The workflow consist of four nodes, three of which are Python nodes and the last which is a calculator node. The first Python node consist of a Python script which changes lines of the Fortran script to the inputs from the optimiser. The second Python node contains a script which runs the 10 cycles Abaqus input file. The third Python node retrieves last values of the time and the average wear value from a text file which the Fortran subroutine writes them to. The reason why the time is retrieved is so that it is noticeable if the simulation failed partway through. The calculator node calculates the mean absolute error between the final average wear of the simulation and the expected value, which the objective is to minimise.

For III we have three inputs and one output/objective, which means that there would be multiple possible optimal combinations. To monitor this we impose some constraints to make sure that the values of the fit at 100, 200, 300, 400 and 500 °C are not too different from the measured values of $k_{w,p}$. The parameter a was set to be equal or smaller to $k_{w,p}$ at $T = 100$ °C, whilst the ranges of b and c were tuned.

The reasoning for why parametric study II is tested is because in the calculation of the wear scaling factors a pressure value is used, and that pressure value should represent the average contact pressure, but in our calculations we used the constant pressure assumption. Since a constant torque was applied in the wear tests it is possible that over the course of the a cycle the pressure was decreased, thus a lower value should have been used in the calculations which would lead to higher wear scaling factors.

The number of iterations were as follows. Study I had two runs, the first with only five iterations and a second with 25 iterations. Study II had one run of 20 iterations. Study III had one run of 100 iterations, with the reason for the many more iterations being that there is a larger number of input variables.

For these studies the disc wear scaling factor was two times larger than they should have been. This was due to a misunderstanding of how the wear was measured in the wear tests, see Section 3.2.2. However, since it is the pad wear that was of interest and the disc wear is very small this should not affect the results of the fits more than marginally.

At a later stage it was also discovered that an initial slightly different method for preventing the adaptive meshing from doing anything in the reset steps had been done improperly, see Section 3.5.1.2. This was however mostly an issue at later cycles, so the results from the optimisation scheme should not have been affected greatly.

The issues mentioned above affected all project runs, except for the second with the constant wear scaling factor. That run also saw a change of the material properties to the values measured by the suppliers.

C

Additional Results for Multiple Cycles Model

C.1 With Constant Wear Scaling Factor

The following pictures and plots are the results for the simulation with constant $k_{w,p}$ as described in Section D.2.1.

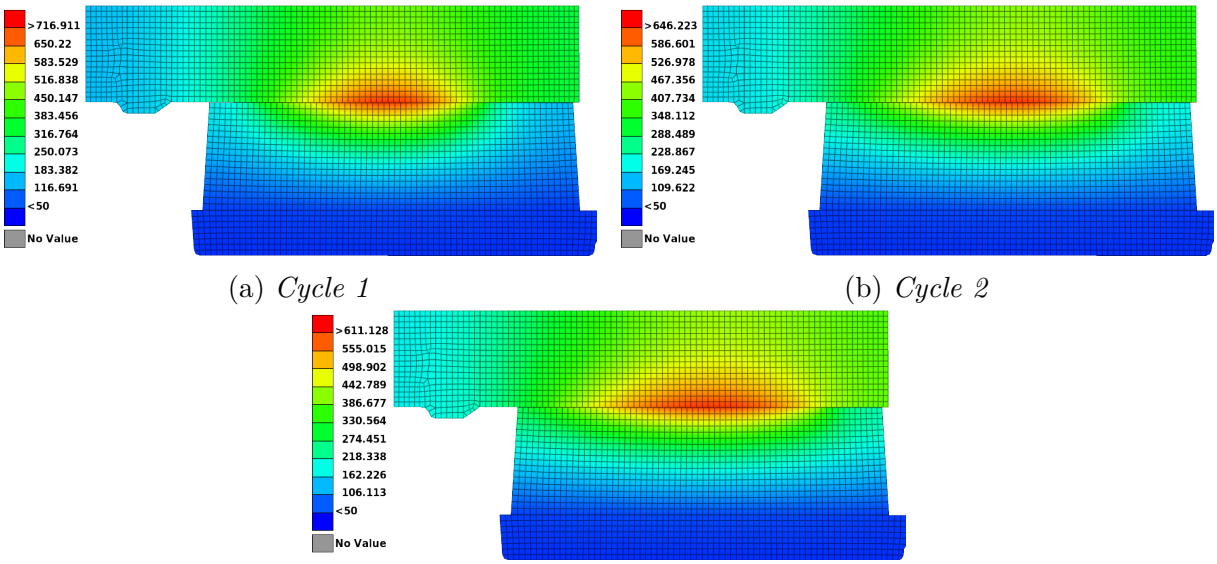

(a) *Cycle 1* (b) *Cycle 2*

(c) *Cycle 3*

Figure C.1: *Temperature at the end of the first three cycles*

Figure C.1 shows the temperature at $t = 40$ s for the first three cycles. Note that the maximum temperature decreases rapidly for each cycle, from 716.911 °C in cycle 1 to 646.223 °C in cycle 2 and to 611.128 °C in cycle 3.

The maximum temperature in cycle 1 is greater than it was for the temperature dependent $k_{w,p}$, for which it was equal to 691.260 °C, see Figure C.1a. This difference is likely due to the temperature dependent $k_{w,p}$ being very high for high temperatures, which reduces the hot-banding.

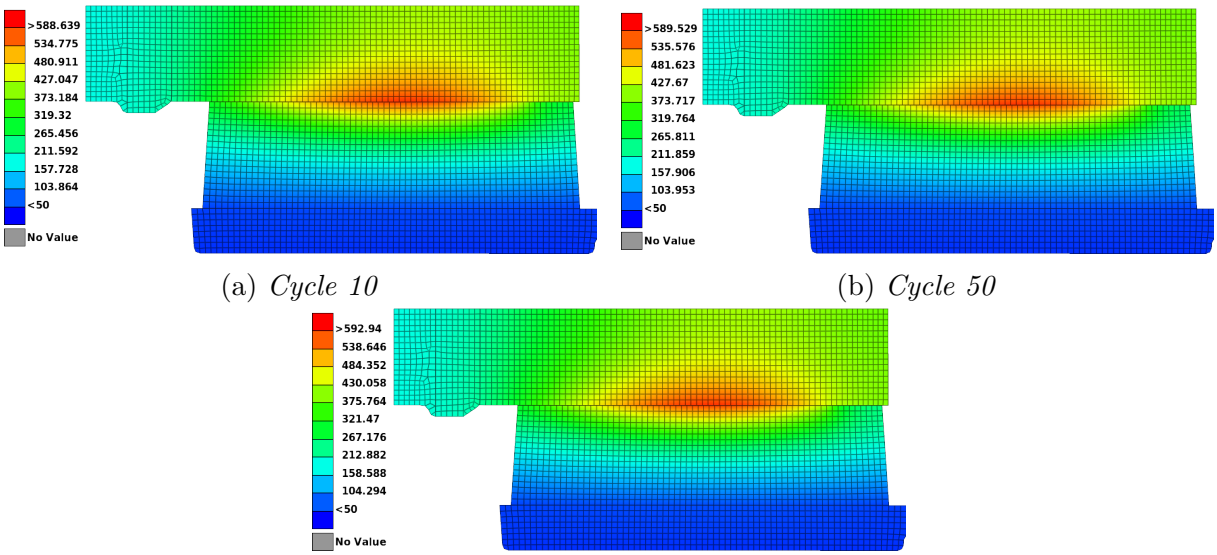

(a) *Cycle 10* (b) *Cycle 50*

(c) *Cycle 100*

Figure C.2: *Temperature at the end of the "intermediary" cycles 10, 50 and 100.*

In Figure C.2 the temperature is shown at cycles 10, 50 and 100. While the maximum temperature has decreased further for cycle 10 to 588 °C, it then increases to 590 °C in cycle 50 and further increases to 593 °C. This is unlike for the temperature dependent wear scaling factor where the maximum temperature continued to decrease in these intermediary cycles, see Figure 4.25.

Comparing Figures 4.25 and C.2 it is also clear that the high temperature is more localised for these intermediary cycles with the constant value of $k_{w,p}$, i.e. hot bands still form even if they are not as warm as in cycle 1.

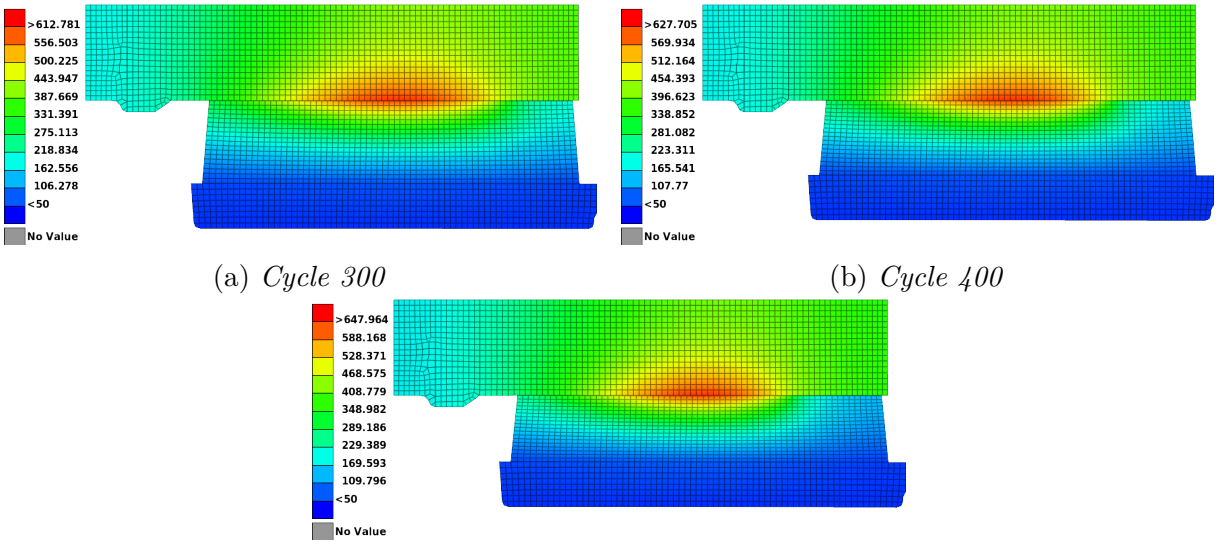

(a) *Cycle 300* (b) *Cycle 400*

(c) *Cycle 500*

Figure C.3: *Temperature at the end of the later "intermediary" cycles 300, 400 and 500.*

Figure C.3 shows the temperature for later cycles 300, 400 and 500. The maximum temperature continues to increase, to 613 °C in cycle 300, to 628 °C in cycle 400 and to 648 °C

in cycle 500.

Contrasting all other subfigures in Figures C.2 and C.3 with C.3c, it is clear that as the maximum temperature increases the warm parts (red in the figures) of the surface becomes more and more localised (covers less of the surface).

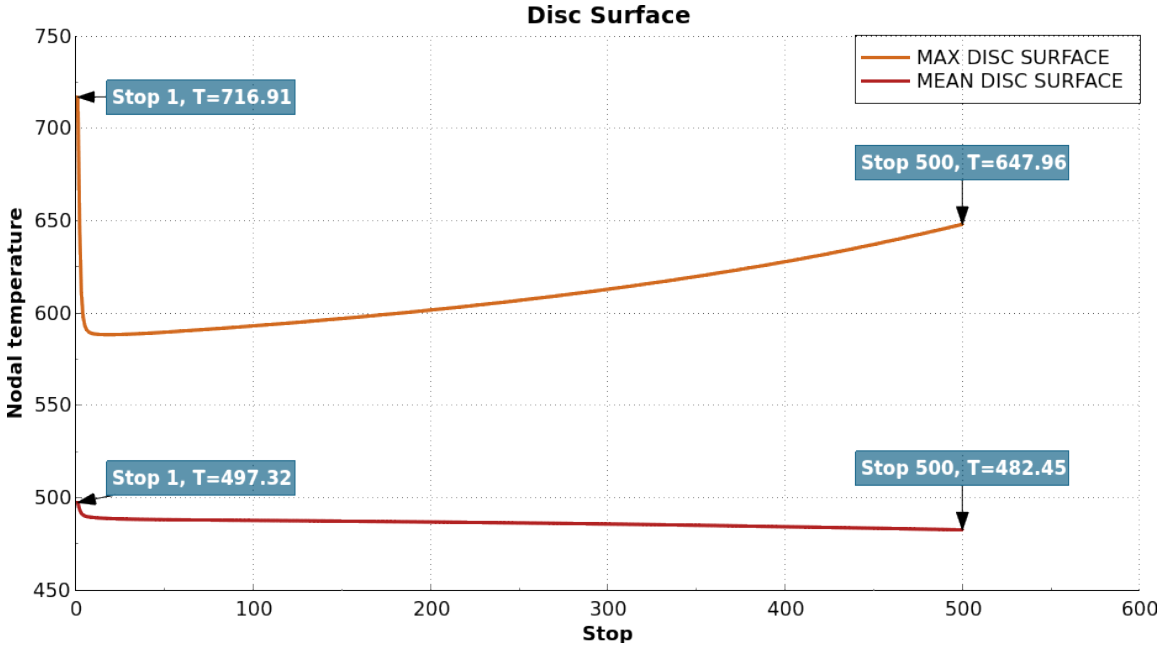

Figure C.4: *Final maximum and mean nodal temperature on the disc surface.*

Figure C.4 shows the final maximum and mean temperatures on the disc surface for each cycle. Like in Figure 4.26 the maximum temperature decreases rapidly for the initial cycles, but unlike for the temperature dependent $k_{w,p}$ it then increases notably after the initial decrease.

The mean temperature on the disc surface, see Figure C.4, decreases somewhat as it did in Figure 4.26.

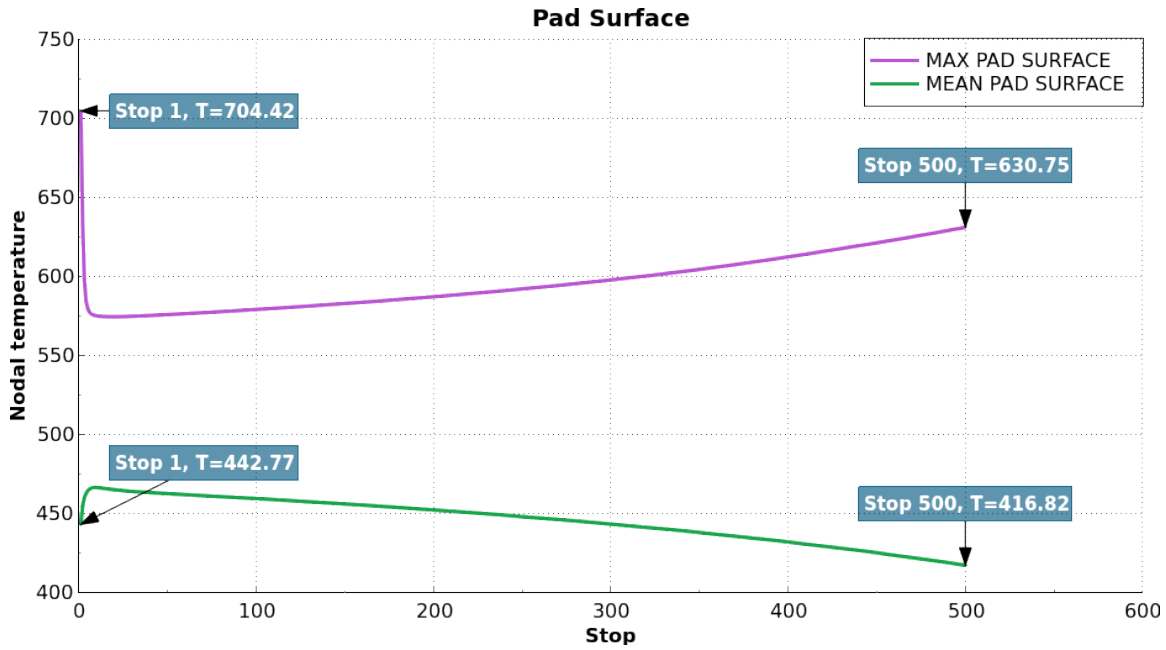

Figure C.5: *Final maximum and mean nodal temperature on the pad surface.*

The final maximum and mean temperatures on the pad contact surface are shown in Figure C.5. The maximum temperature follows the same trend as on the disc surface, see Figure C.4. The mean temperature however increases slightly at the start, as in Figure C.4, which is indicative of less hot-banding, but it the decreases which is an additional indicator of the hot band reforming.

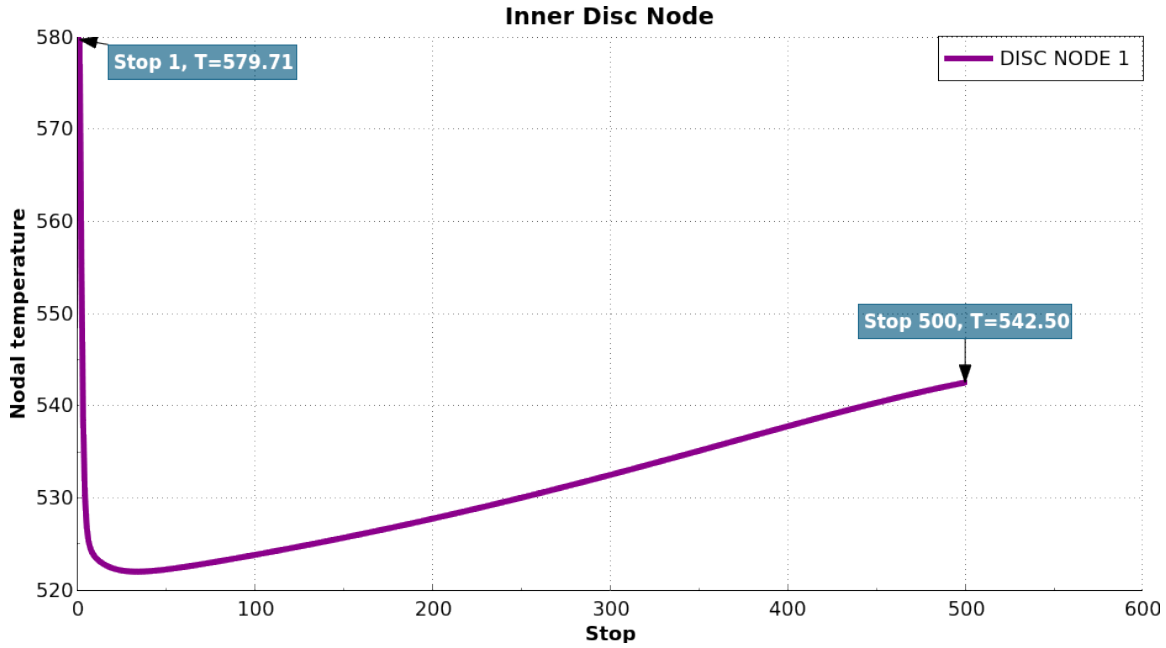

Figure C.6: *Final maximum and mean nodal temperature on an inner disc node. The node is at the start of the simulation approximately in the same placement as the measurement probe.*

Figure C.6 shows the final temperature for the node placed closest to the temperature sensor in the disc. It follows the same trend as on the disc surface, see Figure C.4. Unlike with the temperature dependent $k_{w,p}$ where the temperature became near constant at the

end, and was accurate compared to the measurements, if we compare the results in Figure C.6 with the measurement values in Figure 4.23 we see that the simulation consistently overestimates the temperature in the disc.

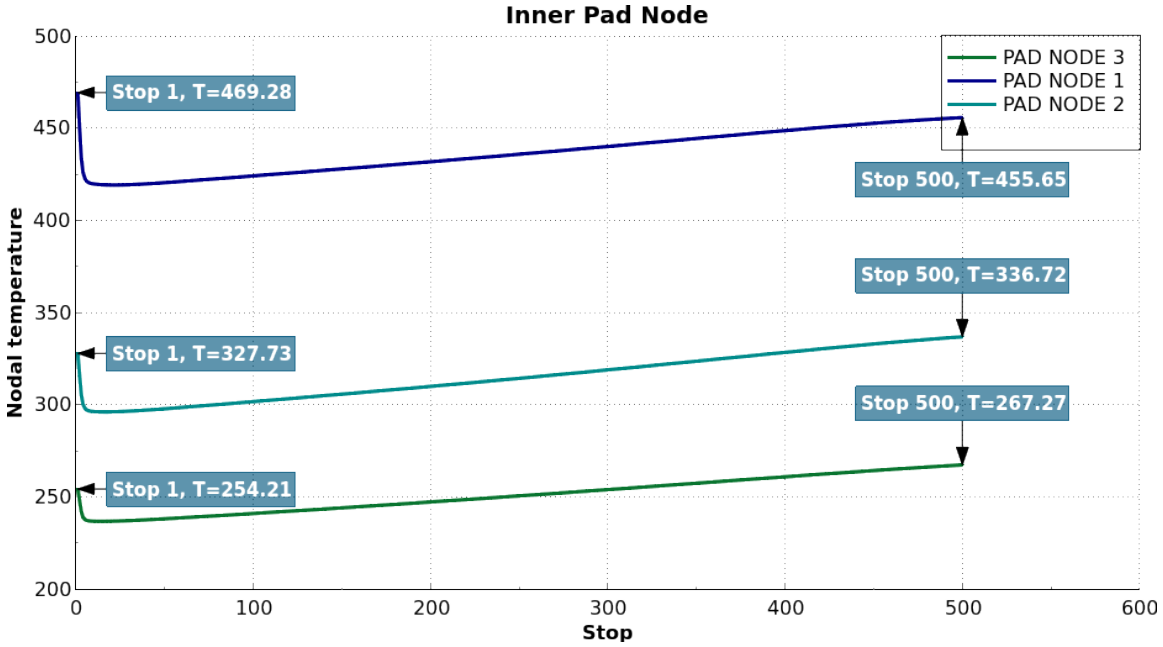

Figure C.7: *Final maximum and mean nodal temperature on inner pad node. The nodes are at the start at approximately the effective radius, with depths roughly of 3, 6, and* 9 mm

Figure C.7 shows the final temperature of nodes in the pad placed at the effective radius at initial depths of roughly 3, 6, and 9 mm. As noted in Section 4.2.1 the node initially placed at $\approx$ 9 mm (node 3) should be placed at an equal or greater depth than the measurement probe would be in the pad at any given time, and thus give a lower limit on the temperature at that point. A comparison with Figure 4.22 shows that node 3 (and node 1, at depth of 3.24 mm to 1.94 mm, and 2, at depth of 6.46 mm to 3.93 mm), gives higher temperatures than the measurements. Note however that measured temperatures in Figure 4.22 are only from the first 100 cycles.

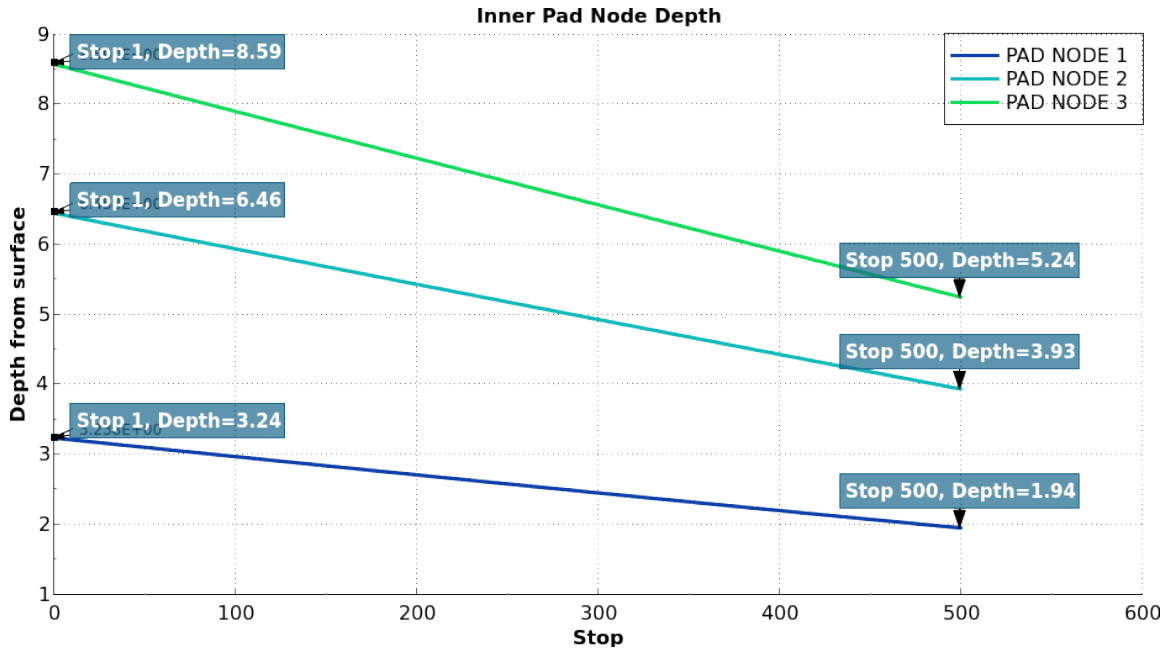

Figure C.8: *The depth of the nodes in the pads from which the results are extracted, and how that depth changes with time.*

The depths of the nodes 1, 2, and 3 in the pad over time are shown in Figure C.8.Note that whilst the measurement probe would be closest to node 3 at the start, it will be closer to node 1 at the end.

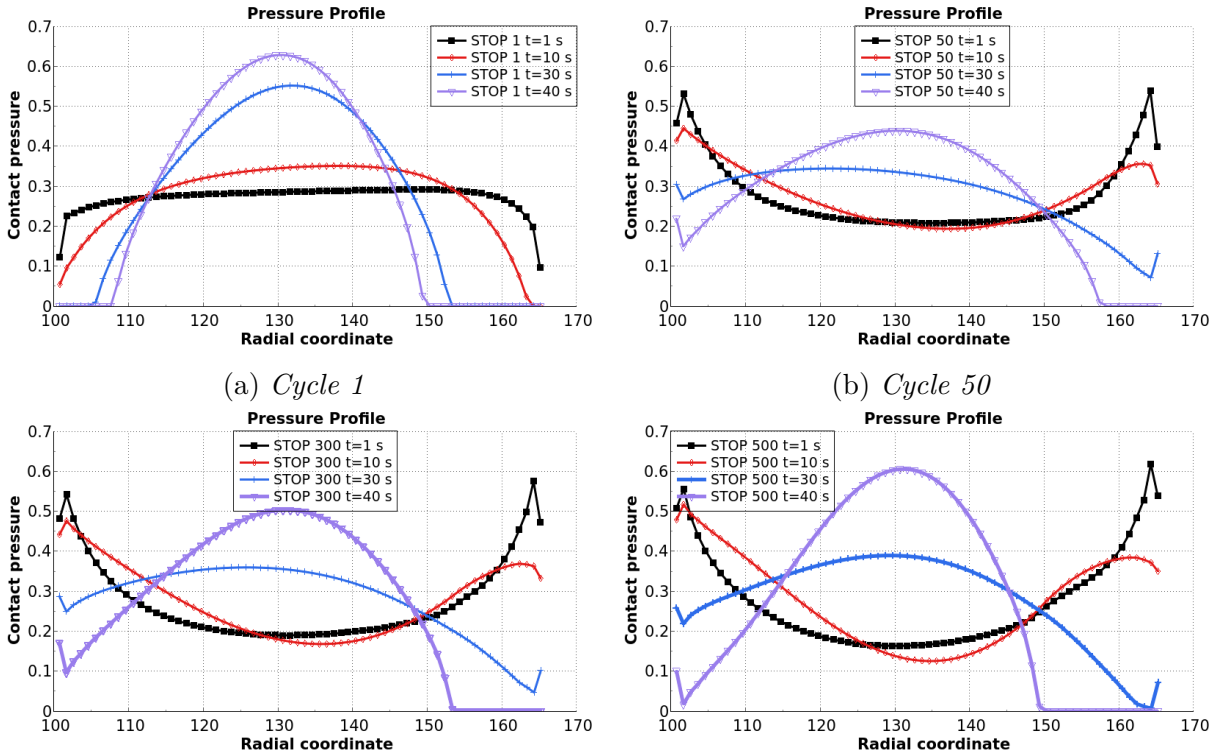

(a) *Cycle 1*

(b) *Cycle 50*

(c) *Cycle 300*

(d) *Cycle 500*

Figure C.9: *The contact pressure profiles at select times for a few select cycles.*

Figure C.9 shows the contact pressure distribution for cycles 1, 50, 300 and 500 for a

select times. Comparing between the different subfigures, and relating back to what was observed for Figure 4.32, several observations can be made. Firstly, we can observe that the hot-banding at $t = 40$ s increases from cycle 50, to 300 and furthermore to cycle 500. Secondly, once again at $t = 10$ s, the contact pressure increases in two radial regions, one inner and one outer, indicating that there are two "hot" bands that develop and then merge into one. Thirdly, the contact pressure distribution at $t = 1$ s is not the same for cycles 50, 300 and 500, with the valley becoming steeper, which indicates that the change in wear depth is not constant over the surface for each cycle.

C.2 With Increased Thermal Expansion

As a test to induce more hot-banding, results were calculated for temperature dependent $k_{w,p}$ values and the thermal expansion coefficient of the pad friction material being increased by a factor of four.

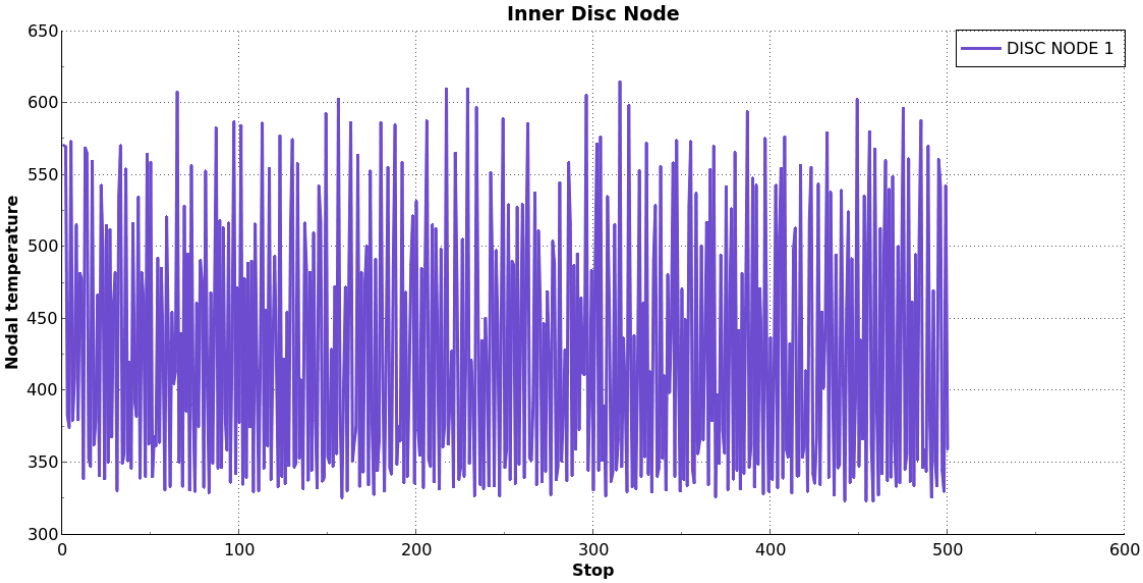

Figure C.10: *Final maximum and mean nodal temperature on an inner disc node. The node is at the start of the simulation approximately in the same placement as the measurement probe.*

Figure C.10 shows the final temperature for each cycle in the node closest to the thermocouple placement in the disc. Unlike in Figures 4.28 and C.6, the final temperature shows a lot of variance, as they did in the tests. This increased variance is indicative of hot bands forming, and with their radial position changing.

The mean of the accumulated wear on the pad surface was 5.165 mm, lower than with constant $k_{w,p}$ but higher than for the temperature dependent $k_{w,p}$ with lower α, see Figure 4.33.

D
modeFRONTIER Results

D.1 Thermal Material Properties

In this section the results of the modeFRONTIER projects for determining the thermal material parameters are presented.

For comparison,s the value of the thermal conductivity of the pad friction material as determined by the supplier is $k_{t,p}/k_t^* \approx 1.28$ at $T = 99$ °C.

D.1.1 Constant Clamp Force

The following tables outline the results of the modeFRONTIER runs where the thermal material properties were to be established, and the clamp force was set to be a constant value of 14.8 kN, see Section B.5.1. Two different runs where done, one with a gap conductance at the splines of 1.125 mW/(mm^{2}K) and one with a value of 0.001125 mW/(mm^{2}K). The full results of these runs, with normalised values, are presented in Tables D.7 and D.8.

Table D.1: Normalised values of the five iterations with lowest MSE for the inboard pad, with Gs= 1.125 mW/(mm^{2}K). The values are sorted from lowest training MSE for the inboard pad. The thermal conductivities are normalised by k_t^*, the specific heat by c_p^*, *rho0* by ρ^*, and *rho1* by α^*. All units are those used in Abaqus, some value should be multiplied by an exponent, see the second header from the bottom. All values are rounded to four significant digits.

Normed						MSE							
						Disc				Pad			
						Training		Validation		Training		Validation	
$[\cdot 10^6]$		$[\cdot 10^{-3}]$	$[\cdot 10^{-10}]$	$[\cdot 10^{-5}]$									
c1	*k0*	*k1*	*rho0*	*rho1*	*zeta*	In	Out	Out	In	In	Out	In	Out
2.481	0.8707	-1.207	2.209	0.6528	0.5415	2757	2535	2579	2930	348.7	340.7	339.0	350.9
2.467	0.8831	-1.249	2.187	1.255	0.7407	2628	2520	2567	2789	348.7	344.2	342.6	351.0
1.347	0.8437	-1.370	2.160	7.959	0.5142	3032	2590	2631	3229	348.7	340.7	339.0	350.9
5.774	0.8976	-1.391	2.240	10.00	0.4372	2901	2560	2603	3086	348.8	343.6	341.9	351.0
0.4572	0.9049	-1.570	2.225	7.712	0.09491	3416	2705	2744	3642	348.8	342.5	340.8	351.0

Table D.1 shows the five best iterations of the run with Gs= 1.125 mW/(mm^{2}K), where best means lowest MSE of the pad inboard temperature. Note that the values of the MSEs are large. Also observe that the values of the input parameter are quite varied and still give near identical MSE values.

Table D.2: Pearson correlation coefficients between some input and output variables for the modeFRONTIER project with constant clamp force and Gs= 1.125 mW/(mm^{2}K). All values are rounded to four significant digits.

Variables	Correlation coefficient
c1/MSE pad in	-0.1813
k0/MSE pad in	-0.6186
k1/MSE pad in	-0.3203
rho0/MSE pad in	-0.1739
rho1/MSE pad in	-0.1958
zeta/MSE pad in	0.06252
MSE disc in/MSE pad in	0.4552
k0/*k1*	-0.3320

Table D.2 shows the correlation between different inputs and outputs of this run. Observe that the correlation, or anti-correlation, shown is valid within the ranges of the input variables, and that the correlation may differ outside those ranges. From the results in Table D.2 one can observe that some inputs have a greater effect on the output than others. *k0* has a relatively strong anti-correlation with the MSE in the inboard pad, meaning that if the thermal conductivity is increased within the range, then the MSE tends to decrease. *k1* is the input with the second highest coefficient, in absolute terms. We can also note that *k0* and *k1* are anti-correlated meaning that the higher the value of *k0* is, the steeper the gradient of *k1* must be. The remaining inputs are only weakly (anti-)correlated with the MSE of the inboard pad, especially *zeta*, our mixed constant wear-pressure parameter ζ, has a low correlation coefficient of only ≈ 0.06 meaning that the value of *zeta* has little effect on the error.

Table D.3: Mean of normalised input variables for the 50 best simulations with regards to MSE for the inboard pad, for the modeFRONTIER project with constant clamp force and Gs= 1.125 mW/(mm^{2}K). The thermal conductivities are normalised by k_t^*, the specific heat by c_p^*, *rho0* by ρ^*, and *rho1* by α^*. All units are those used in Abaqus. All values are rounded to four significant digits.

Variables	Mean
c1	5448000
k0	0.9153
k1	-0.001432
rho0	$2.237 \cdot 10^{-10}$
rho1	$7.247 \cdot 10^{-5}$
zeta	0.2916

Table D.3 shows the normalised mean values of the input parameters for the 50 best iterations of this run. Note that this combination of inputs is not necessarily a combination which would give a low MSE, but rather it represent the aggregate of the combinations which do give a low MSE.

The values of *k0* and *k1* in Table D.3 would give a value of $k_t/k_t^* \approx 0.802$ at $T = 99$ °C.

Table D.4: Normalised values of the five iterations with lowest MSE for the inboard pad, with Gs= 0.001125 mW/(mm^{2}K). The values are sorted from lowest training MSE for the inboard pad. The thermal conductivities are normalised by k_t^*, the specific heat by c_p^*, *rho0* by ρ^*, and *rho1* by α^*. All units are those used in Abaqus, some value should be multiplied by an exponent, see the second header from the bottom. All values are rounded to four significant digits.

Normed						MSE							
						Disc				Pad			
						Training		Validation		Training		Validation	
[$\cdot 10^6$]		[$\cdot 10^{-3}$]	[$\cdot 10^{-10}$]	[$\cdot 10^{-5}$]									
c1	*k0*	*k1*	*rho0*	*rho1*	*zeta*	In	Out	Out	In	In	Out	In	Out
2.481	0.8707	-1.207	2.209	0.6528	0.5415	2759	2535	2580	2932	348.7	340.8	339.1	350.9
2.467	0.8831	-1.249	2.187	1.255	0.7407	2630	2520	2567	2791	348.7	344.3	342.6	351.0
1.347	0.8437	-1.370	2.160	7.959	0.5142	3035	2591	2632	3231	348.7	340.8	339.0	350.9
5.774	0.8976	-1.391	2.240	10.00	0.4372	2903	2561	2603	3088	348.8	343.6	342.0	351.0
0.4572	0.9049	-1.570	2.225	7.712	0.09491	3418	2706	2745	3645	348.8	342.5	340.8	351.0

Table D.4 shows the five best iterations of the run with Gs= 0.001125 mW/(mm^{2}K), where best means lowest MSE of the pad inboard temperature. If one compares the inputs and outputs with those in Table D.1 one finds that the only difference is slightly higher MSE values for the inboard and outboard measurements points in the disc.

Table D.5: Pearson correlation coefficients between some input and output variables for the modeFRONTIER project with constant clamp force and Gs= 0.001125 mW/(mm^{2}K). All values are rounded to four significant digits.

Variables	Correlation coefficient
c1/MSE pad in	-0.2174
k0/MSE pad in	-0.5589
k1/MSE pad in	-0.3488
rho0/MSE pad in	-0.2410
rho1/MSE pad in	-0.1668
zeta/MSE pad in	0.06188
MSE disc in/MSE pad in	0.4396
k0/*k1*	-0.3897

Table D.5 shows the correlation between inputs and outputs of this run. Comparing with Table D.2 the values differ only slightly, likely due to the different number of iterations and what values the optimiser chose for the inputs in the two runs.

The values of *k0* and *k1* in Table D.6 would give a value of $k_t/k_t^* \approx 0.793$ at $T = 99$ °C.

Table D.6: Mean of normalised input variables for the 30 best simulations with regards to MSE for the inboard pad, for the modeFRONTIER project with constant clamp force and Gs= 0.001125 mW/(mm^{2}K). The thermal conductivities are normalised by k_t^*, the specific heat by c_p^*, *rho0* by ρ^*, and *rho1* by α^*. All units are those used in Abaqus. All values are rounded to four significant digits.

Variables	Mean
c1	4967000
k0	0.9027
k1	-0.001388
rho0	$2.236 \cdot 10^{-10}$
rho1	$6.621 \cdot 10^{-5}$
zeta	0.3243

Table D.6 shows the average values of the inputs for the 30 iterations of this run that performed the best. Comparing with Table D.3 the results differ somewhat, but for *k0* and *k1*, which had larger effect on the MSE, the values are almost the same.

Table D.7 shows the 50 iterations with lowest MSE for the inboard pad of the run with Gs= 1.125 mW/(mm^{2}K) and constant clamp force.

Table D.7: Normalised values of the 50 iterations, out of 500, with lowest MSE for the inboard pad, with Gs= 1.125 mW/(mm^{2}K). The values are sorted from lowest training MSE for the inboard pad. The thermal conductivities are normalised by k_t^*, the specific heat by c_p^*, *rho0* by ρ^*, and *rho1* by α^*. All units are those used in Abaqus, some value should be multiplied by an exponent, see the second header from the bottom. All values are rounded to four significant digits.

Normed						MSE							
						Disc				Pad			
						Training		Validation		Training		Validation	
$[\cdot 10^6]$		$[\cdot 10^{-3}]$	$[\cdot 10^{-10}]$	$[\cdot 10^{-5}]$									
c1	*k0*	*k1*	*rho0*	*rho1*	*zeta*	In	Out	Out	In	In	Out	In	Out
2.481	0.8707	-1.207	2.209	0.6528	0.5415	2757	2535	2579	2930	348.7	340.7	339.0	350.9
2.467	0.8831	-1.249	2.187	1.255	0.7407	2628	2520	2567	2789	348.7	344.2	342.6	351.0
1.347	0.8437	-1.370	2.160	7.959	0.5142	3032	2590	2631	3229	348.7	340.7	339.0	350.9
5.774	0.8976	-1.391	2.240	10.00	0.4372	2901	2560	2603	3086	348.8	343.6	341.9	351.0
0.4572	0.9049	-1.570	2.225	7.712	0.09491	3416	2705	2744	3642	348.8	342.5	340.8	351.0
8.042	0.9500	-1.464	2.244	8.352	0.1996	2968	2575	2617	3159	348.8	345.9	344.2	351.1
7.225	0.9570	-1.438	2.259	5.542	0.1134	2992	2580	2622	3184	348.8	346.5	344.8	351.1
7.061	0.9346	-1.438	2.231	6.939	0.2766	2928	2566	2608	3115	348.8	335.6	333.9	350.8
2.915	0.8822	-1.256	2.210	1.792	0.6928	2654	2522	2569	2817	348.9	332.8	331.0	350.8
7.355	0.9371	-1.463	2.245	8.137	0.2368	2972	2576	2617	3163	348.9	333.4	331.6	350.8
7.448	0.9581	-1.525	2.264	8.567	0.1838	3007	2584	2625	3201	348.9	333.5	331.7	350.8
4.631	0.8244	-0.9181	2.197	0.7313	0.9050	2423	2516	2568	2563	348.9	355.1	353.6	351.5
5.974	0.9174	-1.454	2.231	7.758	0.1946	3071	2600	2641	3270	349.0	331.3	329.5	350.8
3.952	0.8919	-1.306	2.246	5.061	0.2850	2975	2576	2618	3167	349.0	355.3	353.8	351.5
3.952	0.8919	-1.306	2.246	5.061	0.2850	2975	2576	2618	3167	349.0	355.3	353.8	351.5
6.128	0.8915	-1.300	2.245	7.298	0.2032	3015	2586	2627	3210	349.0	355.1	353.6	351.6
7.299	0.9256	-1.378	2.258	7.752	0.1280	3034	2590	2632	3230	349.0	354.8	353.3	351.6
7.553	0.9489	-1.519	2.265	9.549	0.2447	2980	2577	2619	3171	349.1	328.9	327.0	350.9
7.904	0.8898	-1.310	2.276	8.457	0.1990	2989	2579	2621	3181	349.2	325.3	323.4	350.9
5.660	0.9348	-1.532	2.246	7.686	0.03012	3231	2645	2685	3443	349.2	325.9	324.0	351.0

Continued on next page

Normed						MSE							
						Disc				Pad			
						Training		Validation		Training		Validation	
$[\cdot 10^{6}]$		$[\cdot 10^{-3}]$	$[\cdot 10^{-10}]$	$[\cdot 10^{-5}]$									
c1	*k0*	*k1*	*rho0*	*rho1*	*zeta*	In	Out	Out	In	In	Out	In	Out
0	0.9082	-1.599	2.254	8.170	0.2627	3269	2657	2696	3484	349.3	324.8	322.9	351.0
8.586	0.8915	-1.300	2.245	7.298	0.2032	2958	2572	2614	3148	349.5	321.8	319.9	351.1
5.297	0.8907	-1.346	2.246	5.518	0.2447	3003	2583	2624	3196	349.5	321.4	319.5	351.1
7.553	0.9497	-1.519	2.249	7.644	0.1903	3005	2583	2625	3199	349.6	319.4	317.4	351.2
7.553	0.9496	-1.519	2.249	7.644	0.1903	3005	2583	2625	3199	349.7	319.2	317.2	351.2
7.062	0.9209	-1.454	2.231	7.758	0.2766	2970	2575	2617	3161	349.7	318.7	316.7	351.2
7.074	0.9323	-1.392	2.222	7.984	0.2674	2932	2567	2609	3120	349.8	368.6	367.3	352.7
7.556	0.9489	-1.519	2.239	7.644	0.2722	2943	2569	2611	3131	349.8	317.6	315.6	351.3
6.576	0.9689	-1.659	2.188	8.003	0.2285	3062	2598	2639	3260	349.9	316.0	313.9	351.4
2.564	0.8798	-1.338	2.208	2.499	0.5322	2829	2546	2590	3008	350.0	315.0	312.9	351.4
1.347	0.8983	-1.478	2.242	9.898	0.3480	3128	2615	2656	3332	350.0	372.9	371.6	353.1
0.6837	0.8866	-1.435	2.246	8.646	0.3738	3108	2610	2650	3311	350.1	373.2	372.0	353.1
7.553	0.9489	-1.519	2.249	7.644	0.2722	2939	2568	2611	3128	350.1	314.7	312.7	351.5
1.314	0.8638	-1.178	2.218	1.500	0.5600	2781	2538	2583	2956	350.3	375.9	374.7	353.4
0	0.9052	-1.627	2.252	9.075	0.2679	3297	2666	2705	3514	350.3	312.9	310.9	351.6
0	0.9052	-1.627	2.252	9.072	0.2679	3297	2666	2705	3514	350.3	312.9	310.8	351.6
7.014	0.9288	-1.360	2.224	7.709	0.2791	2911	2562	2605	3097	350.3	375.5	374.3	353.5
7.914	0.9489	-1.519	2.249	7.644	0.2722	2932	2567	2609	3119	350.5	310.7	308.6	351.8
8.111	0.8963	-1.331	2.276	7.548	0.3053	2887	2557	2600	3070	350.8	308.4	306.3	352.0
6.789	0.9288	-1.360	2.224	7.709	0.2452	2943	2569	2611	3132	350.8	381.1	379.9	354.2
1.460	0.8960	-1.478	2.242	9.898	0.1022	3362	2687	2726	3584	350.9	381.9	380.8	354.2
6.707	0.9490	-1.590	2.263	8.388	0.05035	3194	2634	2674	3403	350.9	307.4	305.3	352.1
7.225	0.9570	-1.438	2.259	8.646	0.1133	3034	2590	2632	3230	351.1	383.0	381.9	354.4
6.478	0.9461	-1.586	2.268	9.286	0.2421	3042	2593	2634	3239	351.1	306.0	303.9	352.2
7.293	0.9749	-1.610	2.199	4.103	0.03859	3114	2612	2652	3317	351.3	304.6	302.4	352.4
7.318	0.8938	-1.411	2.230	7.790	0.2223	3037	2591	2633	3234	351.7	301.8	299.7	352.7
6.037	0.8960	-1.478	2.242	9.898	0.3480	3014	2585	2627	3208	351.9	300.5	298.3	352.9
8.782	0.9347	-1.532	2.234	10.00	0.3754	2896	2559	2602	3081	352.0	300.1	298.0	352.9
6.139	0.8960	-1.478	2.242	9.898	0.3480	3011	2585	2626	3206	352.1	299.5	297.3	353.0
8.782	0.9347	-1.498	2.246	8.646	0.3738	2860	2552	2595	3042	352.2	298.6	296.4	353.2

Table D.8 shows the 30 iterations with lowest MSE for the inboard pad of the run with Gs= 0.001125 mW/(mm^{2}K) and constant clamp force.

Table D.8: Normalised values of the 30 iterations, out of 300, with lowest MSE for the inboard pad, with Gs= 0.001125 mW/(mm^{2}K). The values are sorted from lowest training MSE for the inboard pad. The thermal conductivities are normalised by k_t^*, the specific heat by c_p^*, *rho0* by ρ^*, and *rho1* by α^*. All units are those used in Abaqus, some value should be multiplied by an exponent, see the second header from the bottom. All values are rounded to four significant digits.

Normed						MSE							
						Disc				Pad			
						Training		Validation		Training		Validation	
$[\cdot 10^{6}]$		$[\cdot 10^{-3}]$	$[\cdot 10^{-10}]$	$[\cdot 10^{-5}]$									
c1	*k0*	*k1*	*rho0*	*rho1*	*zeta*	In	Out	Out	In	In	Out	In	Out
2.481	0.8707	-1.207	2.209	0.6528	0.5415	2759	2535	2580	2932	348.7	340.8	339.1	350.9
2.467	0.8831	-1.249	2.187	1.255	0.7407	2630	2520	2567	2791	348.7	344.3	342.6	351.0
1.347	0.8437	-1.370	2.160	7.959	0.5142	3035	2591	2632	3231	348.7	340.8	339.0	350.9
5.774	0.8976	-1.391	2.240	10.00	0.4372	2903	2561	2603	3088	348.8	343.6	342.0	351.0
0.4572	0.9049	-1.570	2.225	7.712	0.09491	3418	2706	2745	3645	348.8	342.5	340.8	351.0

Continued on next page

Normed						MSE							
						Disc				Pad			
						Training		Validation		Training		Validation	
$[\cdot 10^6]$		$[\cdot 10^{-3}]$	$[\cdot 10^{-10}]$	$[\cdot 10^{-5}]$									
c1	*k0*	*k1*	*rho0*	*rho1*	*zeta*	In	Out	Out	In	In	Out	In	Out
7.225	0.9570	-1.438	2.259	5.542	0.1134	2994	2581	2622	3186	348.8	346.5	344.8	351.1
2.915	0.8822	-1.256	2.210	1.792	0.6928	2656	2522	2569	2819	348.9	332.8	331.0	350.8
4.631	0.8244	-0.9181	2.197	0.7313	0.9050	2424	2516	2568	2565	348.9	355.1	353.6	351.5
3.952	0.8919	-1.306	2.246	5.061	0.2850	2977	2577	2619	3169	349.0	355.3	353.8	351.6
3.952	0.8919	-1.306	2.246	5.061	0.2850	2977	2577	2619	3169	349.0	355.3	353.8	351.6
6.128	0.8915	-1.300	2.245	7.298	0.2032	3017	2586	2628	3212	349.0	355.2	353.7	351.6
7.299	0.9256	-1.378	2.258	7.752	0.1280	3035	2591	2632	3232	349.0	354.9	353.4	351.6
7.904	0.8898	-1.310	2.276	8.457	0.1990	2991	2580	2622	3183	349.2	325.3	323.4	350.9
5.660	0.9348	-1.532	2.246	7.686	0.03012	3233	2646	2686	3445	349.2	325.9	324.0	351.0
8.586	0.8915	-1.300	2.245	7.298	0.2032	2960	2573	2615	3150	349.5	321.9	319.9	351.1
5.297	0.8907	-1.346	2.246	5.518	0.2447	3005	2583	2625	3198	349.5	321.4	319.5	351.1
2.564	0.8798	-1.338	2.208	2.499	0.5322	2831	2547	2591	3010	350.0	315.0	313.0	351.4
1.347	0.8983	-1.478	2.242	9.898	0.3480	3130	2616	2656	3334	350.0	372.9	371.7	353.1
0.6837	0.8866	-1.435	2.246	8.646	0.3738	3111	2611	2651	3313	350.1	373.3	372.0	353.1
1.314	0.8638	-1.178	2.218	1.500	0.5600	2783	2539	2583	2958	350.3	376.0	374.8	353.4
8.111	0.8963	-1.331	2.276	7.548	0.3053	2889	2558	2601	3073	350.8	308.5	306.3	352.0
1.460	0.8960	-1.478	2.242	9.898	0.1022	3364	2688	2727	3587	350.9	381.9	380.8	354.2
6.707	0.9490	-1.590	2.263	8.388	0.05035	3196	2635	2675	3406	350.9	307.4	305.3	352.1
7.225	0.9570	-1.438	2.259	8.646	0.1133	3036	2591	2632	3232	351.1	383.0	381.9	354.5
6.478	0.9461	-1.586	2.268	9.286	0.2421	3044	2593	2634	3241	351.1	306.0	303.9	352.2
7.293	0.9749	-1.610	2.199	4.103	0.03859	3116	2612	2653	3319	351.3	304.6	302.4	352.4
6.037	0.8960	-1.478	2.242	9.898	0.3480	3016	2586	2628	3210	351.9	300.5	298.3	352.9
8.782	0.9347	-1.532	2.234	10.00	0.3754	2898	2560	2602	3083	351.9	300.2	298.0	352.9
6.139	0.8960	-1.478	2.242	9.898	0.3480	3014	2586	2627	3208	352.1	299.6	297.4	353.0
8.782	0.9347	-1.498	2.246	8.646	0.3738	2862	2553	2596	3044	352.2	298.6	296.4	353.2

D.1.2 Linear Clamp Force

The following tables outline the results of the modeFRONTIER runs where the thermal material properties were to be decided, and the clamp force was set to vary linearly from 14.8 kN to an input value F, see Section B.5.1. The gap conductance in the splines was set to Gs= 1.125 mW/(mm^{2}K).

Table D.9: Normalised values of the five iterations with lowest MSE for the inboard pad. The values are sorted from lowest training MSE for the inboard pad. The thermal conductivities are normalised by k_t^*, the specific heat by c_p^*, *rho0* by ρ^*, and *rho1* by α^*. All units are those used in Abaqus, some value should be multiplied by an exponent, see the second header from the bottom. All values are rounded to four significant digits.

	Normed						MSE							
							Disc				Pad			
							Training		Validation		Training		Validation	
$[\cdot 10^{-3}]$	$[\cdot 10^6]$		$[\cdot 10^{-3}]$	$[\cdot 10^{-10}]$	$[\cdot 10^{-5}]$									
F	*c1*	*k0*	*k1*	*rho0*	*rho1*	*zeta*	In	Out	Out	In	In	Out	In	Out
11.67	6.071	1.014	-1.403	2.263	9.965	0.9012	1821	3488	3609	1836	348.8	338.2	336.5	350.9
12.47	0	1.050	-1.807	2.175	7.242	0.8319	1846	2901	2989	1903	348.8	341.1	339.4	350.9
11.61	2.098	1.219	-2.099	2.178	3.604	0.4824	1800	3264	3373	1828	348.8	341.9	340.2	351.0
11.78	6.515	1.014	-1.321	2.276	8.848	0.9217	1820	3481	3601	1835	348.8	348.9	347.3	351.2
11.74	6.430	1.014	-1.403	2.268	8.821	0.7462	1806	3364	3478	1828	348.8	334.9	333.1	350.8

Table D.12 shows the five iterations with lowest MSE for the inboard pad. Note that

there is some variance in the inputs parameters.

Table D.10: Pearson correlation coefficients between some input and output variables for the modeFRONTIER project with linear clamp force and Gs= 1.125 mW/(mm^{2}K). All values are rounded to four significant digits.

Variables	Correlation coefficient
c1/MSE pad in	0.3598
k0/MSE pad in	-0.6677
k1/MSE pad in	0.08270
rho0/MSE pad in	0.1813
rho1/MSE pad in	-0.1752
zeta/MSE pad in	0.07561
MSE disc in/MSE pad in	0.02547
k0/*k1*	-0.2481
F/MSE pad in	-0.1016
F/MSE disc in	0.4959
F/k0	-0.1225

Table D.10 shows the correlation between some input and output variables. As in Tables D.2 and D.5 with the constant force it is clear that *k0* is the input with the greatest correlation to the MSE in the pads. Unlike in those projects, the correlation coefficient between *k1* and the MSE is low, and the coefficient between the MSE of the inboard pad and inboard disc is near zero which indicates that there is little correlation.

The correlation coefficient of -0.1016 between F and the MSE for the inboard pad shows that having this reduction in the force, together with the other input parameters, does not mean a lower MSE for the pad. That the correlation coefficient for F and *k0* of -0.1225 shows that this reduction of force makes solutions with higher values of *k0* viable.

That the correlation coefficient between F and the MSE of the inboard disc is relatively high, at 0.4959, together with what was previously stated indicates that F now dictates the MSE for the disc. Previously, the only way to lower the temperature in the disc was to lower the temperature in the pad, something that would be done by raising the *k0*-value, which also created a strong correlation between the MSEs in pad and disc. Now with F the power can be lowered, and thus the temperature in the disc.

Table D.11: Mean of normalised input variables for the 100 best simulations with regards to MSE for the inboard pad, for the modeFRONTIER project with linear clamp force and Gs= 1.125 mW/(mm^{2}K). The thermal conductivities are normalised by k_t^*, the specific heat by c_p^*, *rho0* by ρ^*, and *rho1* by α^*. All units are those used in Abaqus. All values are rounded to four significant digits

Variables	Mean
c1	2767000
k0	1.098
k1	-0.001839
rho0	$2.217 \cdot 10^{-10}$
rho1	$6.468 \cdot 10^{-5}$
zeta	0.3878
F	11910

Table D.11 shows the average value of the 100 best iterations of this run. In comparison with the results for the constant force, see, Tables D.3 and D.6, we note that the value of *k0* is greater, with a lower value of *k1*.

The values of *k0* and *k1* in Table D.11 would give a value of $k_t/k_t^* \approx 0.953$ at $T = 99$ °C.

Table D.12 shows the 100 iterations with lowest MSE for the inboard pad of the run with Gs= 1.125 mW/(mm^{2}K) and linear clamp force.

Table D.12: Normalised values of the 100, out of 1000, iterations with lowest MSE for the inboard pad, with Gs= 1.125 mW/(mm^{2}K). The values are sorted from lowest training MSE for the inboard pad. The thermal conductivities are normalised by k_t^*, the specific heat by c_p^*, *rho0* by ρ^*, and *rho1* by α^*. All units are those used in Abaqus, some value should be multiplied by an exponent, see the second header from the bottom. All values are rounded to four significant digits.

	Normed						MSE							
							Disc				Pad			
							Training		Validation		Training		Validation	
[$\cdot 10^{-3}$]	[$\cdot 10^{6}$]		[$\cdot 10^{-3}$]	[$\cdot 10^{-10}$]	[$\cdot 10^{-5}$]									
F	*c1*	*k0*	*k1*	*rho0*	*rho1*	*zeta*	In	Out	Out	In	In	Out	In	Out
11.67	6.071	1.014	-1.403	2.263	9.965	0.9012	1821	3488	3609	1836	348.8	338.2	336.5	350.9
12.47	0	1.050	-1.807	2.175	7.242	0.8319	1846	2901	2989	1903	348.8	341.1	339.4	350.9
11.61	2.098	1.219	-2.099	2.178	3.604	0.4824	1800	3264	3373	1828	348.8	341.9	340.2	351.0
11.78	6.515	1.014	-1.321	2.276	8.848	0.9217	1820	3481	3601	1835	348.8	348.9	347.3	351.2
11.74	6.430	1.014	-1.403	2.268	8.821	0.7462	1806	3364	3478	1828	348.8	334.9	333.1	350.8
12.78	4.378	1.176	-1.975	2.251	6.969	0.7601	1851	2887	2974	1910	348.8	348.8	347.2	351.3
12.78	4.378	1.176	-1.975	2.251	6.969	0.7601	1851	2887	2974	1910	348.8	348.8	347.2	351.3
10.52	1.391	1.023	-1.292	2.233	2.357	0.5940	1960	4059	4208	1952	348.9	350.1	348.5	351.3
13.24	0.2205	1.078	-1.955	2.238	6.288	0.2954	2213	2552	2610	2330	348.9	334.9	333.1	350.8
12.30	0.2360	1.078	-1.982	2.169	7.301	0.04859	2005	2662	2732	2094	348.9	336.0	334.2	350.9
11.57	2.682	1.073	-1.703	2.217	6.891	0.3446	1801	3150	3253	1837	348.9	351.2	349.7	351.4
10.21	3.825	1.029	-1.399	2.180	4.223	0.2731	1950	4026	4174	1942	348.9	332.8	331.0	350.8
11.61	0.3220	1.071	-1.671	2.197	2.758	0.4824	1799	3202	3307	1832	348.9	352.7	351.2	351.4
11.74	6.430	1.014	-1.403	2.212	8.852	0.7462	1805	3348	3461	1828	348.9	353.0	351.5	351.5
11.31	2.353	1.099	-1.779	2.169	2.162	0.03833	1802	3139	3241	1839	348.9	332.8	331.0	350.9
11.97	2.487	1.008	-1.577	2.221	4.221	0.05503	1876	2830	2912	1941	349.0	332.5	330.7	350.9

Continued on next page

	Normed						MSE							
							Disc				Pad			
							Training		Validation		Training		Validation	
$[\cdot 10^{-3}]$	$[\cdot 10^{6}]$		$[\cdot 10^{-3}]$	$[\cdot 10^{-10}]$	$[\cdot 10^{-5}]$									
F	*c1*	*k0*	*k1*	*rho0*	*rho1*	*zeta*	In	Out	Out	In	In	Out	In	Out
11.13	7.557	1.223	-1.751	2.254	2.873	0.2918	1852	3660	3789	1859	349.0	353.0	351.5	351.5
11.59	2.904	1.122	-1.932	2.205	6.791	0.1232	1817	3017	3111	1863	349.0	332.0	330.2	350.9
11.78	4.688	1.102	-1.806	2.265	6.810	0	1839	2925	3014	1894	349.0	331.4	329.5	350.9
13.29	3.285	0.9844	-1.599	2.195	4.399	0.1587	2250	2541	2599	2372	349.0	331.0	329.2	350.9
12.50	0.006400	1.052	-1.923	2.197	7.250	0.001290	2093	2602	2666	2195	349.0	330.9	329.1	350.9
11.31	2.142	1.099	-1.711	2.188	2.156	0.03313	1801	3156	3258	1837	349.0	354.4	352.9	351.6
12.90	1.058	1.103	-2.084	2.195	7.898	0	2227	2548	2606	2345	349.1	329.8	327.9	350.9
11.71	3.161	1.086	-1.772	2.208	7.134	0.1466	1823	2983	3076	1873	349.1	355.5	354.0	351.7
12.74	2.918	1.122	-1.932	2.170	4.518	0.7153	1874	2833	2915	1939	349.1	328.0	326.1	350.9
12.50	0	1.079	-1.923	2.235	7.251	0	2067	2617	2683	2165	349.1	356.2	354.7	351.7
12.13	2.974	1.165	-1.976	2.222	5.786	0.8164	1800	3169	3272	1835	349.1	327.1	325.2	350.9
11.59	1.317	1.104	-1.932	2.216	6.688	0.1296	1823	2986	3078	1872	349.2	327.4	325.5	350.9
11.55	5.444	1.061	-1.629	2.221	6.896	0.3973	1799	3236	3343	1830	349.2	326.2	324.3	350.9
11.67	3.162	1.078	-1.833	2.198	7.297	0.1408	1826	2973	3065	1876	349.2	326.9	325.0	351.0
12.01	0.3211	1.071	-1.671	2.197	2.758	0.6340	1806	3089	3188	1846	349.2	359.5	358.0	351.9
11.98	1.792	1.182	-1.949	2.215	5.721	0.8817	1801	3294	3404	1827	349.2	359.6	358.2	351.9
12.95	0	1.075	-1.939	2.240	7.457	0	2241	2544	2601	2362	349.2	359.2	357.8	351.9
11.35	2.316	1.090	-1.868	2.206	7.133	0.08693	1807	3084	3182	1848	349.3	324.7	322.8	351.0
11.69	0	1.240	-2.446	2.191	8.255	0	1861	2863	2948	1922	349.3	324.8	322.9	351.0
11.98	2.415	1.068	-1.658	2.276	6.875	1.000	1803	3333	3445	1827	349.3	323.0	321.1	351.0
13.24	0.2205	1.078	-1.955	2.231	7.258	0.01263	2368	2521	2574	2503	349.3	361.4	360.0	352.1
11.24	7.681	1.223	-1.800	2.223	4.349	0.3381	1836	3578	3704	1847	349.4	362.2	360.8	352.2
12.74	2.914	1.122	-1.928	2.172	4.516	0.8791	1844	2905	2993	1901	349.6	319.7	317.8	351.1
12.09	3.115	1.042	-1.712	2.222	4.858	0.07765	1892	2799	2880	1961	349.6	320.5	318.5	351.2
11.73	5.945	1.073	-1.703	2.217	6.891	0.3446	1803	3117	3217	1842	349.7	318.6	316.6	351.2
12.50	0.006400	1.052	-1.846	2.197	7.250	0.001290	2077	2610	2676	2177	349.7	367.7	366.3	352.7
12.50	0.006400	1.052	-1.846	2.197	7.250	0.001290	2077	2610	2676	2177	349.7	367.7	366.3	352.7
13.04	0	1.098	-1.866	2.276	8.109	0.8879	1913	2764	2842	1986	349.8	369.5	368.2	352.8
12.19	4.151	1.121	-1.975	2.161	8.637	0.7578	1811	3046	3142	1855	349.9	316.4	314.4	351.3
13.04	0	1.098	-1.866	2.273	8.109	0.8879	1913	2764	2842	1986	349.9	370.3	369.0	352.9
10.02	0	1.228	-2.259	2.160	7.460	0.1409	1925	3942	4085	1920	349.9	316.9	314.9	351.4
11.57	2.682	1.073	-1.703	2.276	4.945	0.3446	1800	3180	3284	1834	349.9	315.7	313.6	351.4
11.95	0.09160	1.050	-1.820	2.256	4.836	0	1906	2777	2856	1977	350.0	315.8	313.8	351.4
11.82	0.0001000	1.079	-1.923	2.273	6.457	0	1883	2816	2898	1950	350.0	315.4	313.4	351.5
12.71	4.368	1.153	-1.975	2.251	6.158	0.8071	1839	2923	3012	1894	350.0	314.5	312.4	351.5
13.16	5.788	1.121	-1.975	2.270	7.544	0.2264	2112	2591	2655	2217	350.2	313.1	311.0	351.6
12.98	1.421	1.091	-2.087	2.195	8.063	0.001990	2270	2537	2593	2394	350.4	312.3	310.2	351.7
12.47	0	1.050	-1.807	2.175	7.242	0.2298	1984	2680	2752	2070	350.5	377.4	376.2	353.7
11.87	2.712	1.073	-1.703	2.274	7.180	1.000	1809	3393	3508	1829	350.6	309.5	307.4	351.8
11.87	2.712	1.073	-1.703	2.274	7.180	1.000	1809	3393	3508	1829	350.6	309.5	307.4	351.8
12.19	7.182	0.8454	-0.7625	2.252	6.969	0.7601	1801	3153	3255	1837	350.6	378.6	377.4	353.8
11.69	0	1.112	-1.982	2.181	9.134	0.00002000	1867	2849	2933	1930	350.6	377.7	376.5	353.8
11.78	6.515	1.015	-1.321	2.200	8.848	0.8397	1810	3404	3520	1830	350.9	381.2	380.1	354.3
12.11	4.165	1.112	-1.982	2.181	9.134	0.6833	1813	3035	3131	1858	351.1	305.2	303.0	352.3
12.30	2.424	1.097	-2.023	2.213	7.428	0.01984	1985	2680	2752	2071	351.2	305.7	303.5	352.3
13.16	3.177	1.031	-1.814	2.258	7.544	0.2264	2186	2560	2620	2299	351.3	304.2	302.1	352.4
11.06	3.843	1.102	-1.925	2.194	9.505	0.2847	1805	3348	3461	1828	351.4	303.7	301.5	352.5
11.99	3.028	1.143	-2.013	2.182	6.678	0.8926	1799	3238	3346	1829	351.4	303.1	300.9	352.5
11.67	1.326	1.121	-2.042	2.193	7.348	0.4685	1804	3104	3203	1844	351.5	302.9	300.7	352.6
11.77	6.431	1.112	-1.605	2.212	6.906	0.3785	1800	3188	3292	1833	351.5	386.7	385.7	355.0
11.59	0.04240	1.127	-1.982	2.163	4.736	0.9918	1818	3473	3593	1835	351.6	301.8	299.7	352.7
12.67	3.704	1.081	-1.676	2.193	3.840	0.1577	1973	2691	2764	2057	351.6	387.4	386.4	355.1

Continued on next page

	Normed						MSE							
							Disc				Pad			
							Training		Validation		Training		Validation	
$[\cdot 10^{-3}]$	$[\cdot 10^{6}]$		$[\cdot 10^{-3}]$	$[\cdot 10^{-10}]$	$[\cdot 10^{-5}]$									
F	*c1*	*k0*	*k1*	*rho0*	*rho1*	*zeta*	In	Out	Out	In	In	Out	In	Out
11.67	1.326	1.121	-2.042	2.198	7.348	0.4684	1804	3105	3204	1844	351.7	301.8	299.6	352.7
11.67	1.326	1.121	-2.042	2.198	7.348	0.4684	1804	3105	3204	1844	351.7	301.7	299.5	352.7
11.73	5.945	1.116	-1.751	2.254	2.873	0.2814	1801	3158	3261	1836	351.7	301.5	299.3	352.7
12.55	2.090	1.219	-2.099	2.178	3.604	0.2930	1908	2773	2852	1980	351.7	388.4	387.4	355.3
12.81	7.512	1.094	-1.774	2.276	3.907	0.06455	2003	2664	2734	2091	351.8	301.5	299.3	352.8
12.08	0.7462	1.077	-2.020	2.172	7.420	0.1722	1915	2763	2841	1988	351.9	300.7	298.5	352.9
11.78	0.01310	1.234	-2.521	2.161	8.637	0.02048	1886	2811	2892	1953	351.9	300.8	298.6	352.9
11.46	7.157	1.030	-1.568	2.260	7.134	0.1466	1801	3157	3260	1837	351.9	300.6	298.4	352.9
11.10	7.326	1.209	-1.952	2.239	4.151	0.4026	1849	3643	3772	1856	352.0	299.5	297.3	353.0
11.70	3.225	1.059	-1.891	2.234	10.00	0.09761	1847	2901	2988	1904	352.1	299.4	297.1	353.1
10.02	0	1.228	-1.713	2.257	6.329	1.000	2305	4929	5118	2272	352.3	392.6	391.6	356.0
11.98	1.517	1.124	-2.041	2.225	7.039	0.5852	1813	3033	3128	1859	352.3	297.8	295.6	353.2
12.53	5.233	1.058	-1.795	2.262	5.892	0	2004	2662	2733	2093	352.3	298.1	295.8	353.3
11.59	2.475	1.069	-1.888	2.220	7.222	0.1223	1825	2974	3066	1876	352.4	297.7	295.5	353.3
12.14	5.204	1.061	-1.820	2.269	7.802	0.0007000	1916	2761	2839	1990	352.4	297.6	295.4	353.3
12.93	1.929	1.068	-1.888	2.273	7.802	0.8361	1906	2775	2854	1977	352.4	297.1	294.9	353.4
10.88	0.9712	1.014	-1.647	2.263	5.453	0.03741	1801	3287	3397	1828	352.5	297.0	294.8	353.4
10.91	0.1952	1.192	-1.815	2.204	4.598	0.7291	1906	3877	4017	1904	352.8	396.7	395.8	356.6
11.99	3.428	1.127	-1.978	2.163	6.538	0.9918	1801	3290	3400	1827	352.9	294.5	292.2	353.7
11.46	7.157	1.030	-1.568	2.160	7.265	0.8436	1831	3550	3674	1843	352.9	294.6	292.3	353.7
10.56	0.3556	1.223	-2.342	2.180	6.664	0.09349	1825	3515	3637	1839	353.0	294.5	292.3	353.8
10.56	0.3556	1.223	-2.342	2.180	6.664	0.09349	1825	3515	3637	1839	353.0	294.5	292.3	353.8
11.72	1.680	1.044	-1.851	2.182	9.134	0.6833	1801	3152	3255	1837	353.1	293.3	291.1	354.0
11.55	5.331	1.061	-1.740	2.222	6.692	0.3821	1799	3198	3303	1832	353.5	291.8	289.5	354.2
11.55	5.331	1.061	-1.740	2.222	6.692	0.3821	1799	3198	3303	1832	353.5	291.8	289.5	354.2
12.06	5.330	1.081	-1.834	2.271	6.081	0.09787	1868	2846	2930	1931	353.6	291.4	289.1	354.4
11.39	1.766	1.062	-1.801	2.244	4.223	0.1431	1805	3106	3206	1844	353.8	290.7	288.4	354.5
11.84	1.310	1.088	-2.041	2.179	6.993	0.1721	1864	2857	2941	1926	354.1	288.8	286.5	354.8
11.67	1.610	1.220	-1.941	2.192	3.576	0.4578	1800	3258	3366	1829	354.2	406.4	405.6	358.3
12.38	0	1.030	-1.936	2.199	7.020	0.1351	2021	2649	2718	2112	354.4	287.8	285.5	355.1
11.73	5.945	1.073	-1.703	2.217	6.891	1.000	1824	3509	3631	1838	354.5	286.8	284.5	355.1
10.58	0	1.288	-2.200	2.174	6.012	0.09482	1846	3627	3755	1854	354.5	408.1	407.4	358.7

D.2 Wear

In this section the results of the modeFRONTIER projects in which values of the wear scaling factor of the pad, $k_{w,p}$, was fitted to the values of the total wear of the pads, see Section B.5.2.

D.2.1 Constant Pad Wear Scaling Factor

In the following tables the results are presented for two runs of the modeFRONTIER project in which $k_{w,p}$ was assumed to be constant.

Table D.13: Normalised values of the five iterations for the first run in the constant wear project. The values are sorted from lowest to highest $k_{w,p}$. All values are rounded to four significant digits. h^* is a normalisation factor used, sparingly, for wear depth. MAE in the second column is the mean absolute error when comparing simulated mean wear and measured wear per 10 cycles.

$k_{w,p}/k^*$ $[\cdot 10^{-8}$ MPa$^{-1}]$	MAE$/h^* \cdot 1000$	Average wear depth after 10 cycles$/h^*$
7.909	7.130	0.01287
9.438	4.645	0.01536
12.32	0.04117	0.02004
14.03	2.807	0.02281
15.41	5.056	0.02506

Table D.13 shows the results of all five iterations of the first run. The third row in the column shows the best result, with $k_{w,p}/k^* = 12.32 \cdot 10^{-8}$ MPa^{-1}. This value was used in the simulation presented in Appendix C.1.

Observe that this best constant value of $k_{w,p}$ is greater than the temperature dependent value of $k_{w,p}$ at 500 °C, and lower than the value at 600 °C, see Tables B.1 and B.2 in Section B.1.1.

Table D.14: Normalised values of the 25 iterations for the second run in the constant wear project. The values are sorted from lowest to highest $k_{w,p}$. All values are rounded to four significant digits. h^* is a normalisation factor used, sparingly, for wear depth. MAE in the second column is the mean absolute error when comparing simulated mean wear and measured wear per 10 cycles.

$k_{w,p}/k^*$ $[\cdot 10^{-8}$ MPa$^{-1}]$	MAE$/h^* \cdot 1000$	Average wear depth after 10 cycles$/h^*$
6.784	8.938	0.01106
7.091	8.439	0.01156
7.440	7.869	0.01213
7.890	7.135	0.01286
8.224	6.589	0.01341
8.757	5.720	0.01428
8.881	5.517	0.01448
9.358	4.739	0.01526
9.662	4.244	0.01576
10.23	3.317	0.01668
10.63	2.662	0.01734
11.18	1.768	0.01823
11.32	1.533	0.01847
11.84	0.6824	0.01932
12.34	0.1256	0.02013
12.38	0.1920	0.02019
13.07	1.324	0.02132
13.29	1.672	0.02167
13.70	2.353	0.02235
14.02	2.864	0.02286
14.59	3.807	0.02381
14.96	4.404	0.02440
15.15	4.719	0.02472
15.84	5.847	0.02585
16.16	6.361	0.02636

Table D.14 shows the values from run 2 of the project. The value with the lowest MAE is also the value closest to the best iteration from run 1, and it is $k_{w,p}/k^* =$

$12.34 \cdot 10^{-8}$ MPa^{-1}.

D.2.2 Scaled Up Wear Scaling Factors

In this subsection the results of the modeFRONTIER project are presented where the temperature dependent $k_{w,p}$ values were scaled up by a scaling factor.

Table D.15: Normalised values of the 20 iterations for the only in the project of scaling up the wear scaling factors. The values are sorted from lowest to highest scaling factor. All values are rounded to four significant digits. h^* is a normalisation factor used, sparingly, for wear depth. MAE in the second column is the mean absolute error when comparing simulated mean wear and measured wear per 10 cycles.

Scaling factor	MAE/$h^* \cdot 1000$	Average wear depth after 10 cycles/h^*
1.131	12.38	0.007625
1.512	10.42	0.009581
1.961	8.187	0.01181
2.030	7.846	0.01215
2.623	4.921	0.01508
2.716	4.464	0.01554
3.230	1.921	0.01808
3.326	1.442	0.01856
3.851	1.163	0.02116
4.076	2.280	0.02228
4.525	4.512	0.02451
4.695	5.361	0.02536
4.945	6.603	0.02660
5.303	8.380	0.02838
5.639	10.05	0,03005
6.198	12.82	0.03282
6.434	13.99	0.03399
6.842	16.00	0.03600
6.929	16.42	0.03642
7.221	17.86	0.03786

Table D.15 shows the results of the sole run in this project. The best fit of these iterations is a scaling factor of 3.851.

Table D.16: Normalised temperature dependent wear scaling factors of the pad, measured and scaled up by a factor of 3.851.

T [°C]	$k_{w,p}/k^*$ [$\cdot 10^{-8}$MPa^{-1}]	Scaled up $k_{w,p}/k^*$ [$\cdot 10^{-8}$MPa^{-1}]
100	1.0000	3.851
200	2.0000	7.702
300	2.3000	8.857
400	4.2000	16.17
500	10.200	39.28

Table D.16 shows the values of $k_{w,p}$ if it were to be scaled up by a factor of 3.851.

D.2.3 Fit of Pad Wear Scaling Factor

In this subsection the results of the modeFRONTIER project are presented in which a fit $k_{w,p} = a + c \cdot b^{T/100}$ is done.

Table D.17: Normalised values of the five best iterations of the fit of $k_{w,p}(T) = a + c \cdot b^{T/100}$. The values are sorted after lowest MAE of the average wear depth. All values are rounded to four significant digits. The unit of a and c are MPa^{-1}.

					MAE/k^* of $k_{w,p}$ at T				
a/k^* $[\cdot 10^{-8}]$	b	c/k^* $[\cdot 10^{-18}]$	MAE/h^*	Average wear after 10 cycles/h^*	100 °C	200 °C	300 °C	400 °C	500 °C
0.9123	196.3	1.845	0.002763	0.01724	0.08768	1.088	1.386	3.014	44.47
0.7938	243.4	1.397	0.004544	0.02454	0.2062	1.206	1.504	2.916	110.0
1.060	243.4	1.397	0.004860	0.02486	0.06005	0.9400	1.238	2.650	110.1
0.8616	243.4	1.526	0.005612	0.02561	0.1384	1.138	1.436	2.803	121.0
1.073	179.0	1.954	0.005713	0.01429	0.07278	0.9272	1.226	2.926	26.82

Table D.17 shows the five best iterations of this project. Note that there is a lot of variance in the input parameters. Also observe that whilst the MAE for the wear depth is quite low, the MAE for the $k_{w,p}$ at high temperatures is quite high. Ergo whilst we can produce a fit that gives accurate total wear predictions, it is difficult to at the same time match that fit to the measured values of $k_{w,p}$.

Table D.18 shows the results for all the 100 iterations of the fit of $k_{w,p}(T) = a + c \cdot b^{T/100}$.

Table D.18: Normalised values of the 100 iterations of the fit of $k_{w,p}(T) = a + c \cdot b^{T/100}$. The values are sorted after lowest MAE of the average wear depth. All values are rounded to four significant digits. The unit of a and c are MPa^{-1}.

					MAE/k^* of $k_{w,p}$ at T				
a/k^* $[\cdot 10^{-8}]$	b	c/k^* $[\cdot 10^{-18}]$	MAE/h^*	Mean wear 10 cycles/h^*	100 °C	200 °C	300 °C	400 °C	500 °C
0.9123	196.3	1.845	0.002763	0.01724	0.08768	1.088	1.386	3.014	44.47
0.7938	243.4	1.397	0.004544	0.02454	0.2062	1.206	1.504	2.916	110.0
1.060	243.4	1.397	0.004860	0.02486	0.06005	0.9400	1.238	2.650	110.1
0.8616	243.4	1.526	0.005612	0.02561	0.1384	1.138	1.436	2.803	121.0
1.073	179.0	1.954	0.005713	0.01429	0.07278	0.9272	1.226	2.926	26.82
0.3712	178.0	1.526	0.008611	0.01139	0.6288	1.629	1.928	3.676	17.44
1.074	135.9	2.337	0.01186	0.008141	0.07356	0.9265	1.226	3.047	1.700
0.7938	273.8	1.397	0.01196	0.03196	0.2062	1.206	1.503	2.621	205.7
1.068	134.3	2.333	0.01205	0.007949	0.06849	0.9315	1.231	3.056	1.069
1.072	140.9	1.714	0.01218	0.007818	0.07165	0.9284	1.228	3.061	0.3926
1.070	137.8	1.889	0.01225	0.007754	0.06996	0.9301	1.230	3.062	0.2645
1.071	135.8	1.994	0.01232	0.007684	0.07105	0.9290	1.228	3.061	0.08005
1.074	137.2	1.873	0.01233	0.007670	0.07359	0.9264	1.226	3.060	0.01786
1.074	136.3	1.891	0.01240	0.007599	0.07359	0.9264	1.226	3.061	0.2291
1.073	137.7	1.775	0.01242	0.007581	0.07283	0.9272	1.227	3.063	0.3251
1.070	137.8	1.726	0.01249	0.007512	0.06988	0.9302	1.230	3.068	0.5476
1.071	138.9	1.631	0.01253	0.007475	0.07149	0.9285	1.228	3.068	0.7038
1.074	136.7	1.726	0.01259	0.007408	0.07359	0.9264	1.226	3.066	0.8747
1.073	136.7	1.726	0.01259	0.007406	0.07263	0.9274	1.227	3.067	0.8756
1.073	136.7	1.726	0.01259	0.007406	0.07263	0.9274	1.227	3.067	0.8756
1.074	136.7	1.626	0.01274	0.007262	0.07359	0.9264	1.226	3.070	1.352
1.074	136.3	1.624	0.01278	0.007217	0.07359	0.9264	1.226	3.070	1.485
1.074	138.1	1.504	0.01280	0.007204	0.07359	0.9264	1.226	3.072	1.571

Continued on next page

					MAE/k^* of $k_{w,p}$ at T				
a/k^* [$\cdot 10^{-8}$]	b	c/k^* [$\cdot 10^{-18}$]	MAE/h^*	Mean wear 10 cycles/h^*	100 °C	200 °C	300 °C	400 °C	500 °C
1.074	138.1	1.504	0.01280	0.007204	0.07359	0.9264	1.226	3.072	1.571
1.074	138.1	1.504	0.01280	0.007204	0.07356	0.9265	1.226	3.072	1.571
1.074	137.7	1.519	0.01281	0.007189	0.07356	0.9265	1.226	3.072	1.611
1.074	132.2	1.861	0.01286	0.007143	0.07359	0.9264	1.226	3.070	1.620
1.074	137.1	1.499	0.01289	0.007109	0.07359	0.9264	1.226	3.073	1.854
1.074	135.9	1.504	0.01300	0.007002	0.07356	0.9265	1.226	3.075	2.159
1.073	133.0	1.672	0.01302	0.006979	0.07333	0.9267	1.226	3.074	2.163
0.8569	243.4	2.622	0.01318	0.03318	0.1431	1.143	1.439	2.423	214.5
1.074	139.7	1.077	0.01338	0.006618	0.07359	0.9264	1.226	3.085	3.387
1.074	139.7	1.077	0.01338	0.006618	0.07359	0.9264	1.226	3.085	3.387
1.066	139.7	1.076	0.01339	0.006605	0.06593	0.9341	1.234	3.093	3.400
1.074	139.7	1.068	0.01340	0.006601	0.07359	0.9264	1.226	3.086	3.435
1.045	136.1	1.224	0.01346	0.006540	0.04511	0.9549	1.255	3.113	3.445
1.067	141.6	0.9139	0.01358	0.006421	0.06730	0.9327	1.232	3.096	3.932
1.044	142.2	0.6458	0.01421	0.005790	0.04392	0.9561	1.256	3.130	5.395
1.051	137.8	0.6601	0.01446	0.005535	0.05058	0.9495	1.249	3.126	5.871
1.051	137.8	0.6533	0.01448	0.005519	0.05058	0.9495	1.249	3.126	5.905
1.051	137.8	0.6533	0.01448	0.005519	0.05058	0.9495	1.249	3.126	5.905
0.3254	139.7	1.018	0.01457	0.005427	0.6746	1.675	1.974	3.836	4.449
0.9893	136.7	0.6533	0.01464	0.005358	0.01072	1.011	1.311	3.188	6.090
0.9893	136.7	0.6523	0.01464	0.005356	0.01072	1.011	1.311	3.188	6.095
0.6368	140.3	0.6533	0.01493	0.005073	0.3632	1.363	1.663	3.538	6.016
1.048	133.0	0.5825	0.01497	0.005032	0.04815	0.9519	1.252	3.134	6.730
0.9893	137.7	0.2520	0.01585	0.004149	0.01069	1.011	1.311	3.202	7.961
0.9891	137.7	0.2520	0.01585	0.004149	0.01093	1.011	1.311	3.202	7.961
0.9891	136.7	0.2525	0.01589	0.004111	0.01093	1.011	1.311	3.202	8.005
0.9891	136.7	0.2525	0.01589	0.004111	0.01093	1.011	1.311	3.202	8.005
0.9843	136.7	0.2525	0.01590	0.004103	0.01572	1.016	1.316	3.207	8.010
0.6483	104.3	1.682	0.01600	0.004003	0.3517	1.352	1.652	3.532	7.470
1.074	92.58	1.381	0.01616	0.003842	0.07359	0.9264	1.226	3.116	8.187
1.074	127.1	0.2072	0.01623	0.003766	0.07359	0.9264	1.226	3.121	8.440
0.7144	135.0	0.2771	0.01629	0.003707	0.2856	1.286	1.586	3.476	8.242
1.073	81.73	1.574	0.01653	0.003474	0.07292	0.9271	1.227	3.120	8.553
1.030	69.71	1.237	0.01715	0.002852	0.03033	0.9697	1.270	3.167	8.966
1.030	69.71	0.1713	0.01778	0.002223	0.03025	0.9698	1.270	3.169	9.142
1.074	27.64	1.626	0.01820	0.001796	0.07359	0.9264	1.226	3.126	9.124
1.074	212.7	0	0.01825	0.001753	0.07359	0.9264	1.226	3.126	9.126
1.056	10.00	1.052	0.01828	0.001725	0.05642	0.9436	1.244	3.144	9.144
1.056	10.02	1.018	0.01828	0.001725	0.05642	0.9436	1.244	3.144	9.144
1.049	16.14	1.533	0.01829	0.001715	0.04941	0.9506	1.251	3.151	9.151
0.9979	10.00	0.6382	0.01837	0.001629	0.002149	1.002	1.302	3.202	9.202
0.9979	10.00	0.5611	0.01837	0.001629	0.002149	1.002	1.302	3.202	9.202
0.9911	10.00	0.6382	0.01838	0.001618	0.008854	1.009	1.309	3.209	9.209
0.9400	84.12	0	0.01847	0.001535	0.06001	1.060	1.360	3.260	9.260
0.7323	30.05	1.903	0.01871	0.001292	0.2677	1.268	1.568	3.468	9.463
0.5534	42.71	1.214	0.01873	0.001268	0.4466	1.447	1.747	3.646	9.629
0.7323	30.05	0.6535	0.01877	0.001233	0.2677	1.268	1.568	3.468	9.466
0.6471	10.02	1.533	0.01894	0.001057	0.3529	1.353	1.653	3.553	9.553
0.5485	10.00	1.627	0.01910	0.0008960	0.4515	1.452	1.752	3.652	9.652
0.3713	10.00	1.533	0.01939	0.0006067	0.6287	1.629	1.929	3.829	9.829
0.3646	10.00	1.627	0.01940	0.0005957	0.6354	1.635	1.935	3.835	9.835
0.3646	10.00	1.627	0.01940	0.0005957	0.6354	1.635	1.935	3.835	9.835
0.3253	10.00	1.128	0.01947	0.0005316	0.6747	1.675	1.975	3.875	9.875
0.3253	10.00	0.7377	0.01947	0.0005316	0.6747	1.675	1.975	3.875	9.875
0.7109	283.9	1.681	0.02439	0.04439	0.2891	1.289	1.585	2.398	300.4

Continued on next page

					MAE/k^* of $k_{w,p}$ at T				
a/k^* [$\cdot 10^{-8}$]	b	c/k^* [$\cdot 10^{-18}$]	MAE/h^*	Mean wear 10 cycles/h^*	100 °C	200 °C	300 °C	400 °C	500 °C
0.7948	375.2	0.9441	0.04026	0.06026	0.2052	1.205	1.500	1.534	692.8
1.009	376.2	0.9440	0.04046	0.06046	0.009404	0.9906	1.286	1.300	702.1
1.009	376.2	0.9441	0.04047	0.06047	0.009344	0.9907	1.286	1.300	702.2
0.7938	385.4	1.339	0.04625	0.06625	0.2062	1.206	1.499	0.4525	1129
0.6574	391.8	1.339	0.04707	0.06707	0.3426	1.343	1.635	0.3870	1227
1.061	391.8	1.339	0.04707	0.06707	0.06075	0.9393	1.231	0.01640	1227
1.009	376.2	1.627	0.04710	0.06710	0.009404	0.9906	1.282	0.06815	1217
1.009	386.2	1.627	0.04827	0.06827	0.009404	0.9906	1.281	0.4266	1388
1.009	376.2	3.131	0.04903	0.06903	0.009344	0.9906	1.274	3.081	2350
1.073	457.4	1.938	0.05643	0.07643	0.07330	0.9267	1.208	5.358	3872
0.8108	528.8	1.189	0.06588	0.08588	0.1892	1.189	1.472	5.912	4910
1.061	716.2	0.3251	0.07033	0.09033	0.06076	0.9393	1.227	5.415	6117
0.6806	748.5	0.3251	0.07771	0.09771	0.3194	1.319	1.606	6.688	7631
0.8108	528.8	1.722	0.07835	0.09835	0.1892	1.189	1.464	10.08	7114
0.6574	643.9	1.698	0.1072	0.1272	0.3426	1.343	1.597	25.66	18790
0.6653	748.5	0.8582	0.1086	0.1286	0.3347	1.335	1.599	23.41	20160
0.9988	659.2	1.627	0.1096	0.1296	0.001206	1.001	1.255	27.52	20250
0.8581	704.4	1.716	0.1162	0.1362	0.1419	1.142	1.382	38.91	29750
0.8616	736.3	1.526	0.1194	0.1394	0.1384	1.138	1.377	41.51	33020
0.9891	704.4	1.627	0.1243	0.1443	0.01090	1.011	1.254	36.85	28210
0.5914	848.5	2.906	0.1450	0.1650	0.4086	1.408	1.531	147.0	127800
0.5915	848.5	2.906	0.1450	0.1650	0.4085	1.408	1.531	147.0	127800

E
PINNs

In this appendix information regarding physics-informed neural network (PINNs) and a proposed method on how they could be used to investigate the material properties of the pad.

E.1 PINNs Theory

A PINN is more or less a neural network where the relationship between input and output is assumed to solve one of the partial differential equations in physics, such as for example the heat equation, see Section 2.3. That means with spatial coordinates and time being inputs one can do differentiation and obtain the PDE as a loss term in a cost function for the neural network. Additional terms are also added for boundary conditions and initial conditions [50], [51].

There exist three distinct subcategories of PINNs: forward, inverse and mixed. PINNs can solve the forward problem in which the parameters of the problem (such as k_t, ρ, c_p etc.) are known and it is the goal to determine the spatial-temporal solution of the variables of the PDE (displacement, temperature, etc.). In the inverse problem the parameters are unknown and is determined by the PINN whilst the solution of the function is known. In the mixed problem both the parameters and the function are unknown, except for some measurement values [50], [51].

E.1.1 Model Validation

To validate a machine learning model one tries to determine if it performs a good "fit" on the data. Two opposite issues that can arise are under- and overfitting to the data. Underfitting is when the model has not adapted to the data at all, i.e. it has a high bias and gives a large error. This could be due to a lack of training time or that the model is not complex enough (not enough parameters) to be able to adapt to the data. Overfitting is when the model has adapted well to the data it has trained on but performs poorly on predictions on new data. Overfitting is characterised by the model "going through" all data points of the training data, even those that are outliers. It means that the model has adjusted to noise, and not overall trends [52].

Both under- and overfitting can be evaluated by withholding data from the training, and measuring the error on that data. One divides the data into training, validation and test data with typically a 80%/10%/10% split. Training data is the data which is used to adjust the model parameters. Validation data is data that on which the error is evaluated to test for under- and overfitting, as well as evaluate different sets of choices of hyperpa-

rameters. Test data is data that has not been used at all in the whole process and on which only the final model is evaluated [52].

A characteristic of overfitting is that values of the models parameters become very large. Thus to reduce the overfitting one can add terms to the loss function that depend on the size of the model parameters $\boldsymbol{\theta}$. Two examples are

$$\begin{aligned} &\text{Lasso regularisation: } \lambda_L ||\boldsymbol{\theta}||_1 \\ &\text{and} \\ &\text{Ridge regularisation: } \lambda_R ||\boldsymbol{\theta}||_2^2, \end{aligned} \tag{E.1}$$

where λ_L, λ_R are scalar positive constants and an example of hyperparameters [52].

E.2 PINN Methodology

This section lays out a proposed plan to use a PINN to determine the thermal material parameters. Note that when this plan was established it was uncertain if values for the parameters would be available for the cast iron, hence why they are included as part of the PINN.

The structure of the PINN was as the one proposed in [50], although that was for solving the momentum equation with linear elasticity, with separate neural network for all outputs. Figure E.1 below shows this lay-out.

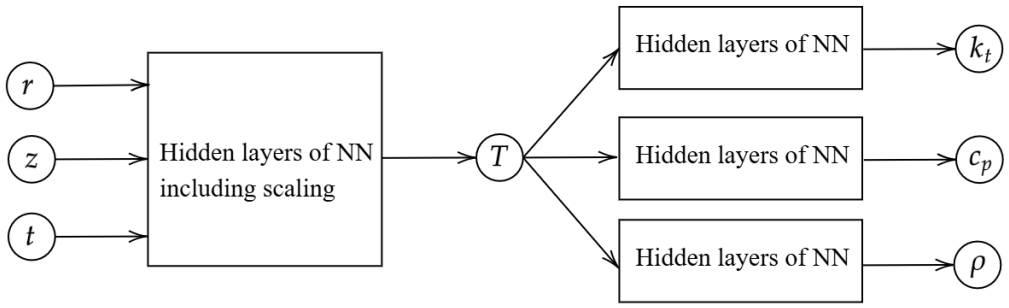

(a) *Possible PINN structure with separate NNs for k_t, c_p and ρ.*

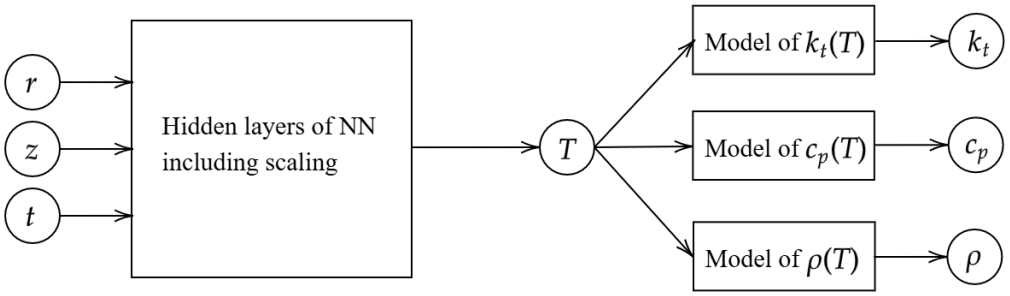

(b) *Possible PINN structure with models with parameters for k_t, c_p and ρ.*

Figure E.1: *Two possible structures of the PINN for a single temperature field.*

In the PINN-model in Figure E.1 the temperature is set as a function of the radius r, the height z and the time t, and the material parameters k_t, c_p and ρ as a function of that predicted temperature. For the PINNs we will only consider the axisymmetric model, the angle θ will not be an input to the NN.

In Figure E.1 two possible set-ups of the PINN are shown. In the first, Figure E.1a, the material parameters' temperature dependence are fitted with their own NNs. In the second, Figure E.1b, the temperature dependence is fitted using existing models, with the coefficients/parameters of those being added as parameters of the ML-model. The coefficients would then be updated in the optimisation algorithm like the weights and biases are.

Note that due to the limited number of data points the 1st PINN model above may be prone to overfitting or unphysical solutions, for example negative values of temperature or parameters. The second approach limits that possible variance, which would hopefully make it possible to determine a model that limits the loss, whilst remaining reasonable. The advantage of this was that something physical should be obtained, the disadvantage was that if the proposed model was not appropriate to the real material behaviour it would not be able to adapt to the data. Overall the advantages exceed the disadvantages,

and thus the PINN-structure would be as in Figure E.1b.

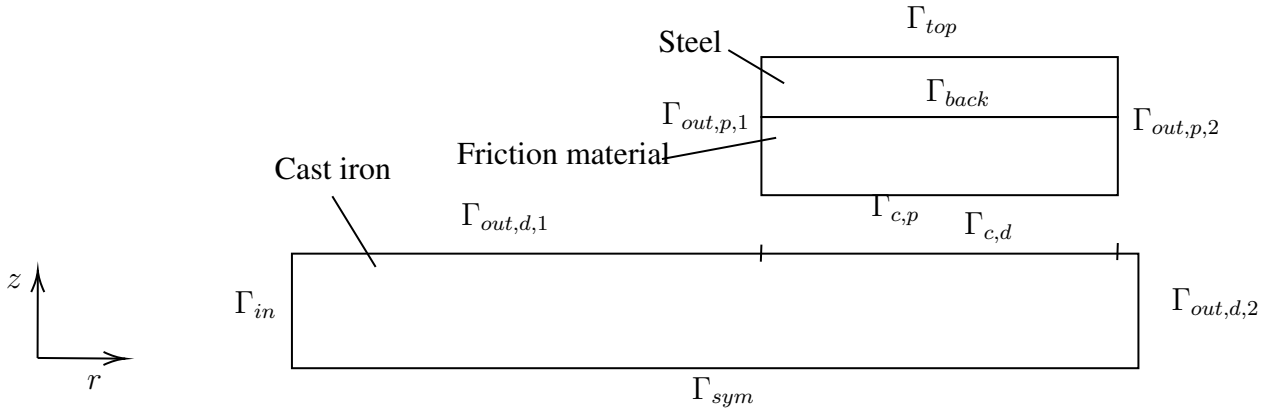

Figure E.2: *The domain on which the PINN should solve the heat equation.*

The PINN would only be used on a simplified axisymmetric 2D-model of the system, see Figure E.2 above. Thus the PDE that would be used is the axisymmetric formulation of the heat equation. This equation would have to be solved in the domains, the brake pads, the brake disc and the steel back plate, for which we would have three different PINN-models, with three temperature fields T_d, T_p and T_s. However, since there is heat that is transferred in the contact surface interface, as well as between pad lining and backplate, driven by the temperature difference on the surfaces (see Section 2.3), the problems in the three domains are coupled through the boundary conditions. We assume contact on surfaces $\Gamma_{c,d}$ and $\Gamma_{c,p}$, whilst we assume convection and radiation cooling on outer surfaces $\Gamma_{out,d} = \Gamma_{out,d,1} \cup \Gamma_{out,d,2}$ and $\Gamma_{out,p} = \Gamma_{out,p,1} \cup \Gamma_{out,p,2}$, insulation on Γ_{in} and Γ_{top}, and symmetry on Γ_{sym}. We assume that there is perfect thermal contact between the lining and backing plate of the pad, which means continuos normal heat flux across the surface Γ_{back}.

Note that since we assume that the material parameters of the steel is known those will not be updated in the learning process.

The cost function would then consist of the loss terms

$$\mathcal{L}_{PDE} = ||\rho\frac{\partial c_p T}{\partial t} - \frac{1}{r}\frac{\partial}{\partial r}\left(rk_t\frac{\partial T}{\partial r}\right) - \frac{\partial}{\partial z}\left(k_t\frac{\partial T}{\partial z}\right)||_2^2$$
$$\mathcal{L}_0 = ||T(t=0) - T_0||_2^2$$
$$\mathcal{L}_{b,1} = {}_{\Gamma_{in}}||q_n||_2^2 = {}_{\Gamma_{in}}||k_{t,d}\frac{\partial T_d}{\partial r}||_2^2$$
$$\mathcal{L}_{b,2} = {}_{\Gamma_{sym}}||q_n||_2^2 = {}_{\Gamma_{sym}}||k_{t,d}\frac{\partial T_d}{\partial z}||_2^2$$
$$\mathcal{L}_{b,3} = {}_{\Gamma_{out,d,1}}||q_n - q_c - q_r||_2^2 = {}_{\Gamma_{out,d,1}}||-k_{t,d}\frac{\partial T_d}{\partial z} - h_d\left(T_d - T_e\right) - \sigma_B\epsilon\left(T_d^4 - T_e^4\right)||_2^2$$
$$\mathcal{L}_{b,4} = {}_{\Gamma_{out,d,2}}||q_n - q_c - q_r||_2^2 = {}_{\Gamma_{out,d,2}}||-k_{t,d}\frac{\partial T_d}{\partial x_n} - h_d\left(T_d - T_e\right) - \sigma_B\epsilon\left(T_d^4 - T_e^4\right)||_2^2$$
$$\mathcal{L}_{b,5} = {}_{\Gamma_{out,p,1}}||q_n - q_c - q_r||_2^2 = {}_{\Gamma_{out,p,1}}||k_{t,p}\frac{\partial T_{p/s}}{\partial r} - h_p\left(T_{p/s} - T_e\right) - \sigma_B\epsilon\left(T_{p/s}^4 - T_e^4\right)||_2^2$$
$$\mathcal{L}_{b,6} = {}_{\Gamma_{out,p,2}}||q_n - q_c - q_r||_2^2 = {}_{\Gamma_{out,p,2}}||-k_{t,p}\frac{\partial T_{p/s}}{\partial r} - h_p\left(T_{p/s} - T_e\right) - \sigma_B\epsilon\left(T_{p/s}^4 - T_e^4\right)||_2^2$$
$$\mathcal{L}_{b,7} = {}_{\Gamma_{c,d}}||-k_{t,d}\frac{\partial T_d}{\partial z} - \frac{\phi_0}{2\pi}\sigma\mu p\omega r - h_c(T_d, T_p, p)\cdot\left(T_p - T_d\right)||_2^2$$
$$\mathcal{L}_{b,8} = {}_{\Gamma_{c,p}}||k_{t,p}\frac{\partial T_p}{\partial z} - (1-\sigma)\,\mu p\omega r - h_c(T_d, T_p, p)\cdot\left(T_d - T_p\right)||_2^2$$
$$\mathcal{L}_{b,9} = {}_{\Gamma_{back}}||k_{t,p}\frac{\partial T_p}{\partial z} - k_{t,s}\frac{\partial T_s}{\partial z}||_2^2 + {}_{\Gamma_{back}}||T_p - T_s||_2^2 \text{ (continuity conditions)}$$
$$\mathcal{L}_{b,10} = {}_{\Gamma_{top}}||q_n||_2^2 = {}_{\Gamma_{top}}||k_{t,s}\frac{\partial T_s}{\partial r}||_2^2$$
$$\mathcal{L}_{data} = \sum_{j=(d,p)}\sum_i ||T_j(r_{m,i}, z_{m,i}, \boldsymbol{t}_{m,i}) - \boldsymbol{T}_j^{m,i}||_2^2$$
$$\mathcal{L}_{param} = \sum_{j=(d,p)}\left(\left(k_{t,j}(T^*) - k_{t,j}^*\right)^2 + \left(c_{p,j}(T^*) - c_{p,j}^*\right)^2 + \left(\rho_j(T^*) - \rho_j^*\right)^2 + \left(\alpha_j(T^*) - \alpha_j^*\right)^2\right) \tag{E.2}$$

In $\mathcal{L}_{PDE}$ and $\mathcal{L}_0$ the losses are determined in a number of sampling points in the domains, both for the temperature fields in the disc and in the pads, with the later ensuring that the initial condition $T = T_0$ is fulfilled. $\mathcal{L}_{b,i}$, $i = 1, ..., 10$, ensures that the boundary conditions are fulfilled. $\mathcal{L}_{data}$ are the error of the predicted temperature in the measurement points, where the thermocouples are situated, to the measured temperatures. $\mathcal{L}_{param}$ is a term that can be included if the parameter values k_t^*, c_p^* and ρ^* are known at some temperature T^*. We have also included possible known values for α, where the temperature dependence is derived from $\rho(T)$ by equation (2.26). Note that the boundary segment $\Gamma_{out,d,2}$ has a part where the normal is z, and another part where the normal is r, hence why the derivative is in terms of "x_n".

The sampling of points in the domain and on the boundaries would have been done with latin hypercube sampling (LHS).

The plan was to firstly train a PINN on the forward problem, ignoring loss terms $\mathcal{L}_{data}$ and $\mathcal{L}_{param}$ and assuming known reasonable values (for example constant) for the material parameters. The weights and biases from that forward model could then have been read into the mixed PINN, which would then have been trained on the data and parameter

values as well.

Ultimately, the PINN approach was not used, and instead the optimization software modeFRONTIER was used, see Appendix B.5, as another form of machine learning. The reason for this was that in running some initial test code it was found to take too long to reach convergence with the available computational resources. With a PINN it would also have been more difficult to implement any study of the wear scaling factors.

DEPARTMENT OF INDUSTRIAL AND MATERIALS SCIENCE
CHALMERS UNIVERSITY OF TECHNOLOGY
Gothenburg, Sweden
www.chalmers.se

CHALMERS
UNIVERSITY OF TECHNOLOGY